

This is to certify that the

dissertation entitled

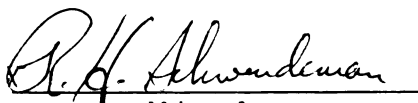
- I. Lineshapes of IR Zero Frequency Double Resonance Spectra in CH_3F . II. IR-MW Sideband Laser Spectroscopy of the ν_3 and $2\nu_3 - \nu_3$ Bands of $^{13}\text{CH}_3\text{F}$ and $^{12}\text{CH}_3\text{F}$. III. IR-IR Double Resonance of $^{13}\text{CH}_3\text{F}$ by means of a Waveguide CO_2 Laser and an IR-MW sideband Laser.

presented by

SANG KUK LEE

has been accepted towards fulfillment
of the requirements for

Ph. D. degree in Chemistry


Major professor
Richard H. Schwendeman

Date 12/10/87



RETURNING MATERIALS:

Place in book drop to
remove this checkout from
your record. FINES will
be charged if book is
returned after the date
stamped below.

--	--	--

- I. LINESHAPES OF INFRARED ZERO FREQUENCY DOUBLE
RESONANCE SPECTRA IN CH_3F
- II. INFRARED-MICROWAVE SIDEBAND LASER SPECTROSCOPY OF
THE ν_3 AND $2\nu_3 - \nu_3$ BANDS OF $^{13}\text{CH}_3\text{F}$ AND $^{12}\text{CH}_3\text{F}$
- III. INFRARED-INFRARED DOUBLE RESONANCE OF $^{13}\text{CH}_3\text{F}$
BY MEANS OF A WAVEGUIDE CO_2 LASER
AND AN INFRARED-MICROWAVE SIDEBAND LASER

By

Sang Kuk Lee

A DISSERTATION

Submitted to
Michigan State University
in partial fulfillment of the requirement
for the degree of

DOCTOR OF PHILOSOPHY

Department of Chemistry

1986

178

o
i
T
r
S
ba
li
th
la
exp

1277428

ABSTRACT

- I. LINESHAPES OF INFRARED ZERO FREQUENCY DOUBLE
RESONANCE SPECTRA IN CH_3F
- II. INFRARED-MICROWAVE SIDEBAND LASER SPECTROSCOPY OF
THE ν_3 AND $2\nu_3 + \nu_3$ BANDS OF $^{13}\text{CH}_3\text{F}$ AND $^{12}\text{CH}_3\text{F}$
- III. INFRARED-INFRARED DOUBLE RESONANCE OF $^{13}\text{CH}_3\text{F}$
BY MEANS OF A WAVEGUIDE CO_2 LASER
AND AN INFRARED-MICROWAVE SIDEBAND LASER

By

Sang Kuk Lee

Experimental measurements and theoretical calculations of infrared zero frequency double resonance (IR-ZF) spectra in a symmetric top molecule without inversion are described. The IR-ZF spectra are infrared radiofrequency double resonance spectra at RF frequencies tending toward zero. Spectra are shown for a near-resonant transition in the ν_3 band of $^{13}\text{CH}_3\text{F}$ that is resonant with the 9P(32) CO_2 laser line in the absence of a D.C. field and for a transition in the ν_3 band of $^{12}\text{CH}_3\text{F}$ that is resonant with the 9P(22) CO_2 laser line in the presence of a D.C. field. All of the experimental lineshapes are in good qualitative agreement

and the spectra in a Stark field are in excellent quantitative agreement with lineshapes predicted by the theory that is presented. The theory treats the effect of the RF radiation as a high-frequency Stark field and is shown to predict the known lineshape of infrared microwave two-photon transitions in symmetric top molecules without inversion.

A large number of transitions in the ν_3 and $2\nu_3 + \nu_3$ bands of $^{12}\text{CH}_3\text{F}$ and $^{13}\text{CH}_3\text{F}$ have been recorded at Doppler-limited resolution by means of an infrared laser microwave sideband spectrometer which was assembled at Michigan State University. For the $^{12}\text{CH}_3\text{F}$ spectra, the spectrometer was modified to include power leveling by incorporating a feed-back control to the microwave source. The sidebands were generated in a CdTe single crystal that was simultaneously irradiated by a CO_2 infrared laser and a high power microwave source operating in the 8.2 - 18.0 GHz region. The J and K structures of the bands were well resolved except for the lowest K values. Frequencies of transitions involving J values up to 39 and K values up to 16 for $^{12}\text{CH}_3\text{F}$ and J values up to 47 and K values up to 16 for $^{13}\text{CH}_3\text{F}$ are reported. Vibration-rotation parameters for the $\nu_3 = 0, 1$, and 2 states were obtained by fitting to the experimental frequencies. These parameters reproduce the experimental values with standard deviations for an object of unit weight (SD) of 1.33 MHz for the fundamental and 1.37 MHz for the hot band for $^{12}\text{CH}_3\text{F}$ and 2.45 MHz for the

fundamental and 1.37 MHz for the hot band for $^{13}\text{CH}_3\text{F}$.

A waveguide CO_2 laser for pumping and an infrared-microwave sideband laser for probing were used to study infrared-infrared double resonance in $^{13}\text{CH}_3\text{F}$. With the tunable range of a sideband system, several kinds of three-level double resonance and many four-level double resonance experiments could be carried out. The evidence for direct pumping of a particular velocity component could be observed by three-level double resonance. Evidence for indirect pumping of all rotational energy levels in the first excited vibrational state ($v_3 = 1$) was obtained by four-level double resonance experiments. Finally, evidence for vibration-vibration energy transfer was confirmed. The indirect pumping effect appeared to be useful not only for identification and observation of hot bands but also for characterizing the mechanism of the optical pumping.

To my family

ACKNOWLEDGMENTS

I would like to thank my advisor, Professor Richard H. Schwendeman for his kindly guidance and encouragement during the course of this study and preparation of this thesis.

I wish to thank all of my family for their support and endurance.

The financial support of the National Science Foundation is gratefully acknowledged.

Finally, I acknowledge all the members of this group and Mr. Martin Rabb for their friendship and stimulating discussions.

C

A

E

P

CE

CE

TABLE OF CONTENTS

Chapter	Page
LIST OF TABLES	VII
LIST OF FIGURES	IX
PART I. LINESHAPES OF INFRARED ZERO FREQUENCY	
DOUBLE RESONANCE SPECTRA IN CH_3F	1
CHAPTER I. INTRODUCTION	2
CHAPTER II. THEORY	6
CHAPTER III. EXPERIMENT	17
CHAPTER IV. CALCULATIONS	25
Doppler Width	26
RF Rabi Frequency	26
IR Rabi Frequency	27
CHAPTER V. RESULTS AND DISCUSSION	30
APPENDIX A	42
REFERENCES	45
PART II. INFRARED MICROWAVE SIDEBAND LASER	
SPECTROSCOPY OF THE ν_3 AND $2\nu_3 + \nu_3$	
BANDS OF $^{13}\text{CH}_3\text{F}$ AND $^{12}\text{CH}_3\text{F}$	47
CHAPTER I. INTRODUCTION.	48
CHAPTER II. THEORY	54

C

C

RE

PA

CHA

CHA

Introduction	54
Rotational Energy - General Theory	55
Rigid Symmetric Top Molecules	59
Symmetric Top Wave Functions	63
Nonrigid Symmetric Top Molecules	66
Intensities of Symmetric Top Transitions	81
CHAPTER III. INSTRUMENTATION	86
Introduction	86
Generation of IR - MW Sideband Radiation	88
Structure of the Modulator	89
Adjustment of the Crystal Position in the Modulator	94
CHAPTER IV. EXPERIMENT	96
CHAPTER V. RESULTS AND DISCUSSION.	108
ν_3 Fundamental and $2\nu_3 + \nu_3$ Hot Bands of $^{13}\text{CH}_3\text{F}$	108
ν_3 Fundamental and $2\nu_3 + \nu_3$ Hot Bands of $^{12}\text{CH}_3\text{F}$	134
REFERENCES	159
 PART III. INFRARED-INFRARED DOUBLE RESONANCE OF $^{13}\text{CH}_3\text{F}$ BY MEANS OF A WAVEGUIDE CO_2 LASER AND AN INFRARED-MICROWAVE SIDEBAND LASER .	164
CHAPTER I. INTRODUCTION.	165
CHAPTER II. THEORY	177

Saturation Process	177
Double Resonance in a Three-Level System . .	184
CHAPTER III. EXPERIMENT	187
Waveguide CO ₂ Laser	189
CHAPTER IV. RESULTS AND DISCUSSION.	192
Three-Level Double Resonance	196
Four-Level Double Resonance	204
REFERENCES	218

VII

LIST OF TABLES

Table		Page
1.	Sources of Data for Fits of the ν_3 Band of $^{13}\text{CH}_3\text{F}$	112
2.	Comparison of Observed and Calculated Frequencies in the ν_3 Band of $^{13}\text{CH}_3\text{F}$	113
3.	Comparison of Observed and Calculated Frequencies in the $2\nu_3 + \nu_3$ Band of $^{13}\text{CH}_3\text{F}$. .	123
4.	Vibration-Rotation Parameters for $^{13}\text{CH}_3\text{F}$. . .	126
5.	The Fitting Parameters of Watson's Form of Pade Approximant for ν_3 Band of $^{13}\text{CH}_3\text{F}$. . .	132
6.	Vibrational Dependence of Vibration-Rotation Parameters for $^{13}\text{CH}_3\text{F}$	133
7.	Sources of Data for Fits of the ν_3 Band of $^{12}\text{CH}_3\text{F}$	137
8.	Comparison of Observed and Calculated Frequencies in the ν_3 Band of $^{12}\text{CH}_3\text{F}$	139
9.	Comparison of Observed and Calculated Frequencies in the $2\nu_3 + \nu_3$ Band of $^{12}\text{CH}_3\text{F}$. .	146
10.	Vibration-Rotation Parameters for $^{12}\text{CH}_3\text{F}$. . .	149

VIII

11.	Comparison of Ground-State Rotational Constants of $^{12}\text{CH}_3\text{F}$	151
12.	The Fitting Parameters of Watson's Form of Pade Approximant for ν_3 Band of $^{12}\text{CH}_3\text{F}$. . .	152
13.	Vibrational Dependence of Vibration-Rotation Parameters for $^{12}\text{CH}_3\text{F}$	153
14.	Coincidences Between Calculated Frequencies for ν_3 Band of $^{13}\text{CH}_3\text{F}$ and CO_2 Laser Frequencies.	155
15.	Coincidences Between Calculated Frequencies for $2\nu_3 + \nu_3$ Band of $^{13}\text{CH}_3\text{F}$ and CO_2 Laser Frequencies.	156
16.	Coincidences Between Calculated Frequencies for ν_3 Band of $^{12}\text{CH}_3\text{F}$ and CO_2 Laser Frequencies.	157
17.	Coincidences Between Calculated Frequencies for $2\nu_3 + \nu_3$ Band of $^{12}\text{CH}_3\text{F}$ and CO_2 Laser Frequencies.	158

IX

LIST OF FIGURES

Figure	Page
--- PART I ---	
1. Block diagram of the infrared radiofrequency double resonance spectrometer used for the study of infrared zero frequency double resonance in a D.C. Stark field.	18
2. IR-ZF spectra in zero D.C. Stark field for the $Q_R(4,3)$ transition in the ν_3 band of $^{13}\text{CH}_3\text{F}$. The infrared source was the 9P(32) CO_2 laser operating at a power of ~100 mW. The amplitude of the RF field was ~1.3 V/cm. The sample pressures were: ... 22.9 mTorr; xxx 35.8 mTorr; +++ 44.0 mTorr.	21
3. IR-ZF spectra in zero D.C. Stark field for the $Q_R(4,3)$ transition in the ν_3 band of $^{13}\text{CH}_3\text{F}$. The infrared source was the 9P(32) CO_2 laser operating at a power of ~100 mW. The sample pressure was 13.2 mTorr. The RF amplitudes were: ... ~1.1 V/cm; xxx ~0.84 V/cm; +++ ~0.67	

- V/cm. 22
4. IR-ZF spectra in a D.C. Stark field of 9738.2 V/cm for the $m = 1 \rightarrow 0$ component of the $Q_P(2,1)$ transition in the ν_3 band of $^{12}\text{CH}_3\text{F}$. The infrared source was the 9P(22)CO₂ laser at a power of ~100 mW. The RF amplitude was ~0.67 V/cm. The sample pressures were: $\bullet\bullet\bullet$ 6.6 mTorr; xxx 4.9 mTorr; +++ 2.9 mTorr. 23
5. IR-ZF spectra in $^{12}\text{CH}_3\text{F}$. The transition, laser, and laser power were the same as in Fig. 4. The sample pressure was 6.6 mTorr. The RF amplitudes were: $\bullet\bullet\bullet$ ~1.1 V/cm; xxx ~0.84 V/cm; +++ ~0.67 V/cm. 24
6. Results of least squares fit of experimental IR-ZF spectrum in $^{12}\text{CH}_3\text{F}$. The transition, laser, and laser power were the same as in Fig. 4. The sample pressure was 6.6 mTorr and the RF amplitude was ~0.67 V/cm. Observed spectrum xxx; observed - calculated spectrum $\bullet\bullet\bullet$ 31
7. Results of least squares fit of experimental IR-ZF spectrum in $^{12}\text{CH}_3\text{F}$. The transition, laser,

XI

and laser power were the same as in Fig. 4. The sample pressure was 6.6 mTorr and the RF amplitude was ~1.1 V/cm. Observed spectrum xxx; observed - calculated spectrum ... 32

8. Pressure dependence of calculated IR-ZF spectrum: laser power 32 mW; RF amplitude 0.73 V/cm; laser frequency offset 0.0 MHz; no. of harmonics 4. Sample pressures: ... 6.5 mTorr; xxx 4.5 mTorr; +++ 3.0 mTorr. 35

9. RF amplitude dependence of calculated IR-ZF spectrum: laser power 32 mW; sample pressure 6.5 mTorr; laser frequency offset 0.0 MHz; no. of harmonics 4. RF amplitude: ... 1.1 V/cm; xxx 0.92 V/cm; +++ 0.73 V/cm. 36

10. Dependence of calculated IR-ZF spectra on laser frequency offset. Laser power 32 mW; sample pressure 6.5 mTorr; RF amplitude 0.73 V/cm; no of harmonics 4. Laser frequency offsets: ... 0.0 MHz; xxx 5.0 MHz; +++ 10.0 MHz. 37

11. Infrared laser power dependence of calculated IR-ZF spectra. Sample pressure 6.5 mTorr; RF

XII

- amplitude 0.73 V/cm; laser frequency offset 0.0 MHz; no of harmonics 4. Laser powers: *** 32 mW; xxx 16 mW; +++ 9mW. 38
12. Dependence of calculated IR-ZF spectra on no. of harmonics included in the calculation. Laser power 32 mW; sample pressure 6.5 mTorr; laser frequency offset 0.0 MHz; RF amplitude 1.5 V/cm. No. of harmonics: *** 4; xxx 3; +++ 2. . . . 39
13. Dependence of calculated IR-ZF spectra on no. of harmonics included in the calculation. Laser power 32 mW; sample pressure 6.5 mTorr; laser frequency offset 0.0 MHz; RF amplitude 0.73 V/cm. No. of harmonics: *** 4; xxx 3; +++ 2. . 41
- PART II ---
1. Classical motion of a symmetric top. This is a combined rotation around the molecular axis associated with P_z and a precession of this axis around the total angular momentum P . The molecule represented is CH_3F 60

XIII

2. Energy levels of typical symmetric top molecules
(A) prolate, (B) oblate symmetric top. 62

3. Normal vibrations of a linear XY_2 molecule and
the effects of Coriolis coupling. ν_2 is a
degenerate bending vibration and the arrows
attached to the atoms represent one component of
the vibration. The other component (not shown)
results from identical motions perpendicular to
the plane of the paper. 68

4. Coriolis coupling of the degenerate bending
vibrations in a XYZ_3 symmetric top. (A) and
(B) illustrate two components of the degenerate
bending mode. (C) shows the coupling effect of
the Coriolis force on the (A) mode as it tends
to induce the (B) mode. In all three
illustrations, the figure axis is perpendicular
to the plane of the paper and only off-axis
atoms are shown. 70

5. Allowed transitions and interactions for an
 A_1 and an E fundamental of a C_{3v} molecule. . . 74

6. Diagrammatic representation of interaction between an A_1 and an E vibration states for $J = 3$. Each dot represents a basis function characterized by a particular values of k and λ_g ; the lines represent Coriolis interactions, connecting states of the same $(k - \lambda_g)$. Except for the extreme values of $(k - \lambda_g)$ the secular equation factors into (3×3) blocks. 75

7. Diagram of the sideband modulator, in which the CdTe crystal embedded between two Al_2O_3 slabs to achieve velocity match. The tapered double-ridged waveguide section (upper half removed) provides impedance match to incoming/outgoing standard waveguide sizes. 91

8. Experimental diagram for adjusting the position of crystal inside modulator. 93

9. Variation of coupling efficiency with the crystal position. (A) represents input microwave power with frequency. (B) and (C) indicate the reflected microwave power from the modulator with improper position and optimum position, respectively. 95

10. Block diagram of IR-MW sideband laser spectrometer used for the measurement of $^{13}\text{CH}_3\text{F}$, set for linear absorption spectroscopy of gases. 97

11. Variation of the output laser power (B) and the differential signal (A) displayed on screen with piezoelectric translator voltage. The signal due to Lamb-dip can be easily distinguished from that due to the end of mode. 99

12. Unnormalized spectrum obtained by IR-MW sideband laser spectrometer. The signal and the reference show the large fluctuation in amplitude with frequency. The lower sideband generated from the $10\text{R}(20)\text{CO}_2$ laser line used with ~ 200 mTorr of $^{13}\text{CH}_3\text{F}$ for the ν_3 P(27,K) transition. 104

13. Block diagram of MW feedback controlled IR-MW sideband laser spectrometer set for linear absorption spectroscopy of gases used for $^{12}\text{CH}_3\text{F}$ 106

14. Typical spectrum obtained by feedback controlled IR-MW sideband system for lineshape experiment.

- The lower sideband generated from the 9P(18)CO₂ laser line used with 3.2 cm long sample cell with 0.1 sec. of time constant. 107
15. Typical spectrum of the ν_3 band of ¹³CH₃F obtained with the IR-MW sideband laser spectrometer. The lower sideband generated from the 10R(20)CO₂ laser line was used with ~200 mTorr of sample pressure in an 1 m long sample cell. From this spectrum, the intensity rule according to K values can be clearly seen. 109
16. Typical spectrum of the $2\nu_3 + \nu_3$ band of ¹³CH₃F obtained with the IR-MW sideband laser spectrometer. The lower sideband generated from the 10R(30)CO₂ laser line was used with ~1.0 Torr of sample pressure in an 1 m long sample cell. 111
17. Typical spectrum of the ν_3 band of ¹²CH₃F obtained with the MW feedback controlled IR-MW sideband laser spectrometer. Two spectra were obtained at different pressure; ~100 mTorr for the spectrum at the left

XVII

and ~50 mTorr for spectrum at the right.
This spectrum shows much improved baseline
and lineshape. The lower sideband generated
from the 9R(12)CO₂ laser line was used. . . . 135

--- PART III ---

1. Diagrammatic representations of three-level
double resonance spectroscopy (A)-(C) and
four-level double resonance spectroscopy
(D)-(F). 168
2. Energy level schemes in four-level double
resonance experiments. The light and heavy
arrows represent low and high power radiation,
respectively. The wavy arrows represent
paths of collisional energy transfer. 170
3. Change in the particle velocity distribution
over two-levels of transition under the action
of a laser wave of frequency ν . The
z-component of velocity of particles
interacting with the light wave is $v_{\text{res}} =$
 $c(\nu - \nu_0)/\nu_0$ 172

XVIII

4. Time evolution of the population of the excited state of a two-level system subjected to a coherent dipole perturbation. On-resonance pumping ($\delta = 0$) results in the slowest oscillations having the greatest amplitude. 180
5. Schematic arrangement of pumping and probing radiation in many infrared-infrared double resonance experiments. 183
6. Experimental diagram of infrared-infrared double resonance by means of a waveguide CO_2 laser for pumping and an infrared-microwave sideband laser for probing. 188
7. Cross sectional view of the waveguide CO_2 laser used for this experiment. 191
8. Energy level diagrams for the waveguide CO_2 laser and infrared-microwave sideband laser system used for infrared-infrared double resonance in $^{13}\text{CH}_3\text{F}$ in this work. 193

XIX

9. Variation of the position of the pumped molecular velocity group with pumping frequency. The transition is $^Q R(5,3)$ of the $2\nu_3 + \nu_3$ band of $^{13}\text{CH}_3\text{F}$. The $^Q R(4,3)$ transition of the ν_3 band was pumped at a different frequency for each the spectra A-F. . 195

10. Variation of the range of the molecular velocity group pumped with the modulation amplitude of the pumping laser. The modulation amplitude was increased in steps from (A) to (E). The $^Q R(4,3)$ transition of the ν_3 band was pumped. 197

11. Observation of a saturation-dip in the $^Q P(6,3)$ transition in the ν_3 band from three-level double resonance with a common level in the upper state. The $^Q R(4,3)$ transition in the ν_3 band was pumped. 199

12. Observation of a saturation-dip in the $^Q P(6,3)$ transition in the ν_3 band from three-level double resonance with a common upper level. The pumping frequency in this figure has been shifted slightly from that in Figure 11. . . 200

13. Observation of a saturation-dip in the $Q_P(4,3)$ transition in the ν_3 band from three-level double resonance with a common level in the lower state. The $Q_R(4,3)$ transition in the ν_3 band was pumped. 202

14. Observation of the increased intensity of the $Q_R(5,3)$ transition in the $2\nu_3 + \nu_3$ band that results from three-level double resonance with a common level that is the upper state for the pumping transition and the lower state for the probing transition. Also shown is the increased intensity of the remaining $Q_R(5,K)$ transitions that result from increased population of the $\nu_3 = 1$ state caused by pumping the $Q_R(4,3)$ transition in the fundamental band. 203

15. Variation of the double resonance effect on the intensity of the $Q_R(5,3)$ transition in the $2\nu_3 + \nu_3$ band with sample pressure. The lower level of this transition is directly pumped by pumping the $Q_R(4,3)$ transition in the ν_3 band. The solid line is a smooth curve drawn through the points. 205

16. Observation of the indirect pumping effect to all rotational energy levels in the first excited vibrational state ($\nu_3 = 1$) by pumping the $Q_R(4,3)$ transition in the ν_3 band. The intensity of all transitions in the $2\nu_3 \leftarrow \nu_3$ band appears to increase with pumping. . . . 207

17. Variation of the effect of indirect pumping on the intensity of the $Q_P(17,3)$ transition of the $2\nu_3 \leftarrow \nu_3$ band with sample pressure. The $Q_R(4,3)$ transition in the ν_3 band was pumped. The solid line is a smooth curve drawn through the points.. . . . 209

18. Schematic diagram of the molecular population changes caused by pumping the $Q_R(4,3)$ transition in the ν_3 band. The numbers above each level are relative populations. . . . 210

19. Comparison of the effects of indirect pumping and heating on transitions in the ν_3 fundamental and $2\nu_3 \leftarrow \nu_3$ hot bands of $^{13}\text{CH}_3\text{F}$. The spectra was recorded (A) without pumping at room temperature, (B) with pumping of the $Q_R(4,3)$ transition in the ν_3 band at room temperature,

XXII

and (C) without pumping at $-100\text{ }^{\circ}\text{C}$	212
20. Observation of the effect of vibrational energy transfer between $^{13}\text{CH}_3\text{F}$ and $^{12}\text{CH}_3\text{F}$ on the intensity of the $^{\text{Q}}\text{Q}(12,9)$ transition in the $2\nu_3 + \nu_3$ band of $^{12}\text{CH}_3\text{F}$. The $^{\text{Q}}\text{R}(4,3)$ in the ν_3 band of $^{13}\text{CH}_3\text{F}$ was pumped.	
	216

- PART I -

**LINESHAPES OF INFRARED ZERO FREQUENCY DOUBLE RESONANCE
SPECTRA IN CH₃F**

CHAPTER I

INTRODUCTION

Infrared radiofrequency double resonance spectra of symmetric top molecules are often characterized by a strong asymmetric absorption lineshape at very low RF frequency. The appearance of this absorption has been used as evidence of a near resonance between the laser line and a molecular transition(1). It therefore identified the laser line as a fruitful one for double resonance at higher RF frequencies.

In a double resonance process, a three level system is simultaneously irradiated by two different fields of different frequencies. One radiation, which has a fixed frequency in resonance, saturates one transition; the other field, which is generally weaker than the first one has a swept frequency. A variation of absorption is then detected on the second field when the pumping field becomes resonant with a transition. These processes were studied by Autler and Townes(2) in 1950. In 1952 Brossel and Bitter performed a double resonance experiment in which the Zeeman splitting of an excited state of a Hg atom screened by Doppler broadening was recorded(3). This technique was ultimately extended to infrared radiofrequency double resonance by Curl and Oka(4).

An absorption peak in normal spectroscopy shows a particular lineshape depending on the molecular environment;

re
in
or
re
9
Q
o
n
c
t

in very low pressure gas the absorption peak exhibits a Gaussian lineshape which is dependent on the frequency of the radiation, temperature of the sample, and the molecular velocity distribution. At higher pressures, the peak is homogeneously pressure broadened, which typically shows a Lorentzian lineshape depending on the molecular dynamics. At intermediate pressures the peak appears as a Voigt profile, which is a convolution of the Gaussian lineshape and the Lorentzian lineshape.

When the infrared zero frequency double resonance was first encountered by A. Jacques at Michigan State University, the observation of an apparently Doppler-free infrared absorption suggested that it might have potential for the determination of collisional relaxation rates. Therefore, an investigation was begun of the dependence on sample pressure and RF power of the infrared zero frequency double resonance that occurs as a result of the well-known near coincidences of the $^Q Q(12,2)$ transition in the ν_3 band of $^{12}\text{CH}_3\text{F}$ with the $9\text{P}(20)\text{CO}_2$ laser line(5) and of the $^Q R(4,3)$ transition in the ν_3 band of $^{13}\text{CH}_3\text{F}$ with the $9\text{P}(32)\text{CO}_2$ laser line(6). Although most IR-RF double resonance studies have been done with an absorption cell inside the laser cavity, an extra-cavity cell was chosen in order to remove the nonlinear effects of laser gain from the recorded lineshape.

An additional interesting feature of the infrared zero

frequency double resonance was the fact that the rotating wave approximation, commonly used in double resonance theories(7), is expected to fail for this effect. The rotating wave approximation is based on the assumption that the frequencies of the radiation are much larger than the relaxation rates or Rabi frequencies involved. This can hardly be true if the frequency of one of the radiation sources is near zero. Thus, it was necessary to extend the double resonance theory to include the IR-ZF effect. The new theory resembles theories previously derived to describe the high-frequency Stark effect(8).

The theory developed to explain the IR-ZF lineshape was in qualitative but not good quantitative agreement with the observed lineshapes(9). This was attributed to the m degeneracies of the states involved in the transitions. At first, a simple sum over the m components was tried without success. It was concluded then that the disagreement between theory and experiment was the result of the many level crossings of the m components that occur at zero field. These crossings were not taken into account in the theory.

In order to determine whether the derived theory could accurately represent an IR-ZF lineshape, I recorded the IR-ZF absorption of a single m component of a transition brought into resonance with the laser by application of a D.C. Stark field. The transition chosen was the $^Q P(2,1)$, m

= 1 ← 0 in the ν_3 band of $^{12}\text{CH}_3\text{F}$. This transition has been shown to be in resonance with the 9P(22) CO_2 laser line in an electric field of 9738.2 V/cm(6).

The purpose of this study is to describe the theory derived for the IR-ZF double resonance effect and to compare observed and calculated lineshapes for a single π component of a transition in resonance with an infrared laser. As a by-product, it is shown that the new high-frequency Stark effect theory provides an alternative to the usual description of infrared microwave two-photon absorption in symmetric top molecules without inversion(10-12).

The next chapter outlines the theory used to calculate lineshapes and Chapter III describes the IR-ZF experimental apparatus. In Chapter IV, the methods and equations for theoretical calculation of the input parameters are derived and in Chapter V, the experimental and calculated lineshapes are compared and discussed. Finally, in Appendix A, the theory is extended to the case of infrared microwave two-photon absorption.

CHAPTER II

THEORY*

We assume a symmetric top in which the inversion splitting is negligible. In the presence of an electric field that is sufficient to separate the m components the states are singly or doubly degenerate (ignoring nuclear spin degeneracy); we assume a transition between doubly degenerate states. The basis functions are chosen to be the linear combinations of mixed parity (i.e., the \pm linear combinations of single parity states), in which case the electric dipole moment matrix element that connects the degenerate partners vanishes. It is therefore sufficient, within the electric dipole approximation for both radiation and collisions, to consider only one of the two pairs of states involved in the transition. We also assume that the rotating wave approximation is valid for the infrared radiation, since the infrared frequency is much greater than either the Rabi frequency or the relaxation rates. This approximation allows the two states to be separated from the states of other rotational levels so that we are left with the simple case of a two-state system.

* The theory described in this chapter was developed by R. H. Schwendeman.

Let us consider a two level system of a symmetric top molecule (that is the case of for CH_3F) irradiated by IR and RF fields whose planes of polarization are perpendicular to one another. The sample is also in a D.C. Stark field which is assumed to be parallel to the RF field. Since the selection rules on the IR transition are $\Delta M = \pm 1$, one M state in the ground vibrational level is connected by the IR field to either the $M+1$ or $M-1$ state in the upper vibrational level. We assume that only one of these transitions has significant probability at the IR frequency of interest.

In the case of a symmetric top, energy levels have a first-order Stark effect, so diagonal perturbation matrix elements are non-zero. In this case, they are also time dependent because of the RF field. Starting from these points, the absorption of IR radiation by a two level system having a first order Stark effect can be calculated by using the density matrix formalism.

As the first step, the Bloch equations are written in the rotating wave approximation for the IR field. The population and coherences are then developed in Fourier series dependent on the RF frequency. Density matrix elements have to be calculated by using the equation of motion of ρ ;

$$\frac{d\rho}{dt} = -\Gamma(\rho - \rho^0) - \frac{i}{\hbar}[\mathbf{H}, \rho] \quad (1)$$

where Γ is the relaxation matrix and ρ^0 is the density matrix at thermal equilibrium.

The time dependence due to the IR field can be treated by using the rotating wave approximation. A change of variables is done as follows;

$$n = \rho_{aa} - \rho_{bb} \quad (2)$$

$$\rho_{ba} = (u + iv)e^{-i(\omega_l t - k_l z)} \quad (3)$$

Here, n is the population difference between levels a and b , ω_l is the IR frequency, and k_l is the wave vector. By substituting from Eqs. (2) and (3) for ρ_{aa} , ρ_{bb} , and ρ_{ba} ($= \rho_{ab}^*$) in the density matrix, Eq. (1), and by ignoring rapidly oscillating terms (rotating wave approximation), we obtain the Bloch equations for a two-state system(7) as

$$dn/dt = -2xv - \gamma_1(n - n^0) \quad (4)$$

$$du/dt = -v\delta - \gamma_2 u \quad (5)$$

$$dv/dt = u\delta + \frac{xn}{2} - \gamma_2 v \quad (6)$$

where

$$x = \mu_{ba} \epsilon_l^0 / \hbar \quad (7)$$

and

$$\delta = \omega_{\text{I}} - \omega_{\text{ba}} \quad . \quad (8)$$

Here, $\mu_{\text{ba}} = \mu_{\text{ab}}$ is the dipole moment matrix element connecting states a and b, ϵ_{I}^0 is the amplitude of the electric field of the infrared radiation written as

$$\epsilon_{\text{I}} = \epsilon_{\text{I}}^0 \cos \omega_{\text{I}} t \quad , \quad (9)$$

and $\omega_{\text{ba}} = (E_{\text{b}} - E_{\text{a}})/\hbar$ with E_{a} and E_{b} the energies of the states. Finally, in Eqs. (4)-(6) γ_1 and γ_2 are relaxation rates for n and ρ_{ba} , respectively, and n^0 is the equilibrium value of n ; ρ_{ba} is assumed to be zero at equilibrium.

The effect of the RF field is introduced as an additional first-order Stark effect. Thus, we assume that

$$\delta = \delta_{\text{a}} + \delta_{\text{b}} (e^{i\omega t} + e^{-i\omega t}) \quad . \quad (10)$$

Here, $\delta = \delta_{\text{a}}$ in the absence of the RF field and

$$\delta_{\text{b}} = (\mu_{\text{bb}} - \mu_{\text{aa}}) \epsilon_{\text{RF}}^0 / 2\hbar \quad (11)$$

where ϵ_{RF}^0 is the amplitude of the RF electric field written as

$$\epsilon_{\text{RF}} = \epsilon_{\text{RF}}^0 \cos \omega t \quad . \quad (12)$$

As a result of the oscillation of δ at RF frequency ω ,

which may be comparable to or even smaller than x , γ_1 , and γ_2 , the density matrix components, n , u , and v will oscillate at frequency ω and overtones of ω .

$$n = \sum_{k=-\infty}^{\infty} n_k e^{ik\omega t} \quad (13)$$

$$u = \sum_{k=-\infty}^{\infty} u_k e^{ik\omega t} \quad (14)$$

$$v = \sum_{k=-\infty}^{\infty} v_k e^{ik\omega t} \quad (15)$$

These Fourier representations for n , u , and v , along with Eq. (10) for δ are substituted into the Bloch Eqs. (4)-(6). We assume that in the steady state \dot{n}_k , \dot{u}_k , and \dot{v}_k , the time derivatives of the Fourier coefficients, vanish. The coefficients of each $e^{ik\omega t}$ are then collected on one side of the equation and set equal to zero. The result is a series of coupled linear equations in the n_k , u_k , and v_k .

For our experiment, the important quantity is the effect of the absorption on the intensity of the infrared beam. The absorption coefficient for infrared radiation is known to be(7)

$$\alpha = (4\pi N \nu_{ab} \omega_l / c) v / \epsilon_l^0 \quad (16)$$

The output of the phase-sensitive detector used to record the spectrum is filtered with a time constant whose reciprocal is much smaller than the lowest usable RF

frequency. Therefore, we need the time-averaged value of α , which is given by

$$\bar{\alpha} = (4\pi N \mu_{ab} \omega_l / c) v_o / \epsilon_l^o. \quad (17)$$

To solve for v_o , expressions for n_k and u_k in terms of the v_k are obtained from Eqs. (4) and (5), respectively, and are substituted into Eq. (6) to give

$$\sum_{l=k-2}^{k+2} a_{k,l} v_l = \delta_{k,0} x n^o / 2 \quad (18)$$

where $\delta_{k,0}$, the Kronecker delta, is equal to one for $k = 0$ and zero otherwise. The fact that only 5 non-zero terms appear in the sum is a result of the first-order perturbation form assumed for the frequency difference δ [Eq. (10)]. In Eq. (18),

$$a_{k,k-2} = a_{k-2,k} = \delta_b^2 / F_{k-1} \quad (19)$$

$$a_{k,k-1} = a_{k-1,k} = \delta_a \delta_b (F_k^{-1} + F_{k-1}^{-1}) \quad (20)$$

$$a_{k,k} = F_k + x^2 / G_k + \delta_a^2 / F_k + \delta_b^2 (F_{k-1}^{-1} + F_{k+1}^{-1}) \quad (21)$$

where $F_k = \gamma_2 + ik\omega$ and $G_k = \gamma_1 + ik\omega$. Eq. (18) can be written in matrix form as

$$\underline{A} \underline{V} = \underline{C} \quad (22)$$

with obvious definitions for \underline{A} , \underline{V} , and \underline{C} . The result is an

infinite complex linear system that must be truncated for solution. The results of calculations for different numbers of harmonics are shown in Chapter V.

It is possible to transform Eq. (22) into a linear system that contains only real numbers. This system can be solved algebraically for any number of harmonics. In order to carry out the transformation of Eq. (22) and to give an algebraic solution for v_0 , the time independent element of v , we apply a transformation to Eq. (22)

$$\underline{S} \underline{A} \underline{S}^{-1} \underline{S} \underline{V} = \underline{S} \underline{C} \quad (23)$$

or

$$\bar{\underline{A}} \bar{\underline{V}} = \bar{\underline{C}} . \quad (24)$$

Here,

$$\bar{\underline{A}} = \underline{S} \underline{A} \underline{S}^{-1} , \quad \bar{\underline{V}} = \underline{S} \underline{V} , \quad \text{and} \quad \bar{\underline{C}} = \underline{S} \underline{C} . \quad (25)$$

For the case of truncation after two harmonics, \underline{S} is chosen to be

$$\underline{S} = \frac{1}{\sqrt{2}} \begin{pmatrix} 1 & 0 & 0 & 0 & 1 \\ 0 & 1 & 0 & 1 & 0 \\ 0 & 0 & \sqrt{2} & 0 & 0 \\ 0 & -i & 0 & i & 0 \\ -i & 0 & 0 & 0 & i \end{pmatrix} \quad (26)$$

in which case \underline{S}^{-1} is easily obtained.

The transformed matrices are

$$\bar{\underline{A}} = \begin{bmatrix} a'_2 & b'_2 & \sqrt{2}c'_1 & -b''_2 & -a''_2 \\ b'_2 & a'_1 + c_0 & \sqrt{2}b'_1 & -a''_1 & -b''_2 \\ \sqrt{2}c'_1 & \sqrt{2}b'_1 & a_0 & \sqrt{2}b''_1 & -\sqrt{2}c''_1 \\ b''_2 & a''_1 & \sqrt{2}b''_1 & a'_1 - c_0 & b'_2 \\ a''_2 & b''_2 & \sqrt{2}c''_1 & b'_2 & a'_2 \end{bmatrix}, \quad (27)$$

$$\bar{\underline{v}} = \begin{bmatrix} \sqrt{2}v'_2 \\ \sqrt{2}v'_1 \\ v_0 \\ \sqrt{2}v''_1 \\ \sqrt{2}v''_2 \end{bmatrix}, \quad \text{and} \quad \bar{\underline{c}} = \begin{bmatrix} 0 \\ 0 \\ xn^0 \\ 0 \\ 0 \end{bmatrix}. \quad (28)$$

In these matrices,

$$a_{k,k} = a'_k + ia''_k, \quad a_{k-1,k} = b'_k + ib''_k, \quad a_{k-1,k+1} = c'_k + ic''_k,$$

$$\text{and } v_k = v'_k + iv''_k.$$

Thus, the linear system in Eq. (24) has only real components.

To solve Eq. (24), we make use of the fact that all of the linear equations in this system except one are homogeneous. This allows development of a general method for reducing the dimensions of the linear system by 2 at a time. In this method the first and last equations are used

to obtain expressions for the first and last components of \bar{v} in terms of the remaining components; these are substituted into the remaining equations. This process is repeated until only a 3x3 linear system remains. The 3x3 linear system can then be solved exactly.

To carry out the procedure just described, we let a_{kl} now be a general element of \bar{A} and v_k be an element of \bar{v} . Then, except for $l = 0$, one of the linear equations in Eq. (22) can be written

$$\sum_{k=-L}^L a_{lk} v_k = 0 \quad (29)$$

where L is the number of harmonics. The dimension of the linear system is $2L+1$. We use the equations for $l = L$ and $l = -L$ to solve for v_L and v_{-L} as follows:

$$v_J = \sum_{k=-L+1}^{L-1} \alpha_{J,k} v_k \quad (30)$$

for $J = \pm L$, where

$$\alpha_{J,k} = \frac{a_{J,-J} a_{-J,k} - a_{J,J} a_{J,k}}{a_{J,J}^2 + a_{-J,J}^2} \quad (31)$$

To obtain these expressions, the symmetry relations $a_{-L,L} = -a_{L,-L}$ and $a_{-L,-L} = a_{L,L}$ were used. These relations hold only for $L \geq 2$, so the reduction process must be stopped when $L = 1$. However, when $L = 1$ the linear system is 3x3 and may be solved trivially.

After substitution for v_L and v_{-L} the linear system is of the form

$$\sum_{k=-L+1}^{L-1} (a_{lk} + a_{l,-L-L,k} + a_{l,L-L,k}) v_k = \delta_{k,0} \quad x n^0/2 \quad (32)$$

which is of dimension $2L-1$.

Two limiting solutions of Eq. (22) are of some interest. First, if $\delta_b = 0$, the usual expression for partially-saturated absorption in a two-level system is obtained. A second limiting solution is that for which $\delta_a = \omega \gg x, \gamma_1, \gamma_2$, or δ_b . This case of two-photon absorption in a symmetric top without inversion is discussed in Appendix A. It is shown there that two-photon absorption in such a molecule can be thought of as a consequence of a high-frequency Stark effect. The expression obtained for the two-photon absorption coefficient is the same as that obtained by a different approach by Oka and Shimizu(10).

In the derivation just given, δ_a [Eq.(10)] depends on ω_l , the infrared frequency seen by the molecule. To take the Doppler effect into account we assume that the overall absorption is a sum of products of the absorption coefficient for each velocity group multiplied by the relative population of each velocity group. The total absorption has to be averaged over the different velocity groups.

$$\bar{\alpha}_\lambda = \int_{-\infty}^{+\infty} \bar{\alpha} f(v_z) dv_z \quad (33)$$

where $f(v_z)$ is the Maxwellian distribution of the velocity component along the propagation axis of the radiation.

However, this Doppler averaging is unusually tedious for case in which the values of x , γ_1 , and γ_2 are small.

Fortunately, toward the end of this project an array processor (FPS-164) became available for the calculations, so that not only individual lineshapes could be calculated, but also a full least squares treatment, including numerical calculation of the required derivatives, could be implemented.

CHAPTER III

EXPERIMENT

Figure 1 is a block diagram of the spectrometer used for this investigation. The CO_2 laser was a 2.2 m water cooled plasma discharge flowing gas system with a 4.0 m cavity mounted on an invar frame, which has been described previously(13). One end of the cavity is a rotatable plane grating with 150 lines/mm and the other end is a partially reflecting (95 %) 10 m radius concave spherical mirror. The combination of the liquid N_2 cooled photovoltaic InSb detector, the phase sensitive detector (PSD), the operational power supply (OPS) and the piezovoltaic (PZT)-driven laser mirror stabilized the laser output to within ± 300 kHz by monitoring the saturation dip in the fluorescence from an intracavity cell filled with CO_2 gas(14). The laser radiation was linearly polarized in a direction determined by the Brewster windows of the discharge tube. The plane of polarization was rotated by using a different mirror configuration for the $\Delta M = \pm 1$ transitions

The sample cell used for this experiment was designed for conventional laser Stark spectroscopy(13) and consisted of a 6-inch glass pipe tee that includes two solid nickel bars, 5 cm x 2 cm x 40 cm, whose large faces are flat to ± 0.5 μm . The bars are separated by optically flat quartz

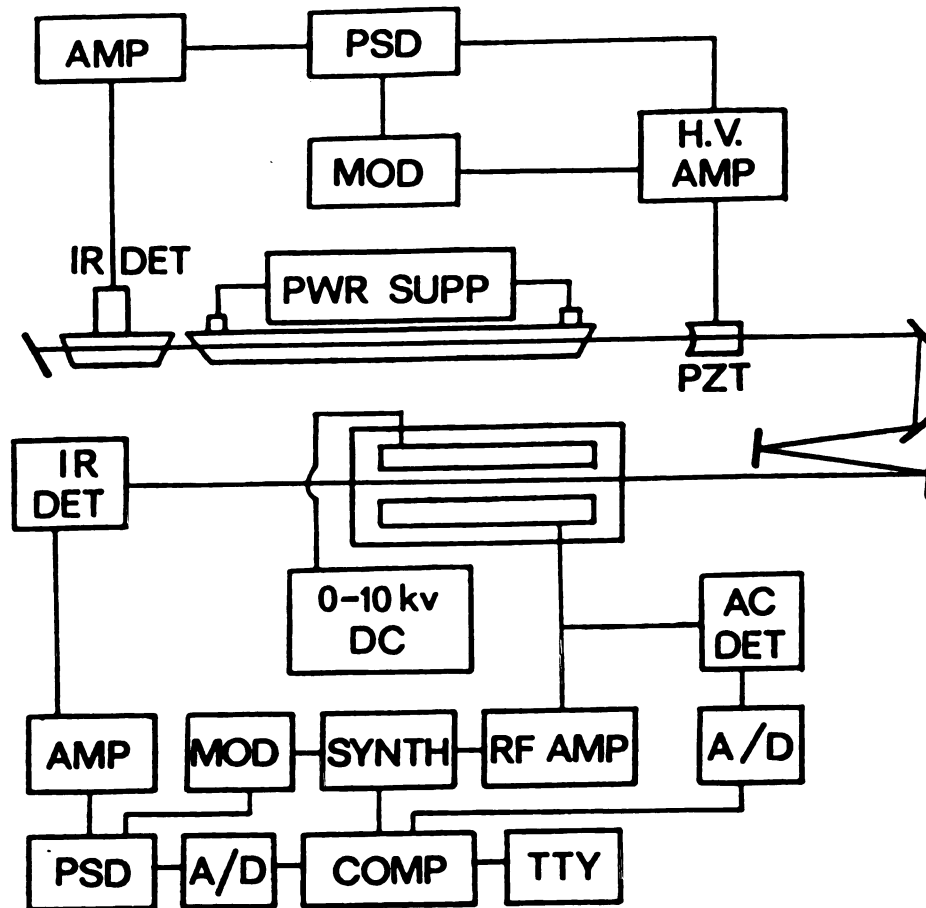


Figure 1. Block diagram of the infrared radiofrequency double resonance spectrometer used for the study of infrared zero frequency double resonance in a D.C. Stark field.

spacers ~3 mm thick. The electrode spacing was determined by measuring the resonant field of the $^Q_{Q(1,1)}$ transition in the ν_3 band of $^{12}\text{CH}_3\text{F}(6)$.

The RF source was a Hewlett Packard Model 8660A synthesizer whose output frequency was controlled by a Digital Equipment Corporation PDP-8E computer through an interface designed by Mr. Martin Rabb at Michigan State University. The output of the synthesizer was chopped at 33.3 kHz by means of a Mini-Circuits Laboratory Model ZAD-3SH double balanced mixer and either amplified or applied directly to the sample cell. The RF voltage at the sample cell was monitored by means of a simple diode detection circuit. The parallel plate Stark cell was shunted by a 50 Ω resistor to improve its high frequency response and seemed to operate satisfactorily over the 0-5 MHz range that was used with it. A maximum of 0.5 V_{rms} of RF amplitude was used.

The laser radiation was monitored by a liquid N₂ cooled Hg-Cd-Te photoconductive detector. The detector output was amplified and processed at the chopping frequency by a phase sensitive detector whose output was digitized and recorded by the minicomputer that controlled the RF frequency. The observed spectrum is the difference between the IR absorption in the presence of the RF field and that without the RF field.

Several spectra recorded at different sample pressures

and RF powers with the 9P(32)CO₂ laser line with ¹³CH₃F in the Stark cell outside the laser cavity are shown in Figs. 2 and 3. The absorption is the result of the near coincidence (~25.8 MHz) between the laser frequency and that of the ^QR(4,3) transition in the ν_3 band(6). Samples of the ¹²CH₃F spectra obtained with the laser Stark cell are shown in Figs. 4 and 5. In these spectra the absorption is of the $m = 1 \leftarrow 0$ component of the ^QP(2,1) transition, which was brought into resonance with the 9P(22)CO₂ laser line by application of a D.C. Stark field of 9738.2 V/cm(6).

The ¹²CH₃F was obtained from Peninsular Chemical Research, whereas the ¹³CH₃F was obtained from Merck. Except for the usual freeze-pump-thaw cycling, the samples were used as received.

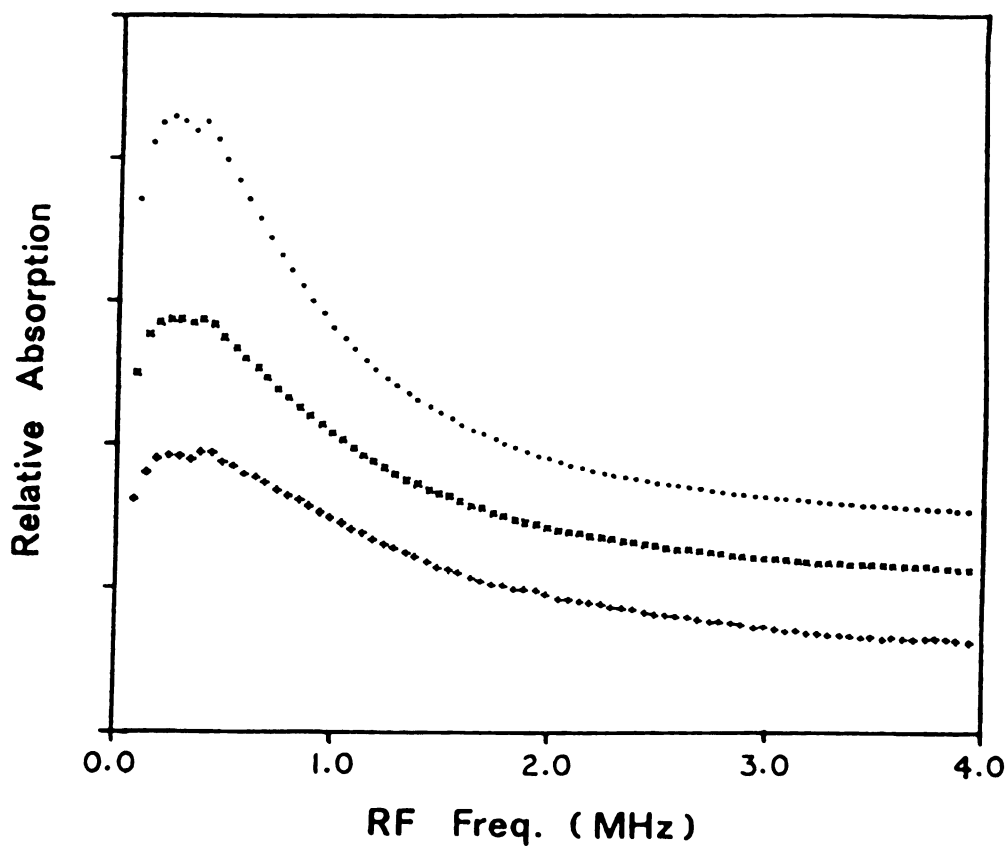


Figure 2. IR-ZF spectra in zero D.C. Stark field for the $Q_R(4,3)$ transition in the ν_3 band of $^{13}\text{CH}_3\text{F}$. The infrared source was the 9P(32) CO_2 laser operating at a power of ~ 100 mW. The amplitude of the RF field was ~ 1.3 V/cm. The sample pressures were: ••• 22.9 mTorr; xxx 35.8 mTorr; +++ 44.0 mTorr.

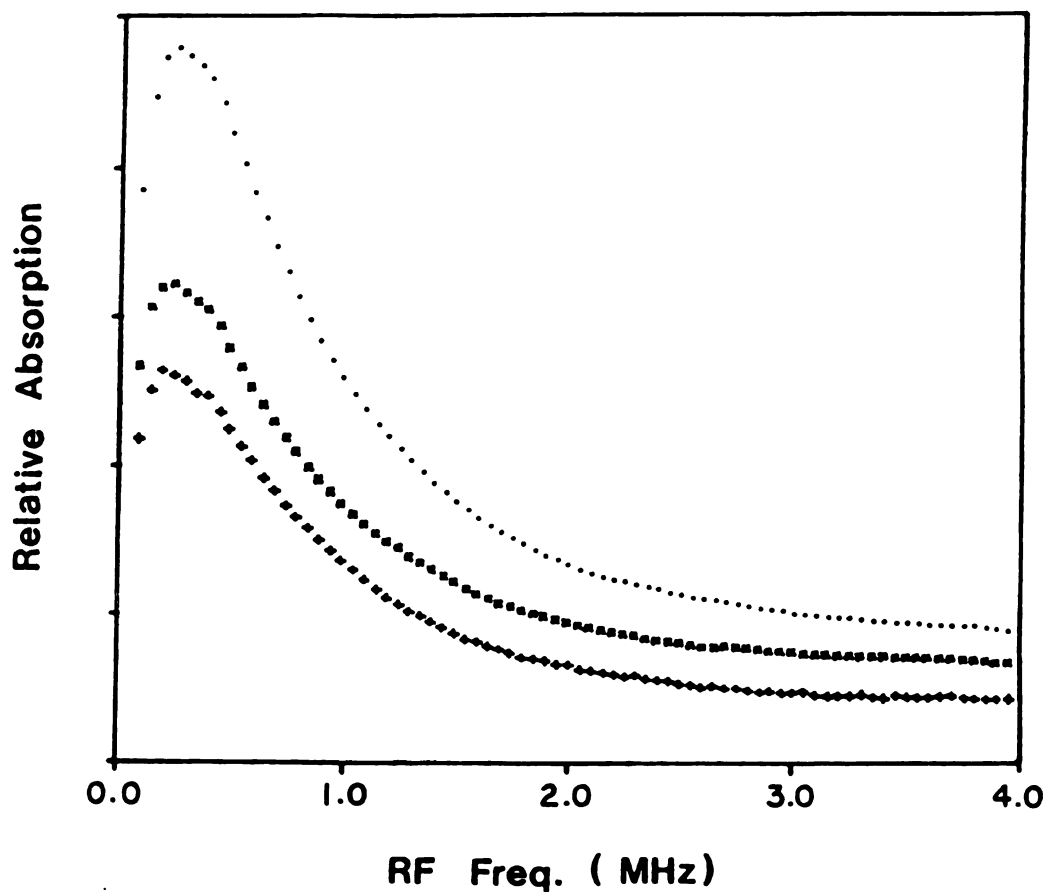


Figure 3. IR-ZF spectra in zero D.C. Stark field for the $Q_R(4,3)$ transition in the ν_3 band of $^{13}\text{CH}_3\text{F}$. The infrared source was the 9P(32) CO_2 laser operating at a power of ~100 mW. The sample pressure was 13.2 mTorr. The RF amplitudes were: ... ~1.1 V/cm; xxx ~0.84 V/cm; +++ ~0.67 V/cm..

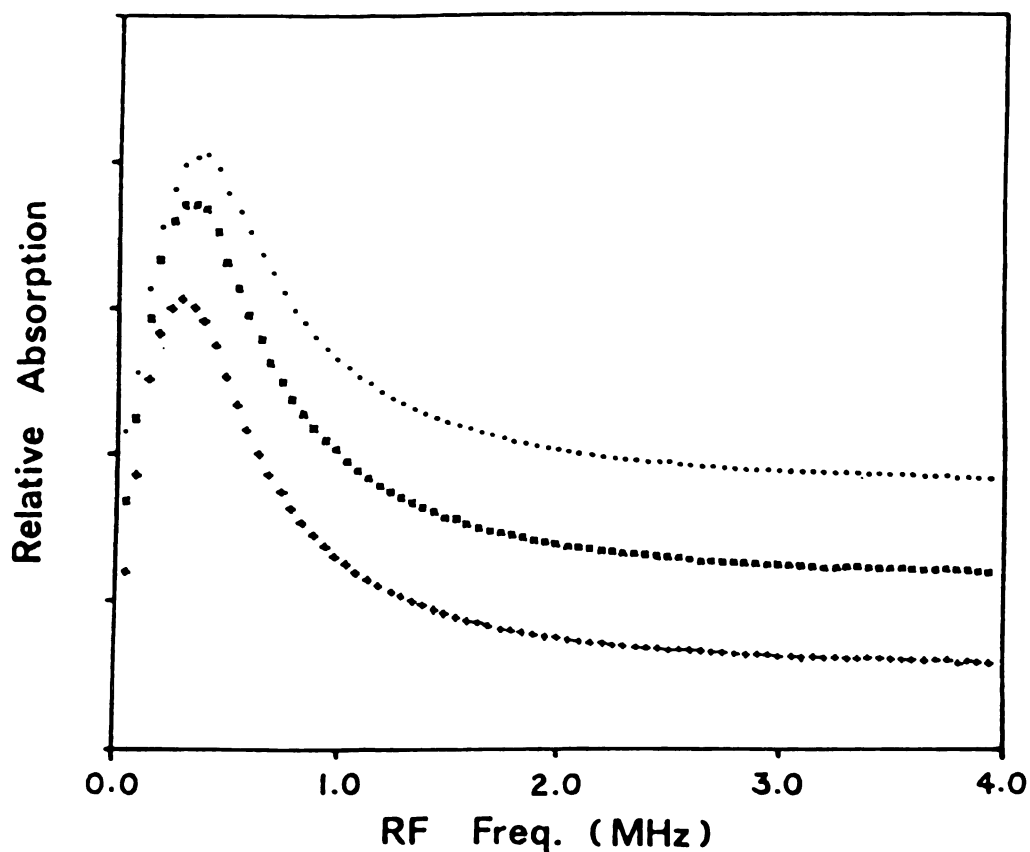


Figure 4. IR-ZF spectra in a D.C. Stark field of 9738.2 V/cm for the $m = 1 \rightarrow 0$ component of the $^Q P(2,1)$ transition in the ν_3 band of $^{12}\text{CH}_3\text{F}$. The infrared source was the 9P(22) CO_2 laser at a power of ~ 100 mW. The RF amplitude was ~ 0.67 V/cm. The sample pressures were: \dots 6.6 mTorr; xxx 4.9 mTorr; $+++$ 2.9 mTorr.

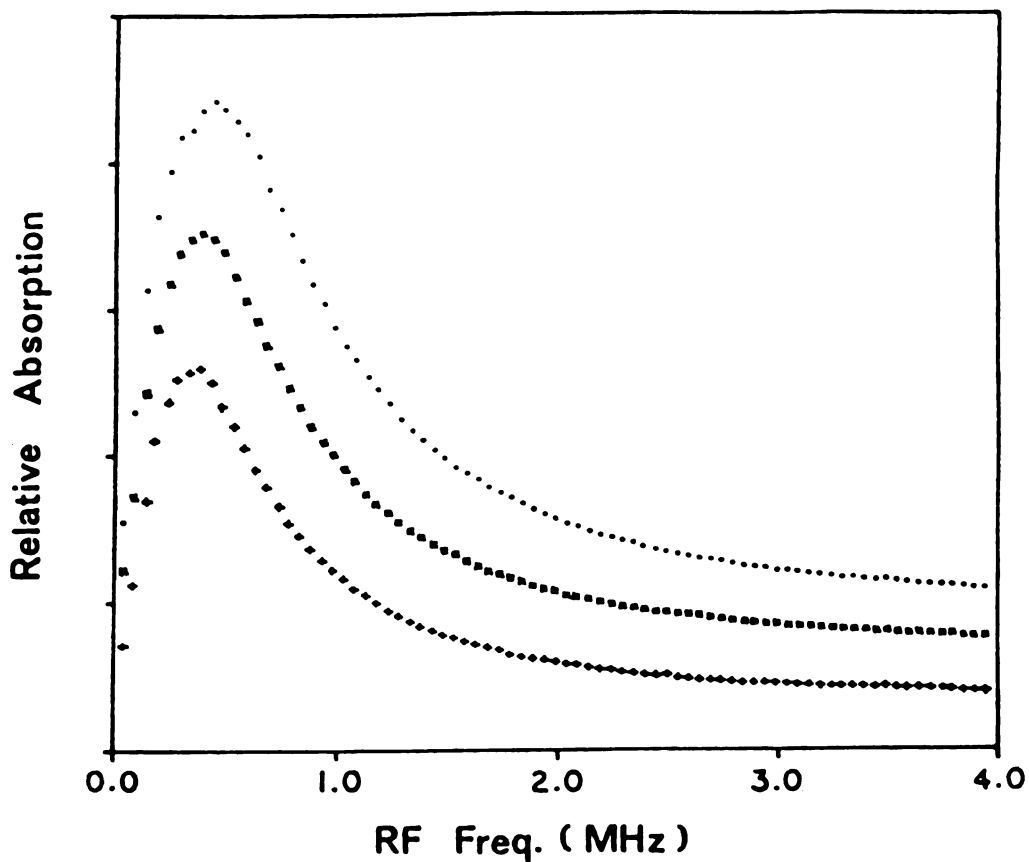


Figure 5. IR-ZF spectra in $^{12}\text{CH}_3\text{F}$. The transition, laser, and laser power were the same as in Fig. 4. The sample pressure was 6.6 mTorr. The RF amplitudes were: $\dots \sim 1.1$ V/cm; $xxx \sim 0.84$ V/cm; $+++ \sim 0.67$ V/cm.

CHAPTER IV

CALCULATIONS

For the theoretical calculations, we need 11 input parameters which are as follows: the number of points in the Doppler integration (NG); the frequency interval in the Doppler integration (DG); the Doppler width (GW); the number of RF frequencies (NV); the RF frequency interval (DV); the starting RF frequency (VA); the IR offset frequency (DA), which is zero for on-resonant pumping; the RF Rabi frequency (DB) for the transition; the IR Rabi frequency (X) for the transition; and the relaxation time for population (γ_1) and for coherence (γ_2).

Of the 11 parameters, 3 (NV, DV, and VA) are chosen to match the experimental conditions, and 2 (NG and DG) are selected to provide an efficient but accurate numerical integration. For the latter, DG should be less than the smaller of γ_1 and γ_2 and $NG \times DG$ should be greater than $6 \times GW$. Of the remaining 6 parameters, δ_a is known from the spectrum and GW can be accurately calculated, as shown below. Also, DB and X can be estimated, but were normally adjusted in the fitting process for reasons that will be described. The estimation of GW, DB, and X is described in the next 3 subsections.

Doppler Width (GW)

The Doppler width ($GW = \Delta\nu_D$) can be accurately calculated from the expression,

$$\Delta\nu_D = \frac{\nu_0}{c} \sqrt{\frac{(2\ln 2)RT}{M}}, \quad (34)$$

where ν_0 is the resonance frequency, c is the speed of light, R is the gas constant, T is the absolute temperature, and M represents the molecular weight.

RF Rabi Frequency (DB)

The RF Rabi frequency for a transition, as it appears in the present theory is given by

$$\delta_b = \frac{(\mu' - \mu'')}{2\hbar} \epsilon_{RF}^0 \quad (35)$$

where ϵ_{RF}^0 is the amplitude of RF and μ' and μ'' represent the diagonal matrix elements for the dipole moment of the upper state and the lower state, respectively. The matrix elements can be obtained from the following equation:

$$\mu = \frac{\mu_D k m}{J(J+1)} \quad (36)$$

where μ_D is the permanent dipole moment in the vibrational

state. The peak RF electric field ϵ_{RF}^0 is related to the root mean square RF voltage, as follows:

$$\epsilon_{RF}^0 = \sqrt{2} V_{rms}/d \quad (37)$$

where d is the distance between the two Stark plates.

IR Rabi Frequency (χ)

The IR Rabi frequency for the transition, as it appears in the theory is given by

$$\chi = \nu_{fi} \epsilon_0 / \hbar \quad (38)$$

where ν_{fi} is the transition dipole moment matrix element between states f and i and ϵ_0 is the peak amplitude of IR radiation.

The dipole moment matrix element can be expressed as

$$\nu_{fi} = \left(\frac{\partial \mu}{\partial Q_3} \right) \int \psi_1^* Q_3 \psi_0 dQ_3 \int \psi_{J',k',m',\cos\theta} \psi_{J''k''m''} d\theta \quad (39)$$

For the ν_3 band of $^{12}\text{CH}_3\text{F}$, the derivative of the molecular dipole moment with respect to the normal coordinate for ν_3 can be obtained from reported absolute

intensity data(15), as follows:

$$\left(\frac{\partial \mu}{\partial Q_3}\right)^2 = \frac{3c^2 \nu_3^0 \Gamma_3}{N_A} \quad (40)$$

where ν_3^0 is the harmonic frequency, c is the speed of light, N_A is Avogadro's number, and Γ_3 is the integrated absorption coefficient for the ν_3 band. The calculated value of $(\partial \mu / \partial Q_3)$ is $117.4 \text{ cm}^{2/3} \text{ sec}^{-1}$ based on $\Gamma_3 = 9056 \text{ cm}^2/\text{mole}$ (16,17) and $\nu_3^0 = 1067 \text{ cm}^{-1}$ (18).

For the second contribution, the normal coordinate integral is given by

$$\int \psi_1^* Q_3 \psi_0 dQ_3 = \sqrt{\frac{1}{2\gamma_3}} ; \quad \gamma_3 = \frac{4\pi^2 \nu_3^0}{h} \quad (41)$$

Thus, $\int \psi_1^* Q_3 \psi_0 dQ_3 = 1.62 \times 10^{-21} \text{ g}^{1/2} \text{ cm}$.

Now, consider the directional cosine element for our experimental arrangement. The equation can be transformed into the matrix element(19)

$$\begin{aligned} \int \psi_{J',k',m'} \cos \theta_{yz} \psi_{J'',k'',m''} d\theta &= \langle J',k',m' | \Phi_{yz} | J'',k'',m'' \rangle \\ &= \langle J' | \Phi_{yz} | J'' \rangle \langle J',k' | \Phi_{yz} | J'',k'' \rangle \langle J',m' | \Phi_{yz} | J'',m'' \rangle \\ &= \langle J'',k'',m'' | \Phi_{yz} | J',k',m' \rangle^* \end{aligned} \quad (42)$$

For the transition ${}^0P(2,1)$, $m = 1 \rightarrow 0$

$$J' = J'' - 1, k' = k'', \text{ and } m' = m'' + 1 \quad (43)$$

Thus, since $J'' = 2$, $k'' = 1$, and $m'' = 0$,

$$\begin{aligned} \langle J'k'm' | \Phi_{Yz} | J''k''m'' \rangle &= \left(\frac{1}{[4J(4J^2-1)]^{1/2}} \right) (2(J^2 - k^2)^{1/2}) \\ &\times ((J-m)(J-m-1))^{1/2} = 0.1581 \end{aligned} \quad (44)$$

For the peak amplitude of the IR radiation, we can obtain the equation

$$\epsilon_0 / (V/cm) = 27.449 \sqrt{\frac{P}{A}} / (\text{watt/cm}) \quad (45)$$

from the relationship

$$P/A = c\epsilon_0^2 / 8\pi \quad (46)$$

where P is the radiation power and A is the area of the beam.

Finally, we can calculate the Rabi frequency from the relationship

$$x = \left(\frac{\mu\epsilon}{h} \right) / \text{MHz} = 0.50345 (\mu/\text{Debye}) (\epsilon/V/cm) \quad (47)$$

CHAPTER V

RESULTS AND DISCUSSION

Sample experimental spectra are shown in Figs. 2-7. As indicated in the Introduction, the spectra of $^{13}\text{CH}_3\text{F}$ in Figs. 2 and 3, taken at zero D.C. field in the presence of multiple m degeneracy, could not be fit quantitatively with the theory presented in this paper. By contrast, spectra similar to that in Figs. 4 and 5, taken with the sample of $^{12}\text{CH}_3\text{F}$ in a resonant D.C. Stark field that split the m degeneracy, could be fit to high accuracy. Examples of such fits are shown in Figs. 6 and 7. The small variation of the residual shown in these figures is within the experimental uncertainty in the lineshapes.

The original purpose was to obtain relaxation parameters from these spectra. Unfortunately, that was not possible in the present work. The zero D.C. field spectra could be taken at relatively high sample pressures (~50 mTorr) where pressure-dependent effects were obvious, but they did not fit the theory. The non-zero D.C. field spectra could be fit well, but because of dielectric breakdown they could not be observed at high enough sample pressure to observe linearly independent pressure effects. The absorption line chosen for the D.C. field studies ($^{12}\text{CH}_3\text{F}$ ν_3 band $^0\text{P}(2,1)$, $m = 1 \rightarrow 0$) required a field of ~9.7

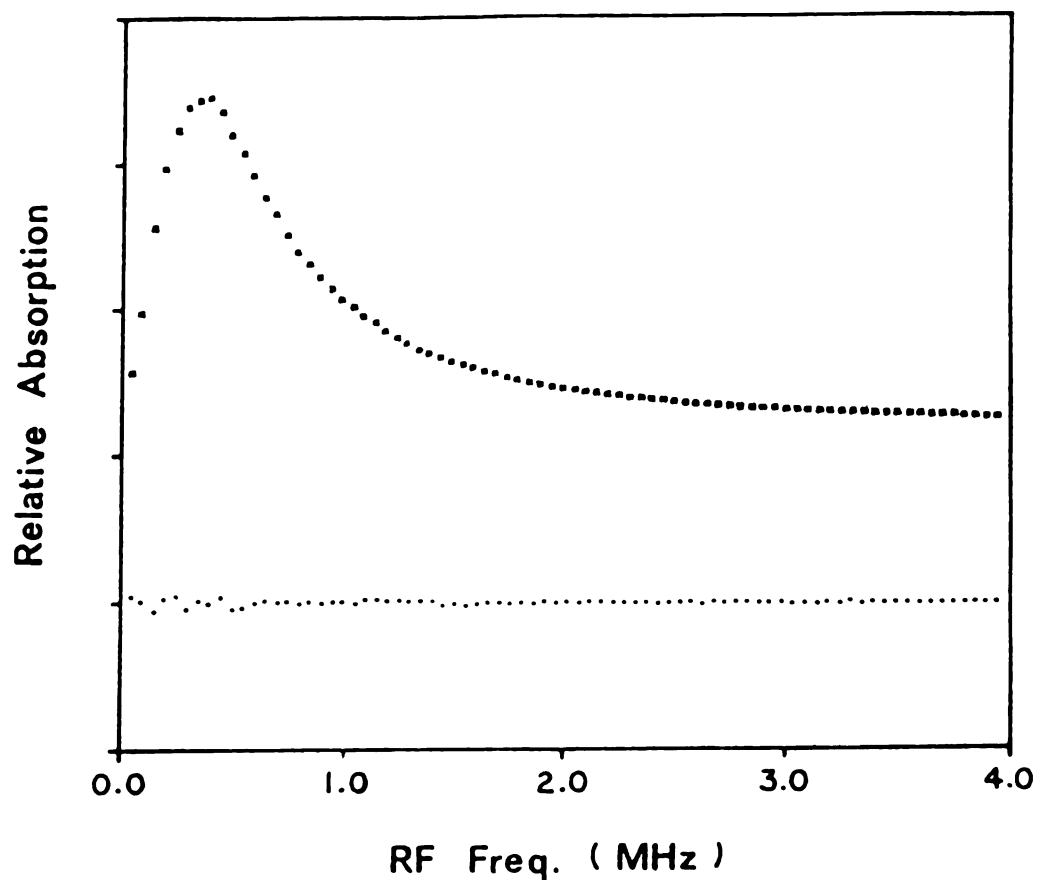


Figure 6. Results of least squares fit of experimental IR-ZF spectrum in $^{12}\text{CH}_3\text{F}$. The transition, laser, and laser power were the same as in Fig. 4. The sample pressure was 6.6 mTorr and the RF amplitude was ~ 0.67 V/cm. Observed spectrum xxx; observed - calculated spectrum ooo.

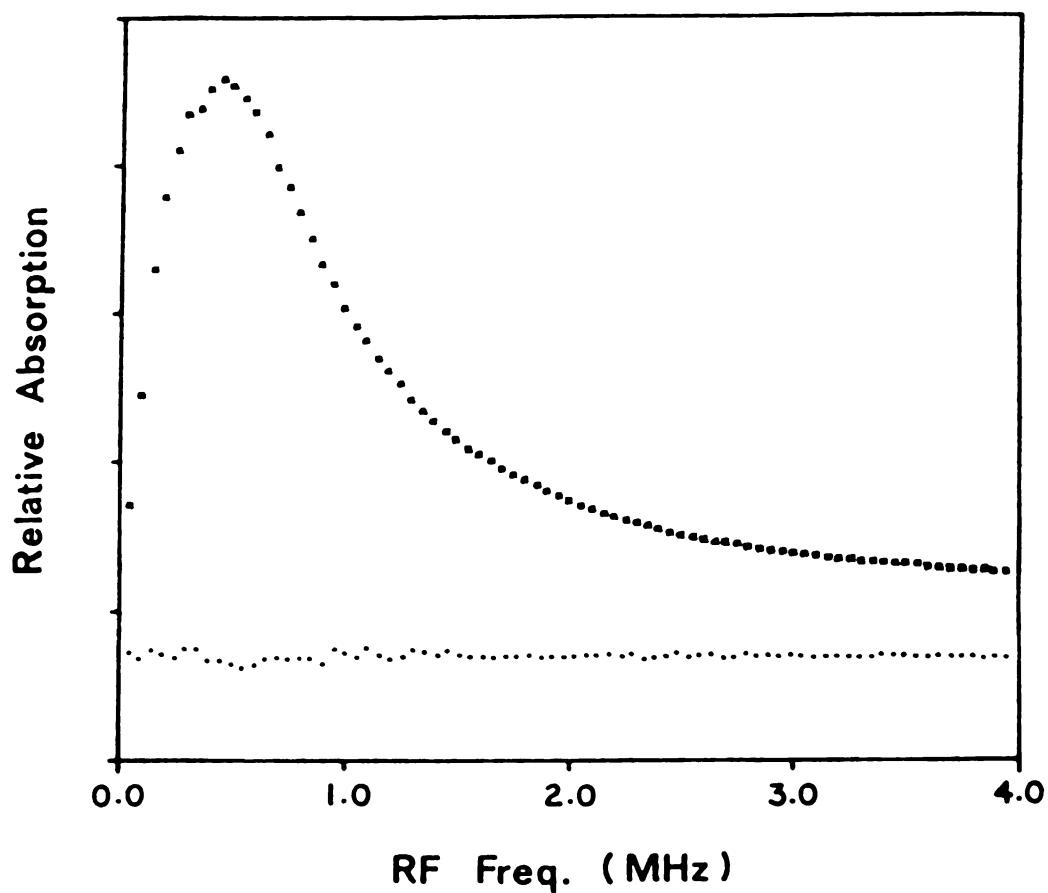


Figure 7. Results of least squares fit of experimental IR-ZF spectrum in $^{12}\text{CH}_3\text{F}$. The transition, laser, and laser power were the same as in Fig. 4. The sample pressure was 6.6 mTorr and the RF amplitude was ~ 1.1 V/cm. Observed spectrum xxx; observed - calculated spectrum ooo.

kV/cm to bring it into resonance with the 9P(22)CO₂ laser line. At this high field the highest sample pressure that could be maintained reliably was ~6 mTorr.

Several attempts were made to fit the highest pressure D.C. field spectra to the lineshape described in the Theory section. For this purpose, we assumed that the spectrometer signal was of the form,

$$S = C_1 \int_{-\infty}^{\infty} W(\delta_a) [v_0(x, \gamma, \delta_b, \delta_a) - v_0(x, \gamma, 0, \delta_a)] d\delta_a + C_2 \quad (48)$$

Here x , $\gamma = \gamma_1 = \gamma_2$, δ_a , and δ_b have already been defined; $W(\delta_a)$ is the probability density for δ_a ; C_1 and C_2 are constants. The functional form assumed for W was the appropriate Doppler-broadened Gaussian centered about $\delta_a = 0$. Care was taken to insure that the numerical integration was sufficiently accurate. The difference in square brackets in the integral in Eq. (48) is needed to represent the combined effect of chopping the RF radiation and phase-sensitive detection.

All least squares fits with independent variation of the 5 parameters x , γ , δ_b , C_1 , and C_2 diverged. By contrast, all fits with γ fixed at the value of 20 MHz/Torr converged rapidly. The results of two such fits for spectra taken with different RF amplitudes are shown in Figs. 6 and

7. Some 4-parameter fits with δ_b fixed at the value predicted from the fits with γ fixed converged slowly, but showed a very high correlation between x and γ . The excessive computer time required by the Doppler averaging and the predicted low reliability of the outcome led me to discontinue the numerical experimentation. It appears that use of this method for evaluation of relaxation parameters will require that the resonance occur at much lower Stark field than was the case in this work. Such an experiment could be carried out with a stable tunable laser source such as the recently developed infrared-microwave sideband laser(20).

Although it was not possible to determine the relaxation parameter, the quality of the fits in Figs. 6 and 7 is sufficiently high to provide strong support for the theory presented above. In order to give an indication of the dependence of the IR-ZF lineshape with variation in parameters, several calculated spectra are shown in Figs. 8-12. Dependence on pressure, RF field, D.C. field, laser electric field, and number of harmonics used in the calculation is shown. The dependence on pressure, RF field, and laser field appears similar at first sight, which accounts for the near linear dependence in the least squares fits. However, closer examination reveals some differences. Of interest is an apparent competition between pressure and laser electric field (Figs. 4 and 8) that is similar to

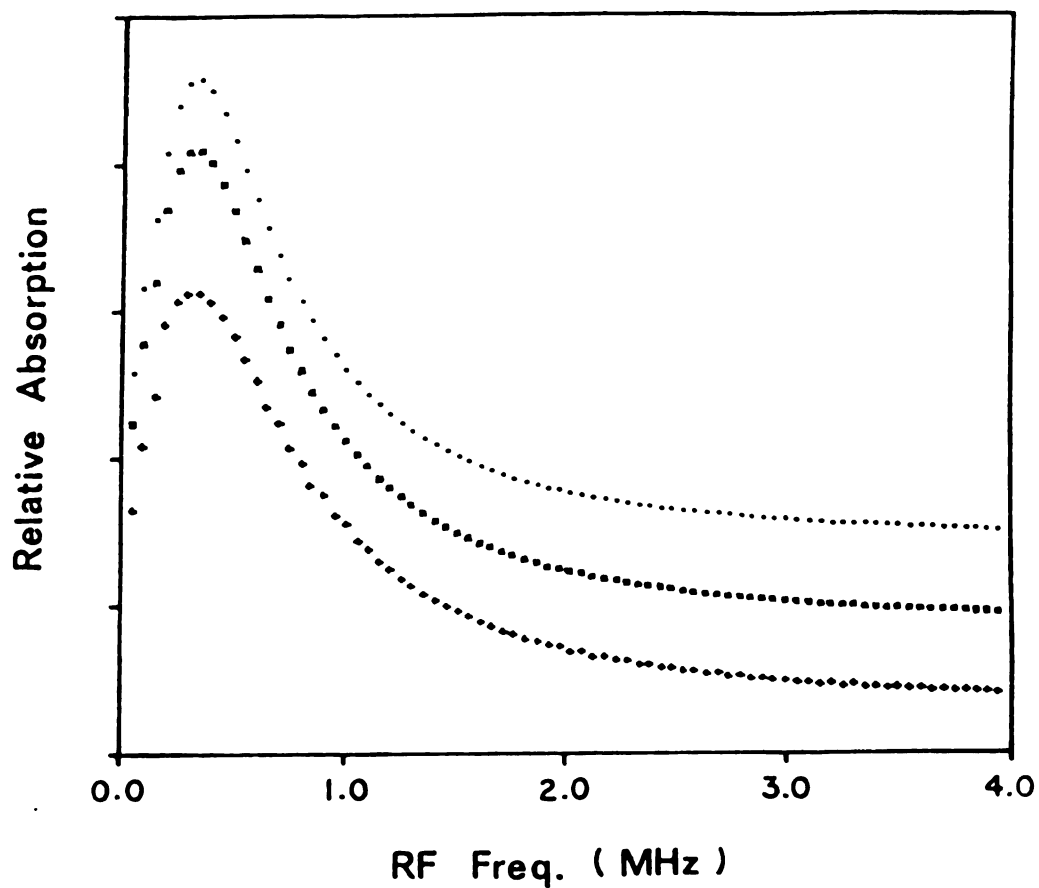


Figure 8. Pressure dependence of calculated IR-ZF spectrum: laser power 32 mW; RF amplitude 0.73 V/cm; laser frequency offset 0.0 MHz; no. of harmonics 4. Sample pressures: ●●● 6.5 mTorr; xxx 4.5 mTorr; +++ 3.0 mTorr.

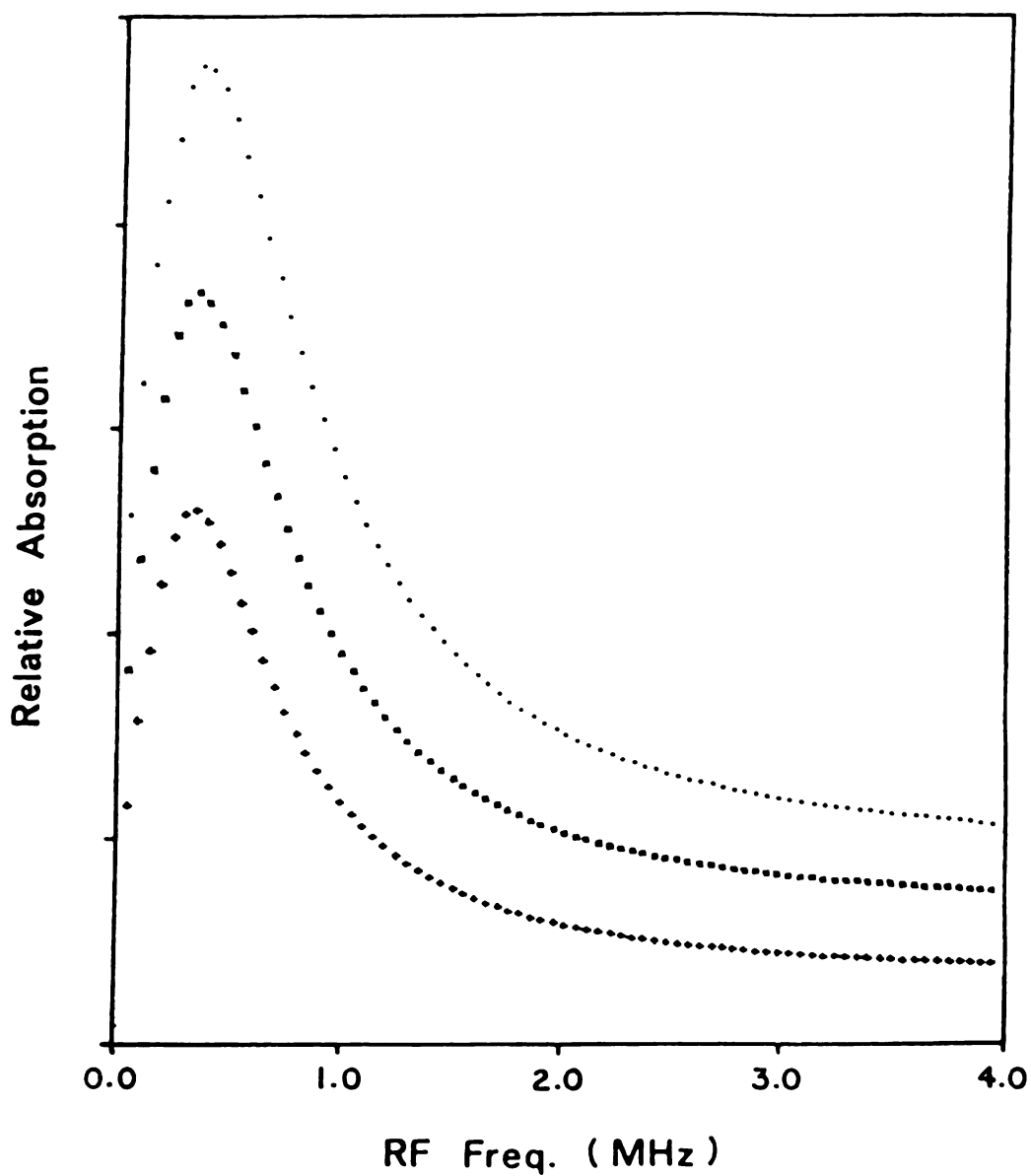


Figure 9. RF amplitude dependence of calculated IR-ZF spectrum: laser power 32 mW; sample pressure 6.5 mTorr; laser frequency offset 0.0 MHz; no. of harmonics 4. RF amplitude: ••• 1.1 V/cm; xxx 0.92 V/cm; +++ 0.73 V/cm.

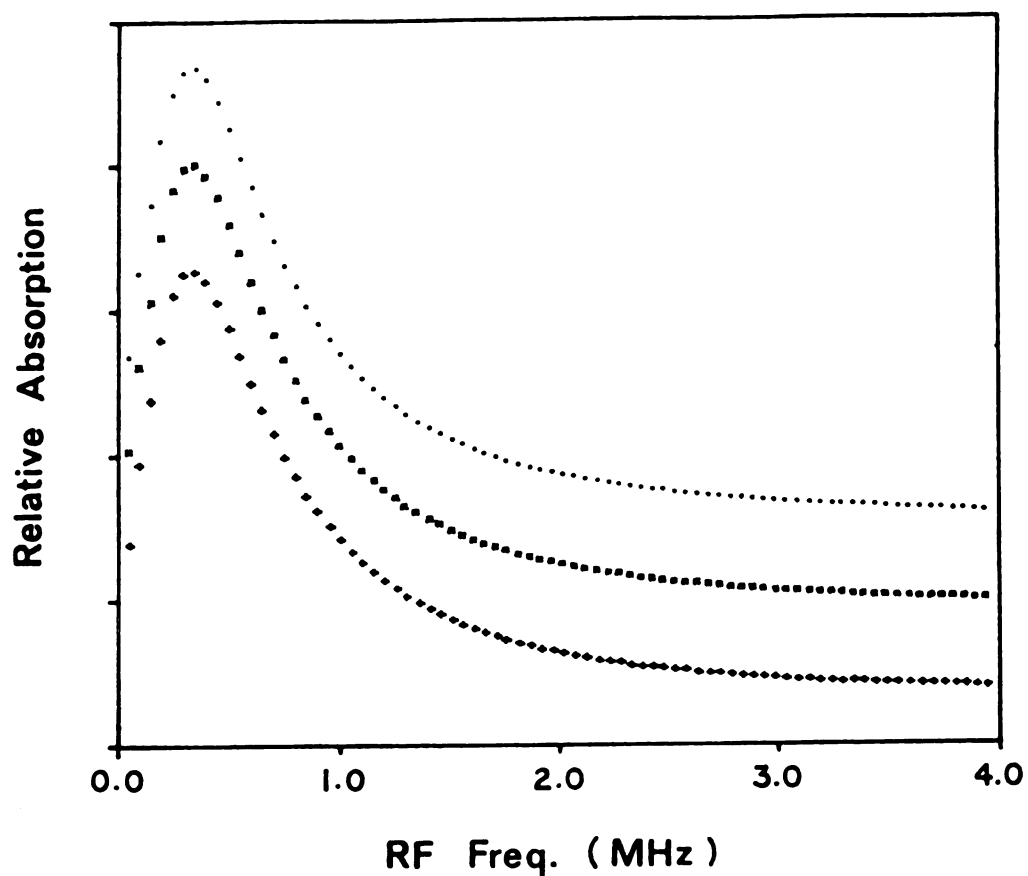


Figure 10. Dependence of calculated IR-ZF spectra on laser frequency offset. Laser power 32 mW; sample pressure 6.5 mTorr; RF amplitude 0.73 V/cm; no of harmonics 4. Laser frequency offsets: ... 0.0 MHz; xxx 5.0 MHz; +++ 10.0 MHz.

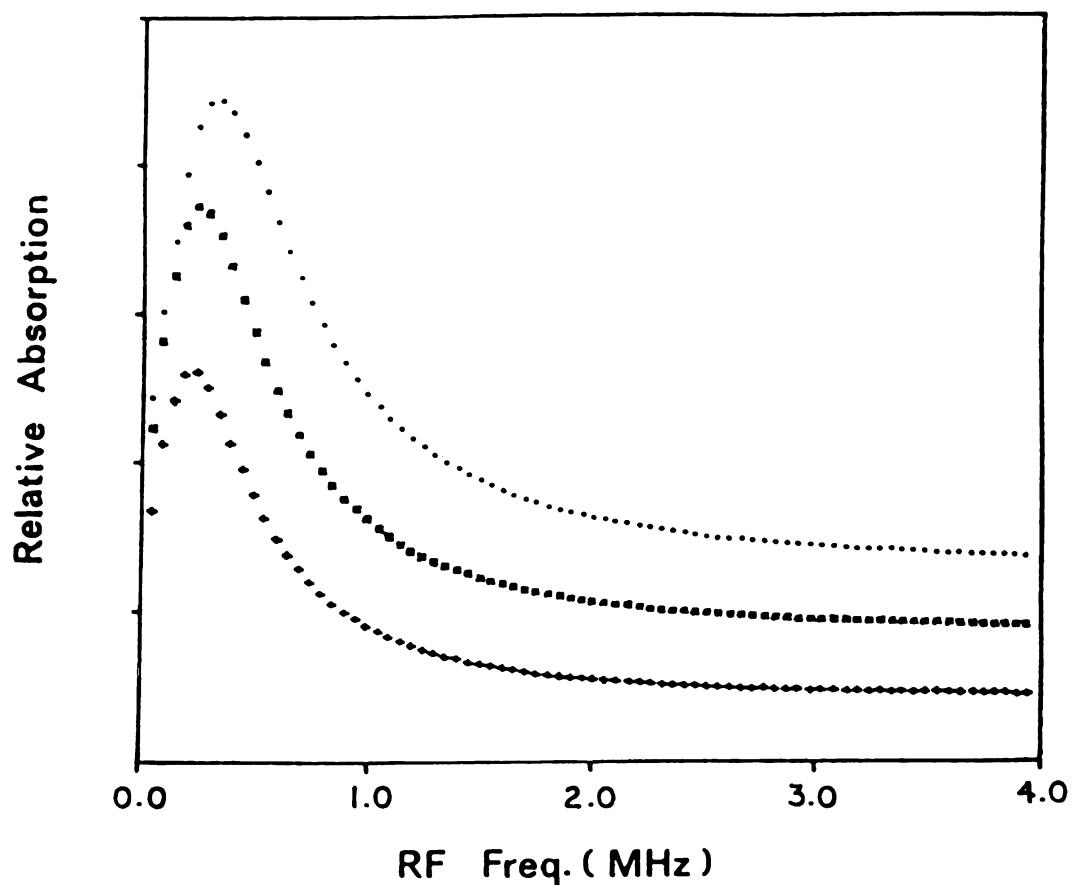


Figure 11. Infrared laser power dependence of calculated IR-ZF spectra. Sample pressure 6.5 mTorr; RF amplitude 0.73 V/cm; laser frequency offset 0.0 MHz; no of harmonics 4. Laser powers: **...** 32 mW; **xxx** 16 mW; **+++** 9mW.

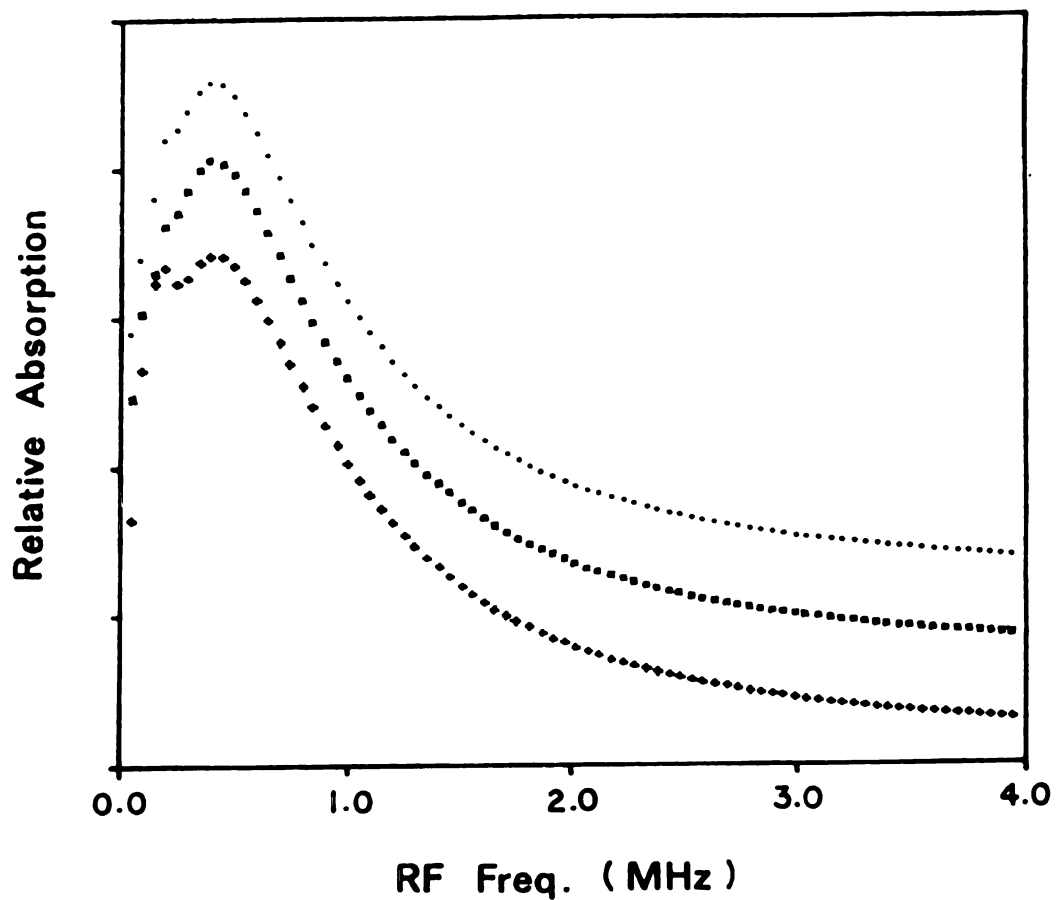


Figure 12. Dependence of calculated IR-ZF spectra on no. of harmonics included in the calculation. Laser power 32 mW; sample pressure 6.5 mTorr; laser frequency offset 0.0 MHz; RF amplitude 1.5 V/cm. No. of harmonics: ... 4; xxx 3; +++ 2.

ordinary saturation effects. In each of these figures, comparison of the relative peak heights to that of the offset shown at the right of the figure indicates that the intensity increases with pressure between the two lower figures, but decreases with pressure between the two upper figures.

Finally, the dependence on the number of harmonics included in the calculation (Fig. 12) justifies the derivation of a theory that goes beyond the rotating wave approximation. As expected, however, and shown in Fig. 13, there is little if any dependence on the number of harmonics when the RF amplitude is low enough.

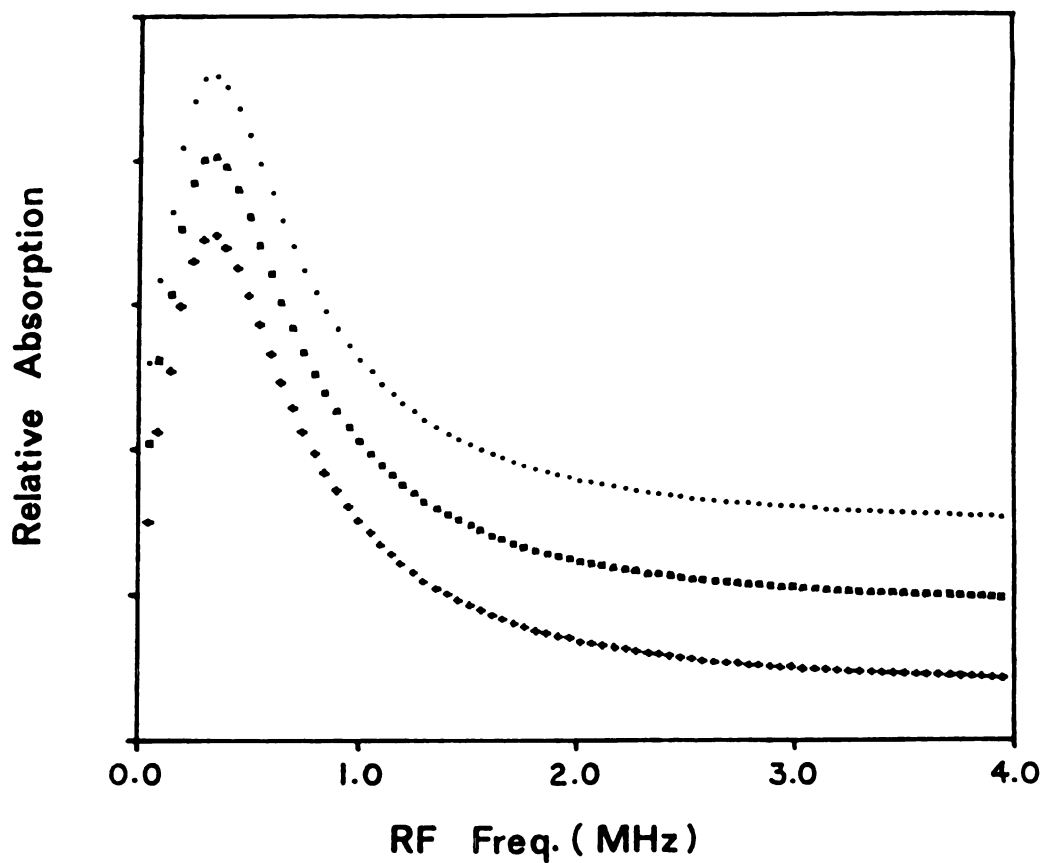


Figure 13. Dependence of calculated IR-ZF spectra on no. of harmonics included in the calculation. Laser power 32 mW; sample pressure 6.5 mTorr; laser frequency offset 0.0 MHz; RF amplitude 0.73 V/cm. No. of harmonics: ... 4; xxx 3; +++ 2.

APPENDIX A

The purpose of this Appendix is to give a solution of Eq. (22) for the case $|\delta_a| = \omega \gg \delta_b, \gamma_1$, and γ_2 . This is the case for infrared radiofrequency or infrared microwave two-photon spectra for a symmetric top without inversion. The solution will be developed to third order in the product of δ_b and x , the factors that depend on RF and infrared amplitudes, respectively.

It is sufficient to consider only one harmonic; therefore, the linear system that must be solved is

$$\begin{bmatrix} a_{11}^* & a_{01}^* & 0 \\ a_{01}^* & a_{00} & a_{01} \\ 0 & a_{01} & a_{11} \end{bmatrix} \begin{bmatrix} v_1^* \\ v_0 \\ v_1 \end{bmatrix} = \begin{bmatrix} 0 \\ xn^0/2 \\ 0 \end{bmatrix}. \quad (A1)$$

The a_{kl} are given by Eqs. (19)-(21). This system is readily solved to yield

$$v_0 = \frac{xn^0/2}{a_{00} \left[1 - \frac{a_{01}^{*2}}{a_{00}a_{11}^*} - \frac{a_{01}^2}{a_{00}a_{11}} \right]} \quad (A2)$$

or

$$v_0 = \frac{x_0}{2a_{00}} \left[1 + \frac{a_{01}^{*2}}{a_{00}a_{11}^*} + \frac{a_{01}^2}{a_{00}a_{11}} \right] \quad (A3)$$

After rationalization, this is

$$v_0 = \frac{x_0}{2a_0} \left[1 + \frac{2a_1'(b_1'^2 - b_1''^2) + 4a_1''b_1'b_1''}{a_0(a_1'^2 + a_1''^2)} \right] \quad (A4)$$

The nomenclature of Chapter II, i.e., $a_{00} = a_0$, $a_{11} = a_1' + ia_1''$, $a_{01} = b_1' + ib_1''$, has been used.

The third-order terms in Eq. (A4) are in the ratio in parentheses. These may be written A/B, where after substitution from Eqs. (19)-(21),

$$\begin{aligned} A &= 2\delta_a^2 \delta_b^2 \left(\frac{1}{\gamma_2} \right) (\gamma_2 + \frac{\delta_a^2 \gamma_2}{\omega^2}) - \frac{4\delta_a^2 \delta_b^2}{\gamma_2 \omega^2} (\omega^2 - \delta_a^2) \\ &= \frac{2\delta_a^2 \delta_b^2}{\gamma_2 \omega^2} (3\delta_a^2 - \omega^2) \end{aligned} \quad (A5)$$

and

$$B = \frac{\delta_a^2}{\gamma_2} \left[(\gamma_2 + \frac{\delta_a^2 \gamma_2}{\omega^2})^2 + (\omega - \frac{\delta_a^2}{\omega})^2 \right] \quad (A6)$$

In these expressions a number of higher order terms and terms that are negligible because of the assumed magnitude of δ_a and ω have been omitted.

To simplify Eqs. (A5) and (A6) we make use of the fact that $|\delta_a| = \omega$. This leads to

$$A = 4 \delta_a^2 \delta_b^2 / \gamma_2 \quad (\text{A7})$$

and

$$B = \frac{\delta_a^2}{\gamma_2} \left[\frac{(\omega - \delta_a)^2 (\omega + \delta_a)^2}{\omega^2} + 4\gamma_2^2 \right]. \quad (\text{A8})$$

Finally, the desired third order contribution to v_0 is

$$v_0^{(3)} = \frac{\chi_n^0}{2a_0} \frac{A}{B} = \frac{n^0 \gamma_2 \delta_b^2}{2\delta_a^2} \left[\frac{(\omega - \delta_a)^2 (\omega + \delta_a)^2}{4\omega^2} + \gamma_2^2 \right]^{-1} \quad (\text{A9})$$

This result is in essential agreement with that derived previously by another method(10). The conclusion is that infrared microwave two-photon absorption in symmetric top molecules without inversion can be viewed as the result of a high-frequency Stark effect created by the microwave electric field. This Stark effect causes absorption sidebands in the molecules such that a resonance occurs when the laser frequency coincides with one of these sidebands. The denominator in Eq. (A9) shows resonances when $\delta_a = \omega_l - \omega_{ba} = \pm\omega$, or when $\omega_l = \omega_{ba} \pm \omega$.

REFERENCES

1. E. Arimondo, P. Glorieux, and T. Oka, Phys. Rev. A17, 1375-1393 (1978).
2. S. H. Autler and C. H. Townes, Phys. Rev. 78, 340 (1950).
3. J. Brossel and F. Bitter, Phys. Rev. 86, 308-316 (1952).
4. R. F. Curl, Jr. and T. Oka, J. Chem. Phys. 58, 4908-4911 (1973).
5. F. Herlemont, M. Lyszyk, J. Lemaire, and J. Demaison, Z. Naturforsch. 36a, 944-947 (1981).
6. S. M. Freund, G. Duxbury, M. Romheld, J. I. Tiedje, and T. Oka, J. Mol. Spectrosc. 52, 38-57 (1974).
7. J. C. McGurk, T. G. Schmalz, and W. H. Flygare, Adv. Chem. Phys. 25, 1-68 (1974).
8. S. H. Autler and C. H. Townes, Phys. Rev. 100, 703-722 (1955).
9. A. Jacques and R. H. Schwendeman, "An infrared zero frequency double-resonance effect in CH_3F ", Symposium on Molecular Spectroscopy, 37th, Columbus, Ohio, 1982.
10. T. Oka and T. Shimizu, Phys. Rev. A2, 587-593 (1970).
11. T. Oka, in "Proceedings of the Summer School of Theoretical Physics", Les Houches, France, 1975.
12. S. M. Freund, M. Romheld, and T. Oka, Phys. Rev. Lett. 35, 1497-1500 (1975).
13. T. Amano and R. H. Schwendeman, J. Chem. Phys. 68, 530-537 (1978).
14. C. Freed and A. Javan, Appl. Phys. Lett. 17, 53-56 (1970).
15. J. W. Russel, C. D. Needham, and J. Overend, J. Chem. Phys. 45, 3383-3398 (1966).
16. C. D. Barnett and D. F. Eggers, Jr. (private communication, cited in Ref.15)

17. S. Saeki, M. Mizuno, and S. Kondo, *Spectrochim. Acta Part A* **32**, 403-413 (1976).
18. J. Aldous and I. M. Mills, *Spectrochim. Acta* **18**, 1079-1091 (1962).
19. C. H. Townes and A. L. Schawlow, "Microwave Spectroscopy", McGraw-Hill, New York, NY, 1955.
20. G. Magerl, W. Schupita, E. Bonek, and W. Kreiner, *J. Mol. Spectrosc.* **83**, 431-439 (1980).

- PART II -

INFRARED-MICROWAVE SIDEBAND LASER SPECTROSCOPY OF
THE ν_3 AND $2\nu_3 + \nu_3$ BANDS OF $^{13}\text{CH}_3\text{F}$ AND $^{12}\text{CH}_3\text{F}$

CHAPTER I

INTRODUCTION

This thesis is concerned with studies of the ν_3 and $2\nu_3 + \nu_3$ bands of $^{12}\text{CH}_3\text{F}$ and $^{13}\text{CH}_3\text{F}$ by infrared microwave sideband laser spectroscopy. Methyl fluoride is a typical prolate symmetric top molecule with C_{3v} symmetry. This molecule possesses six fundamental vibrational modes, three totally symmetric (A_1) and three doubly degenerate (E), all infrared active. The ν_3 mode is of totally symmetric species A_1 , associated mainly with the C-F stretching vibration.

Since the ν_3 band of CH_3F is in coincidence with $10\ \mu\text{m}$ CO_2 laser lines and its rotational fine structure is a good example for a symmetric top molecule, it has been the subject of many publications and has played a key role in the development of molecular microwave and infrared spectroscopy(1,2).

The measurements of pure rotational transitions in $^{12}\text{CH}_3\text{F}$ were done by Gilliam et al.(3), Johnson et al.(4), Thomas et al.(5), Winton and Gordy(6), Sullivan and Frenkel(7), Tanaka and Hirota(8), and Hirota et al.(9) by means of microwave spectroscopy. The most precise measurements were obtained by a microwave Lamb-dip method(6), and high J transitions in the ground state were observed by Sullivan and Frenkel(7). Tanaka and Hirota(8)

and Hirota et al.(9) measured rotational transitions in excited vibrational states.

The infrared spectrum of CH_3F was first reported by Bennett and Meyer(10). Yates and Nielson(11) examined all the fundamental bands with moderate resolving power, and Anderson et al.(12) analyzed all of the perpendicular fundamental bands with relatively low resolution. A detailed high resolution study of the ν_3 band of CH_3F with a conventional infrared spectrometer has been carried out by Smith and Mills(13).

With the advent of lasers, methyl fluoride has been used for various laser spectroscopic experiments because of its near coincidences with laser lines and large intensity of absorption. Laser spectroscopy using these coincidences has been reported by Luntz and Brewer(14), Weitz et al.(15) and Freund et al.(16) who used $10\text{ }\mu\text{m}$ CO_2 lasers for a radiation source. Chang and Bridges(17) and Chang and McGee(18) observed far infrared maser action between the rotational levels in the ν_3 state. Nonlinear spectroscopy of CH_3F and measurement of the dipole moment in the ground and excited states have been reported by Brewer(19,20). Additional nonlinear experiments include infrared-infrared two-photon spectroscopy by Bischel et al.(21) and the use of an infrared-submillimeter wave double resonance technique by Blumberg et al.(22).

More recently, further high precision spectroscopy of

$^{12}\text{CH}_3\text{F}$ has been reported. This includes application of tunable CO_2 laser sideband radiation(23), diode laser measurement(24,25,26), IR-RF two-photon Lamb-dip technique(27,28), and Lamb-dip spectroscopy(29). In addition, methyl fluoride has been of fundamental importance in the development of optically pumped far-infrared lasers(17,18,30,31).

The analysis of the $2\nu_3$ band was first reported by Pickworth and Thompson(32) without resolving the K rotational structure. Smith and Mills(13) performed a study of $2\nu_3 \leftarrow \nu_3$ transitions by a conventional grating spectrometer. Recently, a very accurate study of the overtone band $2\nu_3$ by using an interferometric spectrometer was done by Betrencourt(33), and Freund et al.(16) observed several $2\nu_3 \leftarrow \nu_3$ transitions by means of laser Stark method. But the number of transitions was insufficient to determine the higher order centrifugal distortion constants(16).

The natural abundance of $^{13}\text{CH}_3\text{F}$ is composed of 1.1% of CH_3F so that its spectroscopic interest should be emphasized. But relatively little work was done by infrared laser spectroscopy compared to its isotope $^{12}\text{CH}_3\text{F}$. Pure rotational transitions in the ground state and in the $\nu_3 = 1$ excited state were observed by Gilliam et al.(3) and Tanaka and Hirota(8), by means of microwave spectroscopy. Recently, Matterson and DeLucia reported a number of frequencies measured in the millimeter wave region(35). The

conventional grating infrared spectrum of the ν_3 band of $^{13}\text{CH}_3\text{F}$ was first reported by Smith and Mills(13) and Duncan et al.(34) measured the overtone $2\nu_3$ band. The first study of the $2\nu_3$ overtone band with resolved K structure was made by Betrencourt(33) from an FT-IR spectrum. The actual application of laser spectroscopy to the $^{13}\text{CH}_3\text{F}$ molecule was carried out by Freund et al.(16) by means of laser Stark spectroscopy, by Shoja-Chaghervand and Schwendeman(29) by means of IR-MW two photon spectroscopy, and by Romheld(27) and Freund et al.(28) by IR-RF two photon Lamb-dip spectroscopy. Only quartic centrifugal distortion constants could be obtained because of the relatively limited data (44 transitions, $J \leq 8$)(29).

There has been no previous measurement of the $2\nu_3 + \nu_3$ hot band of $^{13}\text{CH}_3\text{F}$ with or without K structure resolution.

Centrifugal distortion constants for the ground and $\nu_3 = 1$ and 2 states of $^{12}\text{CH}_3\text{F}$ have been reported by a number of authors. Gordy and his group published several progressively improved sets of rotational constants in the ground state(4,5,36,37,38). Winton and Gordy(6) reported sextic centrifugal distortion constants derived from their precise Lamb-dip measurements. Graner(39) has determined the ground state rotational constants, including A_0 and $D_K^{(0)}$, by analysis of ground state combination differences in FT-IR spectra. Betrencourt(33) obtained molecular parameters for the second excited state from an analysis of

the $2\nu_3$ overtone band of $^{12}\text{CH}_3\text{F}$ and $^{13}\text{CH}_3\text{F}$. And Freund et al.(16) also analyzed the rotational constants of $\nu_3 = 2$ for $^{12}\text{CH}_3\text{F}$ from the observation of small number of transitions.

Recently, Arimondo and Inguscio(40), Magerl et al.(23), Herlemont et al.(24), Shoja-Chaghervand and Schwendeman(29), and Arimondo et al.(26) all obtained rotational constants for $^{12}\text{CH}_3\text{F}$ from their observations and compared them to previously reported values. Additional data needed to analyze the $\nu_3 - \nu_6$ Coriolis interaction have been given by DiLauro and Mills(41) and by Hirota(42).

For $^{13}\text{CH}_3\text{F}$, Freund et al.(16), Shoja-Chaghervand and Schwendeman(29), Romheld(27), and Matterson and DeLucia(35) all reported molecular parameters from their observations, just up to quartic centrifugal distortion constants.

In this work, the ν_3 and $2\nu_3 + \nu_3$ transitions of $^{12}\text{CH}_3\text{F}$ and $^{13}\text{CH}_3\text{F}$ were measured by a CO_2 laser-MW sideband laser spectrometer, in which the spectra were obtained by tuning the laser to more than 60 CO_2 laser lines and sweeping a microwave source from 8.2 - 12.2 and 12.4 - 18.0 GHz on each CO_2 laser line. From the analysis of these spectra, the molecular parameters including quartic, sextic, and octic centrifugal distortion constants were determined and will be given.

The next chapter describes the theory used for vibration-rotation interaction (Coriolis interaction), centrifugal distortion, and absorption intensity. Chapter

III gives the theory and its application to the generation of an infrared-microwave sideband laser system. In Chapter IV, the experimental diagram and method for this work will be summarized. Finally the experimental results and their quantum number assignment will be presented with a detailed discussion in Chapter V.

CHAPTER II

THEORY

Introduction

The study of molecular spectra is the most useful of all methods for experimental investigation of molecular structure and motion in free molecules. It affords information on the possible molecular energy levels as well as on the dimensions of molecules. Spectra arise from the emission or absorption of definite quanta of radiation when transitions occur between certain energy levels.

In the theory of molecular spectroscopy, it is customary, according to the Born-Oppenheimer approximation, to consider that the energy of a molecule can be expressed simply as the sum of electronic, vibrational, and rotational contributions;

$$E = E_{\text{elec}} + E_{\text{vib}} + E_{\text{rot}} \quad (1)$$

where E_{elec} is electronic energy, E_{vib} is vibrational energy, and E_{rot} is rotational energy.

The observed spectra correspond to transitions between two energy levels according to the Bohr frequency condition,

$$h\nu = E' - E'' , \quad (2)$$

where the ' and '' refer to the upper and lower states, respectively, and ν is the frequency.

The transition probabilities are determined by the eigenfunctions of the Schrödinger equation by way of the matrix elements of the dipole moment μ such as

$$\int \psi' \mu \psi'' d\tau . \quad (3)$$

Rotational Energy - General Theory

For a body rotating about a fixed axis, the moment of inertia about that axis is given by

$$I = \sum_i m_i r_i^2 \quad (4)$$

where r_i and m_i represent the distance and the mass of the i -th particle from the axis, respectively. If a molecule is considered as a rigid body of point masses, its structure can be described by a tensor whose diagonal elements are the moments of inertia about Cartesian axes. For a Cartesian coordinate system fixed at the center of mass (COM), the diagonal elements of the inertia tensor are

$$I_{xx} = \sum_i m_i (y_i^2 + z_i^2) \quad (5)$$

where I_{yy} and I_{zz} can be formed by a permutation of x , y , and z ; the m_i are atomic masses whose coordinates are x_i , y_i , and z_i . The off-diagonal elements, called products of inertia, are given by

$$I_{xy} = - \sum_i m_i x_i y_i \quad (6)$$

The inertia tensor can be simplified because it is symmetric leaving only 6 independent tensor elements.

The orientation of the coordinate system used to define the inertia system will determine the values of the moments defined above. There is always at least one proper orientation of the coordinate system which forces the off-diagonal elements of the tensor to vanish. The diagonal elements become the principal moments of inertia, and the axis system is termed the principal axis system. As the Cartesian system is rotated into the principal axis system, the moments of inertia approach either maximum or minimum values. The three principal moments of inertia are designated as I_a , I_b , and I_c such that $I_a \leq I_b \leq I_c$.

For any general orientation of the molecule-fixed axes with origin at the COM, the principal moments of inertia can be obtained by diagonalizing the initial tensor. This is

done by solving the determinantal equation, as follows:

$$\begin{vmatrix} I_{xx} - \lambda & I_{xy} & I_{xz} \\ I_{yx} & I_{yy} - \lambda & I_{yz} \\ I_{zx} & I_{zy} & I_{zz} - \lambda \end{vmatrix} = 0 \quad (7)$$

where the roots λ are the principal moments of inertia. Since the trace, which is the sum of the diagonal elements is a constant for the diagonalization procedure,

$$I_{xx} + I_{yy} + I_{zz} = I_a + I_b + I_c . \quad (8)$$

When the principal axis system of a rigid rotor is employed, the energy can be expressed in a simple form in terms of the angular momenta P_i about the three principal axes. Determination of the energy levels in a quantum mechanical system follows from

$$H\psi = E\psi \quad (9)$$

where H is the Hamiltonian operator for the system, ψ is an eigenfunction, and E is an eigenvalue. Since the Hamiltonian operator and eigenfunctions are independent of time, the E values are constants which are the only stationary state energy values of the system. The Hamiltonian is given by

$$H = \frac{P_a^2}{2I_a} + \frac{P_b^2}{2I_b} + \frac{P_c^2}{2I_c} \quad (10)$$

which is commonly written as follows:

$$E = \frac{4\pi^2}{h} (AP_a^2 + BP_b^2 + CP_c^2) \quad (11)$$

where A, B, and C are rotational constants which are defined in frequency units as

$$A = \frac{h}{8\pi^2 I_a}, \quad B = \frac{h}{8\pi^2 I_b}, \quad C = \frac{h}{8\pi^2 I_c}. \quad (12)$$

Since

$$I_a \leq I_b \leq I_c, \quad A \geq B \geq C. \quad (13)$$

The operator for momentum about the principal axes is related to the total angular momentum of the system P by

$$P^2 = P_a^2 + P_b^2 + P_c^2 = P_x^2 + P_y^2 + P_z^2. \quad (14)$$

The axes x, y, z may be identified with the principal axes a, b, c in any of 6 possible ways. For any identification, P_z is conventionally chosen as the component of angular

momentum for which there exists simultaneous eigenstates with P^2 as shown in Fig. 1. The matrix elements are

$$\langle J \ k \ m \mid P^2 \mid J \ k \ m \rangle = J(J+1)\hbar^2 \quad (15)$$

and

$$\langle J \ k \ m \mid P_z \mid J \ k \ m \rangle = k\hbar \quad (16)$$

The energy of a rigid rotor can be obtained by diagonalizing the energy matrix whose nonvanishing elements are

$$\langle Jkm \mid H \mid Jkm \rangle = \frac{\hbar^2}{4} \left\{ \left(\frac{1}{I_x} + \frac{1}{I_y} \right) [J(J+1) - k^2] + \frac{2k^2}{I_z} \right\} \quad (17)$$

$$\begin{aligned} \langle Jkm \mid H \mid Jk \pm 2m \rangle = \frac{\hbar^2}{8} \left\{ \left(\frac{1}{I_y} - \frac{1}{I_x} \right) [(J \mp k)(J \mp k - 1) \right. \\ \left. (J \pm k + 1)(J \pm k + 2)]^{1/2} \right\} \quad (18) \end{aligned}$$

Rigid Symmetric Top Molecules

When a nonlinear molecule possesses two equal moments of inertia, it is classified as a symmetric top molecule. There are two possible identifications for the two equal moments. If I_a is equal to I_b , I_c is the unique moment and is by definition greater than I_a or I_b . The molecule is then designated as an oblate symmetric rotor. If I_b is equal to I_c , the molecule is called as a prolate symmetric

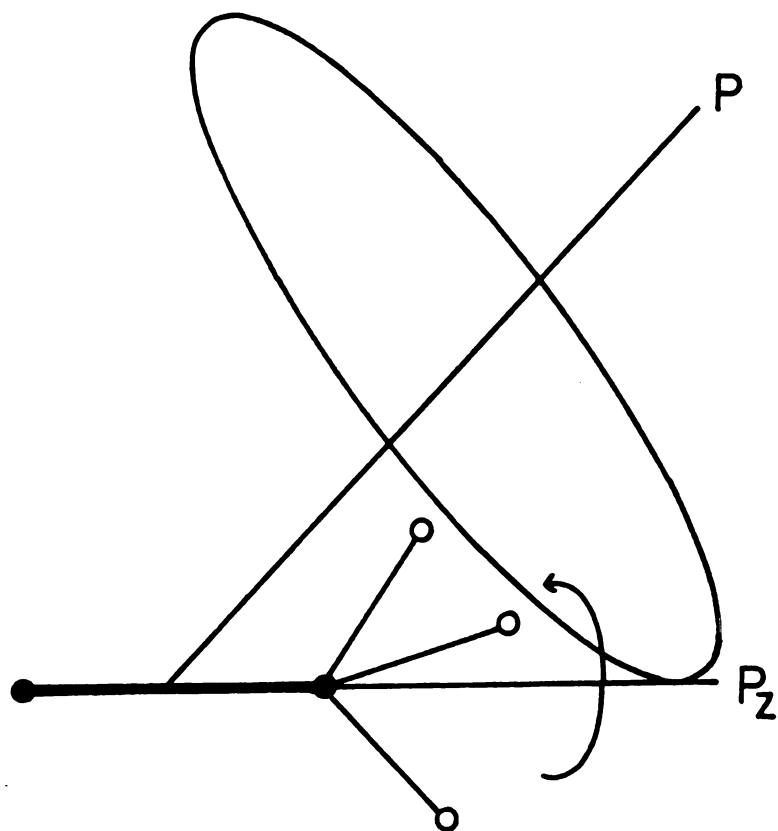


Figure 1. Classical motion of a symmetric top. This is a combined rotation around the molecular axis associated with P_z and a precession of this axis around the total angular momentum P . The molecule represented is CH_3F .

top molecule.

For a prolate rotor, the matrix elements of the Hamiltonian are

$$\langle Jk_m | H | Jk_m \rangle = \frac{\hbar^2}{2I_b} J(J+1) + \frac{\hbar^2}{2} \left(\frac{1}{I_a} - \frac{1}{I_b} \right) k^2 \quad (19)$$

$$\langle Jk_m | H | Jk_{\pm 2m} \rangle = 0 . \quad (20)$$

The energy matrix is diagonal in k , since k is a good quantum number for a true symmetric rotor. In terms of the rotational constants, the energy for a prolate rotor is

$$E = hBJ(J + 1) + h(A - B)k^2. \quad (21)$$

For an oblate top, the energy is

$$E = hBJ(J + 1) + h(C - B)k^2. \quad (22)$$

By convention $A - B \geq 0$ and $C - B \leq 0$. The energy levels for a symmetric top are shown in Fig. 2. Because k is the projection of J on the figure axis, $J \geq |k|$. For a given value of J , however, k may have a number of values, as follows:

$$k = J, J-1, \dots, -J \quad (23)$$

a total of $2J+1$ different values. Since the energy is

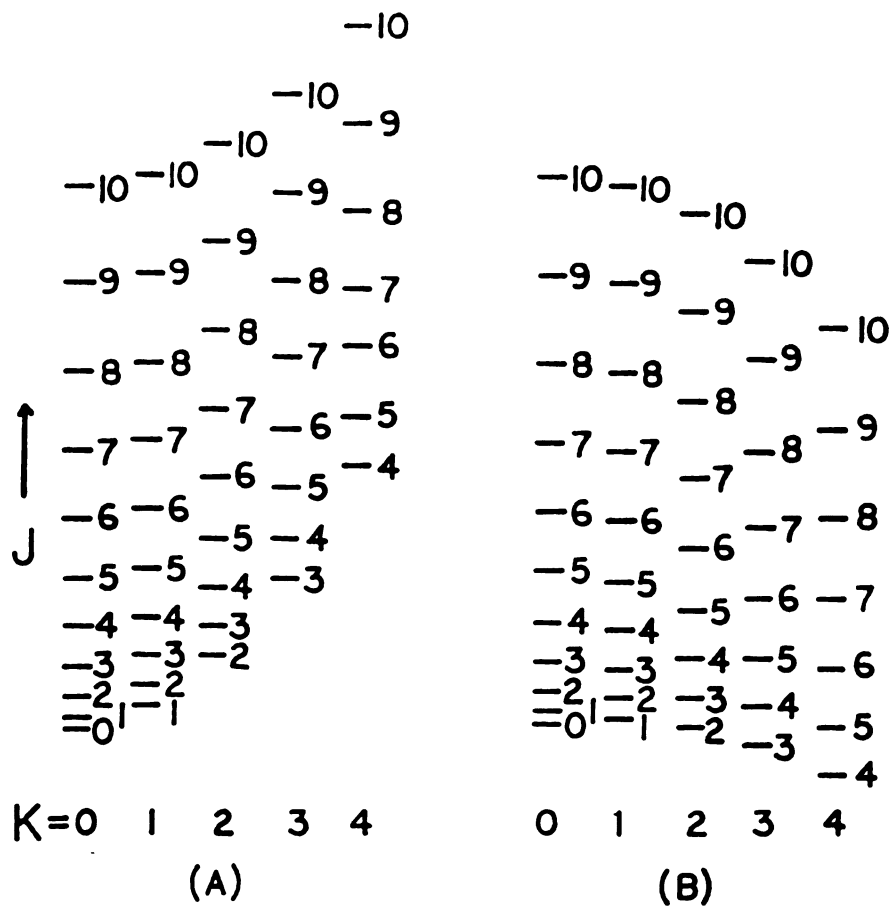


Figure 2. Energy levels of typical symmetric top molecules
 (A) prolate, (B) oblate symmetric top.

independent of the sign of k , levels with the same absolute magnitude of k coincide, so that all levels for which k is greater than zero are doubly degenerate, and there are only $J+1$ different energy values for each possible value of J . For each particular k , there is an infinite series of levels with different values of J .

Symmetric Top Wave Functions

In terms of the Eulerian angles θ , ϕ , and χ , the Schrödinger equation for a prolate symmetric top is

$$\begin{aligned} \frac{1}{\sin \theta} \frac{\partial}{\partial \theta} \left(\sin \theta \frac{\partial \psi}{\partial \theta} \right) + \frac{1}{\sin^2 \theta} \frac{\partial^2 \psi}{\partial \phi^2} + \left(\frac{\cos^2 \theta}{\sin^2 \theta} + \frac{A}{B} \right) \frac{\partial^2 \psi}{\partial \chi^2} \\ - \frac{2 \cos \theta}{\sin^2 \theta} \frac{\partial^2 \psi}{\partial \chi \partial \phi} + \frac{E}{hB} \psi = 0 \end{aligned} \quad (24)$$

The variables in Eq. (24) may be separated, and the solutions written in the form

$$\psi_{Jkm} = \Theta(\theta) e^{im\phi} e^{ik\chi} \quad (25)$$

Because ϕ and χ only appear in the differential terms, they are known as cyclic coordinates and always appear in the wave function as exponential terms. The quantum number m

and k must be integers for ψ to be single-valued. The θ equation has the form

$$\frac{1}{\sin \theta} \frac{d}{d\theta} \left(\sin \theta \frac{d\theta(\theta)}{d\theta} \right) - \left[\frac{m^2}{\sin^2 \theta} + \left(\frac{\cos^2 \theta}{\sin^2 \theta} + \frac{A}{B} \right) k^2 - \frac{2 \cos \theta}{\sin^2 \theta} km - \frac{B}{hB} \right] \theta(\theta) = 0 \quad (26)$$

By introducing the variable

$$x = \frac{1}{2}(1 - \cos \theta) \quad (27)$$

and letting

$$\theta(\theta) = x^{|k-m|/2} (1-x)^{|k+m|/2} F(x) \quad (28)$$

the equation for F is found to be

$$x(1-x) \frac{d^2 F}{dx^2} + (\alpha - \beta x) \frac{dF}{dx} + \gamma F = 0 \quad (29)$$

$$\alpha = |k-m| + 1 \quad (30)$$

$$\beta = |k+m| + |k-m| + 2 \quad (31)$$

and

$$\gamma = \frac{W}{hB} - \frac{ck^2}{B} + k^2 - \left(\frac{1}{2}|k+m| + |k-m| \right) \left(\frac{1}{2}|k+m| + \frac{1}{2}|k-m| + 1 \right) \quad (32)$$

The equation for F can be solved by using the polynomial

$$F(x) = \sum_{n=0}^{\infty} a_n x_n . \quad (33)$$

The resulting recursion relation is

$$a_{n+1} = \frac{n(n-1) + \beta n - \gamma}{(n+1)(n+\alpha)} a_n . \quad (34)$$

For ψ to be a satisfactory normalizable wave function, the series must terminate and become just a polynomial, which requires that the energy W is

$$W = hBJ(J+1) + h(A-B)k^2 \quad (35)$$

with

$$J = n_{\max} + \frac{1}{2} |k+m| + \frac{1}{2} |k-m| \quad (36)$$

n_{\max} is the largest value for which a_n does not vanish.

From Eq. (36), J must be a positive integer which is equal to or larger than $|k|$ or $|m|$, so that

$$\begin{aligned} J &= 0, 1, 2, \dots \\ k &= 0, \pm 1, \pm 2, \dots, \pm J \\ m &= 0, \pm 1, \pm 2, \dots, \pm J \end{aligned} \quad (37)$$

The symmetric top wave functions can be written in terms of the hypergeometric series and a normalization factor,

$$\psi_{Jkm} = N_{Jkm} x^{|k-m|/2} (1-x)^{|k+m|/2} e^{im\phi} e^{ikx} \\ F(-J+\frac{\theta}{2}-1; J+\frac{\theta}{2}; 1-|k-m|; x) \quad (38)$$

where

$$N_{Jkm} = \left[\frac{(2J+1)(J+|k+m|/2+|k-m|/2)!}{8\pi^2 (J-|k+m|/2-|k-m|/2)!} \right. \\ \left. \frac{(J-|k+m|/2+|k-m|/2)!}{(|k-m|!)^2 (J+|k+m|/2-|k-m|/2)!} \right]^{1/2} \quad (39)$$

Nonrigid Symmetric Top Molecules

No real molecule is a rigid rotor. The molecules in a sample cell which are subjected to electromagnetic radiation are vibrating as well as colliding with other molecules and the sample cell walls. Thus the molecular energy levels cannot be predicted exactly by rigid rotor theory but are influenced by perturbations such as those resulting from vibration-rotation interactions (Coriolis interaction) and centrifugal distortion.

The Coriolis force is a vibration-rotation interaction, and vanishes when rotation and vibration are completely separated. If \vec{v} is the linear velocity of the molecule relative to the molecule-fixed axis system and $\vec{\omega}$ is

the angular velocity of rotation of the molecule-fixed system with respect to a space-fixed axis system, the Coriolis force is defined as

$$\vec{F}_c = 2m\vec{v} \times \vec{\omega} \quad (40)$$

Under the proper conditions, the Coriolis force can produce large changes in the rigid rotor energy levels. These deviations may occur as an energy level splitting resulting from the removal of a degeneracy or as a shift of energy levels due to a near degeneracy.

In order to visualize the influence of the Coriolis force more clearly, let us consider classically its effect in a linear symmetric XY_2 molecule. Consider the vibration ν_3 in the rotating molecule. The displacement vectors (solid arrows in Fig. 3) also give the relative velocities at the instant when the nuclei pass through the equilibrium position. The Coriolis force on each nucleus is proportional to this velocity but perpendicular to it, and, for a counterclockwise direction of rotation, always toward the right when looking in the direction of motion.

From Fig. 3 it is seen that during the vibration ν_3 , these forces tend to excite the perpendicular vibration ν_2 , but with the frequency of ν_3 . Conversely, when the vibration ν_2 is excited in the rotating molecule, the Coriolis forces are as given in Fig. 3 and tend to excite

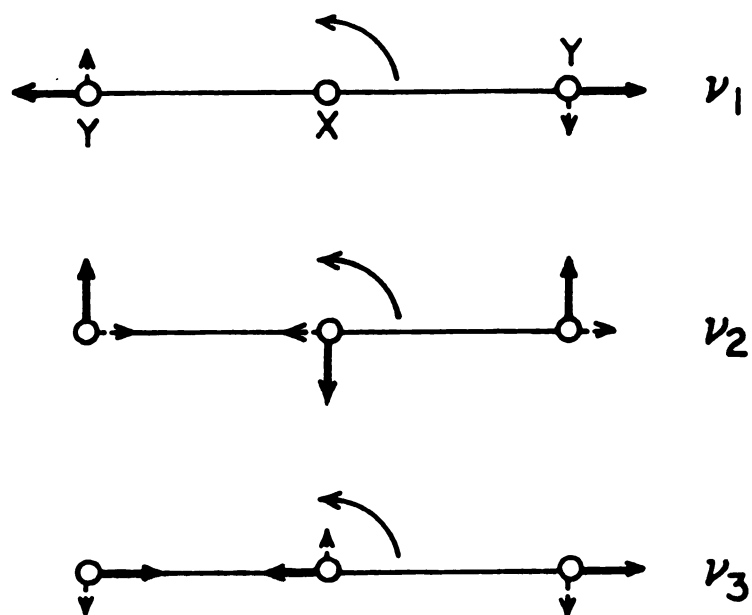


Figure 3. Normal vibrations of a linear XY_2 molecule and the effects of Coriolis coupling. ν_2 is a degenerate bending vibration and the arrows attached to the atoms represent one component of the vibration. The other component (not shown) results from identical motions perpendicular to the plane of the paper.

the parallel vibration ν_3 but with the frequency ν_2 .

If the frequencies of ν_2 and ν_3 were nearly the same accidentally, a strong excitation of one of the two vibrations would take place if the other were first excited, in consequence of this Coriolis coupling. However, this excitation will be very weak when ν_2 and ν_3 have widely different frequencies. No coupling takes place between ν_1 and ν_3 or between the two components of ν_2 . This results from the effective absence of rotation about the figure axis in a linear molecule. This coupling is called the second-order Coriolis interaction. These two components of the degenerate bending mode can couple in a symmetric top molecule where rotation about the figure axis is allowed.

Figure 4 illustrates the effects of a Coriolis force on the degenerate bending mode in a symmetric top molecule. When one of the degenerate components is excited, rotation about the figure axis produces vibrational components which excite the other component. Since the two frequencies are identical, the interaction may be very strong. This is called the first-order interaction because it does not vanish in the absence of rotation about the figure axis ($k=0$). Even when rotation ceases, a vibrational angular momentum coupling the two degenerate components is present. However, the degeneracy is only lifted by the second-order terms in the vibration-rotation Hamiltonian when rotation is present ($k \neq 0$) because the two modes of vibration still

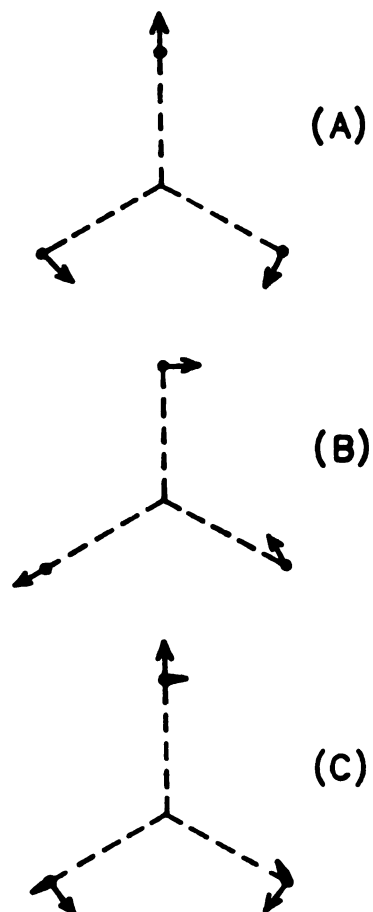


Figure 4. Coriolis coupling of the degenerate bending vibrations in a XYZ_3 symmetric top. (A) and (B) illustrate two components of the degenerate bending mode. (C) shows the coupling effect of the Coriolis force on the (A) mode as it tends to induce the (B) mode. In all three illustrations, the figure axis is perpendicular to the plane of the paper and only off-axis atoms are shown.

have the same energy when $k = 0$. For one level $k = l$ and for the other level $k = -l$, the relative positions of these two levels will depend on the sign of the Coriolis coupling constant. For C_{3v} molecules, the first excited state of a degenerate bending vibration must belong to the degenerate irreducible representation E, and the rotational wave functions belong to the representations of the subgroup C_3 . The important case results when $k = \pm 1$, $l = \pm 1$. The rotational wave functions for $k = \pm 1$ belong to E with the resulting symmetry of $\psi_v \psi_r$ coming from the product

$$E \times E = 2A + E . \quad (41)$$

Of the four levels produced by $k = \pm 1$, $l = \pm 1$ permutations, two will be nondegenerate and two form a degenerate pair whose degeneracy cannot be lifted by any internal permutations of C_3 symmetry.

For $k = 1$ the value of $|k-l|$ may be either 0 or 2. From the symmetry consideration of the group C_{3v} , the levels of A symmetry for a given k must have a value of $|k-l| = 3n$; if $|k-l|$ is not a multiple of three, the level belongs to the representation E. In this case the levels with $k = l$ have A symmetry and can be split by l -type doubling.

With interaction between an A_1 species normal coordinate Q_r and an E species pair of coordinates (Q_{s1}, Q_{s2}) due to rotation about the x and y axes, each pair of

degenerate symmetry coordinates or normal coordinates satisfy the following equations:

$$\hat{C}_3(Q_{s_1} + iQ_{s_2}) = e^{-i2\pi/3}(Q_{s_1} + iQ_{s_2})\hat{C}_3, \quad (42)$$

$$\hat{\sigma}_v^{(xz)}(Q_{s_1} + iQ_{s_2}) = (Q_{s_1} - iQ_{s_2})\hat{\sigma}_v^{(xz)}. \quad (43)$$

Equation(42) defines the relative sense of each pair of degenerate coordinates and Eq. (43) fixes their coordination in the (x,y) plane. The $A_1 - E$ interaction is characterized by a single zeta constant for the above coordinate conventions

$$\zeta_{r,s_1}^y = -\zeta_{r,s_2}^x = \zeta_{rs}^y \quad (44a)$$

and

$$\zeta_{r,s_1}^x = +\zeta_{r,s_2}^y = 0. \quad (44b)$$

The interaction between the pair of coordinates Q_{s_1} and Q_{s_2} due to rotation about the z axis is characterized by the constant

$$\zeta_{s_1,s_2}^z = \zeta_s^z. \quad (45)$$

If the normal coordinate vectors are known, the zeta constants may be conveniently calculated from C matrix

elements defined according to Ref. 47

$$\zeta^\alpha = L^{-1}C^\alpha(L^{-1}), \quad (46)$$

where $\alpha = x, y$ or z .

Considering the matrix representing H in the vibration-rotation basis functions, denoted by $|v_r, v_s^{ls}, J, k\rangle$, the important selection rules for interaction between the first two excited vibrational levels in Q_r (A_1 species) and Q_{s1}, Q_{s2} (E species) are $\Delta k = \Delta l_s = \pm 1$; translated into terms of $K = |k|$ these become: $E(+l)$, $k+l$ interacts with A_1 , k which interacts with $E(-l)$, $k-l$. The interaction is illustrated in Fig. 5. Thus if the interaction is large, k and l_s are not good quantum numbers; the true rovibrational states are some mixture of the basis functions which cannot be characterized by particular values of k and l_s . For each value of J the Hamiltonian matrix factorizes into a number of (3×3) blocks, according to the scheme of Fig. 6, each block being characterized by a particular value of $(k-l_s)$, so that $(k-l_s)$ remains a good quantum number. In addition to the (3×3) blocks there will be two (2×2) blocks, for which $(k-l_s) = \pm J$, and two (1×1) blocks (unperturbed states) for which $(k-l_s) = \pm(J+1)$. A typical (3×3) block of the Hamiltonian has the form

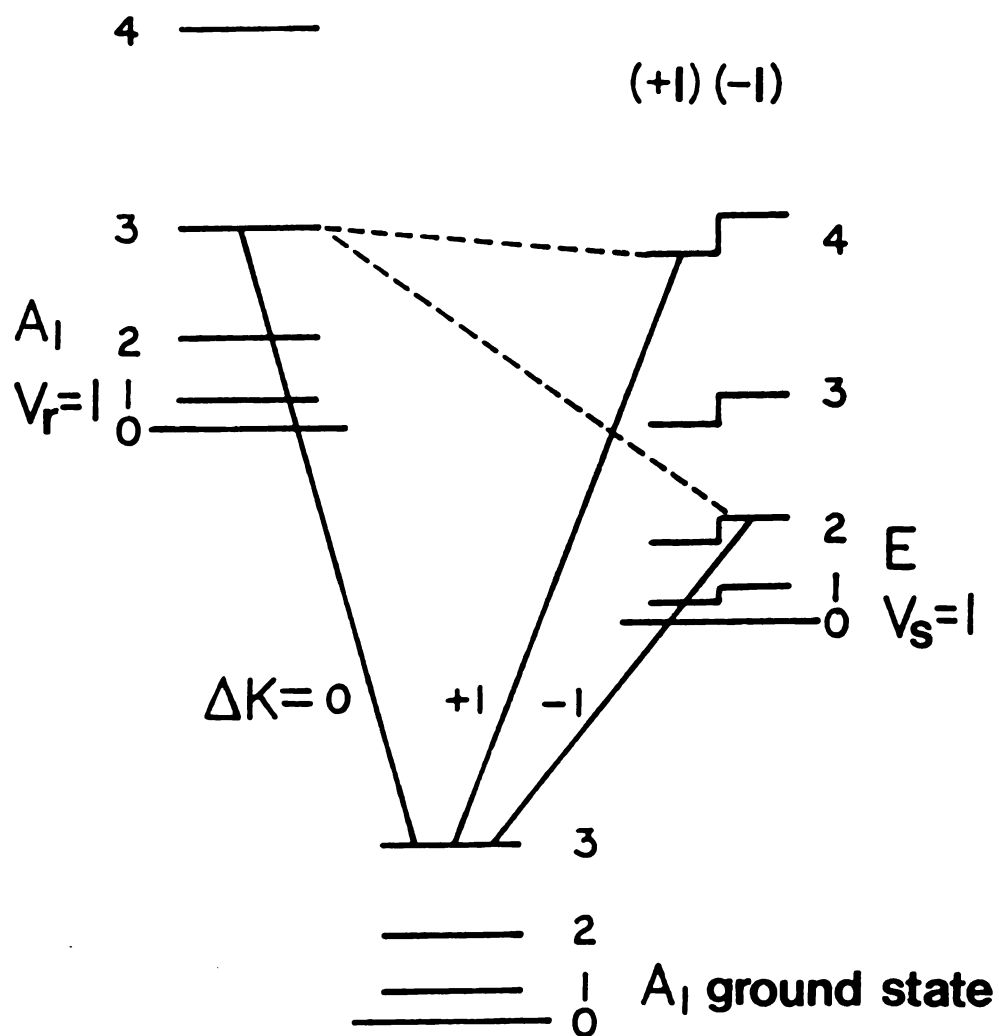


Figure 5. Allowed transitions and interactions for an A_1 and an E fundamental of a C_{3v} molecule.

Vibrational quantum numbers	E	A_1	E
	$V_s = 1$	$V_r = 1$	$V_s = 1$
	$ _s = +1$	$ _s = 0$	$ _s = -1$

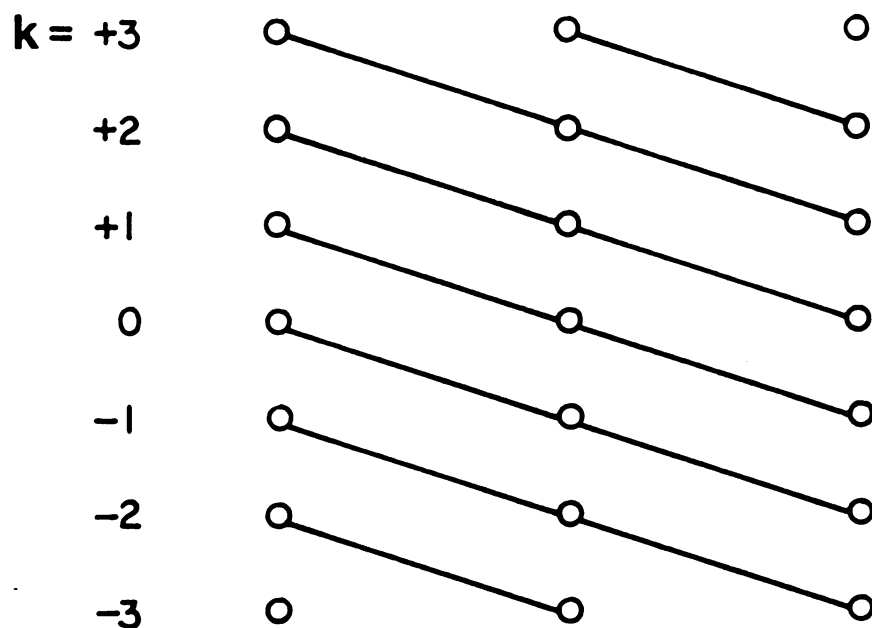


Figure 6. Diagrammatic representation of interaction between an A_1 and an E vibrational state for $J = 3$. Each dot represents a basis function characterized by particular values of k and k_s ; the lines represent Coriolis interactions, connecting states of the same $(k - k_s)$. Except for the extreme values of $(k - k_s)$ the secular equation factors into (3×3) blocks.

$$\begin{aligned}
& \langle \nu_r, \nu_s^{\lambda s}, J, K \rangle = \\
& \left| \begin{array}{ccc}
|0, 1^{+1}; J, k+1\rangle & |1, 0; J, k\rangle & |0, 1^{-1}; J, k-1\rangle \\
\nu_s + F'(J, k+1) & 2^{1/2} B' \Omega_{rs} \zeta_{rs}^y [J, k]^{1/2} & 0 \\
-2A' \zeta_s^z (k+1) & & \\
\nu_r + F'(J, k) & -2^{1/2} B' \Omega_{rs} \zeta_{rs}^y [J, k-1]^{1/2} & \\
\text{(Hermitian)} & & \\
\nu_s + F'(J, k-1) & & \\
+2A' \zeta_s^z (k-1) & &
\end{array} \right| \quad (47)
\end{aligned}$$

where

$$F'(J, k) = B' J(J+1) + (A' - B') k^2 \quad (48)$$

$$\Omega_{rs} = \frac{1}{2} [(\nu_r/\nu_s)^{1/2} + (\nu_s/\nu_r)^{1/2}] \quad (49)$$

and

$$[J, k]^{1/2} = [J(J+1) - k(k+1)]^{1/2} \quad (50)$$

The off-diagonal elements in Eq. (47) arise from the terms $-(2B/\hbar^2)(P_x J_x + P_y J_y)$ in the Hamiltonian. They are obtained by expressing the vibrational angular momenta in terms of the normal coordinates.

For the CH_3F molecule, the Coriolis interaction between the $\nu_3(J, K)$ levels and the $\nu_6(J, K-1, \lambda=-1)$ levels is large enough to produce a deviation from the normal symmetric top energy. At the level of approximation of

second-order perturbation, this interaction energy is incorporated into B_3 , the rotational constant of the ν_3 state. The deviation from the second-order term is given by the fourth-order term(48), as follows:

$$\delta E = \frac{[\langle \nu_3, J, K, 0 | H' | \nu_6, J, K-1, -1 \rangle]^4}{[\nu_6(J, K-1, -1) - \nu_3(J, K)]^3} \quad (51)$$

where

$$\begin{aligned} \langle \nu_3, J, K, 0 | H' | \nu_6, J, K-1, -1 \rangle &= iB\zeta_{36}^{(b)} [(J+K)(J-K+1)]^{1/2} \\ &[\nu_3/\nu_6]^{1/2} + [\nu_6/\nu_3]^{1/2} / 2^{1/2} \end{aligned} \quad (52)$$

and

$$\begin{aligned} \nu_6(J, K-1, -1) - \nu_3(J, K) &= \nu_6^0 - \nu_3^0 - A(2K-1+\zeta)(1-\zeta) \\ &+ 2B(2K-1) . \end{aligned} \quad (53)$$

In modern calculations, the 3x3 matrix in Eq. (47) is diagonalized numerically rather than relying on perturbation theory.

The centrifugal force differs from the Coriolis force in that it does not vanish in the absence of a perturbing vibrational mode. The centrifugal force on a mass m at a distance r from the axis of rotation is

$$\vec{F}_c = m \vec{\omega}^2 \vec{r} . \quad (54)$$

The effects of centrifugal distortion are generally small for low J values but can reach the order of hundreds of megahertz for transitions between levels of high J .

Rotation in a symmetric top is accompanied by centrifugal forces which tend to alter the effective moments of inertia. For rotation about any axis in the molecule, this dynamic effect forces the atom away from the axis of rotation and increases the moment of inertia about that axis. The centrifugal effects enter the energy level expression as higher powers of $J(J+1)$ and K . For a prolate rotor, the first correction due to centrifugal distortion leads to the energy expression

$$\begin{aligned} E/h = & BJ(J+1) + (A-B)K^2 - D_J J^2(J+1)^2 \\ & - D_{JK} J(J+1)K^2 - D_K K^4 . \end{aligned} \quad (55)$$

Here, D_J , D_{JK} , and D_K are centrifugal distortion constants.

Dependence of the rotational and centrifugal distortion constants on the vibrational state is assumed implicitly. The correction terms for centrifugal distortion are found to depend only on even powers of the angular momentum because the distortion effects do not depend on the direction of rotation about any axis. The frequencies of a

symmetric top molecule (selection rules $\Delta J=1$, $\Delta k=0$)
exhibiting detectable centrifugal distortion effects are

$$h\nu(J+1, k \leftarrow J, k) = 2B(J+1) - 2D_{JK}(J+1)K^2 - 4D_J(J+1)^3 \quad (56)$$

Since the effective rotational constants tend to decrease due to the centrifugal force, D_J is normally positive, but D_{JK} may have either sign. The centrifugal distortion constants can be expressed in terms of the moments of inertia (molecular structure) and molecular force constants of the molecule. However, a theoretical calculation of these constants is very difficult except for the simplest structures.

Wilson(49) has given explicit formulas for the distortion constants D_J , D_{JK} , and D_K for a symmetric top molecule with C_{3v} symmetry in the harmonic oscillator approximation. The formulas are given in terms of the constants,

$$I_1 = I_b + I_c = \sum_{\alpha} m_{\alpha} (x_{\alpha}^2 + y_{\alpha}^2 + 2z_{\alpha}^2), \quad (57)$$

$$I_2 = I_b - I_c = \sum_{\alpha} m_{\alpha} (x_{\alpha}^2 - y_{\alpha}^2), \quad (58)$$

$$I_3 = \sum_{\alpha} m_{\alpha} (x_{\alpha}^2 + y_{\alpha}^2), \quad (59)$$

$$I_4 = 2 \sum_{\alpha} m_{\alpha} y_{\alpha} z_{\alpha} \quad , \quad (60)$$

where the z axis corresponds with the a axis (figure axis).

The formulas are as follows:

$$D_J = \frac{8\pi^4}{h} B_e^4 \left[\sum_{i,j} \frac{\partial I_1}{\partial S_i} (F^{-1})_{ij} \frac{\partial I_1}{\partial S_j} + \sum_{i,j} \frac{\partial I_2}{\partial S_i} (F^{-1})_{ij} \frac{\partial I_2}{\partial S_j} \right], \quad (61)$$

$$D_{JK} = -2D_J + \frac{32\pi^4 A_e^2 B_e^2}{h} \left[\sum_{i,j} \frac{\partial I_3}{\partial S_i} (F^{-1})_{ij} \frac{\partial I_3}{\partial S_j} + \sum_{i,j} \frac{\partial I_4}{\partial S_i} (F^{-1})_{ij} \frac{\partial I_4}{\partial S_j} \right], \quad (62)$$

$$D_K = -D_J - D_{JK} + \frac{32\pi^4 A_e^4}{h} \sum_{i,j} \frac{\partial I_3}{\partial S_i} (F^{-1})_{ij} \frac{\partial I_3}{\partial S_j} . \quad (63)$$

In these equations I_b and I_c are regarded as instantaneous moments of inertia. The S_i are internal symmetry coordinates, and the F_{ij} are elements of the force constant matrix consistent with the S_i and S_j . The derivatives of I_1 and I_3 are non-zero only for internal symmetry coordinates which have the symmetry A_1 of C_{3v} . Similarly, the derivatives of I_2 and I_4 vanish unless the S_i have symmetry E.

For large J and K values and/or light molecules, the distortion correction must be extended to higher order. The present study required centrifugal distortion constants that multiplied the eighth power of the angular momentum quantum

numbers. The energy level expression used was

$$\begin{aligned}
 E(J,K) = & BJ(J+1) + (A-B)K^2 - D_J J^2(J+1)^2 - D_{JK} J(J+1)K^2 \\
 & - D_K K^4 + H_J J^3(J+1)^3 + H_{JK} J^2(J+1)^2 K^2 + H_{KJ} J(J+1)K^4 \\
 & + H_K K^6 + L_{4J} J^4(J+1)^4 + L_{3JK} J^3(J+1)^3 K^2 \\
 & + L_{2JKK} J^2(J+1)^2 K^4 + L_{JKKK} J(J+1)K^6 + L_K K^8 \quad (64)
 \end{aligned}$$

where H_J , H_{JK} , H_{KJ} , H_K , L_{4J} , L_{3JK} , L_{2JKK} , L_{JKKK} , and L_K are additional distortion constants.

Intensities of Symmetric Top Transitions

The intensity of a vibration-rotation transition for a symmetric top molecule interacting with plane polarizing radiation may be calculated from the basic formula given as follows:

$$\gamma = \frac{8\pi^2 N f |\mu_{ij}|^2 \nu^2 \Delta\nu}{3ckT[(\nu-\nu_0)^2 + (\Delta\nu)^2]} \quad ; \quad (65)$$

Here N = the number of molecules per unit volume in the absorption cell,

f = the fraction of the molecules in the lower of the two states involved in the transition,

$|\nu_{ij}|^2$ = the square of the dipole moment matrix element for the transition, summed over n components,

ν = the source frequency,

ν_0 = the resonant frequency or, to a good approximation, the center frequency of the absorption line,

$\Delta\nu$ = the half width of the line at half maximum, or the line-breadth parameter,

c = velocity of light,

k = Boltzmann constant,

and T = absolute temperature.

The selection rule for a parallel band, in which the dipole moment matrix element is non-zero only for the component along the molecular axis may be written for a nonplanar symmetric top without inversion, as follows:

$$\Delta J = 0, \pm 1, \quad \Delta k = 0. \quad (66)$$

The matrix elements, which are non-zero only for transitions given by the above selection rules, are as follows;

$$\Delta J = +1, \quad \Delta k = 0; \quad |\nu_{ij}|^2 = \nu^2 \frac{(J+1)^2 - k^2}{(J+1)(2J+1)} \quad (67)$$

$$\Delta J = 0, \quad \Delta k = 0; \quad |\nu_{ij}|^2 = \nu^2 \frac{k^2}{J(J+1)} \quad (68)$$

$$\Delta J = -1, \Delta k = 0; \quad |\nu_{ij}|^2 = \nu^2 \frac{J^2 - k^2}{J(2J+1)} \quad (69)$$

The fraction of the molecules in a particular initial state is the product of the fraction f_v in the vibrational state of interest and the fraction of these f_{JK} in a particular rotational state. If the statistical weight due to nuclear spin is neglected, the probability of a molecule being in a state (J, K) is proportional to

$$(2J+1) e^{-E_{JK}/kT} \quad (70)$$

where E_{JK} is the rotational energy level given by Eq.(64) and $2J+1$ is the statistical weight due to the different orientations of J (different m states). The fraction of molecules in this rotational state is

$$f_{JK} = \frac{(2J+1) e^{-E_{JK}/kT}}{\sum_{J=0}^{\infty} \sum_{k=-J}^J (2J+1) e^{-E_{JK}/kT}} \quad (71)$$

If B and A in E_{JK} are small compared to kT/h and if the small contribution due to centrifugal force can be neglected, the sum may be replaced by integrals giving

$$f_{JK} = (2J+1) e^{-E_{JK}/kT} \sqrt{\frac{B^2 A h^3}{\pi (kT)^3}} \quad (72)$$

Equation(72) applies to one particular value of K , and does

not allow for K degeneracy.

For a C_{3v} symmetric top without inversion, the degeneracy due to spin and K degeneracy for each value of J and K is giving by the following rules:

For K a multiple of 3, but not 0

$$S(I, K) = 2(4I^2 + 4I + 3)(2I + 1)/3 \quad (73a)$$

For K = 0

$$S(I, K) = (4I^2 + 4I + 3)(2I + 1)/3 \quad (73b)$$

For K not a multiple of 3

$$S(I, K) = 2(4I^2 + 4I)(2I + 1)/3 \quad (73c)$$

Allowing for this degeneracy, Eq. (71) becomes

$$f_{JK} = \frac{\sum_{J=0}^{\infty} \sum_{K=0}^J \frac{S(I, K)(2J+1)}{S(I, K)(2J+1)} e^{-E_{JK}/kT}}{\sum_{J=0}^{\infty} \sum_{K=0}^J S(I, K)(2J+1) e^{-E_{JK}/kT}} \quad (74)$$

With the assumption that B and A are much smaller than kT/h , Eq. (74) becomes

$$f_{JK} = \frac{S(I, K)(2J+1)}{4I^2 + 4I + 1} \sqrt{\frac{B^2 A h^3}{\pi (kT)^3}} e^{-E_{JK}/kT} \quad (75)$$

For low values of J and K

$$f_{JK} = \frac{S(I, K)(2J+1)}{4I^2 + 4I + 1} \sqrt{\frac{B^2 A h^3}{\pi (kT)^3}} \quad (76)$$

The fraction of molecules in a given vibrational state may be obtained as

$$f_v = e^{-\omega_n/kT} \prod_n (1 - e^{-\hbar\omega_n/kT})^{d_n} \quad (77)$$

where d_n is the degeneracy of a vibrational mode of frequency ω_n . By substituting Eqs. (67) and (76) into (65), and setting $2B(J+1) = h\nu_0$, the intensity for a transition $J+1 \leftarrow J$, $K \leftarrow K$ is found to be

$$\gamma = \frac{4\pi h^2 N f_v S(I, K)}{(4I^2 + 4I + 1) 3c(kT)^2} \sqrt{\frac{\pi A h}{kT}} \nu^2 \left[1 - \frac{K^2}{(J+1)^2} \right] \frac{\nu_0 \nu^2 \Delta \nu}{(\nu - \nu_0)^2 + (\Delta \nu)^2} \quad (78)$$

CHAPTER III

INSTRUMENTATION

Introduction

The infrared spectrometer is one of the most useful instruments for study of the molecular dynamics such as vibration-rotation interaction, nuclear spin-rotation interaction, effects of molecular collisions, etc.

About 15 years ago it became possible to obtain high resolution spectra in the IR region by using a tunable narrow linewidth laser - the semiconductor diode laser(50). Since that time, several high resolution tunable IR lasers have been developed. Among these are the difference frequency laser(51), the color center laser(52), the spin-flip Raman laser(53), the waveguide laser(54,55,56), and magnetically tuned gas lasers(57,58).

The most useful laser in the mid-IR region is still the CO₂ laser, which provides coherent output radiation of high intensity at a multitude of lines spaced $\sim 2 \text{ cm}^{-1}$ apart. The only drawback to the CO₂ laser is its fixed frequency nature, limiting its spectroscopic applications to accidental coincidences between a laser frequency and some feature of spectroscopic interest.

Several methods have been developed to increase the tunable range of the CO₂ laser. One such method is the

waveguide CO₂ laser which uses the molecular collisional broadening of CO₂ to increase the tuning range. In practice, the tunability of a waveguide laser is limited to ± 500 MHz around each laser line which, although useful, is too narrow for general molecular spectroscopy. A second method for increasing the tuning range is infrared microwave two-photon spectroscopy which uses the simultaneous interaction of an infrared photon, a microwave photon, and an absorbing molecule. This technique has wide tunability but has low sensitivity since it involves a nonlinear absorption. In this method, the transition moment is inversely proportional to the square of the laser frequency mismatch(59). For a symmetric top molecule,

$$M_2 = \frac{(\langle 1 | \vec{\mu}_p \vec{\epsilon}_r | 1 \rangle - \langle 2 | \vec{\mu}_p \vec{\epsilon}_r | 2 \rangle) \langle 1 | \vec{\mu}_v \vec{\epsilon}_l | 2 \rangle}{2\hbar^2 \omega_r} \quad (79)$$

where $\vec{\mu}_p$ and $\vec{\mu}_v$ are the permanent and vibrational dipole moment, respectively; ϵ_r and ϵ_l are the amplitudes of the microwave and laser electric fields, respectively; and ω_r is the angular frequency of the MW radiation. A third method for increasing the tunability of a CO₂ laser is the infrared microwave sideband technique which is the subject of this thesis. With this method the radiation has a frequency of $\nu_{IR} \pm \nu_{MW}$ (60) and has the tunability of the microwave frequency ν_{MW} .

Generation of IR-MW Sideband Radiation

Franken et al.(61) observed the first nonlinear optical effect generated from a dielectric crystal. In this experiment second harmonic energy ($\sim 3472 \text{ \AA}$) was produced upon projection of a beam of 6943 \AA light through crystalline quartz. The sum frequency from two beams at different frequencies was observed by Bass et al.(62), in which two ruby lasers at different temperatures were used for radiation sources.

Corcoran et al.(60) observed the first CO_2 laser-MW sideband radiation by using a GaAs loaded waveguide cell as a modulator to measure CO_2 gain profiles. Since then there have been many developments to increase the tunability and the power for general molecular spectroscopy(63-68). However, the CO_2 laser-MW sideband laser system most useful for molecular spectroscopy was developed by Magerl et al.(69). They described a device that operates in a traveling wave mode with low power and wide tunability, or in a cavity mode with high power and narrow tunability.

The first application of the sideband laser technique to molecular spectroscopy was a report by Magerl et al.(70) in 1977 on the fundamental ν_3 band of the SiH_4 molecule. Even though the sideband power is very weak due to low coupling efficiency between the two kinds of radiation,

sub-Doppler spectroscopy has been performed on the NH_3 molecule(71) by employing modulated sidebands in an optical double resonance experiment and in a saturated Lamb-dip experiment.

Structure of the Modulator

The expression for the sideband power P_{SB} generated by an electrooptic crystal with cubic symmetry (CdTe single crystal) is given by(72)

$$P_{\text{SB}} = P_L \Gamma^2 / 16 \quad (80)$$

Here, P_L is the incident laser carrier power and Γ is the single-pass phase retardation induced by the transverse electrooptic effect. The latter can be written as(73,74)

$$\Gamma = \left(\frac{2\pi}{\lambda_L} \right) n_0^3 r_{41} E_{\text{m}} L_{\text{m}} \text{SINC} (\omega_{\text{m}} L_{\text{m}} / 2W) \quad (81)$$

where λ_L stands for the free-space wavelength of the CO_2 laser, E_{m} denotes the peak microwave electric field strength within the modulator crystal, n_0 is the refractive index, r_{41} is the electrooptic coefficient, and L_{m} is the length of the modulator crystal. The abbreviation $\text{SINC}(x)$ is used for $(\sin x)/x$, ω_{m} is the angular frequency of the modulator

signal, and $1/W$ characterizes the mismatch of the microwave phase velocity (v_M) and of the laser group velocity (v_g) within the modulator, that is,

$$\frac{1}{W} = \frac{1}{v_g} - \frac{1}{v_M} \quad (82)$$

For optimum electrooptic interaction, the laser group velocity (v_g) should be same as the microwave phase velocity (v_M). Since the refractive index of the modulator crystal (CdTe) in the IR region is appreciably smaller than the square root of the microwave dielectric constant, it is necessary to accelerate the microwave signal. The easiest way to do this is to insert the modulator crystal inside a closely fitting rectangular waveguide. The width of the crystal a_M can be obtained as follows:

$$a_M = c_0 / (2f_{M0} \sqrt{E_r} - n_0^2) \quad (83)$$

where f_{M0} is the microwave frequency where exact velocity match occurs, c_0 is the speed of light, and E_r is the relative dielectric constant of the electrooptic crystal.

Figure 7 shows the modulator diagram designed by G. Magerl of the Technical University of Vienna, which is optimized for microwave frequency modulation at 8.2 - 18.0 GHz. In this design, the CdTe crystal ($E_r = 10$) is partly replaced by two less expensive and stronger alumina (Al_2O_3)

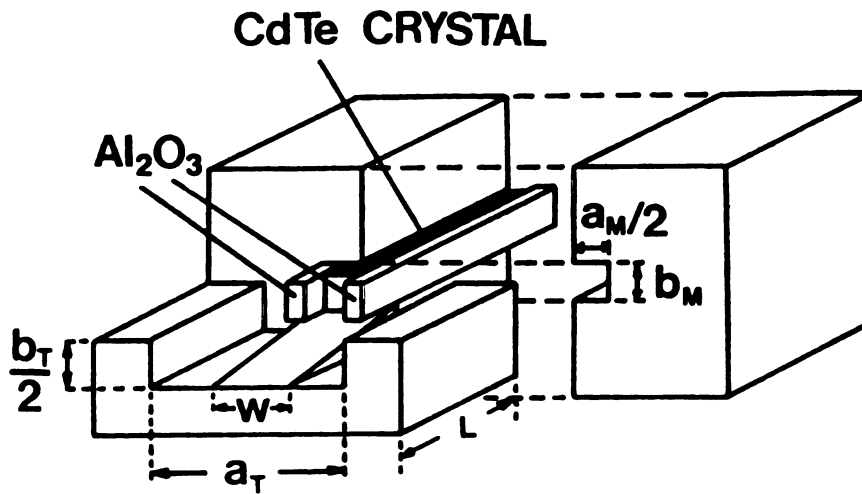


Figure 7. Diagram of the sideband modulator, in which the CdTe crystal is embedded between two Al₂O₃ slabs to achieve velocity match. The tapered double-ridged waveguide section (upper half removed) provides impedance match to incoming/outgoing standard waveguide sizes.

strips with about the same microwave dielectric constant ($\epsilon_r = 9.5$). The crystal cross section is designed to be a square with side b_M , which is chosen as small as possible for high modulating field E_m , but large enough to permit unimpeded laser beam focusing through the modulator.

The excess length of the Al_2O_3 slabs permitted improved coupling of the microwave energy into the modulator. By altering the relative positions of the CdTe and Al_2O_3 in a trial and error process, it is possible to obtain with different arrangements of the crystals either an almost perfectly matched traveling wave modulator (terminated by a power load) or a critically coupled resonant modulator (terminated by a sliding short section for frequency tuning).

Adjustment of the Crystal Position in the Modulator

Since the sideband power depends mainly on the velocity mismatch (l/W) within the modulator, the adjustment of the position of the CdTe and Al_2O_3 crystal is crucial in generating the optimum sideband power over a desirable modulation frequency range for a given laser and microwave power.

Figure 8 is a diagram of the microwave setup used for the adjustment of crystal within the modulator. For this

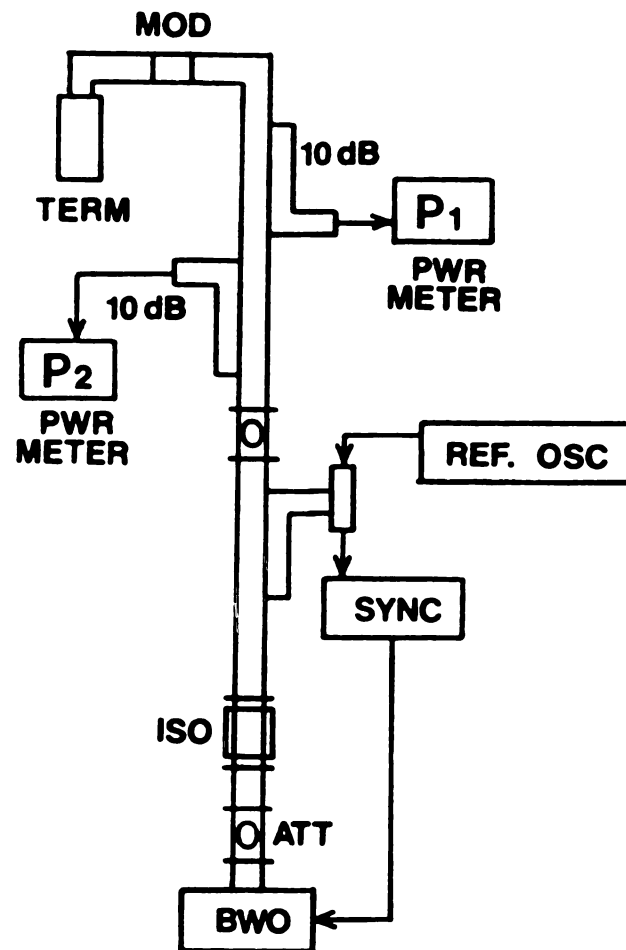


Figure 8. Experimental diagram for adjusting the position of crystal inside modulator.

experiment, 10 dB-directional couplers P_2 and P_1 monitor the input microwave power and the reflected microwave power from the modulator, respectively. By trial and error adjustment of the position of the crystal and of the length of the modulator housing, the almost optimum condition shown in Fig. 9(C) was obtained. In this configuration, the housing is 23 mm long, the CdTe crystal is 0.5 mm behind the edge of modulator and the two alumina slabs are 3.0 mm in front of the modulator.

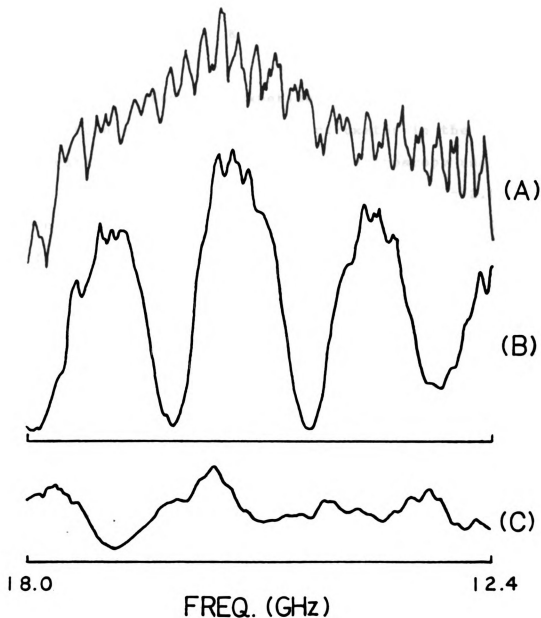


Figure 9. Variation of coupling efficiency with the crystal position. (A) represents input microwave power with frequency. (B) and (C) indicate the reflected microwave power from the modulator with improper position and optimum position, respectively.

CHAPTER IV

EXPERIMENT

Figure 10 shows the experimental diagram of a CO₂ laser-microwave sideband laser spectrometer in the configuration for linear absorption spectroscopy used in the early stages of this work. The laser medium is a 2.2 m water cooled plasma discharge containing less than 10 torr of a flowing gas mixture of CO₂, N₂, and He. The plasma tube is in a 4 m cavity mounted on an invar frame. The laser tube is a 25 mm inner diameter Pyrex glass tube sealed with NaCl windows at the Brewster angle at each end. The windows are oriented such that the output radiation is plane polarized with the electric field of the radiation parallel to the floor. One end of the cavity is a rotatable plane grating of 50 mm diameter ruled with 150 lines/mm. The other end of the cavity is a partially transmitting (95% reflection) concave spherical Ge mirror (50 mm diameter, 10 m radius of curvature) which is mounted on a piezoelectric translator (PZT) to control the length of the laser cavity. For stabilization of the laser frequency the position of the cavity mirror is sinusoidally modulated at 250 Hz, causing modulation of the laser cavity length and therefore modulation of the laser frequency. A cell containing CO₂ at a pressure ranging from 30-100 mTorr, depending on the CO₂

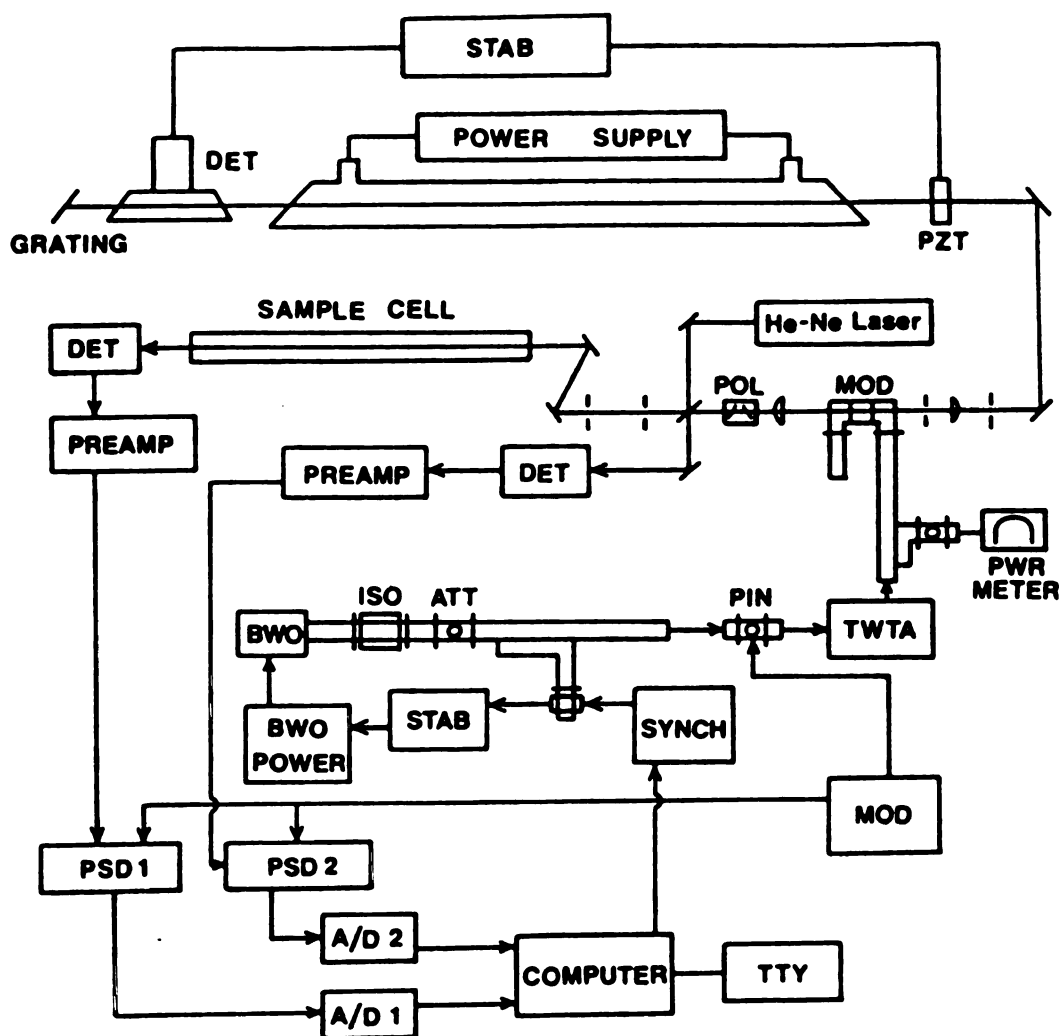


Figure 10. Block diagram of IR-MW sideband laser spectrometer used for the measurement of $^{13}\text{CH}_3\text{F}$, set for linear absorption spectroscopy of gases.

laser line, is inserted in the cavity(29). The frequency modulation of the laser causes amplitude modulation of the saturation-dip in the fluorescence from this cell at $\sim 4.3 \mu\text{m}$ wavelength. The fluorescence is detected by a liquid N_2 cooled InSb photovoltaic detector and is processed at 250 Hz by a phase sensitive detector (PSD). The output of the PSD controls the output of a high voltage operational power supply (OPS) which sets the length of the PZT. By this means the laser frequency is controlled to $\pm 300 \text{ kHz}$ (1 part in 10^8). An Optical Engineering Model 16-A CO_2 laser spectrum analyzer was used to identify the particular CO_2 laser line. The frequency of the laser radiation depends on the orientation of the grating and the length of the laser cavity. The grating is rotated to select a particular laser line and the length of the cavity provides fine frequency control within the laser gain curve. The cavity length is controlled by the PZT crystal whose length is linearly proportional to the voltage applied to crystal. Figure 11 shows the relationship between the PZT voltage (laser cavity length) and the laser gain curve with a saturation Lamb-dip. Thus the laser optics can be adjusted for single frequency, single mode operation at the Lamb-dip of the gain curve with an output power of 10 watts on the strongest laser line.

The laser output radiation is focussed by a ZnSe lens into a CdTe single crystal mounted in double ridge microwave cell where electrooptic interaction with the tunable

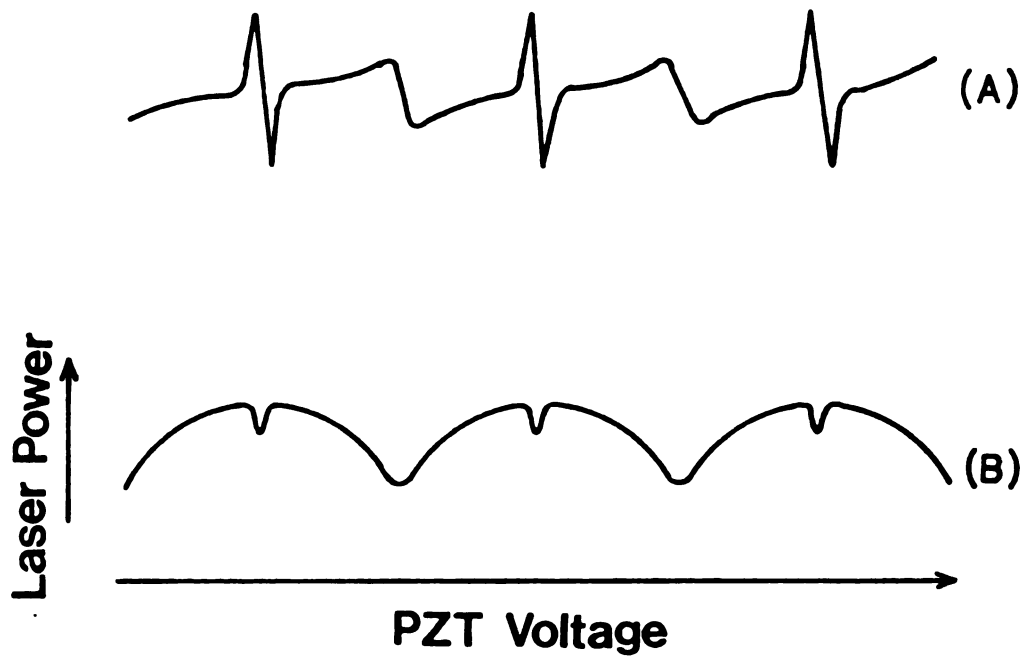


Figure 11. Variation of the output laser power (B) and the differential signal (A) displayed on screen with piezoelectric translator voltage. The signal due to Lamb-dip can be easily distinguished from that due to the end of mode.

microwave signals is accomplished. The infrared power at the entrance of the modulator is kept less than 2 watts by adjusting the size of the diaphragms in the laser to prevent damage to the crystal or to its anti-reflective coating.

The microwave source is either one of two Varian Backward Wave Oscillators (BWO) operating in the 8.0-12.4 GHz or the 12.4-18.0 GHz region. The voltages for the BWO are obtained from a power supply designed at MSU, except for the frequency controlling helix voltage. This voltage is obtained from a Kepco Model 2000 operational power supply, which is controlled by the output from a digital/analog converter that is in turn controlled by a minicomputer. The microwave frequency is brought into the lock range of a phase sensitive synchronizer (Hewlett Packard Model 8709A) by the OPS output. The synchronizer locks the microwave frequency to 20 MHz above a harmonic of a synthesized frequency also controlled by the computer, so that the frequency sweep of the BWO is under complete control of the computer. The attenuated output power of the BWO enters a 3 dB directional coupler, where it is divided into two parts; one part is sent to a diode mixer-multiplier for comparison with a harmonic of a precisely known reference frequency, the other part which has around 1 mW power, is switched at a frequency of 33.3 kHz square wave by a PIN diode. The modulated MW signal is then amplified to more than 20 watts

by means of a traveling wave tube amplifier (Varian Model VZM-6991B1 TWT). The output of the TWT with the polarization of the MW adjusted to be perpendicular to that of the CO_2 laser radiation, is applied directly to the modulator. With the aid of the TWT, we can access a tunable range of 8.2-18.0 GHz on either side of each CO_2 laser line.

Four kinds of radiation are emitted from the modulator: (1) slightly modulated carrier radiation which has almost the same power as the input radiation but whose phase is rotated 90° from that of the sidebands, (2) fully modulated carrier with the same polarization as the sidebands and with comparable amplitude, (3) the fully modulated positive sideband whose frequency is the sum of the CO_2 laser and microwave frequencies, and (4) the fully modulated negative sideband whose frequency is the difference of the CO_2 laser and microwave frequencies. Both sidebands have the same polarization as that of microwave radiation. The fraction of negative sideband within the total sideband power increases with decreasing microwave frequency, reaching almost 100% of total sideband power in the 8-9 GHz region. This appears to be an unexplained property of our particular modulator.

A ZnSe focusing lens with a 20 cm radius of curvature is located ~25 cm from the modulator. A second comparable lens recollimates the radiation. A II-VI Model PAZ-6-AC

polarizer, which consists of six ZnSe windows placed at the Brewster angle substantially attenuates the carrier radiation. A Ge beam splitter divides the sideband radiation into a probe beam, which passes through a sample cell containing the sample gas, and into a reference beam. The sideband radiation that passes through the cell is monitored by a liquid N₂ cooled Santa Barbara Research Center Hg-Cd-Te photoconductive detector, and the reference beam is monitored by a liquid N₂ cooled Honeywell Radiation Center Hg-Cd-Te photovoltaic detector. The outputs of the two detectors are amplified and processed by two phase sensitive lock-in amplifiers whose reference frequencies are obtained from the square wave that drives the PIN switch in the microwave circuit.

The power and the beam direction of the sideband radiation depend on the modulator temperature which is strongly affected by the microwave power and by the alignment of the CO₂ laser beam in the crystal. In order to maintain a constant temperature at the modulator, it was air-cooled by means of a fan. In addition, the modulator position was adjusted to obtain the maximum signal to noise ratio.

For the measurements in this work, less than 200 mTorr of sample pressure for the fundamental band and less than 2 Torr of sample pressure for the hot band were used. For some experiments, the sample cell was heated to ~100 °C to

increase the population of the first excited state, causing increased intensity on the hot band transition. The pressure was measured by our MKS Model 220BHS-2A5-B-10 Baratron.

The spectra were taken by stepping the BWO frequency at 1 or 2 MHz intervals through a range of 500-1000 MHz. The output of the phase sensitive detectors was digitized and recorded almost simultaneously by the PDP8/E computer. Usually 5 sweeps were used and 5 readings at each frequency were averaged during each sweep. The time constants on the phase sensitive detectors ranged from 30-100 ms and the time between readings was 100 ms.

After normalizing the signal spectrum by the reference spectrum, a Gaussian lineshape fitting program was used to determine the peak frequency of the observed transition. Most of the transitions that were not overlapped showed a reproducibility from spectrum to spectrum within ± 1 MHz.

The large fluctuation of microwave power inside the modulator, as shown in Fig. 12, caused a fluctuation in the baseline and the lineshapes of the normalized spectrum. We therefore took steps to modify the microwave pin diode control system to include a feedback loop that maintained constant sideband power as the frequency was changed. The new system includes an absorptive modulator and a feedback control circuit designed by Mr. Martin Rabb at Michigan State University.

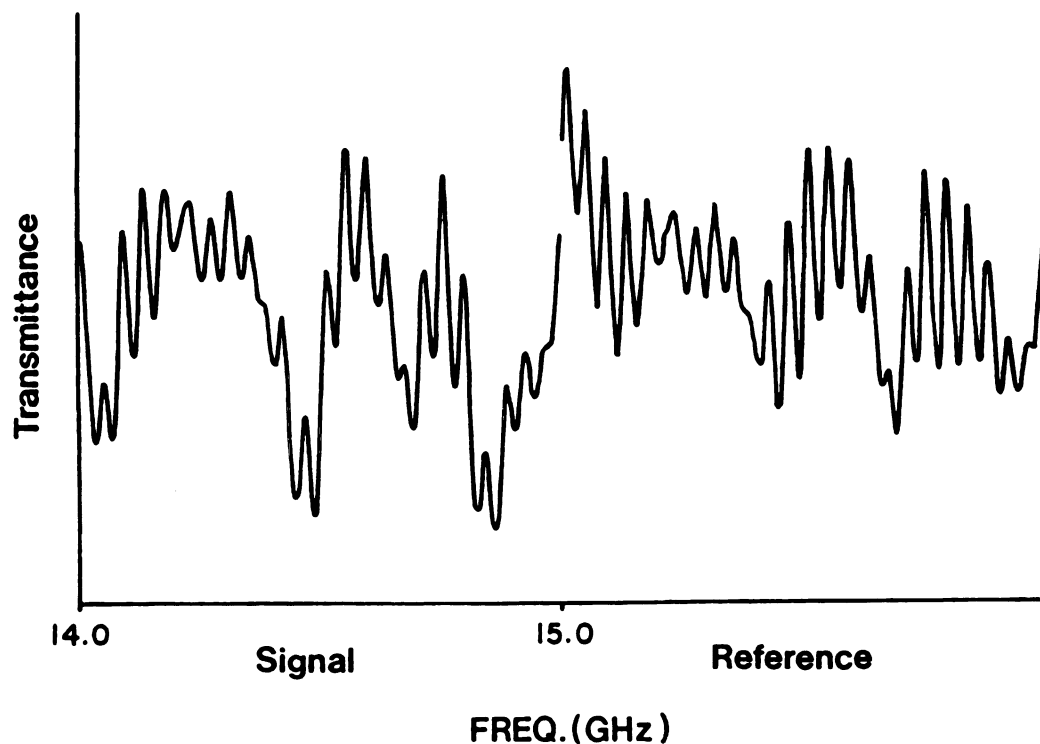


Figure 12. Unnormalized spectrum obtained by IR-MW sideband laser spectrometer. The signal and the reference show the large fluctuation in amplitude with frequency. The lower sideband generated from the 10R(20)CO₂ laser line used with ~200 mTorr of ¹³CH₃F for the ν₃ P(27,K) transition.

According to the experimental diagram shown in Fig. 13, the reference detector monitors the sideband power generated from the modulator. Then, the output of phase sensitive detector No. 2 is fed to an electronic circuit that controls the current to the PIN diode during the "on" position of the on-off cycle. Thus, the input MW power depends on the sideband power monitored by the reference detector.

The necessary conditions for lineshape study are that the radiation should be highly monochromatic relative to the linewidth, that it should have precise frequency control, and that it should have very good amplitude and frequency stability. Since the MW feedback controlled IR-MW sideband laser satisfies all of these conditions, it is a promising radiation source for lineshape study. Figure 14 shows the lineshape obtained by the modified spectrometer for the $Q_Q(5,5)$ transition in the ν_3 band of the $^{12}\text{CH}_3\text{F}$ molecule.

In this work, all $^{13}\text{CH}_3\text{F}$ measurements were done with the normal IR-MW sideband laser spectrometer, while all $^{12}\text{CH}_3\text{F}$ measurements were made with the MW feedback controlled IR-MW sideband laser spectrometer.

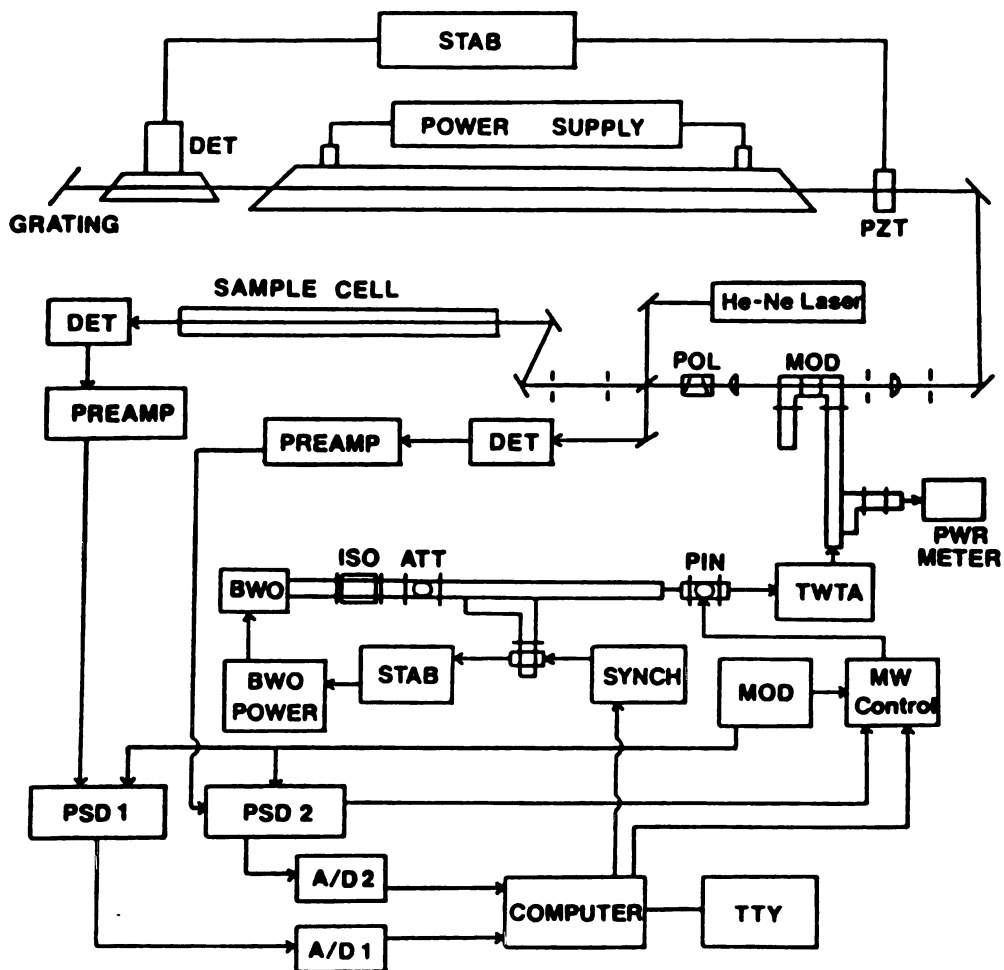


Figure 13. Block diagram of MW feedback controlled IR-MW sideband laser spectrometer set for linear absorption spectroscopy of gases used for $^{12}\text{CH}_3\text{F}$.

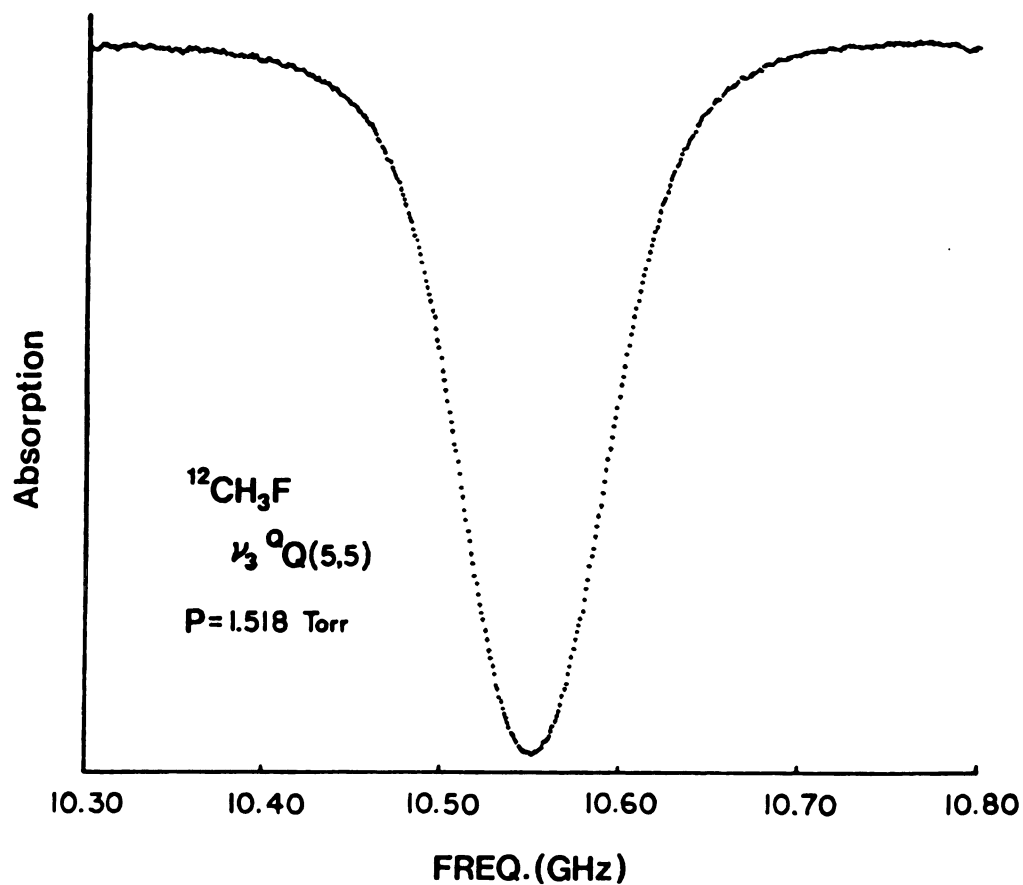


Figure 14. Typical spectrum obtained by feedback controlled IR-MW sideband system for lineshape experiment. The lower sideband generated from the 9P(18)CO₂ laser line used with a 3.2 cm long sample cell with 0.1 sec. time constant.

CHAPTER V
RESULTS AND DISCUSSION

ν_3 Fundamental and $2\nu_3 \leftarrow \nu_3$ Hot Bands of $^{13}\text{CH}_3\text{F}$

In the present study, the spectrometer was operated for more than 60 CO_2 laser lines ranging from 10P(10) - 9R(26). The microwave sources were tuned from 8.2-12.2 GHz and from 12.4-18.0 GHz for each CO_2 laser line so that it was possible to observe a total of 386 ν_3 fundamental band transitions involving J values up to 47 and K values up to 16. Of these transitions, the peak frequencies of 305 transitions could be accurately measured by a Gaussian lineshape fitting program with a good reproducibility, while the others could not be resolved due to overlapping of several transitions. A typical spectrum of the ν_3 fundamental band of $^{13}\text{CH}_3\text{F}$ obtained by the IR-MW sideband spectrometer is shown in Fig. 15. In this spectrum, the intensity doubling for $K = 3n$ that results from nuclear spin statistics is clearly seen.

For the measurement of the frequencies of transitions in the $2\nu_3 \leftarrow \nu_3$ hot band, more than 16 CO_2 laser lines were tuned ranging from 10R(4) - 9P(20) and the microwave sources were scanned from 8.2-12.2 GHz and from 12.4-18.0 GHz. Since there were no previous data, it was very difficult to predict the frequencies of the $2\nu_3 \leftarrow \nu_3$ transitions.

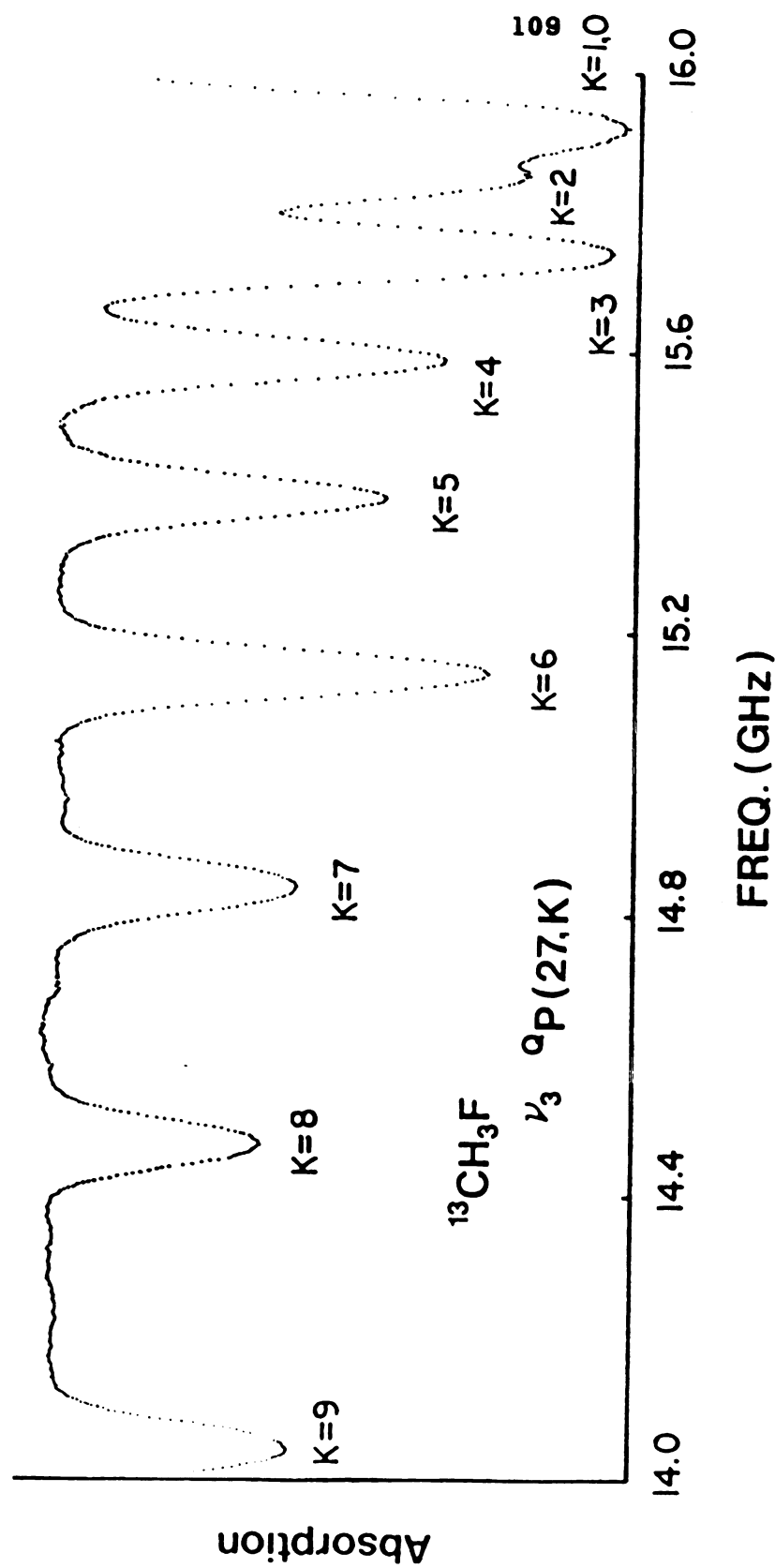


Figure 15. Typical spectrum of the ν_3 band of $^{13}\text{CH}_3\text{F}$ obtained with the IR-MW sideband laser spectrometer. The lower sideband generated from the 10R(20) CO_2 laser line was used with ~200 mTorr of sample pressure in an 1 m long sample cell. From this spectrum, the intensity rule according to K values can be clearly seen.

Fortunately, during the measurement of the ν_3 fundamental band, several $2\nu_3 \leftarrow \nu_3$ hot band transitions were observed even though they were very weak and noisy. From these observations it was possible to extend the prediction of the $2\nu_3 \leftarrow \nu_3$ frequencies. Finally, a total of 101 transitions could be observed, of which 81 transitions could be resolved. Figure 16 shows a typical spectrum of $2\nu_3 \leftarrow \nu_3$ transitions of $^{13}\text{CH}_3\text{F}$ obtained by the IR-MW sideband laser spectrometer.

For the least squares fitting, a total of 296 IR-MW sideband laser frequencies of the ν_3 fundamental band were fitted to Eq. (64) together with the previously reported data listed in Table I. The frequencies of the ν_3 transitions measured in this work are shown with their estimated uncertainties in Table II. For the $2\nu_3 \leftarrow \nu_3$ hot band the frequencies shown in Table III were fit, also to Eq. (64). For the least squares fits, the data were weighted by the inverse of the square of the uncertainties shown in Tables I - III. The parameters obtained from the fitting are given for the ground state and the $\nu_3 = 1$ state in the first two columns and for the $\nu_3 = 2$ state in the last column of Table IV. In these fits, the L constants were constrained to zero for the ground state, but allowed to vary for $\nu_3 = 1$ and 2. Also, the $\nu_3 = 1$ parameters obtained from the fit of the fundamental frequencies were constrained in the fit of the hot band transitions. The

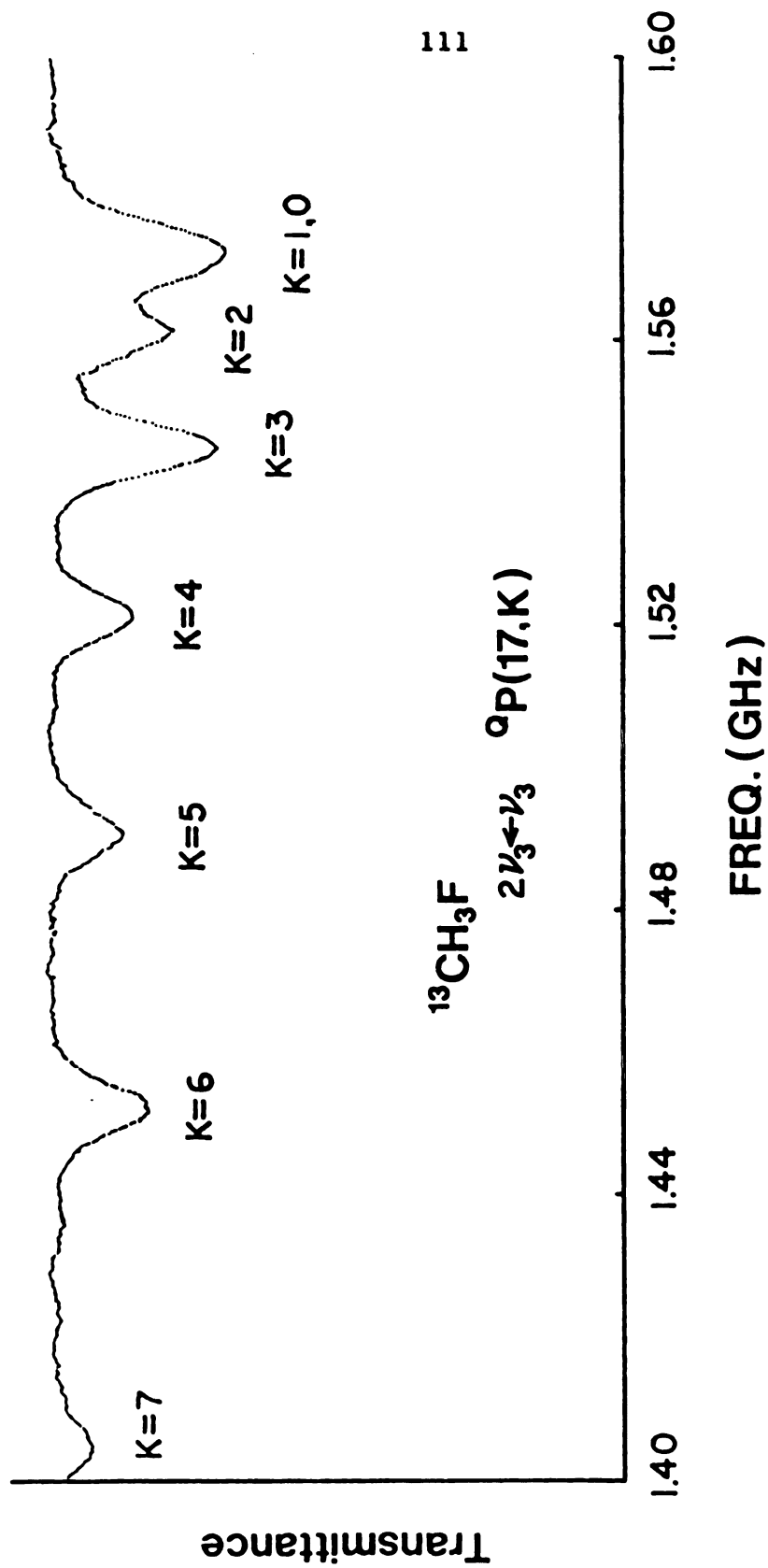


Figure 16. Typical spectrum of the $2\nu_3 - \nu_3$ band of $^{13}\text{CH}_3\text{F}$ obtained with the IR-MW sideband laser spectrometer. The lower sideband generated from the $10\text{R}(30)\text{CO}_2$ laser line was used with ~ 1.0 Torr of sample pressure in an 1 m long sample cell.

Table I.

Sources of Data for Fits of the ν_3 Band of $^{13}\text{CH}_3\text{F}$

Experiment	Source	Transitions	Uncert. ^a
IR-MW Sideband Laser	This work, Table II	High and low J,K; P,Q,R.	1.0- 3.0 MHz
IR-MW Two-Photon	Ref. 29, Table IV	Low J,K; P,Q,R.	6.0 MHz
IR Laser Stark	Ref. 16, Table IV Ref. 27, Appendix A6	Low J,K; P,Q,R.	6.0 MHz
IR Laser Stark Lamb Dips	Ref. 16, Table IV Ref. 27, Appendix A6	Q(J,K), J = 1-3; R(4,K).	2.0 MHz
IR-RF Two-Photon Lamb Dips	Ref. 16, Table IV Ref. 27, Appendix A6	Q(3,K), R(4,K).	2.0 MHz
mm Wave	Ref. 8	R(0,0), pure rot., $\nu_3 = 0, 1$.	0.2 MHz
	Ref. 35	R(J,K), pure rot., J = 3-5, $\nu_3 = 0, 1$.	0.05 MHz

^aUncertainty assumed in least squares fits.

Table II.

Comparison of Observed and Calculated Frequencies

in the ν_3 Band of $^{13}\text{CH}_3\text{F}$

Trans.	Laser ^a	ν_m^b	ν/MHz	O-C ^c	Unc. ^d	ν/cm^{-1} ^e
P(37, 0)	10P(10)	-13735.0	28552914.2	24.3	OVERLAP	952.42270(81)
P(37, 1)	10P(10)	-13735.0	28552914.2	19.3	OVERLAP	952.42270(64)
P(37, 2)	10P(10)	-13735.0	28552914.2	4.3	OVERLAP	952.42270(14)
P(37, 3)	10P(10)	-13735.0	28552914.2	-21.1	OVERLAP	952.42270(-70)
P(37, 4)	10P(10)	-13735.0	28552914.2	-57.1	OVERLAP	952.42270(-190)
P(37, 5)	10P(10)	-13735.0	28552914.2	-104.2	OVERLAP	952.42270(-347)
P(37, 6)	10P(10)	-13572.0	28553077.2	0.5	2.0	952.42814(1)
P(37, 7)	10P(10)	-13502.0	28553147.2	0.8	3.0	952.43047(2)
P(37, 8)	10P(10)	-13424.0	28553225.2	-1.8	2.0	952.43307(-6)
P(37, 9)	10P(10)	-13326.0	28553323.2	5.5	2.0	952.43634(18)
P(37,10)	10P(10)	-13236.0	28553413.2	-3.7	3.0	952.43934(-12)
P(37,11)	10P(10)	-13126.0	28553523.2	1.1	3.0	952.44301(3)
P(37,12)	10P(10)	-13010.0	28553639.2	9.1	3.0	952.44688(30)
P(35,11)	10P(4)	-17836.0	28696301.7	-3.2	1.0	957.20559(-10)
P(35,12)	10P(4)	-17600.0	28696537.7	4.2	1.0	957.21346(13)
P(35,13)	10P(4)	-17356.0	28696781.7	-1.1	3.0	957.22160(-3)
P(35,14)	10P(4)	-17080.0	28697057.7	5.7	3.0	957.23081(19)
P(35,15)	10P(4)	-16784.0	28697353.7	13.5	OMIT	957.24068(44)
P(32, 7)	10R(4)	-17954.1	28905092.4	-2.8	1.0	964.17010(-9)
P(32, 8)	10R(4)	-17724.9	28905321.6	-3.6	1.0	964.17774(-11)
P(32, 9)	10R(4)	-17453.6	28905592.8	-1.7	1.0	964.18679(-5)
P(32,10)	10R(4)	-17144.2	28905902.2	-3.7	1.0	964.19711(-12)
P(32,11)	10R(4)	-16784.8	28906261.6	-1.3	1.0	964.20910(-4)
P(32,12)	10R(4)	-16378.0	28906668.5	-0.4	1.0	964.22267(-1)
P(32,13)	10R(4)	-15915.4	28907131.0	3.0	1.0	964.23810(10)
P(32,14)	10R(4)	-15406.0	28907640.4	-5.0	2.0	964.25509(-16)
P(32,15)	10R(4)	-14818.4	28908228.1	0.3	3.0	964.27469(1)
P(32,16)	10R(4)	-14196.3	28908850.2	-32.9	OMIT	964.29545(-109)
P(32,17)	10R(4)	-13305.8	28909740.6	118.0	OVERLAP	964.32515(393)
P(32,18)	10R(4)	-12481.0	28910565.4	104.5	OVERLAP	964.35266(348)
P(30, 0)	10R(10)	-13002.0	29041070.7	23.5	OVERLAP	968.70585(78)
P(30, 1)	10R(10)	-13002.0	29041070.7	7.0	OVERLAP	968.70585(23)
P(30, 2)	10R(10)	-13002.0	29041070.7	-42.7	OVERLAP	968.70585(-142)
P(30, 3)	10R(10)	-12874.0	29041198.7	1.3	2.0	968.71012(4)
P(30, 4)	10R(10)	-12756.0	29041316.7	-0.2	1.0	968.71405(0)
P(30, 5)	10R(10)	-12601.1	29041471.6	-2.4	1.0	968.71922(-7)
P(30, 7)	10R(10)	-12156.4	29041916.3	5.0	1.0	968.73405(16)
P(30, 8)	10R(10)	-11877.1	29042195.6	-2.7	1.0	968.74337(-8)
P(30, 9)	10R(10)	-11639.7	29042533.0	-2.7	1.0	968.75463(-9)
P(30,10)	10R(10)	-11146.0	29042926.7	-1.8	1.0	968.76776(-6)

Trans.	Laser ^a	ν_{m}^b	ν/MHz	O-C ^c	Unc. ^d	ν/cm^{-1} ^e
P(30, 11)	10R(10)	-10692.6	29043380.1	-1.9	1.0	968.78288(-6)
P(30, 12)	10R(10)	-10172.7	29043900.0	-2.3	1.0	968.80022(-7)
P(30, 13)	10R(10)	-9582.0	29044490.7	-6.0	1.0	968.81993(-19)
P(30, 14)	10R(10)	-8917.2	29045155.5	-18.8	OMIT	968.84210(-62)
P(29, 4)	10R(12)	12538.0	29108812.4	5.5	2.0	970.96547(18)
P(29, 5)	10R(12)	12708.0	29108982.4	3.8	2.0	970.97114(12)
P(29, 6)	10R(12)	12924.1	29109198.5	4.2	2.0	970.97834(14)
P(29, 7)	10R(12)	13187.2	29109461.6	4.3	1.0	970.98712(14)
P(29, 8)	10R(12)	13500.9	29109775.3	3.5	1.0	970.99759(11)
P(29, 9)	10R(12)	13872.8	29110147.2	4.8	1.0	971.00999(16)
P(29, 10)	10R(12)	14301.4	29110575.8	1.1	1.0	971.02429(3)
P(29, 11)	10R(12)	14805.1	29111079.5	4.5	1.0	971.04109(15)
P(29, 12)	10R(12)	15382.6	29111657.0	6.2	1.0	971.06035(20)
P(29, 13)	10R(12)	16040.0	29112314.4	3.3	1.0	971.08228(10)
P(29, 14)	10R(12)	16772.0	29113046.4	-20.3	OMIT	971.10670(-67)
P(29, 15)	10R(12)	17656.0	29113930.4	-0.2	2.0	971.13619(0)
P(27, 0)	10R(20)	-15942.9	29241715.7	6.8	OVERLAP	975.39864(22)
P(27, 1)	10R(20)	-15942.9	29241715.6	-14.2	OVERLAP	975.39864(-47)
P(27, 2)	10R(20)	-15864.5	29241794.0	1.1	2.0	975.40126(3)
P(27, 3)	10R(20)	-15760.3	29241898.2	-1.3	1.0	975.40473(-4)
P(27, 4)	10R(20)	-15608.7	29242049.8	-1.5	1.0	975.40979(-4)
P(27, 5)	10R(20)	-15409.6	29242248.9	-2.2	1.0	975.41643(-7)
P(27, 6)	10R(20)	-15158.2	29242500.3	-1.9	1.0	975.42482(-6)
P(27, 7)	10R(20)	-14851.5	29242807.0	-2.0	1.0	975.43505(-6)
P(27, 8)	10R(20)	-14484.4	29243174.1	-2.6	1.0	975.44729(-8)
P(27, 9)	10R(20)	-14049.4	29243609.2	-2.0	1.0	975.46180(-6)
P(27, 10)	10R(20)	-13542.3	29244116.2	-3.4	1.0	975.47872(-11)
P(27, 11)	10R(20)	-12952.5	29244706.0	-4.5	1.0	975.49839(-14)
P(27, 13)	10R(20)	-11479.9	29246178.7	-2.7	1.0	975.54751(-8)
P(27, 14)	10R(20)	-10578.0	29247080.5	-7.1	3.0	975.57760(-23)
P(27, 15)	10R(20)	-9541.1	29248117.5	-12.5	OMIT	975.61218(-41)
P(27, 16)	10R(20)	-8356.0	29249302.5	-27.2	OMIT	975.65171(-90)
P(26, 0)	10R(22)	11312.5	29307448.9	14.3	OVERLAP	977.59127(47)
P(26, 1)	10R(22)	11312.5	29307448.9	-8.0	OVERLAP	977.59127(-26)
P(26, 2)	10R(22)	11396.5	29307532.9	8.7	2.0	977.59407(28)
P(26, 3)	10R(22)	11506.7	29307643.1	5.3	1.0	977.59775(17)
P(26, 4)	10R(22)	11668.8	29307805.2	5.4	1.0	977.60315(18)
P(26, 5)	10R(22)	11880.8	29308017.1	4.3	1.0	977.61022(14)
P(26, 6)	10R(22)	12141.3	29308277.6	-3.4	1.0	977.61891(-11)
P(26, 7)	10R(22)	12476.1	29308612.5	3.7	1.0	977.63008(12)

Trans.	Laser ^a	ν_m^b	ν/MHz	O-C ^c	Unc. ^d	$\nu/\text{cm}^{-1} \bullet$
P(26, 8)	10R(22)	12868.3	29309004.6	2.8	1.0	977.64316(9)
P(26, 9)	10R(22)	13334.2	29309470.6	3.7	1.0	977.65870(12)
P(26, 10)	10R(22)	13878.3	29310014.6	2.8	1.0	977.67685(9)
P(26, 11)	10R(22)	14512.6	29310649.0	2.8	1.0	977.69801(9)
P(26, 12)	10R(22)	15247.5	29311383.8	2.8	1.0	977.72252(9)
P(26, 13)	10R(22)	16096.7	29312233.1	3.4	1.0	977.75085(11)
P(26, 14)	10R(22)	17075.0	29313211.4	3.0	1.0	977.78348(9)
P(23, 0)	10R(34)	-9968.1	29501098.6	11.4	OVERLAP	984.05073(37)
P(23, 1)	10R(34)	-9968.1	29501098.6	-14.8	OVERLAP	984.05073(-49)
P(23, 2)	10R(34)	-9872.9	29501193.8	1.5	2.0	984.05390(5)
P(23, 3)	10R(34)	-9742.3	29501324.4	-1.2	1.0	984.05826(-3)
P(23, 4)	10R(34)	-9553.0	29501513.7	-1.7	1.0	984.06457(-5)
P(23, 5)	10R(34)	-9301.9	29501764.8	-1.0	1.0	984.07295(-3)
P(23, 6)	10R(34)	-8987.2	29502079.5	-1.5	2.0	984.08345(-4)
P(23, 7)	10R(34)	-8601.3	29502465.4	-1.6	2.0	984.09632(-5)
P(22, 0)	10R(38)	-12078.6	29564466.5	12.3	OVERLAP	986.16445(41)
P(22, 1)	10R(38)	-12078.6	29564466.5	-15.0	OVERLAP	986.16445(-49)
P(22, 2)	10R(38)	-11981.3	29564563.8	-0.2	2.0	986.16770(0)
P(22, 3)	10R(38)	-11843.7	29564701.4	-1.6	1.0	986.17229(-5)
P(22, 4)	10R(38)	-11643.7	29564901.4	-0.1	1.0	986.17896(0)
P(22, 5)	10R(38)	-11384.2	29565161.0	-2.1	1.0	986.18762(-6)
P(22, 6)	10R(38)	-11053.3	29565491.8	-0.8	1.0	986.19865(-2)
P(22, 7)	10R(38)	-10651.1	29565894.1	-2.3	1.0	986.21207(-7)
P(22, 8)	10R(38)	-10164.9	29566380.3	-1.7	1.0	986.22829(-5)
P(22, 9)	10R(38)	-9588.9	29566956.3	-2.2	1.0	986.24750(-7)
P(22, 10)	10R(38)	-8910.5	29567634.6	-2.2	1.0	986.27013(-7)
P(21, 0)	10R(42)	-11643.0	29627237.2	12.4	OVERLAP	988.25826(41)
P(21, 1)	10R(42)	-11643.0	29627237.2	-15.9	OVERLAP	988.25826(-53)
P(21, 2)	10R(42)	-11538.9	29627341.3	2.4	2.0	988.26173(7)
P(21, 3)	10R(42)	-11402.4	29627477.8	-5.8	1.0	988.26628(-19)
P(21, 4)	10R(42)	-11189.4	29627690.8	0.7	1.0	988.27339(2)
P(21, 5)	10R(42)	-10919.2	29627961.0	-1.3	1.0	988.28240(-4)
P(21, 6)	10R(42)	-10576.1	29628304.1	-1.2	1.0	988.29385(-4)
P(21, 7)	10R(42)	-10155.3	29628724.9	-1.0	1.0	988.30788(-3)
P(21, 8)	10R(42)	-9649.9	29629230.3	-1.7	1.0	988.32474(-5)
P(21, 9)	10R(42)	-9048.0	29629832.2	-1.1	3.0	988.34482(-3)
P(21, 10)	10R(42)	-8336.0	29630544.2	2.7	3.0	988.36857(9)
P(20, 0)	10R(46)	-8620.7	29689408.7	12.4	OVERLAP	990.33207(41)
P(20, 1)	10R(46)	-8620.7	29689408.7	-17.0	OVERLAP	990.33207(-56)
P(20, 2)	10R(46)	-8515.9	29689513.4	-1.1	3.0	990.33557(-3)

Trans.	Laser ^a	ν_m^b	ν/MHz	O-C ^c	Unc. ^d	ν/cm^{-1} ^e
P(20, 3)	10R(46)	-8367.9	29689661.5	-3.0	3.0	990.34051(-9)
P(6, 0)	9P(50)	15050.7	30495577.7	20.3	OVERLAP	1017.22298(67)
P(6, 1)	9P(50)	15050.7	30495577.7	-14.7	OVERLAP	1017.22298(-48)
P(6, 2)	9P(50)	15174.0	30495701.0	3.0	1.0	1017.22709(10)
P(6, 3)	9P(50)	15354.2	30495881.2	4.4	1.0	1017.23310(14)
P(6, 4)	9P(50)	15609.9	30496136.9	4.0	1.0	1017.24163(13)
P(6, 5)	9P(50)	15948.5	30496475.5	3.1	1.0	1017.25293(10)
P(4, 0)	9P(46)	-9764.7	30600751.4	11.1	OVERLAP	1020.73120(37)
P(4, 1)	9P(46)	-9764.7	30600751.4	-23.0	OVERLAP	1020.73120(-76)
P(4, 2)	9P(46)	-9635.6	30600880.5	2.7	2.0	1020.73550(8)
P(4, 3)	9P(46)	-9468.1	30601048.0	-4.9	1.0	1020.74109(-16)
P(1, 0)	9P(42)	16089.0	30753745.7	-1.8	3.0	1025.83454(-5)
Q(6, 6)	9P(40)	-8989.6	30791153.0	-1.3	2.0	1027.08231(-4)
Q(6, 5)	9P(40)	-9356.2	30790786.5	-0.4	1.0	1027.07008(-1)
Q(6, 4)	9P(40)	-9644.8	30790497.9	-1.3	1.0	1027.06046(-4)
Q(6, 3)	9P(40)	-9860.7	30790281.9	-1.3	1.0	1027.05325(-4)
Q(6, 2)	9P(40)	-10011.9	30790130.8	-2.2	2.0	1027.04821(-7)
Q(6, 1)	9P(40)	-10102.0	30790040.6	-3.9	3.0	1027.04520(-13)
Q(7, 7)	9P(40)	-13054.5	30787088.2	-2.0	1.0	1026.94672(-6)
Q(7, 6)	9P(40)	-13501.1	30786641.6	-1.8	1.0	1026.93182(-5)
Q(7, 5)	9P(40)	-13859.4	30786283.3	-1.2	1.0	1026.91987(-4)
Q(7, 4)	9P(40)	-14141.0	30786001.6	-2.0	1.0	1026.91048(-6)
Q(7, 3)	9P(40)	-14351.2	30785791.4	-1.5	1.0	1026.90347(-4)
Q(7, 2)	9P(40)	-14498.3	30785644.3	-2.1	2.0	1026.89856(-7)
Q(7, 1)	9P(40)	-14586.0	30785556.6	-3.6	3.0	1026.89563(-11)
Q(8, 8)	9P(40)	-17687.4	30782455.3	-1.7	1.0	1026.79218(-5)
Q(12, 2)	9P(42)	15974.0	30753630.7	0.7	3.0	1025.83070(2)
Q(12, 3)	9P(42)	16096.0	30753752.7	2.1	3.0	1025.83477(7)
Q(12, 4)	9P(42)	16270.7	30753927.4	2.9	1.0	1025.84060(9)
Q(12, 5)	9P(42)	16498.0	30754154.7	-2.4	3.0	1025.84818(-8)
Q(12, 6)	9P(42)	16796.0	30754452.7	-2.9	3.0	1025.85812(-9)
Q(12, 7)	9P(42)	17170.0	30754826.7	-2.2	3.0	1025.87059(-7)
Q(12, 8)	9P(42)	17637.2	30755293.9	5.7	1.0	1025.88618(19)
Q(13, 8)	9P(42)	9234.8	30746891.5	3.6	3.0	1025.60590(11)
Q(13, 9)	9P(42)	9771.3	30747428.0	7.7	2.0	1025.62380(25)
Q(13,10)	9P(42)	10408.0	30748064.7	0.7	3.0	1025.64504(2)
Q(13,11)	9P(42)	11183.9	30748840.6	2.4	2.0	1025.67092(7)
Q(13,12)	9P(42)	12110.0	30749766.7	1.0	3.0	1025.70181(3)
Q(13,13)	9P(42)	13218.0	30750874.7	0.9	3.0	1025.73877(2)
Q(15, 2)	9P(42)	-10878.0	30726778.7	1.4	3.0	1024.93501(4)

Tr

Q(1)
Q(1)
Q(1)
Q(1)
Q(1)
Q(1)
Q(1)
Q(1)
Q(1)
Q(1)

Q(1)
Q(1)
Q(1)
Q(1)
Q(1)
Q(1)
Q(1)
Q(1)
Q(1)
Q(1)
Q(1)

Q(2)
Q(2)
Q(2)
Q(2)
Q(2)
Q(2)
Q(2)
Q(2)
Q(2)
Q(2)
Q(2)

Q(2)
Q(2)
Q(2)
Q(2)
Q(2)
Q(2)
Q(2)
Q(2)
Q(2)
Q(2)

Trans.	Laser ^a	ν_m^b	ν/MHz	O-C ^c	Unc. ^d	ν/cm^{-1} ^e
Q(15, 3)	9P(42)	-10779.9	30726876.9	0.2	3.0	1024.93829(0)
Q(15, 4)	9P(42)	-10638.2	30727018.5	-2.0	1.0	1024.94301(-6)
Q(15, 5)	9P(42)	-10446.0	30727210.7	-3.1	3.0	1024.94942(-10)
Q(15, 6)	9P(42)	-10189.4	30727467.3	4.3	1.0	1024.95798(14)
Q(15, 7)	9P(42)	-9881.5	30727775.2	-1.3	2.0	1024.96825(-4)
Q(15, 8)	9P(42)	-9493.2	30728163.5	-0.7	1.0	1024.98121(-2)
Q(15, 9)	9P(42)	-9019.4	30728637.4	-1.2	2.0	1024.99701(-4)
Q(15,10)	9P(42)	-8434.1	30729222.6	8.1	2.0	1025.01653(27)
Q(16,12)	9P(42)	-17394.1	30720262.6	-0.9	1.0	1024.71766(-3)
Q(16,13)	9P(42)	-16448.0	30721208.7	0.4	3.0	1024.74922(1)
Q(16,14)	9P(42)	-15317.0	30722339.7	-1.3	1.0	1024.78694(-4)
Q(16,15)	9P(42)	-13957.5	30723699.2	2.7	1.0	1024.83229(8)
Q(19, 9)	9P(44)	8946.0	30683391.8	-2.5	3.0	1023.48778(-8)
Q(19,10)	9P(44)	9369.4	30683815.2	3.7	2.0	1023.50191(12)
Q(19,11)	9P(44)	9880.9	30684326.7	4.4	2.0	1023.51897(14)
Q(19,12)	9P(44)	10501.1	30684946.8	2.3	1.0	1023.53965(7)
Q(19,13)	9P(44)	11253.3	30685699.1	-0.3	2.0	1023.56474(0)
Q(19,14)	9P(44)	12160.0	30686605.8	-6.7	3.0	1023.59499(-22)
Q(19,15)	9P(44)	13260.0	30687705.8	-8.7	3.0	1023.63168(-29)
Q(19,16)	9P(44)	14597.1	30689042.8	0.7	1.0	1023.67628(2)
Q(21, 7)	9P(44)	-17965.6	30656480.2	-2.6	2.0	1022.59011(-8)
Q(21, 8)	9P(44)	-17755.4	30656690.4	-0.2	1.0	1022.59712(0)
Q(21, 9)	9P(44)	-17494.0	30656951.8	-0.9	1.0	1022.60584(-2)
Q(21,10)	9P(44)	-17169.2	30657276.6	-3.8	1.0	1022.61667(-12)
Q(21,11)	9P(44)	-16761.9	30657683.9	-3.0	1.0	1022.63026(-10)
Q(21,12)	9P(44)	-16253.9	30658191.9	3.7	1.0	1022.64720(12)
Q(21,13)	9P(44)	-15648.3	30658797.5	-5.6	1.0	1022.66740(-18)
Q(21,14)	9P(44)	-14896.5	30659549.2	-5.2	1.0	1022.69248(-17)
Q(21,15)	9P(44)	-13986.0	30660459.8	-9.7	3.0	1022.72285(-32)
Q(23, 1)	9P(46)	16883.0	30627399.1	54.5	OVERLAP	1021.62007(181)
Q(23, 2)	9P(46)	16883.0	30627399.1	40.2	OVERLAP	1021.62007(134)
Q(23, 3)	9P(46)	16883.0	30627399.1	14.7	OVERLAP	1021.62007(48)
Q(23, 4)	9P(46)	16883.0	30627399.1	-24.4	OVERLAP	1021.62007(-81)
Q(23, 5)	9P(46)	16966.0	30627482.1	2.5	3.0	1021.62284(8)
Q(23, 6)	9P(46)	17041.4	30627557.6	0.3	1.0	1021.62535(1)
Q(23, 7)	9P(46)	17152.9	30627669.0	7.2	1.0	1021.62907(23)
Q(23, 8)	9P(46)	17287.6	30627803.7	3.4	1.0	1021.63356(11)
Q(23, 9)	9P(46)	17469.2	30627985.3	4.6	1.0	1021.63962(15)
Q(23,10)	9P(46)	17699.8	30628216.0	3.3	1.0	1021.64731(10)
Q(23,11)	9P(46)	17994.0	30628510.1	2.2	3.0	1021.65713(7)

Trans.	Laser ^a	ν_{M}^b	ν/MHz	O-C ^c	Unc. ^d	ν/cm^{-1} ^e
Q(25, 1)	9P(46)	-14254.0	30596262.1	30.1	OVERLAP	1020.58145(100)
Q(25, 2)	9P(46)	-14254.0	30596262.1	28.7	OVERLAP	1020.58145(95)
Q(25, 3)	9P(46)	-14254.0	30596262.1	24.9	OVERLAP	1020.58145(83)
Q(25, 4)	9P(46)	-14254.0	30596262.1	16.6	OVERLAP	1020.58145(55)
Q(25, 5)	9P(46)	-14254.0	30596262.1	0.9	OVERLAP	1020.58145(2)
Q(25, 6)	9P(46)	-14254.0	30596262.1	-26.2	OVERLAP	1020.58145(-87)
Q(25, 7)	9P(46)	-14254.0	30596262.1	-69.5	OVERLAP	1020.58145(-231)
Q(25, 8)	9P(46)	-14122.0	30596394.1	-2.7	3.0	1020.58585(-9)
Q(25, 9)	9P(46)	-14026.0	30596490.1	-0.8	3.0	1020.58905(-2)
Q(25, 10)	9P(46)	-13900.3	30596615.8	-6.2	2.0	1020.59325(-20)
Q(25, 11)	9P(46)	-13718.5	30596797.6	-2.2	1.0	1020.59931(-7)
Q(25, 12)	9P(46)	-13481.8	30597034.3	-1.4	1.0	1020.60721(-4)
Q(25, 13)	9P(46)	-13177.6	30597338.5	-4.8	1.0	1020.61735(-16)
Q(25, 14)	9P(46)	-12772.7	30597743.5	4.4	1.0	1020.63086(14)
Q(27, 1)	9P(48)	16647.0	30562521.3	-111.5	OVERLAP	1019.45598(-371)
Q(27, 2)	9P(48)	16647.0	30562521.3	-99.4	OVERLAP	1019.45598(-331)
Q(27, 3)	9P(48)	16647.0	30562521.3	-80.5	OVERLAP	1019.45598(-268)
Q(27, 4)	9P(48)	16647.0	30562521.3	-56.5	OVERLAP	1019.45598(-188)
Q(27, 5)	9P(48)	16647.0	30562521.3	-30.0	OVERLAP	1019.45598(-100)
Q(27, 6)	9P(48)	16647.0	30562521.3	-4.3	OVERLAP	1019.45598(-14)
Q(27, 7)	9P(48)	16647.0	30562521.3	16.6	OVERLAP	1019.45598(55)
Q(27, 8)	9P(48)	16647.0	30562521.3	27.9	OVERLAP	1019.45598(93)
Q(27, 9)	9P(48)	16647.0	30562521.3	24.1	OVERLAP	1019.45598(80)
Q(27, 10)	9P(48)	16647.0	30562521.3	-1.4	OVERLAP	1019.45598(-4)
Q(27, 11)	9P(48)	16647.0	30562521.3	-56.3	OVERLAP	1019.45598(-187)
Q(27, 12)	9P(48)	16647.0	30562521.3	-149.6	OVERLAP	1019.45598(-499)
Q(27, 13)	9P(48)	16940.0	30562814.3	0.9	2.0	1019.46575(2)
Q(27, 14)	9P(48)	17142.0	30563016.3	-1.7	2.0	1019.47249(-5)
Q(27, 15)	9P(48)	17423.0	30563297.3	-3.2	1.0	1019.48186(-10)
Q(27, 16)	9P(48)	17807.0	30563681.3	1.3	3.0	1019.49467(4)
Q(32, 3)	9P(50)	-12822.0	30467705.0	-2.3	2.0	1016.29325(-7)
Q(32, 4)	9P(50)	-12930.0	30467597.0	-0.7	3.0	1016.28964(-2)
Q(32, 5)	9P(50)	-13066.0	30467461.0	1.7	3.0	1016.28511(5)
Q(32, 6)	9P(50)	-13234.0	30467293.0	-0.7	1.0	1016.27950(-2)
Q(32, 7)	9P(50)	-13422.0	30467105.0	2.2	1.0	1016.27323(7)
Q(32, 8)	9P(50)	-13637.9	30466889.1	0.3	1.0	1016.26603(0)
Q(32, 9)	9P(50)	-13875.6	30466651.4	-2.4	1.0	1016.25810(-8)
Q(32, 10)	9P(50)	-14130.0	30466397.0	-3.0	2.0	1016.24962(-10)
Q(32, 11)	9P(50)	-14400.0	30466127.0	-2.9	2.0	1016.24061(-9)
Q(32, 12)	9P(50)	-14688.0	30465839.0	-7.1	2.0	1016.23100(-23)

Trans.	Laser ^a	ν_m^b	ν/MHz	O-C ^c	Unc. ^d	ν/cm^{-1} ^e
Q(32,13)	9P(50)	-14970.0	30465557.0	5.5	2.0	1016.22160(18)
R(0, 0)	9P(38)	-9341.8	30852555.7	-0.9	1.0	1029.13048(-2)
R(3, 0)	9P(34)	12777.0	30995967.8	18.2	OVERLAP	1033.91419(60)
R(3, 1)	9P(34)	12777.0	30995967.8	-8.8	OVERLAP	1033.91419(-29)
R(3, 2)	9P(34)	12872.0	30996062.8	4.5	2.0	1033.91736(14)
R(3, 3)	9P(34)	13012.2	30996202.9	5.6	1.0	1033.92204(18)
R(5, 5)	9P(30)	-12534.0	31088958.2	-3.3	1.0	1037.01602(-11)
R(5, 4)	9P(30)	-12774.4	31088717.8	-1.8	1.0	1037.00800(-5)
R(5, 3)	9P(30)	-12954.9	31088537.3	-1.9	1.0	1037.00198(-6)
R(5, 2)	9P(30)	-13077.8	31088414.4	-0.1	3.0	1036.99788(0)
R(5, 1)	9P(30)	-13165.0	31088327.2	-14.2	OVERLAP	1036.99497(-47)
R(5, 0)	9P(30)	-13165.0	31088327.2	10.0	OVERLAP	1036.99497(33)
R(12,11)	9P(20)	9535.4	31393435.8	3.0	2.0	1047.17230(9)
R(12,12)	9P(20)	10214.0	31394114.4	4.5	3.0	1047.19494(15)
R(14,11)	9P(16)	-17960.0	31473477.4	-2.0	2.0	1049.84220(-6)
R(14,12)	9P(16)	-17412.4	31474025.0	-1.6	1.0	1049.86047(-5)
R(14,13)	9P(16)	-16724.0	31474713.4	-2.3	2.0	1049.88343(-7)
R(14,14)	9P(16)	-15862.0	31475575.4	-2.0	3.0	1049.91218(-6)
R(19, 0)	9P(10)	15000.0	31661843.4	-131.1	OVERLAP	1056.12541(-437)
R(19, 1)	9P(10)	15000.0	31661843.4	-124.8	OVERLAP	1056.12541(-416)
R(19, 2)	9P(10)	15000.0	31661843.4	-106.4	OVERLAP	1056.12541(-354)
R(19, 3)	9P(10)	15000.0	31661843.4	-77.6	OVERLAP	1056.12541(-258)
R(19, 4)	9P(10)	15000.0	31661843.4	-41.3	OVERLAP	1056.12541(-137)
R(19, 5)	9P(10)	15000.0	31661843.4	-1.7	OVERLAP	1056.12541(-5)
R(19, 6)	9P(10)	15000.0	31661843.4	36.0	OVERLAP	1056.12541(120)
R(19, 7)	9P(10)	15000.0	31661843.4	65.0	OVERLAP	1056.12541(216)
R(19, 8)	9P(10)	15000.0	31661843.4	76.8	OVERLAP	1056.12541(256)
R(19, 9)	9P(10)	15000.0	31661843.4	61.7	OVERLAP	1056.12541(205)
R(19,10)	9P(10)	15000.0	31661843.4	7.4	OVERLAP	1056.12541(24)
R(19,11)	9P(10)	15000.0	31661843.4	-100.3	OVERLAP	1056.12541(-334)
R(19,12)	9P(10)	15278.0	31662121.4	-0.4	2.0	1056.13469(-1)
R(19,13)	9P(10)	15544.5	31662387.9	-2.9	2.0	1056.14358(-9)
R(19,14)	9P(10)	15934.3	31662777.6	2.4	1.0	1056.15658(8)
R(19,15)	9P(10)	16464.0	31663307.4	3.2	1.0	1056.17425(10)
R(19,16)	9P(10)	17162.0	31664005.4	-7.4	3.0	1056.19753(-24)
R(21, 0)	9P(6)	-13042.0	31733441.8	-13.2	OVERLAP	1058.51368(-43)
R(21, 1)	9P(6)	-13042.0	31733441.8	-1.2	OVERLAP	1058.51368(-4)
R(21, 2)	9P(6)	-13042.0	31733441.8	34.1	OVERLAP	1058.51368(113)
R(21, 3)	9P(6)	-13132.0	31733351.8	1.1	2.0	1058.51068(3)
R(21, 4)	9P(6)	-13208.0	31733275.8	1.4	2.0	1058.50814(4)

Trans.	Laser ^a	ν_m^b	ν/MHz	O-C ^c	Unc. ^d	ν/cm^{-1} ^e
R(21, 5)	9P(6)	-13302.0	31733181.8	-0.8	2.0	1058.50501(-2)
R(21, 6)	9P(6)	-13406.0	31733077.8	-2.4	2.0	1058.50154(-7)
R(21, 7)	9P(6)	-13514.0	31732969.8	-3.4	2.0	1058.49794(-11)
R(21, 8)	9P(6)	-13618.0	31732865.8	-3.2	2.0	1058.49447(-10)
R(21, 9)	9P(6)	-13711.0	31732772.8	-3.7	2.0	1058.49136(-12)
R(21,10)	9P(6)	-13786.0	31732697.8	-8.5	3.0	1058.48886(-28)
R(29, 0)	9R(4)	-10908.1	31993109.3	-20.0	OVERLAP	1067.17526(-66)
R(29, 1)	9R(4)	-10908.1	31993109.3	16.5	OVERLAP	1067.17526(55)
R(29, 2)	9R(4)	-11037.2	31992980.2	-3.3	2.0	1067.17095(-11)
R(29, 3)	9R(4)	-11219.3	31992798.1	-4.3	1.0	1067.16487(-14)
R(29, 4)	9R(4)	-11469.0	31992548.4	-2.4	1.0	1067.15654(-8)
R(29, 5)	9R(4)	-11788.2	31992229.2	-1.5	1.0	1067.14590(-5)
R(29, 6)	9R(4)	-12173.6	31991843.8	-0.8	1.0	1067.13304(-2)
R(29, 7)	9R(4)	-12626.2	31991391.2	-4.1	1.0	1067.11795(-13)
R(29, 8)	9R(4)	-13134.3	31990883.1	-3.3	1.0	1067.10100(-10)
R(29, 9)	9R(4)	-13699.4	31990318.0	-3.4	1.0	1067.08215(-11)
R(29,10)	9R(4)	-14315.1	31989702.2	-2.5	1.0	1067.06161(-8)
R(29,11)	9R(4)	-14976.8	31989040.6	-0.6	2.0	1067.03954(-2)
R(29,12)	9R(4)	-15679.1	31988338.3	1.8	1.0	1067.01611(6)
R(29,13)	9R(4)	-16420.4	31987597.0	0.2	2.0	1066.99139(0)
R(30, 4)	9R(4)	17990.1	32022007.4	1.9	3.0	1068.13919(6)
R(30, 5)	9R(4)	17640.2	32021657.6	2.3	1.0	1068.12752(7)
R(30, 6)	9R(4)	17217.9	32021235.3	3.7	1.0	1068.11344(12)
R(30, 7)	9R(4)	16722.2	32020739.6	2.4	1.0	1068.09690(8)
R(30, 8)	9R(4)	16158.9	32020176.3	1.6	1.0	1068.07811(5)
R(30, 9)	9R(4)	15536.0	32019553.4	6.2	1.0	1068.05734(20)
R(30,10)	9R(4)	14845.4	32018862.7	4.5	1.0	1068.03430(14)
R(30,11)	9R(4)	14100.0	32018117.4	5.8	1.0	1068.00943(19)
R(30,12)	9R(4)	13297.7	32017315.1	3.7	2.0	1067.98267(12)
R(32, 0)	9R(8)	-11992.0	32079660.7	-25.0	OVERLAP	1070.06230(-83)
R(32, 1)	9R(8)	-11992.0	32079660.7	21.3	OVERLAP	1070.06230(71)
R(32, 2)	9R(8)	-12155.0	32079497.7	-2.8	3.0	1070.05686(-9)
R(32, 3)	9R(8)	-12380.0	32079272.7	3.0	3.0	1070.04936(10)
R(32, 4)	9R(8)	-12706.4	32078946.3	-1.6	1.0	1070.03847(-5)
R(32, 5)	9R(8)	-13116.0	32078536.7	0.2	3.0	1070.02481(0)
R(32, 6)	9R(8)	-13617.9	32078034.8	-2.1	1.0	1070.00807(-7)
R(32, 7)	9R(8)	-14208.7	32077444.0	-6.9	1.0	1069.98836(-23)
R(32, 8)	9R(8)	-14870.0	32076782.7	2.5	3.0	1069.96630(8)
R(32, 9)	9R(8)	-15625.0	32076027.7	1.3	3.0	1069.94111(4)
R(32,10)	9R(8)	-16460.7	32075192.0	0.8	1.0	1069.91324(2)

Trans.	Laser ^a	ν_m^b	ν/MHz	O-C ^c	Unc. ^d	ν/cm^{-1} ^e
R(32, 11)	9R(8)	-17375.5	32074277.1	0.9	2.0	1069.88272(3)
R(33, 0)	9R(8)	15560.0	32107212.7	-15.1	OVERLAP	1070.98133(-50)
R(33, 1)	9R(8)	15560.0	32107212.7	34.6	OVERLAP	1070.98133(115)
R(33, 2)	9R(8)	15380.1	32107032.8	3.6	1.0	1070.97533(12)
R(33, 3)	9R(8)	15132.9	32106785.6	4.0	1.0	1070.96709(13)
R(33, 4)	9R(8)	14784.0	32106436.7	0.5	3.0	1070.95545(1)
R(33, 5)	9R(8)	14345.2	32105997.9	4.0	1.0	1070.94081(13)
R(33, 6)	9R(8)	13807.5	32105460.2	4.2	1.0	1070.92288(13)
R(33, 7)	9R(8)	13176.0	32104828.7	4.9	3.0	1070.90181(16)
R(33, 8)	9R(8)	12450.0	32104102.7	4.3	3.0	1070.87760(14)
R(35, 0)	9R(12)	-15765.5	32160314.0	-34.9	OVERLAP	1072.75260(-116)
R(35, 1)	9R(12)	-15765.5	32160314.0	21.5	OVERLAP	1072.75260(71)
R(35, 2)	9R(12)	-15961.4	32160118.1	-5.3	1.0	1072.74607(-17)
R(35, 3)	9R(12)	-16239.8	32159839.7	-2.3	1.0	1072.73678(-7)
R(35, 4)	9R(12)	-16631.6	32159447.9	-0.8	1.0	1072.72372(-2)
R(35, 5)	9R(12)	-17136.5	32158943.0	-1.3	1.0	1072.70687(-4)
R(35, 6)	9R(12)	-17753.1	32158326.4	-2.9	1.0	1072.68630(-9)
R(37, 6)	9R(14)	-8505.2	32208586.1	-0.1	1.0	1074.36279(0)
R(37, 7)	9R(14)	-9326.9	32207764.3	-3.2	1.0	1074.33538(-10)
R(37, 8)	9R(14)	-10273.4	32206817.9	-4.1	1.0	1074.30381(-13)
R(37, 9)	9R(14)	-11340.1	32205751.1	3.4	1.0	1074.26822(11)
R(37, 10)	9R(14)	-12556.2	32204535.0	-6.8	1.0	1074.22766(-22)
R(37, 11)	9R(14)	-13893.4	32203197.9	-2.7	2.0	1074.18306(-8)
R(37, 12)	9R(14)	-15384.0	32201707.3	-11.2	OMIT	1074.13334(-37)
R(38, 0)	9R(14)	17982.0	32235073.3	-55.5	OVERLAP	1075.24631(-184)
R(38, 1)	9R(14)	17982.0	32235073.3	11.1	OVERLAP	1075.24631(37)
R(38, 2)	9R(14)	17775.5	32234866.8	4.2	1.0	1075.23942(14)
R(38, 3)	9R(14)	17443.2	32234534.5	4.5	1.0	1075.22833(15)
R(38, 4)	9R(14)	16972.0	32234063.3	-1.2	2.0	1075.21262(-4)
R(38, 5)	9R(14)	16378.0	32233469.3	3.1	3.0	1075.19280(10)
R(38, 6)	9R(14)	15648.7	32232740.0	5.2	1.0	1075.16848(17)
R(38, 7)	9R(14)	14780.1	32231871.4	1.9	1.0	1075.13950(6)
R(38, 8)	9R(14)	13779.6	32230870.8	2.1	1.0	1075.10613(7)
R(38, 9)	9R(14)	12640.0	32229731.3	1.2	3.0	1075.06812(3)
R(40, 0)	9R(18)	-15004.0	32281713.1	-6.3	3.0	1076.80204(-20)
R(40, 1)	9R(18)	-15072.0	32281645.1	-0.9	3.0	1076.79977(-2)
R(40, 2)	9R(18)	-15292.7	32281424.4	-1.5	1.0	1076.79241(-4)
R(40, 3)	9R(18)	-15659.0	32281058.0	-1.0	1.0	1076.78019(-3)
R(40, 4)	9R(18)	-16174.0	32280543.1	-2.2	1.0	1076.76302(-7)
R(40, 5)	9R(18)	-16832.5	32279884.6	0.2	1.0	1076.74105(0)

Trans.	Laser ^a	ν_m^b	ν/MHz	O-C ^c	Unc. ^d	ν/cm^{-1}^e
R(40, 6)	9R(18)	-17641.0	32279076.1	0.8	2.0	1076.71408(2)
R(42, 0)	9R(20)	-9633.9	32325700.1	-4.4	2.0	1078.26929(-14)
R(42, 1)	9R(20)	-9714.5	32325619.6	-4.8	2.0	1078.26660(-15)
R(42, 2)	9R(20)	-9955.2	32325378.9	-5.0	1.0	1078.25858(-16)
R(42, 3)	9R(20)	-10353.0	32324981.1	-1.7	1.0	1078.24531(-5)
R(42, 4)	9R(20)	-10914.9	32324419.1	-1.7	1.0	1078.22656(-5)
R(42, 5)	9R(20)	-11636.8	32323697.2	0.0	1.0	1078.20248(0)
R(42, 6)	9R(20)	-12523.3	32322810.7	0.0	2.0	1078.17291(0)
R(42, 7)	9R(20)	-13573.2	32321760.8	1.8	2.0	1078.13789(6)
R(42, 8)	9R(20)	-14796.0	32320538.0	-0.5	3.0	1078.09710(-1)
R(42, 9)	9R(20)	-16195.6	32319138.4	-5.8	2.0	1078.05042(-19)
R(42, 10)	9R(20)	-17763.2	32317570.9	1.8	2.0	1077.99813(5)
R(43, 0)	9R(20)	11392.0	32346726.0	4.5	2.0	1078.97064(14)
R(43, 1)	9R(20)	11310.1	32346644.1	6.1	2.0	1078.96791(20)
R(43, 2)	9R(20)	11053.4	32346387.4	0.2	2.0	1078.95934(0)
R(43, 3)	9R(20)	10642.0	32345976.0	7.0	1.0	1078.94562(23)
R(43, 4)	9R(20)	10056.0	32345390.0	7.0	3.0	1078.92608(23)
R(45, 3)	9R(22)	12839.7	32385995.9	2.2	2.0	1080.28054(7)
R(45, 4)	9R(22)	12200.0	32385356.2	-3.4	3.0	1080.25920(-11)
R(45, 5)	9R(22)	11394.0	32384550.2	7.5	2.0	1080.23232(24)
R(45, 6)	9R(22)	10366.0	32383522.2	-18.7	OMIT	1080.19803(-62)
R(47, 0)	9R(24)	14110.0	32424295.7	-4.6	3.0	1081.55809(-15)
R(47, 1)	9R(24)	14008.0	32424193.7	-9.4	3.0	1081.55468(-31)
R(47, 2)	9R(24)	13718.8	32423904.5	-7.1	2.0	1081.54504(-23)
R(47, 3)	9R(24)	13245.5	32423431.2	5.9	2.0	1081.52925(19)
R(47, 4)	9R(24)	12568.0	32422753.7	10.1	OMIT	1081.50665(33)

^aCO₂ laser line used.

^bMicrowave frequency in MHz. The signed microwave frequency is added to the laser frequency to obtain the absorption frequency.

^cObserved minus calculated frequency in MHz. The parameters for the calculation are in the last two columns of Table IV.

^dEstimated uncertainty in the observed frequency in MHz. An "OMIT" and an "OVERLAP" mean that the frequency was omitted from the least squares fits and the transition was overlapped by another transition(s), respectively.

^eObserved frequency in cm⁻¹. The numbers in parentheses are the observed minus calculated frequencies in units of 0.00001 cm⁻¹.

Table III.

Comparison of Observed and Calculated Frequencies in the

 $2\nu_3 + \nu_3$ Band of $^{13}\text{CH}_3\text{F}$

Trans.	Laser ^a	ν_{m} ^b	ν/MHz	O-C ^c	Unc. ^d	ν/cm^{-1} ^e
P(25, 3)	10R(4)	12492.0	28935538.4	-3.8	3.0	965.18567(-12)
P(25, 4)	10R(4)	12691.7	28935738.1	-5.2	2.0	965.19233(-17)
P(25, 5)	10R(4)	12961.4	28936007.8	-2.3	2.0	965.20133(-7)
P(25, 6)	10R(4)	13305.9	28936352.3	4.1	2.0	965.21282(13)
P(25, 7)	10R(4)	13722.0	28936768.4	4.7	3.0	965.22670(15)
P(25, 8)	10R(4)	14196.3	28937242.7	-19.7	OMIT	965.24252(-65)
P(25, 9)	10R(4)	14818.4	28937864.8	16.6	OMIT	965.26327(55)
P(24, 3)	10R(8)	-12131.0	28999001.0	-2.2	2.0	967.30255(-7)
P(24, 4)	10R(8)	-11923.0	28999210.0	-1.1	2.0	967.30952(-3)
P(24, 5)	10R(8)	-11646.0	28999487.0	0.8	2.0	967.31876(2)
P(24, 6)	10R(8)	-11298.0	28999835.0	0.8	2.0	967.33037(2)
P(24, 7)	10R(8)	-10870.0	29000263.0	1.8	2.0	967.34465(6)
P(24, 9)	10R(8)	-9760.0	29001373.0	-0.7	2.0	967.38167(-2)
P(22, 0)	10R(14)	-13793.1	29123943.0	9.6	OVERLAP	971.47017(32)
P(22, 1)	10R(14)	-13793.1	29123943.0	-20.3	OVERLAP	971.47017(-67)
P(22, 2)	10R(14)	-13680.3	29124055.9	2.1	2.0	971.47393(6)
P(22, 3)	10R(14)	-13529.6	29124206.5	-0.2	1.0	971.47896(0)
P(22, 4)	10R(14)	-13311.7	29124424.4	-0.8	1.0	971.48623(-2)
P(22, 5)	10R(14)	-13023.8	29124712.4	-1.2	3.0	971.49583(-4)
P(22, 6)	10R(14)	-12657.1	29125079.0	1.6	3.0	971.50806(5)
P(22, 8)	10R(14)	-11682.0	29126054.1	-1.8	2.0	971.54059(-6)
P(22, 9)	10R(14)	-11056.0	29126680.1	-1.2	3.0	971.56147(-4)
P(22,10)	10R(14)	-10336.0	29127400.1	-0.3	3.0	971.58549(-1)
P(21, 8)	10R(16)	9366.0	29187821.7	-0.7	3.0	973.60093(-2)
P(21, 9)	10R(16)	9997.6	29188453.3	-4.7	3.0	973.62200(-15)
P(21,10)	10R(16)	10736.5	29189192.2	2.8	3.0	973.64665(9)
P(20, 0)	10R(20)	-10833.8	29246824.7	13.9	OVERLAP	975.56906(46)
P(20, 1)	10R(20)	-10833.8	29246824.7	-17.2	OVERLAP	975.56906(-57)
P(20, 2)	10R(20)	-10722.3	29246936.3	0.4	2.0	975.57278(1)
P(20, 3)	10R(20)	-10562.1	29247096.4	2.1	1.0	975.57812(6)
P(20, 4)	10R(20)	-10337.7	29247320.9	0.4	2.0	975.58561(1)
P(20, 5)	10R(20)	-10041.5	29247617.0	-1.5	1.0	975.59549(-4)
P(20, 6)	10R(20)	-9666.7	29247991.9	-2.1	2.0	975.60799(-6)
P(20, 7)	10R(20)	-9206.0	29248452.5	-0.4	3.0	975.62336(-1)
P(20, 8)	10R(20)	-8657.9	29249000.6	-1.4	3.0	975.64164(-4)
P(19, 6)	10R(22)	12440.0	29308576.4	3.7	3.0	977.62888(12)
P(19, 8)	10R(22)	13460.0	29309596.4	4.1	3.0	977.66290(13)
P(19, 9)	10R(22)	14108.0	29310244.4	-0.1	2.0	977.68451(0)
P(17, 0)	10R(30)	-15727.5	29426755.8	16.0	OVERLAP	981.57092(53)
P(17, 1)	10R(30)	-15727.5	29426755.8	-16.2	OVERLAP	981.57092(-53)

Trans.	Laser ^a	ν_{m}^b	ν/MHz	O-C ^c	Unc. ^d	ν/cm^{-1} ^e
P(17, 2)	10R(30)	-15613.7	29426869.6	0.7	2.0	981.57471(2)
P(17, 3)	10R(30)	-15452.2	29427031.2	-1.4	1.0	981.58010(-4)
P(17, 4)	10R(30)	-15218.2	29427265.1	-0.7	1.0	981.58791(-2)
P(17, 5)	10R(30)	-14909.7	29427573.6	0.8	1.0	981.59820(2)
P(17, 6)	10R(30)	-14525.8	29427957.5	-1.6	1.0	981.61100(-5)
P(17, 7)	10R(30)	-14054.3	29428429.0	-2.3	1.0	981.62673(-7)
P(17, 8)	10R(30)	-13490.0	29428993.3	-3.0	3.0	981.64555(-9)
P(17, 9)	10R(30)	-12823.6	29429659.7	-0.9	2.0	981.66778(-2)
P(17, 12)	10R(30)	-10218.0	29432265.3	3.2	3.0	981.75470(10)
P(16, 5)	10R(32)	9216.0	29486376.9	2.8	3.0	983.55966(9)
P(16, 6)	10R(32)	9606.4	29486767.3	4.8	2.0	983.57268(15)
P(16, 7)	10R(32)	10082.0	29487242.9	5.5	2.0	983.58855(18)
P(16, 8)	10R(32)	10646.1	29487807.0	1.2	3.0	983.60737(4)
P(16, 9)	10R(32)	11316.9	29488477.8	3.2	3.0	983.62974(10)
P(16, 12)	10R(32)	13938.0	29491098.9	-4.0	3.0	983.71717(-13)
P(13, 0)	10R(44)	-10481.3	29658374.5	18.6	OVERLAP	989.29689(61)
P(13, 1)	10R(44)	-10481.3	29658374.5	-14.0	OVERLAP	989.29689(-46)
P(13, 2)	10R(44)	-10367.4	29658488.4	1.8	2.0	989.30068(5)
P(13, 3)	10R(44)	-10202.0	29658653.8	1.7	3.0	989.30620(5)
P(13, 4)	10R(44)	-9966.0	29658889.8	2.0	1.0	989.31407(6)
P(13, 5)	10R(44)	-9655.6	29659200.3	2.1	1.0	989.32443(6)
P(13, 6)	10R(44)	-9266.2	29659589.6	0.7	2.0	989.33742(2)
P(13, 7)	10R(44)	-8787.4	29660068.4	1.5	3.0	989.35339(5)
P(12, 0)	10R(48)	-11611.8	29714782.9	16.8	OVERLAP	991.17847(56)
P(12, 1)	10R(48)	-11611.8	29714782.9	-15.7	OVERLAP	991.17847(-52)
P(12, 2)	10R(48)	-11496.8	29714897.9	1.4	2.0	991.18230(4)
P(12, 3)	10R(48)	-11336.1	29715058.7	-2.9	1.0	991.18767(-9)
P(12, 4)	10R(48)	-11100.4	29715294.4	-2.5	2.0	991.19553(-8)
P(12, 5)	10R(48)	-10788.4	29715606.4	-0.3	1.0	991.20593(0)
P(12, 6)	10R(48)	-10398.2	29715996.6	-0.1	1.0	991.21895(0)
P(12, 7)	10R(48)	-9921.0	29716473.8	-0.2	2.0	991.23487(0)
P(12, 8)	10R(48)	-9350.0	29717044.8	-2.0	3.0	991.25391(-6)
R(3, 0)	9P(48)	-11425.7	30534448.6	29.2	OVERLAP	1018.51957(97)
R(3, 1)	9P(48)	-11425.7	30534448.6	7.8	OVERLAP	1018.51957(26)
R(3, 2)	9P(48)	-11366.9	30534507.5	1.8	2.0	1018.52154(6)
R(3, 3)	9P(48)	-11260.6	30534613.7	-1.8	2.0	1018.52508(-6)
R(5, 0)	9P(46)	15249.8	30625766.0	31.7	OVERLAP	1021.56559(105)
R(5, 1)	9P(46)	15249.8	30625766.0	13.0	OVERLAP	1021.56559(43)
R(5, 2)	9P(46)	15249.8	30625766.0	-43.5	OVERLAP	1021.56559(-145)
R(5, 3)	9P(46)	15393.5	30625909.7	4.1	2.0	1021.57039(13)

Trans.	Laser ^a	ν_m^b	ν/MHz	O-C ^c	Unc. ^d	ν/cm^{-1} ^e
R(5, 4)	9P(46)	15525.0	30626041.1	-3.1	2.0	1021.57477(-10)
R(5, 5)	9P(46)	15713.0	30626229.2	-0.6	3.0	1021.58104(-2)
R(10, 8)	9P(38)	-17994.0	30843903.5	-0.6	3.0	1028.84188(-1)
R(10, 9)	9P(38)	-17696.0	30844201.5	-2.2	3.0	1028.85182(-7)
R(13, 0)	9P(34)	-17340.0	30965850.8	17.3	OVERLAP	1032.90960(57)
R(13, 1)	9P(34)	-17340.0	30965850.8	12.3	OVERLAP	1032.90960(40)
R(13, 2)	9P(34)	-17340.0	30965850.8	-3.3	OVERLAP	1032.90960(-11)
R(13, 3)	9P(34)	-17312.0	30965878.8	-3.1	3.0	1032.91053(-10)
R(13, 6)	9P(34)	-17120.0	30966070.8	-2.0	3.0	1032.91694(-6)
R(13, 7)	9P(34)	-17002.0	30966188.8	-1.1	3.0	1032.92087(-3)
R(13, 8)	9P(34)	-16850.0	30966340.8	-3.9	3.0	1032.92594(-12)
R(13, 9)	9P(34)	-16644.0	30966546.8	3.1	2.0	1032.93282(10)
R(13,10)	9P(34)	-16398.0	30966792.8	1.3	3.0	1032.94102(4)
R(13,11)	9P(34)	-16102.8	30967088.0	0.3	2.0	1032.95087(1)
R(20, 0)	9P(26)	13388.0	31230149.3	-14.3	OVERLAP	1041.72565(-47)
R(20, 1)	9P(26)	13388.0	31230149.3	-3.9	OVERLAP	1041.72565(-12)
R(20, 5)	9P(26)	13178.0	31229939.3	5.4	2.0	1041.71864(17)
R(20, 6)	9P(26)	13096.0	31229857.3	5.0	2.0	1041.71591(16)
R(20, 9)	9P(26)	12863.0	31229624.3	-0.2	2.0	1041.70814(0)
R(25, 2)	9P(20)	15940.0	31399840.4	3.1	2.0	1047.38594(10)
R(25, 6)	9P(20)	15225.9	31399126.3	-2.1	2.0	1047.36212(-7)

^aCO₂ laser line used.

^bMicrowave frequency in MHz. The signed microwave frequency is added to the laser frequency to obtain the absorption frequency.

^cObserved minus calculated frequency in MHz. The parameters for the calculation are in the last two columns of Table IV.

^dEstimated uncertainty in the observed frequency in MHz. An "OMIT" and an "OVERLAP" mean that the frequency was omitted from the least squares fits and the transition was overlapped by another transition(s), respectively.

^eObserved frequency in cm⁻¹. The numbers in parentheses are the observed minus calculated frequencies in units of 0.00001 cm⁻¹.

Table IV.

Vibration-Rotation Parameters for $^{13}\text{CH}_3\text{F}$.

Parameter ^a	$v_3 = 0^b$	$v_3 = 1^b$	$v_3 = 2^{c,e}$
E_v /GHz	0.0000 ^d	30803.4726(8)	61147.771(3)
B_v /MHz	24862.6460(34)	24542.1245(36)	24231.981(36)
$\Delta(A_v - B_v)$ /MHz	0.0000	31.3483(650)	57.308(294)
D_J /kHz	57.7386(156)	55.0634(147)	52.808(193)
D_{JK} /kHz	424.7361(2852)	477.5582(3141)	516.564(1958)
ΔD_K /kHz	0.0000	-69.8591(10668)	-115.718(6958)
H_J /Hz	-0.0172(100)	-0.1349(97)	-1.443(417)
H_{JK} /Hz	1.5815(1425)	9.8596(1894)	23.931(4992)
H_{KJ} /Hz	20.3809(13806)	-40.2484(16926)	-54.356(23928)
ΔH_K /Hz	0.0000	55.9988(62308)	208.862(61590)
L_J /mHz	0.0000 ^d	0.0078(15)	1.600(303)
L_{JJJK} /mHz	0.0000 ^d	-0.7656(433)	-17.569(4004)
L_{JJKK} /mHz	0.0000 ^d	11.3394(5012)	64.984(23322)
L_{JKKK} /mHz	0.0000 ^d	-81.6815(27527)	-352.961(101561)
ΔL_K /mHz	0.0000	49.2839(118569)	-700.256(204238)

^aVibration-rotation parameter. $\Delta P = P(v_3) - P(v_3=0)$.

^b Obtained from fit of frequencies indicated in Table I and listed in Table II. Number in parenthesis is one standard error in units of last digit in the parameter.

^c Obtained from fit of frequencies in Table III. Parameters for $v_3=1$ were constrained to values shown in this table. Number in parenthesis is one standard error in units of last digit of the parameter.

^d Constrained to zero in the least squares fit

^e It should be noted that the parameters for $v_3=2$ are given to one less significant figure than the parameters for $v_3=0$ and 1.

standard deviations for an object of unit weight (SD) were 2.45 and 1.37 MHz (r.m.s. deviations 3.38 and 2.49 MHz) for the fits to the fundamental and hot band frequencies, respectively.

If the L constants for the $\nu_3 = 1$ state were constrained to zero for the fundamental frequencies, the SD rose to 9.77 MHz. In addition, there was a definite increase in the residual for increasing J and K. On the other hand, allowing the L constants to vary for the ground state led to only a slight improvement in the SD (from 2.45 to 2.44 MHz). These findings are probably a result of the $\nu_3 - \nu_6$ Coriolis coupling, which strongly affects the energies for $\nu_3 = 1$ and 2. The effect of this coupling can be expanded in a power series in $J(J+1)$ and K^2 and apparently L constants are required to calculate the frequencies to within a few MHz for the high J's (≤ 47) and K's (≤ 16) in the present study.

The standard deviation for an object of unit weight obtained from the fit of the ν_3 fundamental band (2.45 MHz) is more than twice the value expected (1.00 MHz) if the uncertainties are accurately estimated. This large value of the SD is probably the result of model error rather than underestimation of the experimental uncertainty. The SD for the $2\nu_3 - \nu_3$ hot band (1.37 MHz) was much closer to the expected value, which can be explained as being a result of smaller effects of model error for the lower J's and K's

included in the fits of the hot band.

The least squares fits to Eq. (64), although providing an accurate representation of the experimental frequencies, are not entirely satisfactory. Part of the problem is the unexpectedly large SD just discussed. In addition, however, there is a question of convergence of that part of the expansion having to do with K^{2n} . This is best seen by calculating the contributions from the terms involving ΔD_K , ΔH_K , and ΔL_K . For the largest $K(=16)$ value studied, there is slow convergence in these terms (e.g., $\Delta H_K K^6 / \Delta L_K K^8 = 4.5$). For large K values, however, the convergence rapidly decreases and for $K=40$, which is still smaller than the largest J values studied, these terms are diverging. For these reasons, the values in Table IV, especially the L constants, should be regarded as fitting constants for the range of J and K values studied (Tables II and III).

In order to try to obtain a convergent set of parameters to represent the experimental frequencies for the fundamental band, several fittings to equations in the forms of a Pade approximant(76), which is famous for fits of the NH_3 inversion frequencies, were applied. The first Pade form tried was similar to Young's form(76,77), which was applied to the NH_3 inversion frequencies with a great success. This can be expressed as

$$E_p(v, J, K) = \left[\sum_{m=0}^{m+n \leq 3} \sum_{n=0} B_{mn} f^m g^n \right] / [1 + b_{10}f + b_{01}g] \quad (84)$$

where $f = J(J+1)$ and $g = K^2$. Least squares fits with this Pade approximant form of the energy showed exceptionally high correlations between the parameters, even when the denominator and the coefficients of K^{2n} were omitted for the ground state. The second Pade approximant tried is Burenin's form(78) given by

$$E = \frac{E_0 + \sum_{1 \leq m+n \leq 2} \sum_{n=0} B_{mn} f^m g^n}{1 + R \sum_{1 \leq m+n \leq 3} \sum_{n=0} B_{mn} f^m g^n} \quad (85)$$

And the last one tried is Watson's form(79,80), which is

$$E = E_0 + B_{10}f + B_{01}g + \frac{\sum_{m+n \geq 2} \sum_{n=0} B_{mn} f^m g^n}{1 + b_{10}f + b_{01}g} \quad (86)$$

The application of Watson's form of Pade approximant to the experimental frequencies worked very well for the case of $m+n \leq 3$. Of a total of 24 parameters used for this fit, 6 parameters (E_0 , B_{01} , B_{02} , B_{03} , b_{10} , and b_{01}) for the ground state were fixed to zero. The least squares fits to Eq. (86) showed good convergence and small deviation in the

region of high J and K values. Also, the fitting uncertainty is much better compared to the fits to Eq. (64). Moreover, the SD was improved to 2.99 MHz (r.m.s. deviation 3.77 MHz) for these fits, which proves that the Watson's form of Pade approximant is very useful for high J and K region. The fitting parameters to Eq. (86) are given in Table V. No attempt was made to include the Coriolis interaction explicitly because there is not enough information available for the interacting bands (ν_6 or $\nu_3 + \nu_6$).

The data in Table IV are sufficient to allow estimation of the first 3 constants in an expansion of the vibration-rotation parameters for $^{13}\text{CH}_3\text{F}$ in powers of ν_3 . If a parameter $P(\nu)$ is expressed as

$$P(\nu) = P(0) + c_1\nu + c_2\nu^2 \quad (87)$$

then

$$c_1 = [P(0) - 2P(1) + P(2)]/2 \quad (88)$$

and

$$c_2 = -[3P(0) - 4P(1) + P(2)]/2 \quad (89)$$

The values of $P(0)$, c_1 , and c_2 for the vibrational energy,

Table V

The Fitting Parameters of Watson's Form of Pade Approximant
for ν_3 Band of $^{13}\text{CH}_3\text{F}$

Parameters	$\nu_3 = 0^a$	$\nu_3 = 1^a$
B /GHz	0.00000 ^b	30803.47561(0)
B_{10} /MHz	24862.64766(0)	24542.11570(0)
B_{01} /MHz	0.00000 ^b	31.05489(4)
B_{20} /kHz	57.72178(2)	-55.04668(2)
B_{11} /kHz	424.78897(34)	-476.49688(33)
B_{02} /kHz	0.00000 ^b	72.73522(42)
B_{30} /Hz	-0.03717(1)	-2.46022(30)
B_{21} /Hz	1.86983(17)	55.65918(355)
B_{12} /Hz	19.35117(165)	528.17178(1466)
B_{03} /Hz	0.00000 ^b	-41.25928(266)
$b_{10} \times 10^3$	0.00000 ^b	41.93419(550)
$b_{01} \times 10^3$	0.00000 ^b	-120.51669(2989)

^aObtained from fit of frequencies indicated Table I and listed in Table II. Number in parenthesis is one standard error in units of last digit in the parameter.

^bConstrained to zero in the least squares fit.

Table VI.

Vibrational Dependence of Vibration-Rotation Parameters for $^{13}\text{CH}_3\text{F}$

$P(v)^a$	$P(0)^b$	c_1^b	c_2^b
E_v /GHz	0.000	$\nu_3 = 31033.060(2)$	$x_{33} = -229.587(1)$
B_v /MHz	24862.646(3)	$-\alpha_3^B = -325.710(20)$	5.189(18)
ΔA_v /MHz	0.000	$-\alpha_3^A = -291.668(197)$	2.494(162)
D_J /kHz	57.739(15)	-2.885(103)	0.210(98)
D_{JK} /kHz	424.736(285)	59.730(1239)	-6.908(1038)
ΔD_K /kHz	0.000	-81.859(4081)	12.000(3639)

^aVibration-rotation parameter. $P(v) = P(0) + c_1 v + c_2 v^2$.
 $P(0)$, c_1 , and c_2 were derived from the parameters in Table IV.

^bUncertainties in parentheses, in units of the last digit in the parameter, were propagated from one standard error in the parameters.

rotational constants, and quartic distortion parameters are given in Table VI together with the more conventional symbols for some of them.

ν_3 Fundamental and $2\nu_3 + \nu_3$ Hot Bands of $^{12}\text{CH}_3\text{F}$

By using a MW feedback controlled CO_2 infrared laser-MW sideband laser, more than 30 CO_2 laser lines ranging from 10R(40) - 9R(26) were tuned according to the predictions of approximate frequencies for the ν_3 fundamental band of $^{12}\text{CH}_3\text{F}$ obtained from many transitions observed previously. However, the predictions turned out to be not so accurate, particularly for high J and K transitions in the P branch. By scanning the MW frequency from 8.2-12.2 GHz and from 12.4-18.0 GHz for each CO_2 laser line, a total of 266 ν_3 fundamental band transitions could be observed, of which 212 transitions could be resolved, and of which 206 transitions were used for the vibration-rotation analysis. The estimated accuracy of these frequencies is 1-3 MHz, depending on the signal to noise ratio of the spectra. Figure 17 shows a typical spectrum from the ν_3 band of $^{12}\text{CH}_3\text{F}$ obtained by the MW feedback controlled IR-MW sideband system.

For the least squares fits, the data were weighted by the inverse of the square of the uncertainties shown in

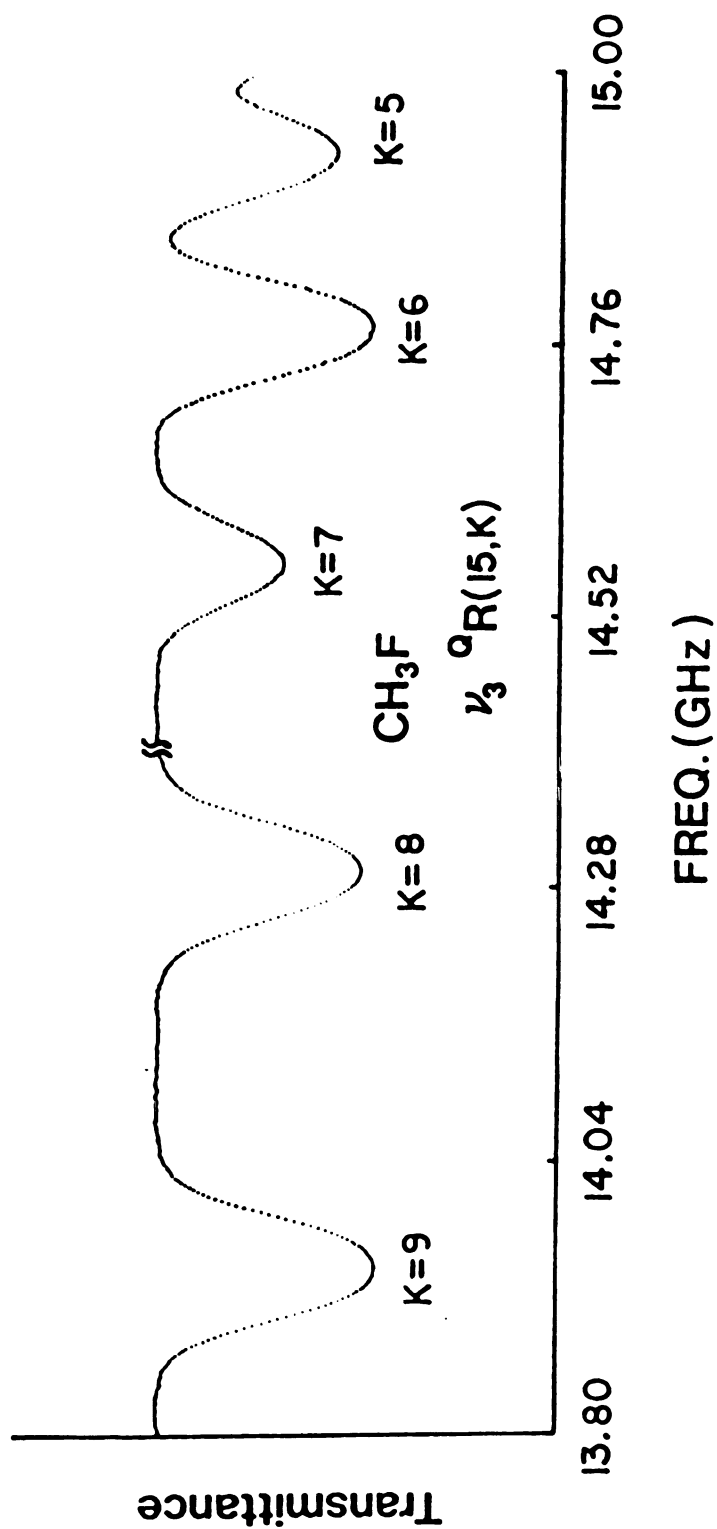


Figure 17. Typical spectrum of the ν_3 band of $^{12}\text{CH}_3\text{F}$ obtained with MW feedback controlled IR-MW sideband laser spectrometer. Two spectra were obtained at different pressure; ~100 mTorr for the spectrum at the left and ~50 mTorr for the spectrum at the right. This spectrum shows much improved baseline and lineshape. The lower sideband generated from the $9\text{R}(12)\text{CO}_2$ laser line was used.

Table VII, and the present data were combined with the available millimeter wave and laser-based frequencies and fitted by least squares adjustment of the parameters.

The $2\nu_3 + \nu_3$ hot band of $^{12}\text{CH}_3\text{F}$ was observed with the same instrument as the ν_3 fundamental band. According to the rough predictions based on the data from a previously published IR laser Stark experiment(16), a total of 11 CO_2 laser lines were tuned while sweeping the microwave frequency from 8.2-12.2 GHz and/or from 12.4-18.0 GHz. From these measurements, a total of 84 transitions in the $2\nu_3 + \nu_3$ hot band could be observed, of which 70 transitions were resolved and used for the least squares fits. The estimated accuracy was again 1-3 MHz depending on the S/N. In the fit of the $2\nu_3 + \nu_3$ transitions the energy levels of the $\nu_3 = 1$ state were assumed from the fit of the $\nu_3 = 1 + 0$ transitions.

With the same method as $^{13}\text{CH}_3\text{F}$, the transitions of ν_3 fundamental and $2\nu_3 + \nu_3$ hot bands were fitted to Eq. (64). With the L constants being constrained to zero for the ground state and allowed to vary for $\nu_3 = 1$ and 2 state, the standard deviations for an object of unit weight were 1.33 and 1.37 MHz (r.m.s. deviations 7.43 and 2.22 MHz) for the fits to the fundamental and hot bands frequencies, respectively.

If the L constants are allowed to vary for the ground state, the SD was slightly decreased to 1.29 MHz. Tables

Table VII.

Sources of Data for Fits of the ν_3 Band of $^{12}\text{CH}_3\text{F}$

Experiment	Source	Transitions	Uncert. ^a
IR-MW Sideband Laser	This work, Table VIII	High and low J,K; P,Q,R.	1.0-3.0 MHz
	Ref. 23, Table I	High J,K; Q,R. Low J; P,R.	10.0 MHz 10.0 MHz
IR-MW Two-Photon	Ref. 29, Table I	Low J; P,Q,R.	5.0 MHz
IR Laser Stark	Ref. 16, Table III	Low J; P,Q,R.	5.0 MHz
IR Laser Stark Lamb Dips	Ref. 16, Table III	Q(1,1), Q(2,2).	1.0 MHz
IR-RF Two-Photon	Ref. 16, Table III	Q(12,2).	1.0 MHz
	Ref. 40, Table III	Q(12,3).	1.0 MHz
Waveguide Laser	Ref. 24, Table I	Q(12,1), Q(12,2).	0.5 MHz
Diode Laser	Ref. 24, Table I	High J,K; Q, P(1,0).	10.0 MHz
	Ref. 26, Table I	High J,K; P, R.	30.0 MHz
FIR Emission	Ref. 17, Table I	High J, pure rot., $\nu_3 = 0$ and 1.	5.0 MHz
mm Wave Lamb Dips	Ref. 6, Table 2	R(1-3,K), pure rot., $\nu_3 = 0$.	0.01 MHz
mm Wave	Ref. 7, Table I	R(4,K), pure rot., $\nu_3 = 0$.	0.1 MHz
	Ref. 8, Table VI	R(0,0), pure rot., $\nu_3 = 1$.	0.1 MHz
	Ref. 9, Table I	R(1,K), pure rot., $\nu_3 = 1$.	0.5 MHz
	Ref. 75	High and low J; R, pure rot., $\nu_3 = 0, 1$.	0.1 MHz

^aUncertainty assumed in least squares fits.

VIII and IX show the measured frequencies with their estimated uncertainties for the ν_3 and $2\nu_3 + \nu_3$ transitions, respectively. The parameters in Table X were obtained from fits to Eq. (64) in which the L constants were constrained to zero for the ground state.

The small SD for $^{12}\text{CH}_3\text{F}$ compared to $^{13}\text{CH}_3\text{F}$ can be explained as being the result of the lower maximum $J(=39)$ value ($J \leq 47$ on $^{13}\text{CH}_3\text{F}$) and a larger number of data for $^{12}\text{CH}_3\text{F}$.

The molecular parameters for the vibrational ground state were compared with the data obtained from combination difference of several thousand transitions by Graner(39). Table XI shows the comparison between two data, in which the present parameters are in very good agreement with the previous ones.

The least squares fits of the $\nu_3 = 1$ transitions to Eq. (86) were done by the same method as for $^{13}\text{CH}_3\text{F}$ by constraining 6 parameters for the ground state to zero and allowing the other parameters to vary. The results show that the SD decreased to 1.63 MHz (r.m.s. deviation 7.39 MHz) and the fitting uncertainties are much improved. This phenomenon can be explained in the same way as for $^{13}\text{CH}_3\text{F}$. The fitting parameters to Eq. (86) are shown on Table XII. Also the vibrational dependence of vibration-rotation parameters for $^{12}\text{CH}_3\text{F}$ is given in Table XIII.

Table VIII.
Comparison of Observed and Calculated Frequencies
in the ν_3 Band of $^{12}\text{CH}_3\text{F}$

Trans.	Laser ^a	ν_m^b	ν/MHz	O-C ^c	Unc. ^d	ν/cm^{-1} ^e
P(30, 0)	10R(40)	10610.0	29618718.1	5.8	OVERLAP	987.97409(19)
P(30, 1)	10R(40)	10610.0	29618718.1	-5.3	OVERLAP	987.97409(-17)
P(30, 2)	10R(40)	10610.0	29618718.1	-39.0	OVERLAP	987.97409(-129)
P(30, 3)	10R(40)	10708.0	29618816.1	2.0	3.0	987.97736(6)
P(30, 4)	10R(40)	10791.0	29618899.1	3.4	2.0	987.98013(11)
P(30, 5)	10R(40)	10895.0	29619003.1	-0.5	2.0	987.98360(-1)
P(30, 6)	10R(40)	11035.0	29619143.1	3.8	1.0	987.98827(12)
P(30, 7)	10R(40)	11196.0	29619304.1	-0.3	2.0	987.99364(-1)
P(30, 8)	10R(40)	11396.6	29619504.7	4.6	1.0	988.00033(15)
P(30, 9)	10R(40)	11615.4	29619723.5	-3.3	1.0	988.00763(-10)
P(30, 10)	10R(40)	11870.6	29619978.7	-5.9	1.0	988.01614(-19)
P(30, 11)	10R(40)	12162.0	29620270.1	-2.9	2.0	988.02586(-9)
P(30, 12)	10R(40)	12481.8	29620589.9	-0.9	1.0	988.03653(-3)
P(30, 13)	10R(40)	12830.0	29620938.1	0.7	1.0	988.04814(2)
P(30, 14)	10R(40)	13209.9	29621318.1	5.5	2.0	988.06082(18)
P(30, 15)	10R(40)	13618.0	29621726.1	7.8	2.0	988.07443(25)
P(29, 0)	10R(46)	-9530.5	29688498.8	12.1	OVERLAP	990.30173(40)
P(29, 1)	10R(46)	-9530.5	29688498.8	-1.7	OVERLAP	990.30173(-5)
P(29, 2)	10R(46)	-9530.5	29688498.8	-43.4	OVERLAP	990.30173(-144)
P(29, 3)	10R(46)	-9418.8	29688610.5	-2.2	2.0	990.30545(-7)
P(29, 4)	10R(46)	-9313.4	29688716.0	2.5	2.0	990.30897(8)
P(29, 5)	10R(46)	-9182.0	29688847.3	0.9	2.0	990.31335(2)
P(29, 6)	10R(46)	-9014.6	29689014.7	1.1	1.0	990.31893(3)
P(29, 7)	10R(46)	-8813.6	29689215.7	-1.5	1.0	990.32564(-4)
P(29, 8)	10R(46)	-8576.1	29689453.2	-6.0	2.0	990.33356(-20)
P(29, 9)	10R(46)	-8294.0	29689735.3	-6.0	OVERLAP	990.34297(-20)
P(15, 0)	9P(46)	-10175.8	30600340.3	23.8	OVERLAP	1020.71748(79)
P(15, 1)	9P(46)	-10175.8	30600340.3	-17.9	OVERLAP	1020.71748(-59)
P(15, 2)	9P(46)	-10031.5	30600484.7	0.5	1.0	1020.72230(1)
P(15, 3)	9P(46)	-9820.3	30600695.8	-1.1	1.0	1020.72934(-3)
P(15, 4)	9P(46)	-9516.1	30601000.1	-0.9	1.0	1020.73949(-2)
P(15, 5)	9P(46)	-9113.1	30601403.1	0.6	1.0	1020.75293(1)
P(15, 6)	9P(46)	-8604.5	30601911.6	1.5	2.0	1020.76990(4)
P(14, 0)	9P(44)	-13761.7	30660684.1	1.5	OVERLAP	1022.73033(5)
P(14, 1)	9P(44)	-13761.7	30660684.1	-41.3	OVERLAP	1022.73033(-137)
P(14, 2)	9P(44)	-13593.9	30660851.9	-3.0	1.0	1022.73593(-10)
P(14, 3)	9P(44)	-13374.0	30661071.7	-2.0	1.0	1022.74326(-6)
P(14, 4)	9P(44)	-13059.9	30661385.8	-0.7	1.0	1022.75374(-2)
P(14, 5)	9P(44)	-12647.9	30661797.9	-1.9	1.0	1022.76749(-6)
P(14, 6)	9P(44)	-12124.6	30662321.2	-1.2	1.0	1022.78494(-3)

Trans.	Laser ^a	ν_{m}^b	ν/MHz	O-C ^c	Unc. ^d	ν/cm^{-1} ^e
P(14, 7)	9P(44)	-11480.8	30662964.9	-0.8	1.0	1022.80642(-2)
P(14, 8)	9P(44)	-10701.3	30663744.5	0.4	1.0	1022.83242(1)
P(14, 9)	9P(44)	-9769.6	30664676.1	0.8	1.0	1022.86350(2)
P(14,10)	9P(44)	-8664.0	30665781.8	0.0	2.0	1022.90038(0)
P(13, 0)	9P(42)	-17238.8	30720417.9	19.3	OVERLAP	1024.72284(64)
P(13, 1)	9P(42)	-17238.8	30720417.9	-24.7	OVERLAP	1024.72284(-82)
P(13, 2)	9P(42)	-17079.2	30720577.5	2.2	1.0	1024.72816(7)
P(13, 3)	9P(42)	-16857.8	30720798.9	-0.6	1.0	1024.73555(-1)
P(13, 4)	9P(42)	-16537.2	30721119.5	-0.6	1.0	1024.74624(-1)
P(13, 5)	9P(42)	-16112.8	30721543.9	0.1	1.0	1024.76040(0)
P(13, 6)	9P(42)	-15576.7	30722080.0	0.0	1.0	1024.77828(0)
P(13, 7)	9P(42)	-14916.5	30722740.2	-0.1	1.0	1024.80030(0)
P(13, 8)	9P(42)	-14117.0	30723539.8	0.0	1.0	1024.82697(0)
P(13, 9)	9P(42)	-13159.7	30724497.0	0.0	1.0	1024.85890(0)
P(13,10)	9P(42)	-12022.8	30725633.9	-1.5	1.0	1024.89683(-4)
P(13,11)	9P(42)	-10675.0	30726981.7	-1.9	1.0	1024.94178(-6)
P(13,12)	9P(42)	-9078.1	30728578.6	0.9	1.0	1024.99505(3)
P(12, 8)	9P(40)	-17469.1	30782673.6	-0.2	1.0	1026.79947(0)
P(12, 9)	9P(40)	-16488.2	30783654.5	0.1	1.0	1026.83219(0)
P(12,10)	9P(40)	-15321.5	30784821.2	-0.1	1.0	1026.87110(0)
P(12,11)	9P(40)	-13940.6	30786202.1	-2.8	1.0	1026.91716(-9)
P(5, 0)	9P(28)	14967.8	31174476.0	22.2	OVERLAP	1039.86859(74)
P(5, 1)	9P(28)	14967.8	31174476.0	-25.1	OVERLAP	1039.86859(-83)
P(5, 2)	9P(28)	15136.0	31174644.2	0.2	1.0	1039.87420(0)
P(5, 3)	9P(28)	15378.8	31174887.0	1.1	1.0	1039.88230(3)
P(5, 4)	9P(28)	15724.3	31175232.4	0.0	2.0	1039.89382(0)
P(4, 0)	9P(26)	11481.4	31228242.7	23.0	OVERLAP	1041.66205(76)
P(4, 1)	9P(26)	11481.4	31228242.7	-24.0	OVERLAP	1041.66205(-80)
P(4, 2)	9P(26)	11648.0	31228409.3	0.5	1.0	1041.66761(1)
P(4, 3)	9P(26)	11889.3	31228650.6	1.0	1.0	1041.67566(3)
Q(39,12)	9P(36)	-15133.5	30907781.9	0.5	2.0	1030.97263(1)
Q(38, 9)	9P(36)	14669.9	30937585.3	1.5	2.0	1031.96676(5)
Q(33, 3)	9P(32)	17624.0	31060342.1	-11.9	OMIT	1036.06149(-39)
Q(33, 4)	9P(32)	17420.0	31060138.1	-9.0	3.0	1036.05469(-30)
Q(33, 5)	9P(32)	17158.0	31059876.1	-6.6	2.0	1036.04595(-21)
Q(33, 6)	9P(32)	16839.1	31059557.2	-3.6	1.0	1036.03531(-12)
Q(33, 7)	9P(32)	16470.6	31059188.6	7.6	OMIT	1036.02302(25)
Q(33, 8)	9P(32)	16029.2	31058747.3	5.9	1.0	1036.00829(19)
Q(33, 9)	9P(32)	15523.3	31058241.4	3.2	1.0	1035.99142(10)
Q(33,10)	9P(32)	14946.5	31057664.6	-1.2	1.0	1035.97218(-3)



Trans.	Laser ^a	ν_m^b	ν/MHz	O-C ^c	Unc. ^d	ν/cm^{-1} ^e
Q(33,11)	9P(32)	14297.3	31057015.4	-0.1	1.0	1035.95052(0)
Q(33,12)	9P(32)	13555.4	31056273.5	-3.1	1.0	1035.92578(-10)
Q(33,13)	9P(32)	12711.8	31055429.9	-5.4	2.0	1035.89764(-17)
Q(29, 8)	9P(28)	-16017.2	31143491.0	0.7	2.0	1038.83504(2)
Q(29, 9)	9P(28)	-16236.6	31143271.6	-3.4	1.0	1038.82772(-11)
Q(29,10)	9P(28)	-16478.0	31143030.2	-9.6	OMIT	1038.81967(-32)
Q(29,11)	9P(28)	-16721.7	31142786.4	2.2	2.0	1038.81154(7)
Q(29,12)	9P(28)	-17001.8	31142506.4	-1.3	2.0	1038.80220(-4)
Q(29,13)	9P(28)	-17293.0	31142215.1	5.5	1.0	1038.79248(18)
Q(29,14)	9P(28)	-17609.3	31141898.9	8.4	2.0	1038.78193(28)
Q(29,15)	9P(28)	-17962.2	31141546.0	-6.7	2.0	1038.77016(-22)
Q(26,14)	9P(26)	-16174.0	31200587.3	1.4	2.0	1040.73957(4)
Q(26,15)	9P(26)	-15961.4	31200799.9	-2.7	1.0	1040.74666(-9)
Q(26,16)	9P(26)	-15682.0	31201079.3	-31.3	OVERLAP	1040.75598(-104)
Q(26,17)	9P(26)	-15332.0	31201429.3	-113.5	OVERLAP	1040.76765(-378)
Q(23,17)	9P(24)	-17151.7	31256095.5	-60.4	OVERLAP	1042.59112(-201)
Q(23,18)	9P(24)	-15562.1	31257685.1	38.4	OVERLAP	1042.64414(127)
Q(21,11)	9P(24)	9628.6	31282875.8	1.8	2.0	1043.48442(5)
Q(21,12)	9P(24)	10212.0	31283459.2	1.0	3.0	1043.50387(3)
Q(21,13)	9P(24)	10934.1	31284181.3	6.2	2.0	1043.52796(20)
Q(21,14)	9P(24)	11809.8	31285057.0	1.8	2.0	1043.55717(5)
Q(21,15)	9P(24)	12890.2	31286137.3	-0.2	1.0	1043.59321(0)
Q(21,16)	9P(24)	14215.0	31287462.2	-10.2	OMIT	1043.63740(-33)
Q(21,17)	9P(24)	15845.5	31289092.7	-31.1	OVERLAP	1043.69179(-103)
Q(21,18)	9P(24)	17926.2	31291173.3	-1.0	2.0	1043.76119(-3)
Q(19,11)	9P(22)	-17734.9	31311226.6	2.9	1.0	1044.43010(9)
Q(19,12)	9P(22)	-16965.5	31311996.0	-3.6	1.0	1044.45576(-11)
Q(19,13)	9P(22)	-16018.0	31312943.5	0.6	2.0	1044.48737(1)
Q(19,14)	9P(22)	-14870.7	31314090.8	0.2	1.0	1044.52564(0)
Q(19,15)	9P(22)	-13473.3	31315488.2	-1.5	1.0	1044.57225(-4)
Q(19,16)	9P(22)	-11765.1	31317196.4	-3.2	1.0	1044.62923(-10)
Q(19,17)	9P(22)	-9663.1	31319298.4	2.5	2.0	1044.69934(8)
Q(17,13)	9P(22)	10017.4	31338978.9	3.2	2.0	1045.35581(10)
Q(17,14)	9P(22)	11414.3	31340375.8	2.7	1.0	1045.40241(8)
Q(17,15)	9P(22)	13111.6	31342073.1	5.7	3.0	1045.45903(18)
Q(17,16)	9P(22)	15175.6	31344137.1	10.1	2.0	1045.52787(33)
Q(17,17)	9P(22)	17680.0	31346641.5	3.9	2.0	1045.61141(13)
Q(16, 2)	9P(22)	15826.0	31344787.5	0.2	2.0	1045.54957(0)
Q(16, 3)	9P(22)	15955.1	31344916.6	5.1	2.0	1045.55388(17)
Q(16, 4)	9P(22)	16130.0	31345091.5	0.4	2.0	1045.55971(1)

Trans.	Laser ^a	ν_{m}^b	ν/MHz	O-C ^c	Unc. ^d	ν/cm^{-1} ^e	
Q(16, 5)	9P(22)	16372.0	31345333.5	1.6	1.0	1045.56778(5)
Q(16, 6)	9P(22)	16682.1	31345643.6	2.0	1.0	1045.57812(6)
Q(16, 7)	9P(22)	17069.2	31346030.7	0.8	1.0	1045.59104(2)
Q(16, 8)	9P(22)	17550.2	31346511.7	2.2	2.0	1045.60708(7)
Q(14, 4)	9P(20)	-17839.5	31366060.9	-0.9	1.0	1046.25917(-2)
Q(14, 5)	9P(20)	-17556.8	31366343.6	-1.5	1.0	1046.26860(-4)
Q(14, 6)	9P(20)	-17192.8	31366707.6	-0.7	1.0	1046.28075(-2)
Q(14, 7)	9P(20)	-16738.0	31367162.4	0.0	2.0	1046.29591(0)
Q(14, 8)	9P(20)	-16179.6	31367720.8	-0.3	1.0	1046.31454(0)
Q(14, 9)	9P(20)	-15495.0	31368405.4	3.9	2.0	1046.33738(12)
Q(14, 10)	9P(20)	-14676.7	31369223.7	-1.3	1.0	1046.36467(-4)
Q(14, 11)	9P(20)	-13681.7	31370218.7	0.8	1.0	1046.39786(2)
Q(14, 12)	9P(20)	-12490.2	31371410.2	-3.1	1.0	1046.43760(-10)
Q(14, 13)	9P(20)	-11049.5	31372850.9	-1.0	1.0	1046.48566(-3)
Q(14, 14)	9P(20)	-9313.0	31374587.4	2.5	3.0	1046.54359(8)
Q(13, 2)	9P(20)	-8745.1	31375155.3	-1.5	2.0	1046.56253(-5)
Q(13, 3)	9P(20)	-8587.9	31375312.5	-1.7	1.0	1046.56777(-5)
Q(13, 4)	9P(20)	-8361.4	31375539.0	-2.0	1.0	1046.57533(-6)
Q(11, 6)	9P(20)	9325.3	31393225.7	-27.1	OVERLAP	1047.16529(-90)
Q(11, 7)	9P(20)	9896.4	31393796.8	5.1	1.0	1047.18434(17)
Q(11, 8)	9P(20)	10555.4	31394455.8	3.1	1.0	1047.20633(10)
Q(11, 9)	9P(20)	11356.9	31395257.3	1.8	1.0	1047.23306(5)
Q(11, 11)	9P(20)	13489.0	31397389.4	0.7	1.0	1047.30418(2)
Q(10, 2)	9P(20)	15591.1	31399491.5	0.6	2.0	1047.37430(1)
Q(10, 3)	9P(20)	15776.3	31399676.7	1.0	1.0	1047.38048(3)
Q(10, 4)	9P(20)	16042.3	31399942.7	1.2	1.0	1047.38935(3)
Q(10, 5)	9P(20)	16396.6	31400297.0	1.4	1.0	1047.40117(4)
Q(10, 6)	9P(20)	16849.1	31400749.5	1.5	2.0	1047.41626(4)
Q(10, 7)	9P(20)	17412.6	31401313.0	1.7	1.0	1047.43506(5)
Q(6, 1)	9P(18)	-15679.2	31422381.0	0.3	2.0	1048.13781(1)
Q(6, 2)	9P(18)	-15555.1	31422505.1	-0.2	1.0	1048.14195(0)
Q(6, 3)	9P(18)	-15344.0	31422716.2	-0.3	1.0	1048.14899(0)
Q(6, 4)	9P(18)	-15041.2	31423019.0	-0.9	1.0	1048.15909(-3)
Q(6, 5)	9P(18)	-14637.5	31423422.7	-1.0	1.0	1048.17256(-3)
Q(6, 6)	9P(18)	-14121.0	31423939.2	0.5	1.0	1048.18979(1)
Q(5, 2)	9P(18)	-11491.8	31426568.3	-1.5	1.0	1048.27748(-4)
Q(5, 3)	9P(18)	-11275.8	31426784.3	-1.5	1.0	1048.28469(-4)
Q(5, 4)	9P(18)	-10965.1	31427095.1	-0.9	1.0	1048.29506(-2)
Q(5, 5)	9P(18)	-10552.0	31427508.2	-0.5	1.0	1048.30883(-1)
R(2, 0)	9P(12)	-10109.9	31585721.9	18.0	OVERLAP	1053.58627(60)

Trans.	Laser ^a	ν_m^b	ν/MHz	O-C ^c	Unc. ^d	ν/cm^{-1} ^e
R(2, 1)	9P(12)	-10109.9	31585721.9	-22.8	OVERLAP	1053.58627(-76)
R(2, 2)	9P(12)	-9962.1	31585869.7	1.3	2.0	1053.59120(4)
R(3, 0)	9P(10)	-12766.4	31634077.0	18.1	OVERLAP	1055.19923(60)
R(3, 1)	9P(10)	-12766.4	31634077.0	-21.3	OVERLAP	1055.19923(-71)
R(3, 2)	9P(10)	-12623.9	31634219.5	2.0	1.0	1055.20398(6)
R(3, 3)	9P(10)	-12424.0	31634419.4	-0.4	1.0	1055.21065(-1)
R(4, 0)	9P(8)	-15313.0	31681748.4	16.7	OVERLAP	1056.78937(55)
R(4, 1)	9P(8)	-15313.0	31681748.4	-21.0	OVERLAP	1056.78937(-70)
R(4, 2)	9P(8)	-15175.5	31681885.9	2.3	2.0	1056.79396(7)
R(4, 3)	9P(8)	-14985.5	31682075.9	-1.7	1.0	1056.80030(-5)
R(4, 4)	9P(8)	-14705.3	31682356.1	-1.0	1.0	1056.80965(-3)
R(5, 0)	9P(6)	-17745.2	31728738.6	17.3	OVERLAP	1058.35680(57)
R(5, 1)	9P(6)	-17745.2	31728738.6	-18.5	OVERLAP	1058.35680(-61)
R(5, 2)	9P(6)	-17620.0	31728863.8	-2.1	2.0	1058.36097(-7)
R(5, 3)	9P(6)	-17433.9	31729049.9	-0.9	1.0	1058.36718(-2)
R(5, 4)	9P(6)	-17167.8	31729316.0	-1.4	1.0	1058.37606(-4)
R(5, 5)	9P(6)	-16809.9	31729673.9	0.1	1.0	1058.38800(0)
R(13, 0)	9R(8)	-11697.8	32079954.9	16.1	OVERLAP	1070.07211(53)
R(13, 1)	9R(8)	-11697.8	32079954.9	-0.2	OVERLAP	1070.07211(0)
R(13, 2)	9R(8)	-11697.8	32079954.9	-49.8	OVERLAP	1070.07211(-166)
R(13, 3)	9R(8)	-11563.0	32080089.7	-0.6	2.0	1070.07661(-1)
R(13, 4)	9R(8)	-11436.0	32080216.7	0.3	1.0	1070.08084(1)
R(13, 5)	9R(8)	-11263.0	32080389.6	0.3	1.0	1070.08661(1)
R(13, 6)	9R(8)	-11034.8	32080617.9	0.1	1.0	1070.09423(0)
R(13, 7)	9R(8)	-10740.4	32080912.3	-0.5	1.0	1070.10405(-1)
R(13, 8)	9R(8)	-10364.1	32081288.6	0.4	1.0	1070.11660(1)
R(13, 9)	9R(8)	-9890.8	32081761.9	0.7	1.0	1070.13239(2)
R(13,10)	9R(8)	-9298.9	32082353.7	0.5	2.0	1070.15213(1)
R(13,11)	9R(8)	-8559.2	32083093.5	2.6	3.0	1070.17680(8)
R(14, 0)	9R(10)	-13508.6	32120758.3	14.1	OVERLAP	1071.43317(46)
R(14, 1)	9R(10)	-13508.6	32120758.3	0.9	OVERLAP	1071.43317(2)
R(14, 2)	9R(10)	-13508.6	32120758.3	-39.5	OVERLAP	1071.43317(-131)
R(14, 3)	9R(10)	-13400.0	32120866.9	-1.1	3.0	1071.43679(-3)
R(14, 4)	9R(10)	-13294.8	32120972.2	0.0	2.0	1071.44030(0)
R(14, 5)	9R(10)	-13150.0	32121116.9	0.3	1.0	1071.44513(0)
R(14, 6)	9R(10)	-12958.5	32121308.4	-1.0	1.0	1071.45152(-3)
R(14, 7)	9R(10)	-12706.5	32121560.4	-0.7	1.0	1071.45992(-2)
R(14, 8)	9R(10)	-12404.0	32121862.9	-22.0	OVERLAP	1071.47001(-73)
R(14, 9)	9R(10)	-11965.6	32122301.3	4.1	1.0	1071.48464(13)
R(14,10)	9R(10)	-11447.3	32122819.6	1.4	1.0	1071.50192(4)

Trans.	Laser ^a	$\nu_{\text{M}}^{\text{b}}$	ν/MHz	O-C ^c	Unc. ^d	ν/cm^{-1} ^e
R(14,11)	9R(10)	-10792.1	32123474.8	1.7	1.0	1071.52378(5)
R(14,12)	9R(10)	-9973.3	32124293.6	0.2	1.0	1071.55109(0)
R(15, 0)	9R(12)	-15205.0	32160874.5	14.4	OVERLAP	1072.77130(48)
R(15, 1)	9R(12)	-15205.0	32160874.5	4.4	OVERLAP	1072.77130(14)
R(15, 2)	9R(12)	-15205.0	32160874.5	-26.5	OVERLAP	1072.77130(-88)
R(15, 3)	9R(12)	-15131.3	32160948.2	-6.9	OVERLAP	1072.77376(-22)
R(15, 4)	9R(12)	-15044.0	32161035.5	-1.0	2.0	1072.77667(-3)
R(15, 5)	9R(12)	-14929.6	32161149.9	-1.3	1.0	1072.78049(-4)
R(15, 6)	9R(12)	-14773.7	32161305.8	-1.1	1.0	1072.78569(-3)
R(15, 7)	9R(12)	-14567.6	32161511.9	-1.7	1.0	1072.79256(-5)
R(15, 8)	9R(12)	-14296.3	32161783.1	-0.6	1.0	1072.80161(-2)
R(15, 9)	9R(12)	-13947.0	32162132.5	-0.3	1.0	1072.81326(0)
R(15,10)	9R(12)	-13499.3	32162580.2	0.3	1.0	1072.82819(0)
R(15,11)	9R(12)	-12930.1	32163149.4	0.6	1.0	1072.84718(1)
R(15,12)	9R(12)	-12200.0	32163879.5	10.6	OVERLAP	1072.87154(35)
R(15,13)	9R(12)	-11301.6	32164777.9	0.7	1.0	1072.90150(2)
R(15,14)	9R(12)	-10154.0	32165925.5	5.9	2.0	1072.93978(19)
R(16, 0)	9R(14)	-16800.0	32200291.3	5.2	OVERLAP	1074.08610(17)
R(16, 1)	9R(14)	-16800.0	32200291.3	-1.5	OVERLAP	1074.08610(-5)
R(16, 2)	9R(14)	-16800.0	32200291.3	-22.5	OVERLAP	1074.08610(-74)
R(16, 3)	9R(14)	-16800.0	32200291.3	-59.9	OVERLAP	1074.08610(-199)
R(16, 4)	9R(14)	-16800.0	32200291.3	-117.8	OVERLAP	1074.08610(-392)
R(16, 5)	9R(14)	-16601.5	32200489.8	-3.2	2.0	1074.09272(-10)
R(16, 6)	9R(14)	-16482.1	32200609.2	-1.1	1.0	1074.09671(-3)
R(16, 7)	9R(14)	-16321.7	32200769.6	-0.7	1.0	1074.10206(-2)
R(16, 8)	9R(14)	-16108.1	32200983.2	-1.6	1.0	1074.10918(-5)
R(16, 9)	9R(14)	-15824.3	32201266.9	-1.4	1.0	1074.11865(-4)
R(16,10)	9R(14)	-15453.3	32201638.0	-0.8	1.0	1074.13102(-2)
R(16,11)	9R(14)	-14972.5	32202118.7	0.5	1.0	1074.14706(1)
R(16,12)	9R(14)	-14356.7	32202734.6	0.1	1.0	1074.16760(0)
R(16,13)	9R(14)	-13567.1	32203524.2	2.2	1.0	1074.19394(7)
R(16,14)	9R(14)	-12568.3	32204523.0	-1.0	1.0	1074.22726(-3)
R(16,15)	9R(14)	-11300.7	32205790.6	-4.2	1.0	1074.26954(-14)
R(17, 7)	9R(16)	-17972.4	32239330.9	-0.3	1.0	1075.38832(0)
R(17, 8)	9R(16)	-17816.7	32239486.7	-1.6	1.0	1075.39352(-5)
R(17, 9)	9R(16)	-17601.5	32239701.8	-2.1	1.0	1075.40070(-7)
R(17,10)	9R(16)	-17310.4	32239993.0	-2.2	1.0	1075.41041(-7)
R(17,11)	9R(16)	-16922.0	32240381.3	-0.9	1.0	1075.42336(-3)
R(17,12)	9R(16)	-16412.8	32240890.6	-0.4	1.0	1075.44035(-1)
R(17,13)	9R(16)	-15736.3	32241567.0	13.7	OMIT	1075.46291(45)

Trans.	Laser ^a	ν_m^b	ν/MHz	O-C ^c	Unc. ^d	ν/cm^{-1} ^e
R(17,14)	9R(16)	-14890.8	32242412.6	2.8	1.0	1075.49112(9)
R(17,15)	9R(16)	-13796.5	32243506.9	-4.1	2.0	1075.52762(-13)
R(18,13)	9R(18)	-17838.0	32278879.0	6.7	OMIT	1076.70751(22)
R(18,14)	9R(18)	-17141.3	32279575.7	-2.7	1.0	1076.73075(-9)
R(18,15)	9R(18)	-16208.3	32280508.9	4.4	2.0	1076.76187(14)
R(22, 0)	9R(24)	12150.0	32422335.7	-13.9	OVERLAP	1081.49271(-46)
R(22, 1)	9R(24)	12150.0	32422335.7	1.3	OVERLAP	1081.49271(4)
R(22, 2)	9R(24)	12150.0	32422335.7	46.5	OVERLAP	1081.49271(154)
R(22, 3)	9R(24)	12028.0	32422213.7	-2.1	2.0	1081.48864(-6)
R(22, 4)	9R(24)	11931.0	32422116.7	0.1	2.0	1081.48540(0)
R(22, 5)	9R(24)	11808.0	32421993.7	-1.6	2.0	1081.48130(-5)
R(22, 6)	9R(24)	11670.0	32421855.7	-1.0	2.0	1081.47670(-3)
R(22, 7)	9R(24)	11522.0	32421707.7	1.4	2.0	1081.47176(4)
R(22, 8)	9R(24)	11366.0	32421551.7	0.7	2.0	1081.46656(2)
R(22, 9)	9R(24)	11214.0	32421399.7	1.0	2.0	1081.46149(3)
R(22,10)	9R(24)	11074.0	32421259.7	0.5	2.0	1081.45682(1)
R(23, 0)	9R(26)	10500.0	32456925.0	-20.4	OVERLAP	1082.64648(-67)
R(23, 1)	9R(26)	10500.0	32456925.0	-1.2	OVERLAP	1082.64648(-3)
R(23, 2)	9R(26)	10460.0	32456885.0	16.0	OVERLAP	1082.64515(53)
R(23, 3)	9R(26)	10350.0	32456775.0	-0.4	2.0	1082.64148(-1)
R(23, 4)	9R(26)	10222.1	32456647.1	-0.6	1.0	1082.63721(-1)
R(23, 5)	9R(26)	10067.7	32456492.6	3.4	1.0	1082.63206(11)
R(23, 6)	9R(26)	9880.0	32456304.9	0.7	1.0	1082.62580(2)
R(23, 7)	9R(26)	9673.7	32456098.6	0.9	1.0	1082.61892(2)
R(23, 8)	9R(26)	9450.6	32455875.6	0.0	1.0	1082.61148(0)
R(23, 9)	9R(26)	9222.7	32455647.6	2.9	1.0	1082.60387(9)

^aCO₂ laser line used.

^bMicrowave frequency in MHz. The signed microwave frequency is added to the laser frequency to obtain the absorption frequency.

^cObserved minus calculated frequency in MHz. The parameters for the calculation are in the last two columns of Table X.

^dEstimated uncertainty in the observed frequency in MHz. An "OMIT" and an "OVERLAP" mean that the frequency was omitted from the least squares fits and the transition was overlapped by another transition(s), respectively.

^eObserved frequency in cm⁻¹. The numbers in parentheses are the observed minus calculated frequencies in units of 0.00001 cm⁻¹.

Table IX.

Comparison of Observed and Calculated Frequencies in the
 $2\nu_3 + \nu_3$ Band of $^{12}\text{CH}_3\text{F}$

Trans.	Laser ^a	ν_{M} ^b	ν/MHz	O-C ^c	Unc. ^d	ν/cm^{-1} ^e
R(17,12)	9P(6)	10835.0	31757318.8	-0.7	2.0	1059.31013(-2)
R(17, 9)	9P(6)	10006.0	31756489.8	14.6	OVERLAP	1059.28248(48)
R(15,12)	9P(8)	-16500.0	31680561.4	16.4	OVERLAP	1056.74978(54)
R(15, 9)	9P(8)	-17765.0	31679296.4	-3.8	2.0	1056.70758(-12)
R(12,10)	9P(14)	14935.0	31558963.9	-1.5	3.0	1052.69372(-5)
R(12, 9)	9P(14)	14453.4	31558482.3	1.7	2.0	1052.67766(5)
R(12, 8)	9P(14)	14057.9	31558086.8	-2.2	2.0	1052.66447(-7)
R(12, 7)	9P(14)	13749.0	31557777.9	2.6	1.0	1052.65416(8)
R(12, 6)	9P(14)	13494.9	31557523.8	-2.6	1.0	1052.64569(-8)
R(12, 5)	9P(14)	13303.7	31557332.6	0.5	1.0	1052.63931(1)
R(12, 4)	9P(14)	13152.0	31557180.9	-2.8	2.0	1052.63425(-9)
R(12, 3)	9P(14)	13045.0	31557073.9	-0.8	3.0	1052.63068(-2)
R(12, 2)	9P(14)	12925.0	31556953.9	-46.4	OVERLAP	1052.62668(-154)
R(12, 1)	9P(14)	12925.0	31556953.9	-3.1	OVERLAP	1052.62668(-10)
R(12, 0)	9P(14)	12925.0	31556953.9	11.1	OVERLAP	1052.62668(37)
R(10,10)	9P(16)	-16282.7	31475154.7	-1.8	2.0	1049.89816(-5)
R(10, 9)	9P(16)	-16866.1	31474571.3	1.4	1.0	1049.87869(4)
R(10, 8)	9P(16)	-17349.9	31474087.5	-3.0	2.0	1049.86255(-9)
R(10, 7)	9P(16)	-17737.1	31473700.3	-1.3	1.0	1049.84964(-4)
R(9, 3)	9P(18)	-8380.0	31429680.2	-1.9	3.0	1048.38128(-6)
R(9, 2)	9P(18)	-8488.0	31429572.2	-2.3	2.0	1048.37768(-7)
R(9, 1)	9P(18)	-8562.0	31429498.2	-13.2	OVERLAP	1048.37521(-44)
R(9, 0)	9P(18)	-8562.0	31429498.2	7.6	OVERLAP	1048.37521(25)
R(7, 6)	9P(22)	13218.7	31342180.2	0.7	2.0	1045.46260(2)
R(7, 5)	9P(22)	12899.9	31341861.4	0.1	2.0	1045.45196(0)
R(7, 4)	9P(22)	12651.7	31341613.2	-0.6	1.0	1045.44368(-1)
R(7, 3)	9P(22)	12463.7	31341425.2	-3.7	1.0	1045.43742(-12)
R(4, 4)	9P(26)	-12455.9	31204305.4	0.1	1.0	1040.86359(0)
R(4, 3)	9P(26)	-12677.7	31204083.6	1.5	1.0	1040.85619(4)
R(4, 2)	9P(26)	-12835.0	31203926.3	-0.8	2.0	1040.85094(-2)
R(4, 1)	9P(26)	-12938.9	31203822.4	-13.4	OVERLAP	1040.84748(-44)
R(4, 0)	9P(26)	-12938.9	31203822.4	16.7	OVERLAP	1040.84748(55)
Q(23,12)	9P(40)	-15667.8	30784474.9	0.0	1.0	1026.85955(0)
Q(23, 9)	9P(40)	-16924.0	30783218.6	-0.7	2.0	1026.81765(-2)
Q(21, 9)	9P(40)	12598.8	30812741.5	3.5	2.0	1027.80242(11)
Q(18,10)	9P(38)	-9140.0	30852757.5	-4.9	3.0	1029.13721(-16)
Q(18, 9)	9P(38)	-9701.4	30852196.1	-1.2	1.0	1029.11849(-3)
Q(18, 8)	9P(38)	-10169.1	30851728.4	0.4	1.0	1029.10289(1)
Q(18, 7)	9P(38)	-10557.5	30851340.1	-0.9	1.0	1029.08993(-3)
Q(18, 6)	9P(38)	-10875.0	30851022.5	-2.5	1.0	1029.07934(-8)

Trans.	Laser ^a	ν_m^b	ν/MHz	O-C ^c	Unc. ^d	ν/cm^{-1} ^e	
Q(18, 5)	9P(38)	-11125.2	30850772.3	1.2	1.0	1029.07099(3)
Q(18, 4)	9P(38)	-11325.0	30850572.5	0.3	1.0	1029.06433(1)
Q(18, 3)	9P(38)	-11475.0	30850422.5	-0.2	2.0	1029.05933(0)
Q(16, 12)	9P(38)	15683.1	30877580.6	0.3	1.0	1029.96522(1)
Q(16, 11)	9P(38)	14769.6	30876667.1	0.9	1.0	1029.93475(2)
Q(16, 10)	9P(38)	13998.0	30875895.5	-2.7	2.0	1029.90902(-9)
Q(16, 9)	9P(38)	13358.2	30875255.7	0.5	1.0	1029.88767(1)
Q(16, 8)	9P(38)	12825.7	30874723.2	3.6	1.0	1029.86991(11)
Q(16, 6)	9P(38)	12020.0	30873917.5	3.5	2.0	1029.84304(11)
Q(13, 13)	9P(36)	-14028.6	30908886.8	0.0	1.0	1031.00949(0)
Q(13, 12)	9P(36)	-15278.9	30907636.6	-1.3	2.0	1030.96778(-4)
Q(13, 11)	9P(36)	-16323.4	30906592.0	10.5	OVERLAP	1030.93294(35)
Q(13, 10)	9P(36)	-17224.0	30905691.4	0.7	2.0	1030.90290(2)
Q(13, 9)	9P(36)	-17973.4	30904942.0	-0.6	2.0	1030.87790(-1)
Q(12, 10)	9P(36)	-8605.5	30914310.0	1.2	2.0	1031.19038(3)
Q(12, 9)	9P(36)	-9388.1	30913527.4	-1.4	1.0	1031.16428(-4)
Q(12, 8)	9P(36)	-10040.4	30912875.1	-1.6	1.0	1031.14252(-5)
Q(12, 7)	9P(36)	-10579.0	30912336.4	0.7	3.0	1031.12455(2)
Q(12, 6)	9P(36)	-11022.0	30911893.4	1.4	3.0	1031.10978(4)
Q(12, 5)	9P(36)	-11329.0	30911536.6	2.4	3.0	1031.09787(8)
Q(12, 4)	9P(36)	-11660.0	30911255.4	2.5	3.0	1031.08849(8)
Q(12, 3)	9P(36)	-11874.0	30911041.4	0.3	1.0	1031.08136(0)
Q(9, 9)	9P(36)	12434.1	30935349.5	0.8	1.0	1031.89219(2)
Q(9, 8)	9P(36)	11710.0	30934625.4	0.9	3.0	1031.86803(2)
Q(9, 7)	9P(36)	11110.0	30934025.4	2.3	3.0	1031.84802(7)
Q(9, 6)	9P(36)	10614.0	30933529.4	0.0	3.0	1031.83148(0)
Q(9, 5)	9P(36)	10218.0	30933133.4	2.4	2.0	1031.81827(8)
Q(9, 4)	9P(36)	9903.1	30932818.5	0.8	2.0	1031.80776(2)
Q(9, 3)	9P(36)	9668.0	30932583.4	1.7	3.0	1031.79992(5)
Q(8, 8)	9P(36)	17647.0	30940562.5	0.6	3.0	1032.06607(2)
Q(8, 7)	9P(36)	17026.6	30939942.1	-1.1	2.0	1032.04538(-3)
Q(8, 6)	9P(36)	16521.4	30939436.8	1.6	1.0	1032.02852(5)
Q(8, 5)	9P(36)	16112.0	30939027.5	2.4	1.0	1032.01487(7)
Q(8, 4)	9P(36)	15785.5	30938701.0	-1.7	1.0	1032.00398(-5)
Q(8, 3)	9P(36)	15547.4	30938462.9	3.0	1.0	1031.99604(10)
Q(8, 2)	9P(36)	15378.2	30938293.6	3.0	3.0	1031.99039(10)
P(1, 0)	9P(36)	-11660.0	30911255.4	-1.7	3.0	1031.08849(-5)
P(7, 6)	9P(46)	-13658.6	30596857.6	-0.8	1.0	1020.60131(-2)
P(7, 5)	9P(46)	-14171.0	30596345.2	-2.7	1.0	1020.58422(-8)
P(7, 4)	9P(46)	-14570.0	30595946.1	2.0	2.0	1020.57091(6)

Trans.	Laser ^a	ν_m^b	ν/MHz	O-C ^c	Unc. ^d	ν/cm^{-1} ^e
P(7, 3)	9P(46)	-14877.0	30595639.1	0.5	1.0	1020.56067(1)
P(7, 2)	9P(46)	-15090.7	30595425.5	0.7	1.0	1020.55354(2)
P(7, 1)	9P(46)	-15239.8	30595276.3	-22.0	OVERLAP	1020.54857(-73)
P(7, 0)	9P(46)	-15239.8	30595276.3	19.9	OVERLAP	1020.54857(66)

^aCO₂ laser line used.

^bMicrowave frequency in MHz. The signed microwave frequency is added to the laser frequency to obtain the absorption frequency.

^cObserved minus calculated frequency in MHz. The parameters for the calculation are in the last two columns of Table X.

^dEstimated uncertainty in the observed frequency in MHz. An "OMIT" and an "OVERLAP" mean that the frequency was omitted from the least squares fits and the transition was overlapped by another transition(s), respectively.

^eObserved frequency in cm^{-1} . The numbers in parentheses are the observed minus calculated frequencies in units of 0.00001 cm^{-1} .

Table X.

Vibration-Rotation Parameters for $^{12}\text{CH}_3\text{F}$

Parameter ^a	$v_3 = 0^b$	$v_3 = 1^b$	$v_3 = 2^{c,e}$
E_v /GHz	0.0000 ^d	31436.5567(3)	62398.209(1)
B_v /MHz	25536.1498(7)	25197.5027(22)	24870.976(40)
$\Delta(A_v - B_v)$ /MHz	0.0000	44.3433(214)	81.290(111)
D_J /kHz	60.2330(48)	56.8509(100)	53.434(376)
D_{JK} /kHz	439.5279(488)	518.0548(739)	576.102(1074)
ΔD_K /kHz	0.0000	-94.1387(3113)	-169.779(3174)
H_J /Hz	-0.0214(81)	-0.2737(165)	-6.672(1173)
H_{JK} /Hz	1.7321(951)	16.0470(1644)	57.728(5559)
H_{KJ} /Hz	21.4254(2708)	-93.1078(8176)	-208.694(20427)
ΔH_K /Hz	0.0000	106.7283(17075)	173.320(39066)
L_J /mHz	0.0000 ^d	0.0795(73)	8.370(1603)
L_{JJJK} /mHz	0.0000 ^d	-2.9636(825)	-46.610(15279)
L_{JJKK} /mHz	0.0000 ^d	41.7067(5323)	107.530(50419)
L_{JKKK} /mHz	0.0000 ^d	-237.9115(19977)	-238.983(57475)
ΔL_K /mHz	0.0000	155.1981(32803)	142.063(105343)

^aVibration-rotation parameter. $\Delta P = P(v_3) - P(v_3=0)$.

^b Obtained from fit of frequencies indicated in Table VII and listed in Table VIII. Number in parenthesis is one standard error in units of last digit in the parameter.

^c Obtained from fit of frequencies in Table IX. Parameters for $v_3=1$ were constrained to values shown in this table. Number in parenthesis is one standard error in units of last digit of the parameter.

^d Constrained to zero in the least squares fit.

^e It should be noted that the parameters for $v_3=2$ are given to one less significant figure than the parameters for $v_3=0$ and 1.

Table XI.

Comparison of Ground-State Rotational
Constants of $^{12}\text{CH}_3\text{F}$.

Parameter	This Work ^a	Graner ^b
A_0 /MHz	—	155352.72
B_0 /MHz	25536.1498	25536.14929
D_J /kHz	60.2330	60.228
D_{JK} /kHz	439.5279	439.50
D_K /kHz	—	2108.4
H_J /Hz	-0.0214	—
H_{JK} /Hz	1.7321	1.29
H_{KJ} /Hz	21.4254	24.5
H_K /Hz	—	—

^aObtained from fit of frequencies indicated in Table VII and listed in Table VIII.

^bObtained from the Table 3 in Ref. 39.

Table XII.

The Fitting Parameters of Watson's Form of Pade Approximant
for ν_3 Band of $^{12}\text{CH}_3\text{F}$

Parameters	$\nu_3 = 0^a$	$\nu_3 = 1^a$
E /GHz	0.00000 ^b	30803.47561(0)
B_{10} /MHz	25536.15001(0)	25197.49134(0)
B_{01} /MHz	0.00000 ^b	44.16021(1)
B_{20} /kHz	60.22898(1)	-56.83832(1)
B_{11} /kHz	439.57479(6)	-517.35781(5)
B_{02} /kHz	0.00000 ^b	97.12210(11)
B_{30} /Hz	-0.00863(1)	-3.53175(20)
B_{21} /Hz	1.44265(11)	63.66537(197)
B_{12} /Hz	22.27008(32)	624.42425(601)
B_{03} /Hz	0.00000 ^b	-44.91134(126)
$b_{10} \times 10^3$	0.00000 ^b	58.26188(353)
$b_{01} \times 10^3$	0.00000 ^b	-1388.91964(1088)

^a Obtained from fit of frequencies indicated Table VII and listed in Table VIII. Number in parenthesis is one standard error in units of last digit in the parameter.

^b Constrained to zero in the least squares fit.

Table XIII.

Vibrational Dependence of Vibration-Rotation Parameters for $^{12}\text{CH}_3\text{F}$

$P(v)^a$	$P(0)^b$	c_1^b	c_2^b
E_v /GHz	0.000	$v_3 = 31674.009(1)$	$x_{33} = -237.452(1)$
B_v /MHz	25536.150(1)	$-\alpha_3^B = -344.708(21)$	6.060(21)
ΔA_v /MHz	0.000	$-\alpha_3^A = -296.666(73)$	2.362(63)
D_J /kHz	60.233(5)	-3.365(190)	-0.017(189)
D_{JK} /kHz	439.528(49)	88.767(562)	-10.240(543)
ΔD_K /kHz	0.000	-103.388(1705)	9.249(1618)

^aVibration-rotation parameter. $P(v) = P(0) + c_1 v + c_2 v^2$.
 $P(0)$, c_1 , and c_2 were derived from the parameters in Table X.

^bUncertainties in parentheses, in units of the last digit in the parameter, were propagated from one standard error in the parameters.

For the Coriolis interaction between ν_3 and ν_6 bands, Shoja-Chaghervand and Schwendeman(29) gave a detailed explanation on the formulas relating the perturbed state to unperturbed state. By using the formulas, they calculated the unperturbed molecular constants of the ν_3 and ν_6 states with assumption of $\zeta_{36} = 0.318$.

Finally, Tables XIV - XVII show the coincidences between the calculated frequencies of the ν_3 fundamental and the $2\nu_3 - \nu_3$ hot band transitions of $^{13}\text{CH}_3\text{F}$ and $^{12}\text{CH}_3\text{F}$ and the $10\ \mu\text{m}$ region fixed frequency gas laser lines(81,82,83). In this comparison, the calculated frequencies were obtained by the parameters obtained from the fittings in which the $\nu_3 = 1$ state parameters were fixed from the fits of the $\nu_3 = 1 \rightarrow 0$ transition and the L constants were constrained to zero for the ground state only. The results from the coincidences may be useful both for analysis of far infrared laser experiments and for the observation of the $\nu_3 = 3$ state by an infrared-infrared double resonance experiment.

Table XIV.

Coincidences Between Calculated Frequencies
for ν_3 Band of $^{13}\text{CH}_3\text{F}$ and CO_2 Laser Frequencies.

Trans. ^a	Frequency ^b	$\nu_0 - \nu_L$ ^c	Laser ^d		
P(44, 15)	28034726.1	58.9	$^{13}\text{C}^{16}\text{O}_2$	BAND I	R(30)
P(36, 9)	28624893.5	-52.8	N_2O		R(19)
P(36, 10)	28625035.8	89.5	N_2O		R(19)
P(30, 0)	29041047.2	-21.8	N_2O		R(38)
P(30, 1)	29041063.7	-5.3	N_2O		R(38)
P(30, 2)	29041113.4	44.5	N_2O		R(38)
P(26, 13)	29312229.7	12.9	$^{12}\text{C}^{18}\text{O}_2$	BAND I	R(16)
P(25, 15)	29379942.4	-3.2	$^{12}\text{C}^{18}\text{O}_2$	BAND I	R(20)
P(24, 10)	29440019.4	82.3	$^{12}\text{C}^{16}\text{O}^{18}\text{O}$	BAND I	R(23)
P(24, 13)	29442534.9	51.6	$^{12}\text{C}^{16}\text{O}_2$	BAND I	R(30)
P(23, 12)	29505764.1	85.0	$^{12}\text{C}^{18}\text{O}_2$	BAND I	R(28)
P(16, 12)	29938027.2	47.9	$^{13}\text{C}^{18}\text{O}_2$	BAND II	P(36)
P(15, 13)	29998669.7	19.6	$^{13}\text{C}^{16}\text{O}_2$	BAND II	P(20)
P(13, 0)	30107614.5	61.4	$^{13}\text{C}^{16}\text{O}_2$	BAND II	P(16)
P(13, 1)	30107648.9	95.8	$^{13}\text{C}^{16}\text{O}_2$	BAND II	P(16)
Q(8, 6)	30791154.4	-88.3	$^{12}\text{C}^{16}\text{O}^{18}\text{O}$	BAND II	P(52)
Q(20, 15)	30674416.2	-29.5	$^{12}\text{C}^{16}\text{O}_2$	BAND II	P(44)
Q(21, 13)	30658803.1	99.5	$^{13}\text{C}^{18}\text{O}_2$	BAND II	P(6)
Q(29, 11)	30525857.4	59.6	$^{13}\text{C}^{18}\text{O}_2$	BAND II	P(12)
Q(29, 12)	30525802.9	5.1	$^{13}\text{C}^{18}\text{O}_2$	BAND II	P(12)
Q(29, 13)	30525774.2	-23.7	$^{13}\text{C}^{18}\text{O}_2$	BAND II	P(12)
Q(29, 14)	30525780.4	-17.5	$^{13}\text{C}^{18}\text{O}_2$	BAND II	P(12)
Q(29, 15)	30525833.0	35.1	$^{13}\text{C}^{18}\text{O}_2$	BAND II	P(12)
R(4, 3)	31042692.2	-25.9	$^{12}\text{C}^{16}\text{O}_2$	BAND II	P(32)
R(12, 7)	31391833.2	-27.6	$^{13}\text{C}^{16}\text{O}_2$	BAND II	R(48)
R(14, 9)	31472712.0	-25.0	$^{13}\text{C}^{18}\text{O}_2$	BAND II	R(38)
R(21, 1)	31733443.0	95.9	$^{13}\text{C}^{18}\text{O}_2$	BAND II	R(58)
R(21, 2)	31733407.7	60.6	$^{13}\text{C}^{18}\text{O}_2$	BAND II	R(58)
R(21, 3)	31733350.6	3.5	$^{13}\text{C}^{18}\text{O}_2$	BAND II	R(58)
R(21, 4)	31733274.4	-72.8	$^{13}\text{C}^{18}\text{O}_2$	BAND II	R(58)

^aTransition in the ν_3 band of $^{13}\text{CH}_3\text{F}$; $J \leq 47$, $K \leq 15$.

^bFrequency of ν_3 band transition in MHz.

^cFrequency of ν_3 band transition minus laser frequency in MHz. Laser frequencies calculated from constants in Refs. 81, 82, and 83.

^dIdentification of CO_2 or N_2O laser. Band I is 10 μm band; Band II is 9 μm band.

Table XV.

Coincidences Between Calculated Frequencies for
 $2\nu_3 + \nu_3$ Band of $^{13}\text{CH}_3\text{F}$ and CO_2 Laser Frequencies.

Trans. ^a	Frequency ^b	$\nu_0 - \nu_L$ ^c	Laser ^d	
P(25, 0)	28935291.8	-5.1	N ₂ O	R(33)
P(25, 1)	28935319.2	22.3	N ₂ O	R(33)
P(24, 3)	28999003.2	-80.5	N ₂ O	R(36)
P(23, 3)	29061892.7	-6.3	N ₂ O	R(39)
P(18, 7)	29369030.5	-92.1	$^{12}\text{C}^{18}\text{O}^{18}\text{O}$ BAND I	R(19)
P(15, 4)	29544270.2	73.8	$^{12}\text{C}^{18}\text{O}_2$ BAND I	R(36)
P(14, 7)	29603057.1	48.8	$^{12}\text{C}^{18}\text{O}^{18}\text{O}$ BAND I	R(33)
P(12, 9)	29717723.1	73.3	$^{12}\text{C}^{18}\text{O}_2$ BAND I	R(44)
P(11, 0)	29770575.1	-93.1	$^{13}\text{C}^{18}\text{O}_2$ BAND II	P(28)
P(11, 1)	29770607.4	-60.8	$^{13}\text{C}^{18}\text{O}_2$ BAND II	P(28)
P(11, 2)	29770704.9	36.7	$^{13}\text{C}^{18}\text{O}_2$ BAND II	P(28)
P(11, 6)	29771800.7	-42.0	$^{12}\text{C}^{18}\text{O}^{18}\text{O}$ BAND I	R(45)
P(5, 4)	30093194.4	-25.8	$^{13}\text{C}^{18}\text{O}_2$ BAND II	P(30)
Q(13, 12)	30291610.6	-74.6	$^{13}\text{C}^{18}\text{O}_2$ BAND II	P(22)
Q(14, 7)	30280267.9	-54.4	$^{12}\text{C}^{18}\text{O}_2$ BAND II	P(56)
Q(25, 5)	30143668.8	-87.6	$^{13}\text{C}^{18}\text{O}_2$ BAND II	P(28)
Q(25, 6)	30143728.2	-28.2	$^{13}\text{C}^{18}\text{O}_2$ BAND II	P(28)
Q(25, 7)	30143814.3	57.9	$^{13}\text{C}^{18}\text{O}_2$ BAND II	P(28)
R(12, 11)	30927031.0	38.0	$^{13}\text{C}^{18}\text{O}_2$ BAND II	R(6)
R(13, 0)	30965833.5	-36.2	$^{13}\text{C}^{18}\text{O}_2$ BAND II	R(8)
R(13, 1)	30965838.5	-31.2	$^{13}\text{C}^{18}\text{O}_2$ BAND II	R(8)
R(13, 2)	30965854.1	-15.6	$^{13}\text{C}^{18}\text{O}_2$ BAND II	R(8)
R(13, 3)	30965881.8	12.1	$^{13}\text{C}^{18}\text{O}_2$ BAND II	R(8)
R(13, 4)	30965924.6	54.9	$^{13}\text{C}^{18}\text{O}_2$ BAND II	R(8)
R(24, 9)	31365843.9	86.9	$^{13}\text{C}^{18}\text{O}_2$ BAND II	R(46)

^aTransition in the $2\nu_3 + \nu_3$ band of $^{13}\text{CH}_3\text{F}$; $J \leq 25$, $K \leq 12$.

^bFrequency of $2\nu_3 + \nu_3$ band transition in MHz.

^cFrequency of $2\nu_3 + \nu_3$ band transition minus laser frequency in MHz. Laser frequencies calculated from constants in Refs. 81, 82, and 83.

^dIdentification of CO_2 or N_2O laser. Band I is 10 μm band; Band II is 9 μm band.

Table XVI.

Coincidences Between Calculated Frequencies
for ν_3 Band of $^{12}\text{CH}_3\text{F}$ and CO_2 Laser Frequencies.

Trans. ^a	Frequency ^b	$\nu_0 - \nu_L$ ^c	Laser ^d
P(27, 11)	29828909.0	-16.6	$^{13}\text{C}^{16}\text{O}_2$ BAND II P(26)
Q(6, 4)	31423019.9	-87.4	$^{12}\text{C}^{16}\text{O}^{18}\text{O}$ BAND II P(30)
Q(11, 1)	31391948.0	87.2	$^{13}\text{C}^{16}\text{O}_2$ BAND II R(48)
Q(12, 1)	31383841.7	-58.7	$^{12}\text{C}^{16}\text{O}_2$ BAND II P(20)
Q(12, 2)	31383940.1	39.7	$^{12}\text{C}^{16}\text{O}_2$ BAND II P(20)
Q(13, 13)	31382754.9	61.2	$^{13}\text{C}^{16}\text{O}_2$ BAND II R(32)
Q(14, 2)	31365702.8	-54.2	$^{13}\text{C}^{16}\text{O}_2$ BAND II R(46)
Q(14, 3)	31365849.8	92.8	$^{13}\text{C}^{16}\text{O}_2$ BAND II R(46)
Q(15, 15)	31365845.0	88.0	$^{13}\text{C}^{16}\text{O}_2$ BAND II R(46)
Q(21, 15)	31286137.6	-28.7	$^{12}\text{C}^{16}\text{O}^{18}\text{O}$ BAND II P(35)
Q(28, 3)	31163602.8	93.3	$^{12}\text{C}^{16}\text{O}_2$ BAND II P(54)
Q(28, 4)	31163526.6	17.1	$^{12}\text{C}^{16}\text{O}_2$ BAND II P(54)
Q(28, 5)	31163432.1	-77.4	$^{12}\text{C}^{16}\text{O}_2$ BAND II P(54)
Q(33, 8)	31058741.4	-79.0	$^{12}\text{C}^{16}\text{O}^{18}\text{O}$ BAND II P(43)
Q(34, 15)	31029723.8	23.5	$^{12}\text{C}^{16}\text{O}^{18}\text{O}$ BAND II P(44)
Q(38, 2)	30941471.5	53.4	$^{12}\text{C}^{16}\text{O}^{18}\text{O}$ BAND II P(47)
Q(39, 8)	30912521.1	42.4	$^{13}\text{C}^{16}\text{O}_2$ BAND II R(18)
R(10, 3)	31953615.9	17.2	$^{12}\text{C}^{16}\text{O}^{18}\text{O}$ BAND II P(9)
R(11, 9)	31998587.9	-26.2	$^{12}\text{C}^{16}\text{O}_2$ BAND II P(22)
R(11, 11)	32000205.2	-78.7	$^{12}\text{C}^{16}\text{O}^{18}\text{O}$ BAND II P(7)
R(26, 15)	32550672.7	24.6	$^{12}\text{C}^{16}\text{O}_2$ BAND II R(2)
R(31, 4)	32708073.7	-22.7	$^{12}\text{C}^{16}\text{O}_2$ BAND II R(10)
R(34, 3)	32791507.1	38.0	$^{12}\text{C}^{16}\text{O}^{18}\text{O}$ BAND II R(32)
R(35, 12)	32807743.3	-48.4	$^{12}\text{C}^{16}\text{O}^{18}\text{O}$ BAND II R(33)

^aTransition in the ν_3 band of $^{12}\text{CH}_3\text{F}$; $J \leq 40$, $K \leq 15$.

^bFrequency of ν_3 band transition in MHz.

^cFrequency of ν_3 band transition minus laser frequency in MHz. Laser frequencies calculated from constants in Refs. 81, 82, and 83.

^dIdentification of CO_2 or N_2O laser. Band I is 10 μm band; Band II is 9 μm band.

Table XVII.

Coincidences Between Calculated Frequencies for
 $2\nu_3 + \nu_3$ Band of $^{12}\text{CH}_3\text{F}$ and CO_2 Laser Frequencies.

Trans. ^a	Frequency ^b	$\nu_0 - \nu_L$ ^c	Laser ^d
P(22, 0)	29705011.1	-95.2	$^{12}\text{C}^{18}\text{O}^{18}\text{O}$ BAND I R(40)
P(22, 1)	29705048.0	-58.3	$^{12}\text{C}^{18}\text{O}^{18}\text{O}$ BAND I R(40)
P(22, 2)	29705159.4	53.1	$^{12}\text{C}^{18}\text{O}^{18}\text{O}$ BAND I R(40)
P(21, 7)	29770679.7	11.5	$^{13}\text{C}^{18}\text{O}_2$ BAND II P(28)
P(20, 6)	29833266.8	-67.2	$^{12}\text{C}^{18}\text{O}^{18}\text{O}$ BAND I R(50)
Q(10, 6)	30926970.0	-23.0	$^{13}\text{C}^{18}\text{O}_2$ BAND II R(6)
Q(16, 5)	30873622.0	-58.4	$^{13}\text{C}^{18}\text{O}_2$ BAND II R(16)
Q(17, 1)	30861966.1	68.6	$^{12}\text{C}^{18}\text{O}_2$ BAND II P(38)
Q(18, 8)	30851728.0	-37.0	$^{12}\text{C}^{18}\text{O}^{18}\text{O}$ BAND II P(50)
Q(25, 12)	30752051.6	-7.3	$^{13}\text{C}^{18}\text{O}_2$ BAND II R(10)
R(7, 3)	31341429.0	5.7	$^{12}\text{C}^{18}\text{O}^{18}\text{O}$ BAND II P(33)
R(10, 0)	31472640.0	-97.1	$^{13}\text{C}^{18}\text{O}_2$ BAND II R(38)
R(10, 1)	31472658.6	-78.4	$^{13}\text{C}^{18}\text{O}_2$ BAND II R(38)
R(10, 2)	31472715.3	-21.7	$^{13}\text{C}^{18}\text{O}_2$ BAND II R(38)
R(10, 3)	31472812.2	75.2	$^{13}\text{C}^{18}\text{O}_2$ BAND II R(38)
R(12, 4)	31557183.7	-54.3	$^{13}\text{C}^{18}\text{O}_2$ BAND II R(44)
R(12, 5)	31557332.0	94.1	$^{13}\text{C}^{18}\text{O}_2$ BAND II R(44)
R(13, 6)	31598591.2	35.1	$^{12}\text{C}^{18}\text{O}_2$ BAND II P(38)

^aTransition in the $2\nu_3 + \nu_3$ band of $^{12}\text{CH}_3\text{F}$; $J \leq 25$, $K \leq 12$.

^bFrequency of $2\nu_3 + \nu_3$ band transition in MHz.

^cFrequency of $2\nu_3 + \nu_3$ band transition minus laser frequency in MHz. Laser frequencies calculated from constants in Refs. 81, 82, and 83.

^dIdentification of CO_2 or N_2O laser. Band I is 10 μm band; Band II is 9 μm band.

REFERENCES

1. P. D. Coleman, J. Opt. Soc. Amer. 67, 894-901 (1977).
2. J. R. Izatt and P. Mathieu, Canad. J. Phys. 58, 1401-1415 (1980).
3. O. R. Gilliam, H. D. Edwards, and W. Gordy, Phys. Rev. 75, 1014-1016 (1949).
4. C. M. Johnson, R. Trambarulo, and W. Gordy, Phys. Rev. 84, 1178-1180 (1951).
5. W. J. Orville Thomas, J. T. Cox, and W. Gordy, J. Chem. Phys. 22, 1718-1722 (1954).
6. R. S. Winton and W. Gordy, Phys. Lett. 32A, 219-220 (1970).
7. T. E. Sullivan and L. Frenkel, J. Mol. Spectrosc. 39, 185-201 (1971).
8. T. Tanaka and E. Hirota, J. Mol. Spectrosc. 54, 437-446 (1975).
9. E. Hirota, T. Tanaka, and S. Saito, J. Mol. Spectrosc. 63, 478-484 (1976).
10. W. H. Bennett and C. F. Meyer, Phys. Rev. 32, 888-905 (1928).
11. K. P. Yates and H. H. Nielson, Phys. Rev. 71, 349-359 (1947).
12. F. A. Andersen, B. Bak, and S. Brodersen, J. Chem. Phys. 24, 989-992 (1956).
13. W. L. Smith and I. M. Mills, J. Mol. Spectrosc. 11, 11-38 (1963).
14. A. C. Luntz and R. G. Brewer, J. Chem. Phys. 54, 3641-3642 (1971).
15. E. Weitz, G. Flynn, and A. M. Ronn, J. Appl. Phys. 42, 5187-5190 (1971).
16. S. M. Freund, G. Duxbury, M. Romheld, J. T. Tiedje, and T. Oka, J. Mol. Spectrosc. 52, 38-57 (1974).

17. T. Y. Chang and T. J. Bridges, *Opt. Commun.* **1**, 423-426 (1970).
18. T. Y. Chang and J. D. McGee, *Appl. Phys. Lett.* **19**, 103-105 (1971).
19. R. G. Brewer, *Phys. Rev. Lett.* **25**, 1639-1641 (1970).
20. R. G. Brewer, *Science* **178**, 247-255 (1972).
21. W. K. Bischel, P. J. Kelly, and C. K. Rhodes, *Phys. Rev. Lett.* **34**, 300-303 (1975).
22. W. A. M. Blumberg, H. R. Fetterman, D. D. Peck, and P. F. Goldsmith, *Appl. Phys. Lett.* **35**, 582-585 (1979).
23. G. Magerl, W. Schupita, E. Bonek, and W. A. Kreiner, *J. Mol. Spectrosc.* **83**, 431-439 (1980).
24. F. Herlemont, M. Lyszyk, J. Lemaire, and J. Demaison, *Z. Naturforsch* **36a**, 944-947 (1981).
25. J. P. Sattler and G. J. Simonis, *IEEE J. Quantum Electron.* **QE-13**, 461-465 (1977).
26. E. Arimondo, M. I. Schisano, P. B. Davies, and P. A. Hamilton, *Infrared Phys.* **25**, 209-213 (1985).
27. M. Romheld, Ph. D. Thesis, University of Ulm, 1979.
28. S. M. Freund, M. Romheld, and T. Oka, *Phys. Rev. Lett.* **35**, 1497-1500 (1975).
29. P. Shoja-Chaghervand and R. H. Schwendeman, *J. Mol. Spectrosc.* **98**, 27-40 (1983).
30. E. Bava, A. DeMarchi, A. Godone, R. Benetti, M. Inguscio, P. Minguzzi, F. Strumia, and M. Tonelli, *Opt. Commun.* **21**, 46-48 (1977).
31. H. E. Radford, F. R. Peterson, D. A. Jennings, and J. A. Mucha, *IEEE J. Quantum Electron.* **QE-13**, 92-94 (1977).
32. J. Pickworth and H. W. Thompson, *Proc. Roy. Soc. Ser. A* **222**, 443-455 (1954).
33. M. Betrencourt, *J. Mol. Spectrosc.* **47**, 275-285 (1973).
34. J. L. Duncan, D. C. McKean, and G. K. Speirs, *Molec. Phys.* **24**, 553-565 (1972).

35. W. H. Matterson and F. C. DeLucia, J. Opt. Soc. Am. B2, 336-342 (1985).
36. S. H. Ghosh, R. Trambarulo, and W. Gordy, J. Chem. Phys. 20, 605-607 (1952).
37. W. C. King and W. Gordy, Phys. Rev. 93, 407-412 (1954).
38. P. A. Steiner and W. Gordy, J. Mol. Spectrosc. 21, 291-301 (1966).
39. G. Graner, Molec. Phys. 31, 1833-1843 (1976).
40. E. Arimondo and M. Inguscio, J. Mol. Spectrosc. 75, 81-86 (1979).
41. C. DiLauro and I. M. Mills, J. Mol. Spectrosc. 21, 386-413 (1966).
42. E. Hirota, J. Mol. Spectrosc. 74, 209-216 (1979).
43. C. H. Townes and A. L. Schawlow, "Microwave Spectroscopy", McGraw-Hill Inc., New York, NY, 1955.
44. J. E. Wollrab, "Rotational Spectra and Molecular Structure", Academic Press, New York, NY, 1967.
45. H. W. Kroto, "Molecular Rotation Spectra", John Wiley & Sons, New York, NY, 1975.
46. G. Herzberg, "Molecular Spectra and Molecular Structure (Infrared and Raman Spectra of Polyatomic Molecules)", Van Nostrand Reinhold Co., 1945.
47. J. H. Meal and S. R. Polo, J. Chem. Phys. 24, 1126-1133 (1956).
48. T. Oka, J. Chem. Phys. 47, 5410-5426 (1967).
49. E. B. Wilson, Jr., J. Chem. Phys. 27, 986-987 (1957).
50. R. S. McDowell, Adv. in IR and Raman Spectroscopy, Vol. 5, ed. by R. J. H. Clark and R. E. Hester, Heydon & Son, London, 1978.
51. A. S. Pine, in Laser Spectroscopy III (ed. by J. L. Hall and J. L. Carlstein), Springer-Verlag, Berlin, 1977, p. 376.
52. L. F. Mollenauer and D. H. Alson, Appl. Phys. Lett.

- 24, 386-388 (1974).
53. C. K. N. Patel and E. D. Shaw, Phys. Rev. Lett. 24, 451-455 (1970).
 54. R. L. Abrams and W. B. Bridges, IEEE J. Quantum Electron. QE-9, 940-946 (1973).
 55. P. W. Smith, in Laser Spectroscopy (ed. by R. G. Brewer and A. Mooradian), Plenum Press, New York, NY, 1974, p. 247.
 56. R. L. Abrams, *ibid.*, p.263.
 57. T. Kasuya, Appl. Phys. 2, 339 (1973).
 58. T. Kasuya, Appl. Phys. 3, 223 (1974).
 59. T. Oka and T. Shimizu, Phys. Rev. A2, 587-593 (1970).
 60. V. J. Corcoran, R. E. Cupp, J. J. Gallagher, and W. T. Smith, Appl. Phys. Lett. 16, 316-318 (1970).
 61. P. A. Franken, A. E. Hill, C. W. Peters, and G. Weinreich, Phys. Rev. Lett. 7, 118-119 (1961).
 62. M. Bass, P. A. Franken, A. E. Hill, C. W. Peters, and G. Weinreich, Phys. Rev. Lett. 8, 18 (1962).
 63. P. K. Cheo and M. Gilden, Appl. Phys. Lett. 28, 626-627 (1976).
 64. P. K. Cheo and M. Gilden, Optics. Lett. 1, 38-39 (1977).
 65. E. Bonek and H. Korechy, Appl. Phys. Lett. 25, 750-741 (1974).
 66. G. Magerl and E. Bonek, J. Appl. Phys. 47, 4901-4903 (1976).
 67. G. Magerl and E. Bonek, Appl. Phys. Lett. 34, 452-454 (1979).
 68. G. Magerl and E. Bonek, "Direct-frequency reading IR spectroscopy", presented at the Int. Conf. LASER '79, Orlando, FL, 1979.
 69. G. Magerl, W. Schupita, and E. Bonek, IEEE J. Quantum Electron. QE-18, 1214-1220 (1982).

70. G. Magerl, E. Bonek, and W. A. Kreiner, Chem. Phys. Lett. 52, 473-475 (1977).
71. G. Magerl, J. M. Frye, W. A. Kreiner, and T. Oka, Appl. Phys. Lett. 42, 656-659 (1983).
72. N. McAvoy, J. Osmundson, and G. Schiffner, Appl. Opt. 11, 473-474 (1972).
73. S. Namba, J. Opt. Soc. Amer. 51, 76-79 (1961).
74. I. P. Kaminow and J. Liu, Proc. IEEE. 51, 132-136 (1963).
75. D. Statrud and F. C. Delucia, private communication.
76. L. D. G. Young and A. T. Young, J. Quant. Spectrosc. Radiat. Transfer 20, 533-537 (1978).
77. M. Mizushima, "The Theory of Rotating Diatomic Molecules", Wiley, New York, NY, 1982, p. 282.
78. A. V. Burenin and Vl. G. Tyuterev, J. Mol. Spectrosc. 108, 153-154 (1984).
79. J. K. G. Watson, J. Mol. Spectrosc. 103, 350-363 (1984).
80. J. K. G. Watson, S. C. Foster, A. R. W. Mckellar, P. Bernath, T. Amano, F. S. Pan, M. W. Crofton, R. S. Altman, and T. Oka, Can. J. Phys. 62, 1875-1885 (1984).
81. F. R. Peterson, E. C. Beaty, and C. R. Pollock, J. Mol. Spectrosc. 102, 112-122 (1983).
82. B. G. Whitford, K. J. Siemsen, H. D. Riccius, and G. R. Hanes, Opt. Commun. 14, 70-74 (1975).
83. C. Freed, L. C. Bradley, and R. G. O'Donnell, IEEE J. Quantum Electron. QE-16, 1195-1206 (1980).

- PART III -

INFRARED-INFRARED DOUBLE RESONANCE OF $^{13}\text{CH}_3\text{F}$
BY MEANS OF A WAVEGUIDE CO_2 LASER
AND AN INFRARED-MICROWAVE SIDEBAND LASER

CHAPTER I

INTRODUCTION

A molecule in a quantum state Φ collides with another molecule and changes its quantum state to Φ' . For most molecules at room temperature, the energy transfer may be characterized as being between vibration and rotation (V - R), between vibration and translation (V - T), between rotation and translation (R - T), between vibration and vibration (V - V), between rotation and rotation (R - R), and between translation and translation (T - T). Normally, the R - R processes have the highest rate constants with V - R and V - V processes being much slower. The experiments to be described in this section provide information about the relative rates of the various modes of energy transfer.

Since the molecular interaction is a result of collision, the rates of energy transfer provide information about the mechanism of the collision process.

In discussing the theoretical treatment of the collision process, we usually introduce the concept of strong and weak collisions. This is because, contrary to the situation for a radiative interaction in which the energy of interaction is much smaller than the energy spacing, a collision interaction has a wide range of energy values. For a limiting case of weak collisions, in which the intermolecular interaction is small and of long range, a

perturbation technique for the rotational energy changes can be used to a good approximation. For such collisions, the conversion from rotational energy to translational energy is small and the molecular path is not deflected significantly. Most of the $\text{NH}_3 - \text{NH}_3$ collisions at room temperature are examples of weak collisions(1). Also, when the interaction is weak, a molecule in a certain initial level has appreciable transition probabilities to only a few levels, and the selection rules can be understood by using the known symmetry properties of the long range potential.

For strong collisions, for which the energy of interaction is larger than the rotational energy spacing, the molecular path is deflected by a large angle, and a molecule has transition probabilities to many rotational levels. For such collisions, no selection rules can be established. In reality, however, most collisions lie in a difficult region between these two extreme cases.

For the study of collision processes, three experimental methods - molecular beams, optical fluorescence, and double resonance have been developed and used widely for the last two decades. In these methods a known non-Boltzmann distribution is established in some molecular levels of a gas at low pressure, and the consequence of collisions is obtained by monitoring populations of molecules in other levels.

In the molecular beam method(2), a beam of molecules

in a single rotational level is selected by an inhomogeneous electric field and, after passing through a region in which collisions occur, is analyzed by a second state selector. The advantage of this method is that the analysis of the results gives a single transition probability directly, and, further, it is possible to control the relative angle and velocity of the collision partners. The application of this method has been limited by the experimental difficulties. However, with the advance of molecular beam technique, this method may become a powerful tool for the study of collisions.

In the optical fluorescence method(3), the molecules are pumped by monochromatic radiation into a single rotational level in an excited electronic or vibrational state and collision-induced rotational transitions in the excited state are detected in the fluorescence spectrum. So far, these experiments have been done by using accidental coincidences between the exciting radiation and the molecular absorption lines, but this method may become more generally applicable by using tunable lasers. One limitation of this method is that the lifetime of the excited state, which cannot be controlled, has to be of the order of collision time.

The double resonance method uses two resonant one-photon interactions in a single molecule to probe molecular structure and relaxation properties. Figure 1 shows energy

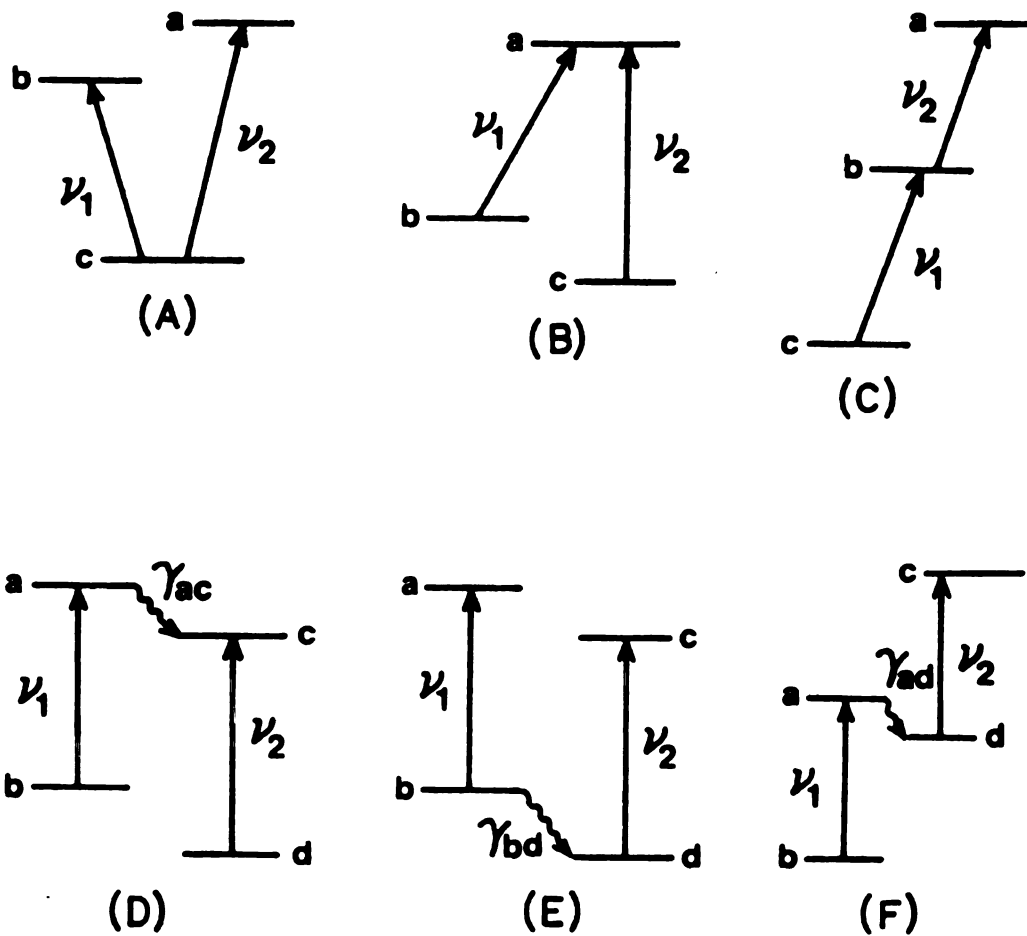


Figure 1. Diagrammatic representations of three-level double resonance spectroscopy (A)-(C) and four-level double resonance spectroscopy (D)-(F).

level diagrams for several kinds of double resonance.

The fundamental double resonance process is that of three-level double resonance, in which fields at two different frequencies, ν_1 and ν_2 , couple a given molecular energy level to two other levels. The common level may be either lower in energy than the other two, as in Fig. 1(A), higher than the other two, as in Fig. 1(B), or intermediate in energy, as in Fig. 1(C). A second process is four-level double resonance, in which the two radiation fields probe pairs of levels not having a level in common. For this kind of double resonance to occur, at least one level in each of the two pairs must be coupled to the other by collisional or other relaxation processes. This can occur by relaxation in the excited state, Fig. 1(D), in the ground state, Fig. 1(E), or both. Another variant is shown in Fig. 1(F), in which relaxation occurs to an intermediate level d.

Figure 2 shows several kinds of pumping and monitoring schemes in four-level double resonance. Figure 2(A) is an energy diagram for microwave-microwave double resonance, in which strong and weak microwave fields are used for the pumping and probing radiation sources, respectively. The ease of handling microwave radiation has made this method widely applicable to many rotational levels of simple polyatomic molecule. Since the non-Boltzmann distribution is introduced into two rotational levels rather than in one level, the interpretation of the results is more complicated

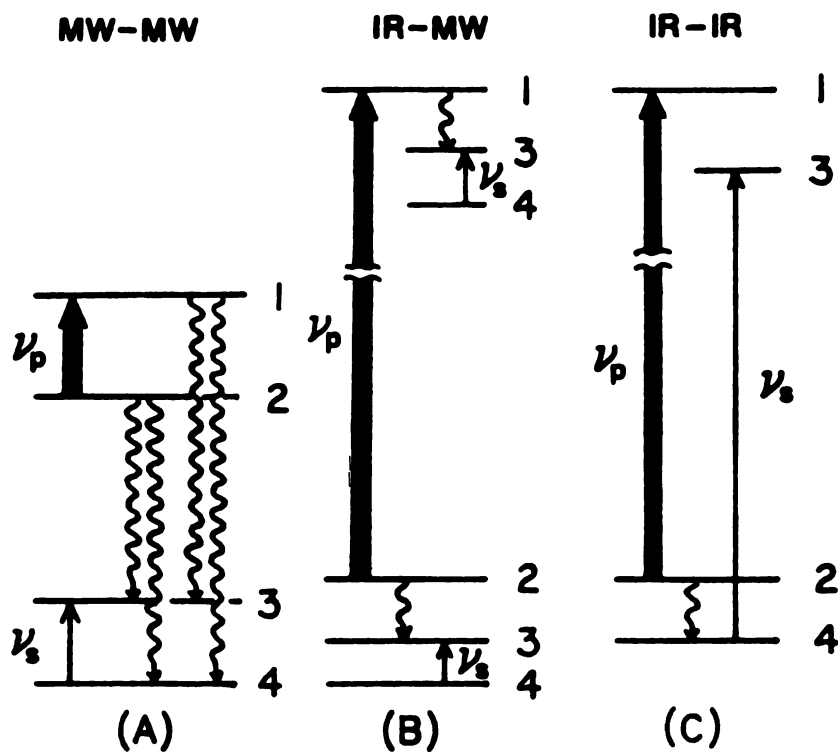


Figure 2. Energy level schemes in four-level double resonance experiments. The light and heavy arrows represent low and high power radiation, respectively. The wavy arrows represent paths of collisional energy transfer.

than for other methods. Nevertheless, most of our information about selection rules for collision processes has been obtained by this technique(1).

The infrared-microwave double resonance, Fig. 2(B) has usually used strong infrared and weak microwave radiation sources for the pumping and probing fields, respectively. This method has been widely used for the measurement of rotational frequencies and relaxation rates in the excited state because a large non-Boltzmann distribution is introduced in a single rotational level in an excited vibrational state by the infrared pumping. However, in most cases of infrared pumping, it has been necessary to rely on an accidental coincidence between a fixed frequency laser and the frequency of a molecular transition. Infrared-infrared double resonance of the type shown in Fig. 2(C) is even more difficult because it is necessary to rely on a double coincidence, in which strong infrared and weak infrared radiations are used for pumping and probing sources, respectively. Since in most cases the infrared source for pumping is a coherent radiation with a very narrow bandwidth, the molecules with a particular velocity component are depleted from the pumped level, that is, a hole is "burned" in the Doppler profile of the molecular absorption(1,4,5), as in Fig. 3.

The first true double resonance was performed by Brossel and Bitter(6) in 1952. They used a mercury

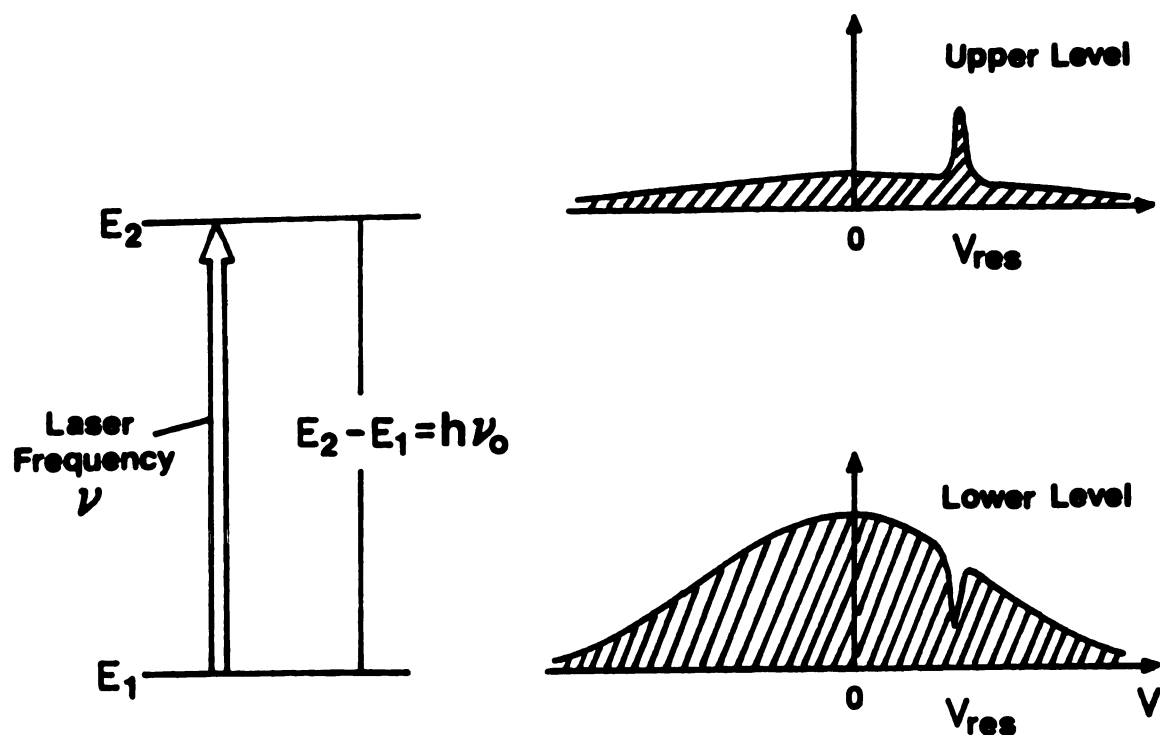


Figure 3. Change in the particle velocity distribution over two-levels of transition under the action of a laser wave of frequency ν . The z-component of velocity of particles interacting with the light wave is $v_{res} = c(\nu - \nu_0)/\nu_0$.

resonance lamp to excite mercury atoms which were simultaneously subjected to a radiofrequency field. Double resonance as a general technique in molecular spectroscopy was first realized in the microwave spectroscopy of rotational levels by E. B. Wilson's group at Harvard University(7-11) and by T. Oka at the National Research Council of Canada(12-20). With the introduction of the laser, it became possible to extend these techniques to the infrared and optical regions of the spectrum. For most infrared-microwave double resonance experiments(21-37), coherent gas lasers in the 10 μm region, such as CO_2 and N_2O lasers, have been used for the pumping source. It would be very useful to be able to extend these techniques to a wide range of rotational energy levels in different vibrational states. Such studies would greatly increase our knowledge of molecular structure and the mechanism of collisional interaction.

Until 1970, a true infrared-infrared double resonance experiment had not been done because of the limitation on the availability of a tunable infrared laser for the probing source. Rhodes et al.(38) had earlier tried to measure a collisional relaxation rate by using two fixed frequency CO_2 lasers for pumping and probing sources on CO_2 molecules.

In the early 1970's, Luntz, working in Brewer's laboratory(39-42), exploited the nonlinear behavior in three-level systems, which was originally worked out by

Schlossberg and Javan(43), to study double resonance in a molecular system. In these experiments, two laser radiations with slightly different frequencies were used in the presence of D.C. Stark field to measure the Stark shifts with high accuracy. At about the same time, Steinfeld and his collaborators(44-47) and Preses and Flynn(48) measured the vibrational relaxation by monitoring the population change due to pumping in SF_6 , BCl_3 , and CH_3F molecules, respectively.

In order to increase the tunability of an infrared source, Freund et al.(49) introduced the two-photon technique into infrared-infrared double resonance by carrying out a four-level double resonance experiment on $^{15}\text{NH}_3$. From this experiment, they observed not only the non-Boltzmann distribution, but also the hole being transferred to the signal levels. Shoemaker et al.(50,51) observed the same phenomenon in $^{13}\text{CH}_3\text{F}$, by using two fixed-frequency CO_2 lasers and a D.C. Stark field.

Although the two-photon technique has a wide range of tunability, the transition intensity is much weaker than that of one-photon spectroscopy, especially for the case of a large difference between the laser frequency and the one-photon allowed molecular transition(52). So, Orr and Oka(53,54) developed an infrared-infrared double resonance technique that employed the sidebands generated by passing CO_2 laser radiation through an electro-optic modulator

driven by the combination of a radiofrequency and a D.C. Stark field. With this technique they could accurately measure the dipole moment for several symmetric top molecules. With the same method, Duxbury et al.(55,56) used isotopic CO_2 laser radiation to measure the dipole moment of CH_3F and its isotopes, Weber and Terhune(57) extended the infrared-infrared double resonance technique into the $6\text{ }\mu\text{m}$ wavelength region by employing a CO laser as the pumping source and a tunable diode laser as the probing source. By using two laser sources in different frequency regions, they were able to see the double resonance effect in three different vibrational states in the NH_3 molecule. Recently, another infrared-infrared double resonance experiment on vibrational energy transfer between $^{15}\text{NH}_3$ and $^{14}\text{NH}_3$ was done by Kuze et al.(58) by means of a CO_2 and a tunable diode laser as pumping and probing sources, respectively. From the analysis of the experimental results, a preference for dipole-allowed ($\Delta J = 0, \pm 1, \Delta K = 0$) transitions and a prohibition of ortho-para conversion were confirmed, which is in agreement with the previous studies by microwave-microwave double resonance(16) and by infrared-microwave double resonance(37,59).

The study of vibrational energy transfer is also very important to understanding the collisional process and its elementary mechanisms. Preses and Flynn(60) used an infrared-infrared double resonance technique to study the

vibration-vibration energy transfer between $^{12}\text{CH}_3\text{F}$ and $^{13}\text{CH}_3\text{F}$ with two-fixed frequency CO_2 lasers operating on different laser lines. The analysis of the experimental results showed that one quantum of ν_3 energy is transferred between $^{12}\text{CH}_3\text{F}$ and $^{13}\text{CH}_3\text{F}$ in every six collisions.

In the study to be described in this thesis, a waveguide CO_2 laser and an infrared-microwave sideband laser were applied for the first time to infrared-infrared double resonance as pumping and probing radiation sources, respectively. The sample was $^{13}\text{CH}_3\text{F}$ and many kinds of three-level and four-level double resonance experiments were carried out. The results of the three-level double resonance measurements are in good agreement with the previous studies. However, four-level double resonance showed the evidence of indirect pumping to all rotational energy levels in the first excited state ($\nu_3 = 1$), which is extremely useful for identification as well as observation of hot bands.

The next chapter gives the theoretical background of saturation effects and double resonance. Chapter III provides an explanation of experimental details which is similar to that in the second part of this thesis. Finally, Chapter IV describes the experimental results and presents an analysis of the results and several spectra.

CHAPTER II

THEORY

Saturation Process(62)

When a molecular transition is subjected to high intensity radiation, the fraction of light absorbed by the molecule becomes less than that for low intensity light, that is, the absorption coefficient appears to saturate.

Consider a two-level system, with states 1 and 2 coupled by electric-dipole radiation:

$$H = H_0 - \mu_{12} \epsilon \cos \omega t \quad (1)$$

where μ_{12} is the dipole moment matrix element between states 1 and 2, ω is the frequency of the radiation, and ϵ is the amplitude of radiation field. Let the quantum mechanical amplitude of the upper state be a_2 , and that of the lower state be a_1 . Then

$$\begin{aligned} \frac{da_1}{dt} &= \frac{i}{2} \kappa \epsilon a_2 \left[e^{i(\omega - \omega_0)t} + e^{-i(\omega + \omega_0)t} \right] \\ \frac{da_2}{dt} &= \frac{i}{2} \kappa \epsilon a_1 \left[e^{i(\omega - \omega_0)t} + e^{-i(\omega + \omega_0)t} \right] \end{aligned} \quad (2)$$

where $\kappa = \mu_{12}/\hbar$ and $\omega_0 = (E_1 - E_2)/\hbar$. As long as the Rabi

frequency $\omega_1 = \kappa\epsilon \ll \omega_0$, we may neglect the high frequency terms (rotating wave approximation) to give

$$\frac{d^2 a_2}{dt^2} + i(\omega - \omega_0) \frac{da_2}{dt} + \frac{(\kappa\epsilon)^2}{4} a_2 = 0 \quad (3)$$

The solution to Eq. (3) is

$$a_2(t) = e^{-i\Delta t/2} (A e^{i\Omega t/2} + B e^{-i\Omega t/2}) \quad (4)$$

and

$$a_1(t) = -\frac{1}{\kappa\epsilon} e^{i\Delta t/2} [(\Delta - \Omega) A e^{i\Omega t/2} + (\Delta + \Omega) B e^{-i\Omega t/2}] \quad (5)$$

where $\Delta = \omega - \omega_0$ and $\Omega = [\Delta^2 + (\kappa\epsilon)^2]^{1/2}$.

Let us assume the initial conditions $a_1(t_0) = e^{i\theta}$ and $a_2(t_0) = 0$. This gives the coefficients

$$a_1(t) = e^{[i\theta + i\Delta(t-t_0)]/2} \left[\cos \frac{\Omega}{2}(t-t_0) - i \frac{\Delta}{\Omega} \sin \frac{\Omega}{2}(t-t_0) \right] \quad (6)$$

and

$$a_2(t) = i \frac{\kappa\epsilon}{\Omega} e^{[i\theta - i\Delta(t-t_0)]/2} \sin \frac{\Omega}{2}(t-t_0) \quad (7)$$

The corresponding expressions for the populations are

$$n_1(t) = |a_1(t)|^2 = \frac{\Delta^2}{\Omega^2} + \frac{(\kappa\epsilon)^2}{\Omega^2} \cos^2 \frac{\Omega}{2}(t-t_0) \quad (8)$$

and

$$n_2(t) = |a_2(t)|^2 = \frac{(\kappa\epsilon)^2}{\Omega^2} \sin^2 \frac{\Omega}{2}(t-t_0) \quad (9)$$

Figure 4 shows the population variation of the excited state subjected to a coherent dipole perturbation.

The effect of collisions can be incorporated in this treatment by averaging Eq. (9) over a Poisson distribution of dephasing collisions with characteristic time T_2' ;

$$dn_2(t) = \frac{1}{T_2'} e^{-(t-t_0)/T_2'} dt \quad (10)$$

to give

$$\begin{aligned} \langle |a_2|^2 \rangle_{av} &= \frac{1}{T_2'} \int_{-\infty}^t |a_2(t, t_0)|^2 e^{-(t-t_0)/T_2'} dt_0 \\ &= \frac{1}{2} \frac{(\kappa\epsilon)^2}{(\omega-\omega_0)^2 + (1/T_2')^2 + (\kappa\epsilon)^2} \quad (11) \end{aligned}$$

This expression indicates that the line shape is that of a Lorentzian, modified by power broadening proportional to ϵ^2 , the intensity of the radiation field. Also this equation

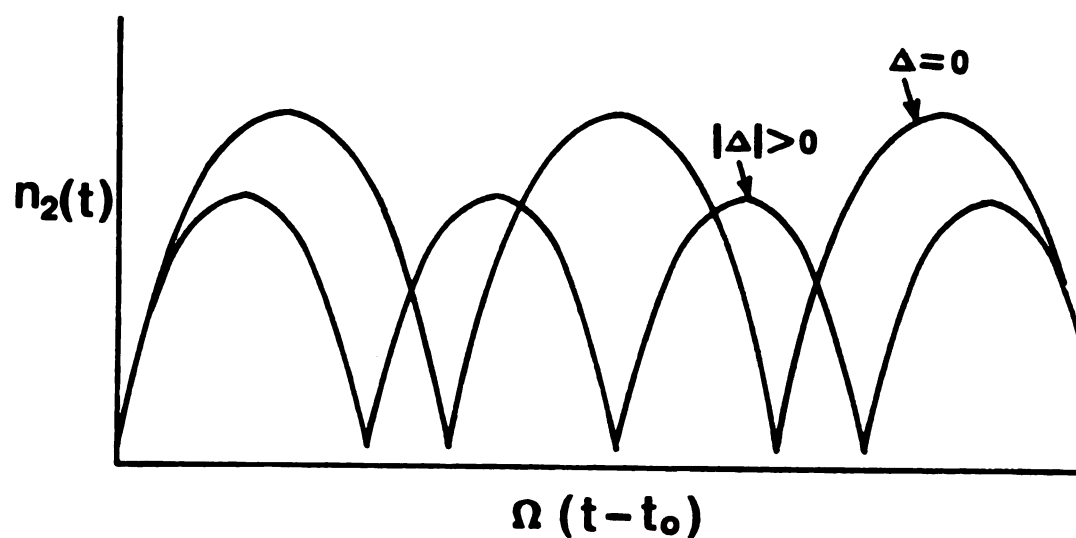


Figure 4. Time evolution of the population of the excited state of a two-level system subjected to a coherent dipole perturbation. On-resonance pumping ($\Delta = 0$) results in the slowest oscillations having the greatest amplitude.

shows that a very intense field will eventually equalize populations between upper and lower levels of a transition because $\langle |a_2|^2 \rangle_{av} \rightarrow 0.5$ as $\epsilon \rightarrow \infty$.

The power absorbed, which is the observable in this system, can be written as

$$\Delta P = \frac{dw}{dt} = \frac{N_1 - N_2}{2T_2'} \frac{\hbar\omega(\kappa\epsilon)^2}{(\omega - \omega_0)^2 + (1/T_2')^2 + (\kappa\epsilon)^2} \quad (12)$$

Here N_1 and N_2 are the equilibrium populations of states 1 and 2, respectively. As $\epsilon \rightarrow \infty$, ΔP becomes a constant. Thus, the absorption coefficient,

$$\begin{aligned} \alpha = \frac{\Delta P}{P} &= \frac{\Delta P}{c|\epsilon|^2/8\pi} \\ &= \frac{N_1 - N_2}{T_2'} \frac{4\pi\mu_{12}^2\omega}{c\hbar[(\omega - \omega_0)^2 + (1/T_2')^2 + (\kappa\epsilon)^2]} \end{aligned} \quad (13)$$

approaches zero and the medium saturates.

Figure 3 shows the particle velocity distribution in the two levels of a transition subjected to a laser wave of frequency ν , in which the laser light is intense enough to stimulate transitions of a considerable proportion of the molecules to an excited state. The excitation of particles with a certain velocity (v_{res}) changes the equilibrium distribution of particle velocities in each level of the

transition. In the lower level there is a lack of particles whose velocity complies with the resonance condition, that is, a hole in the velocity distribution. By contrast, in the upper level there is an excess of particles with resonance velocities, or a peak in the velocity distribution. The hole depth and the peak height depend on the degree of absorption saturation by the radiation field.

With a single propagating field, there will be no appearance of a Doppler free resonance as the frequency is tuned across the transition. The nonlinear dependence on the intensity of the strong (pumping) radiation requires a second transition to appear as a change in absorption coefficient of the weak (probing) radiation.

Let us assume a pumping radiation at a fixed frequency ω , saturating the Doppler broadened resonance, and the direction of propagation to be the $+z$ direction. Also, we assume that a probing radiation at the frequency ω_p is propagating in the opposite direction of the strong radiation at the same time. This is the actual experimental scheme for most double resonance studies as shown in Fig. 5.

For molecules with a velocity component $v_z = v$, the frequency of the intense field at the molecules will be Doppler shifted to $\omega \rightarrow \omega(1 - v/c)$. The weak probe field, however, will be Doppler shifted to $\omega_p \rightarrow \omega_p(1 + v/c)$. Therefore, if $v > 0$, the intense field will be down-shifted in frequency, but the weak field will be up-shifted.

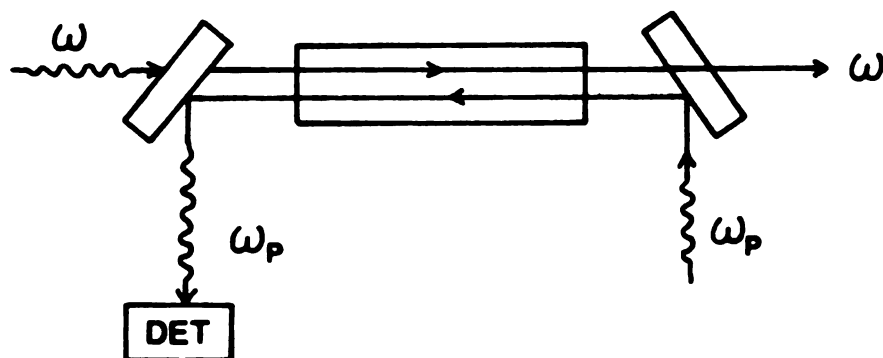


Figure 5. Schematic arrangement of pumping and probing radiation in many infrared-infrared double resonance experiments.

Consider the absorption of the probe field in the presence of an intense field at a fixed frequency ω . The change in radiation power δI_p due to molecules with a velocity v in a narrow range dv is given by (63)

$$\delta I_p = (dn_1 - dn_2) \hbar \omega_p R(\omega_p) \quad (14)$$

where $(dn_1 - dn_2)$ is the change in the population difference between two states 1 and 2 over velocity distribution range dv , and $R(\omega_p)$ is the transition rate induced by the probing field. Here, $R(\omega_p)$ has the following form

$$R(\omega_p) = \frac{\frac{1}{2} \left(\frac{\nu_{12} \epsilon^0}{\hbar} \right)^2 T}{[\omega_p (1 + \frac{v}{c}) - \omega_0]^2 T^2 + 1} \quad (15)$$

Thus, the probe field will show a Lorentz shaped resonance at $\omega_p = \omega_0 / (1 + v/c)$.

Double Resonance in a Three-Level System

Double resonance in a three-level system, as shown in Fig. 1(A)-(C), means that two transitions induced by strong and weak fields share a common level. Consider a three-level system of the type shown in Fig. 1(B), and let a_1 , a_2 ,

and a_3 be the quantum mechanical amplitudes of the states c , b , and a , respectively. Suppose that a strong field ϵ_p at frequency ω_p is applied close to the transition frequency $\omega_{31} = \omega_{ac}$, and a weak field ϵ is applied at frequency ω close to $\omega_{32} = \omega_{ab}$. The equations of motion for the amplitudes are then

$$\frac{da_1}{dt} = \frac{i}{2} \kappa_p \epsilon_p a_3 e^{i(\omega_p - \omega_{31})t} \quad (16)$$

$$\frac{da_2}{dt} = \frac{i}{2} \kappa \epsilon a_3 e^{i(\omega - \omega_{32})t} \quad (17)$$

$$\frac{da_3}{dt} = \frac{i}{2} [\kappa_p \epsilon_p a_1 e^{-i(\omega_p - \omega_{31})t} + \kappa a_2 e^{-i(\omega - \omega_{32})t}] \quad (18)$$

with $\kappa_p = 2\nu_{13}/\hbar$ and $\kappa = 2\nu_{23}/\hbar$. Let us impose the initial conditions $a_1(t_0) = e^{i\theta}$, $a_2(t_0) = a_3(t_0) = 0$. The steady state solution for ϵ_p and ϵ being constant may be found by setting $da_1/dt = 0$, yielding

$$\begin{aligned} a_1(t) &= A_1 e^{i(\omega_p - \omega_{31} - \lambda)t} \\ a_2(t) &= A_2 e^{i(\omega - \omega_{32} - \lambda)t} \\ a_3(t) &= A_3 e^{-i\lambda t} \end{aligned} \quad (19)$$

where

$$\lambda^3 - (\omega_p - \omega_{31} + \omega - \omega_{32})\lambda^2 + [(\omega_p - \omega_{31})(\omega - \omega_{32}) - (\kappa_p \epsilon_p)^2 - (\kappa \epsilon)^2]\lambda + (\kappa_p \epsilon_p)(\omega - \omega_{32}) + (\kappa \epsilon)(\omega_p - \omega_{31}) = 0 \quad (20)$$

The complicated cubic expression for λ can be solved approximately by recognizing that $\epsilon_p \gg \epsilon$ in typical experiments. We then find that

$$a_{13}(t) = i \frac{\kappa_p \epsilon_p}{\Omega_p} e^{i\omega - i(\omega_p - \omega_{31})(t+t_0)/2} \sin \frac{\Omega_p(t-t_0)}{2} \quad (21)$$

where $\Omega_p = [(\omega_p - \omega_{31})^2 + (\kappa_p \epsilon_p)^2]^{1/2}$ and

$$a_{12}(t) = \frac{\kappa \epsilon \kappa_p \epsilon_p}{2\Omega_p} \exp\left\{i\omega \left[\frac{e^{i(\Omega_p + \delta)(t-t_0)} - 1}{\Omega_p + \delta} - \frac{e^{-i(\Omega_p - \delta)(t-t_0)} - 1}{\Omega_p - \delta} \right]\right\} \quad (22)$$

where $\delta = 2(\omega - \omega_{32}) - (\omega - \omega_{31})$.

CHAPTER III

EXPERIMENT

Figure 6 shows the experimental diagram for the infrared-infrared double resonance studies described in this research. A waveguide CO₂ laser (Laakmann Electro-Optics Inc. Model RFG 88-S) and a microwave feedback controlled infrared-microwave sideband laser system were used for the pumping and the probing radiation sources, respectively. The system for the probing radiation was explained in detail in Chapter IV of the second part of this thesis. However, the sample cell was slightly modified to prevent the reflection of the pumping radiation from the window of sample cell to the detector. In order to do this, the NaCl window was sealed at the slant angle, in which the angle of window was rotated to let the probing radiation transmit more favorably. The pumping radiation, whose polarization was perpendicular to that of the probing beam, passed through the sample cell after reflection by the beam splitter.

In this experiment, the frequency of the pumping radiation was locked by means of its internal pyroelectric detector stabilizing system. The amplitude of the frequency modulation required for this stabilization was minimized to keep the fluctuation of the frequency of the pumping laser as small as possible.

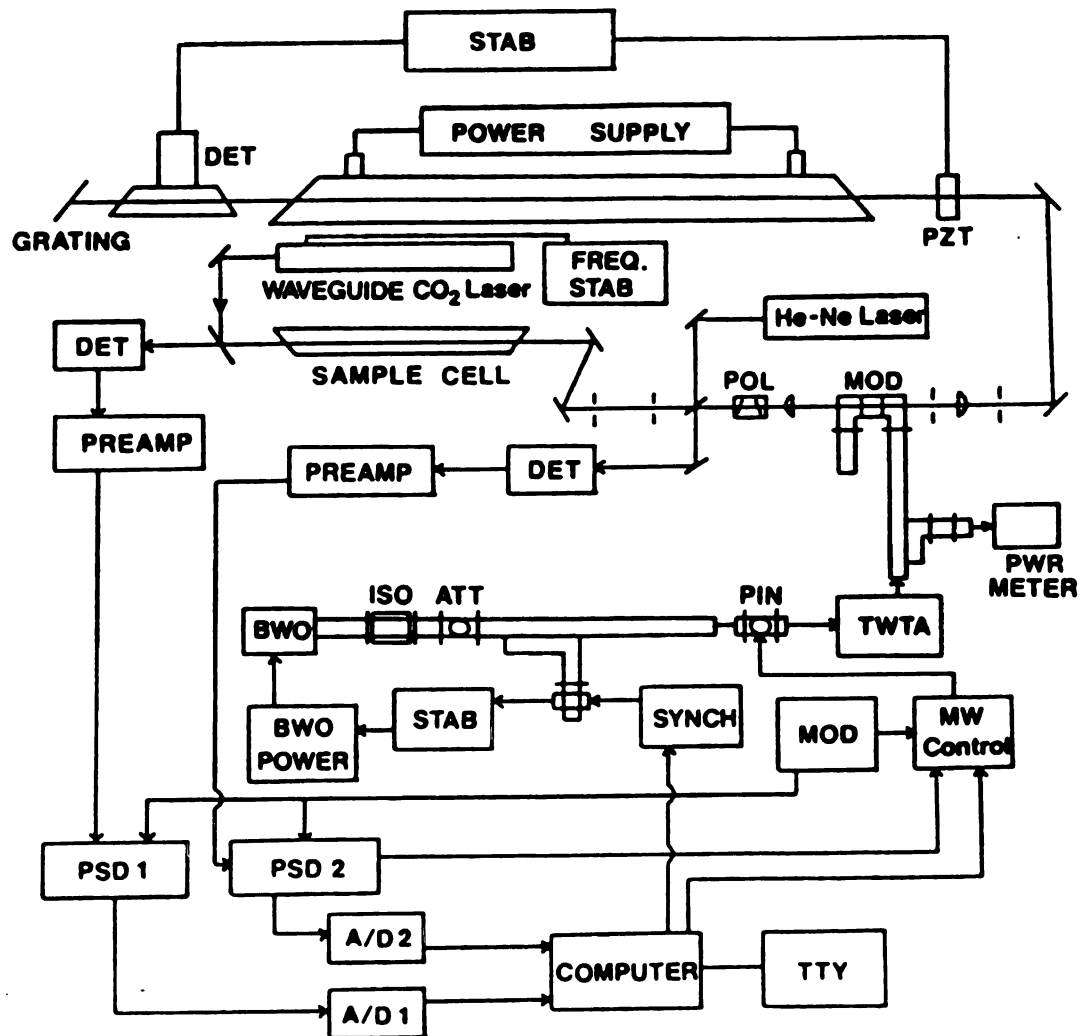


Figure 6. Experimental diagram of infrared-infrared double resonance by means of a waveguide CO₂ laser for pumping and an infrared-microwave sideband laser for probing.

Waveguide CO₂ Laser

As a result of molecular collision broadening, it has been possible to increase the tunability of the frequency of a gas laser by developing small, high pressure, and sealed-off waveguide CO₂ lasers. Since the CO₂ Doppler full width at half maximum at 300 °K is approximately 50 MHz and the collision broadening is ~5.3 MHz/Torr(65), collision broadening will dominate the lineshape for operating pressures greater than about 10 Torr. At pressures above several hundred Torr, it is theoretically possible to increase the tunable range of a CO₂ laser to several GHz. For most gas lasers, the electron temperature, and hence the characteristics of the discharge tube diameter are determined by the product of the pressure and the discharge tube diameter, so by going to small diameter tubes one can increase the pressure and still obtain high gain performance. These arguments led to the development of the waveguide CO₂ laser(65,66), in which the discharge is contained in a hollow dielectric waveguide with an inside diameter of a millimeter or less.

Since the individual vibration-rotation lines of CO₂ in the ~10 μm region are separated by 1 to 2 cm⁻¹, pressures of about 10 atm. are necessary to provide adequate overlap for continuous tuning. But it is difficult to obtain population inversion and gain in this pressure region, and

when laser action can be achieved the linewidths tend to be the order of a few tenths of a cm^{-1} .

Figure 7 shows a composite metal-ceramic waveguide laser structure, in which the tube is surrounded by two ceramic plates which are separated by precisely formed metal electrodes. The gas mixture in this small tube is RF-excited. The laser tube is bonded into a hermetically sealed aluminium tube and support structure, which also functions as the gas reservoir. The end mirror is mounted at the output end of the laser to seal the system, and a grating is placed inside the vacuum envelope at the other end. A single micrometer control allows the grating to rotate for tuning the system over a wide range of laser lines without causing any severe problem in optical alignment.

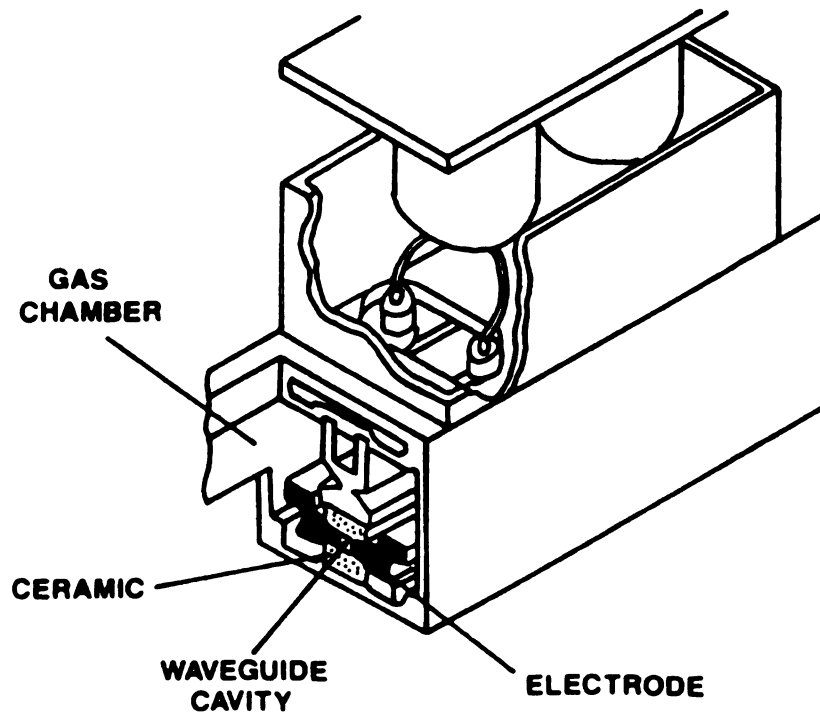


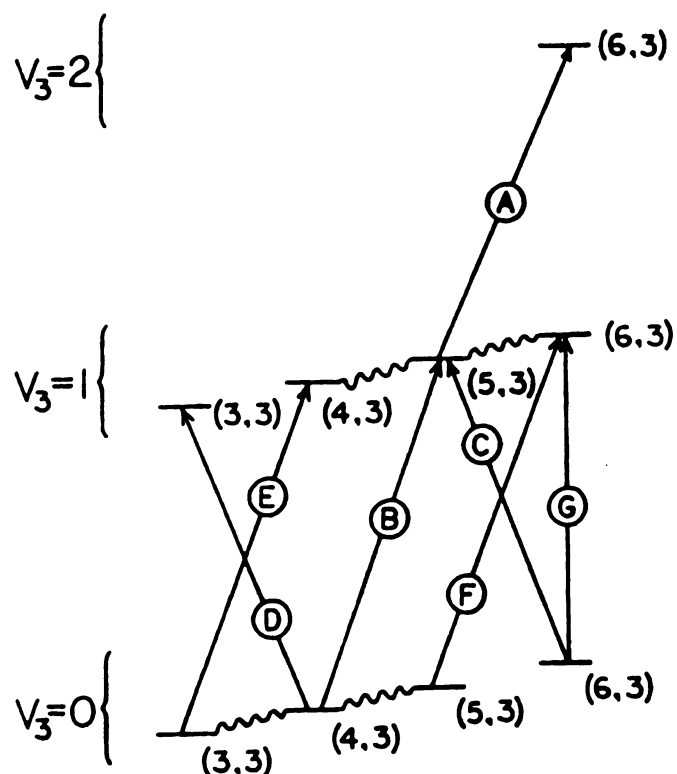
Figure 7. Cross sectional view of the waveguide CO₂ laser used for this experiment.

CHAPTER IV

RESULTS AND DISCUSSION

For an infrared-infrared double resonance experiment, a waveguide CO_2 laser and an infrared-microwave sideband laser were used for pumping and probing radiation sources, respectively. Figure 8 shows the energy level diagram for three-level double resonances within the tunable range of the sideband system, in which a microwave oscillator was swept from 8.2 to 18.0 GHz for each CO_2 laser line. The 'famous' $9\text{P}(32)\text{CO}_2$ laser line of the waveguide CO_2 laser was used for a pumping source because the frequency of the $^{\text{Q}}\text{R}(4,3)$ molecular transition of the ν_3 band of $^{13}\text{CH}_3\text{F}$ is just 25.8 MHz below the laser frequency. Within the tunability of the sideband system, three kinds of three-level double resonances could be observed, all of which involved pumping the $^{\text{Q}}\text{R}(4,3)$ transition (B in Fig. 8). The signal transitions were A (intermediate common level), C (upper common level), and D (lower common level). In addition, two four-level double resonance experiments (combinations of B and E and B and F) were performed without observing any significant pumping effect, in agreement with the selection rules ($\Delta K = 0$) for a collisional process.

Since many transitions in the $2\nu_3 + \nu_3$ band of $^{13}\text{CH}_3\text{F}$ could be observed by using the infrared-microwave sideband system(61), it was possible to observe many four-level



- A : R (5,3) 9P(46)+15393.5 MHz
 B : R (4,3) 9P(32)-25.8 : Pumping
 C : P (6,3) 9P(50)+15354.2
 D : P (4,3) 9P(46)-9468.1
 E : R (3,3) 9P(34)+13012.2
 F : R (5,3) 9P(30)-12954.9
 G : Q (6,3) 9P(40)-9860.7

Figure 8. Energy level diagrams for the waveguide CO_2 laser and infrared-microwave sideband laser system used for infrared-infrared double resonance in $^{13}\text{CH}_3\text{F}$ in this work.

double resonances that were apparently the result of cascading collisional processes(67) or of vibration-vibration energy transfer(60).

We concluded from these preliminary experiments that a waveguide CO₂ laser and infrared-microwave sideband laser system is a very useful combination for infrared-infrared double resonance, at least for the pumping of a single transition and the observation of a variety of double resonances.

With the experimental diagram shown in Fig. 6, in which the pumping and probing beams travel in opposite directions, the sum of two laser frequencies at resonance in a three-level experiment should be equal to the sum of the frequencies of the two molecular transitions, irrespective of the molecular velocity components; that is,

$$\omega_{\text{pump}} + \omega_{\text{probe}} = \omega_0^{\text{pump}} + \omega_0^{\text{probe}} = \text{constant} . \quad (24)$$

Figure 9 shows the variation in frequency of the pumped molecular velocity group with pumping frequency for a three-level double resonance (combination of B and A). The spectra shown were obtained by probing transition A with the positive sideband generated by combination of the 9P(46)CO₂ laser line and P-band microwave radiation. Each time the pumping frequency is changed, the laser pumps a different velocity group. The saturation effect of one particular

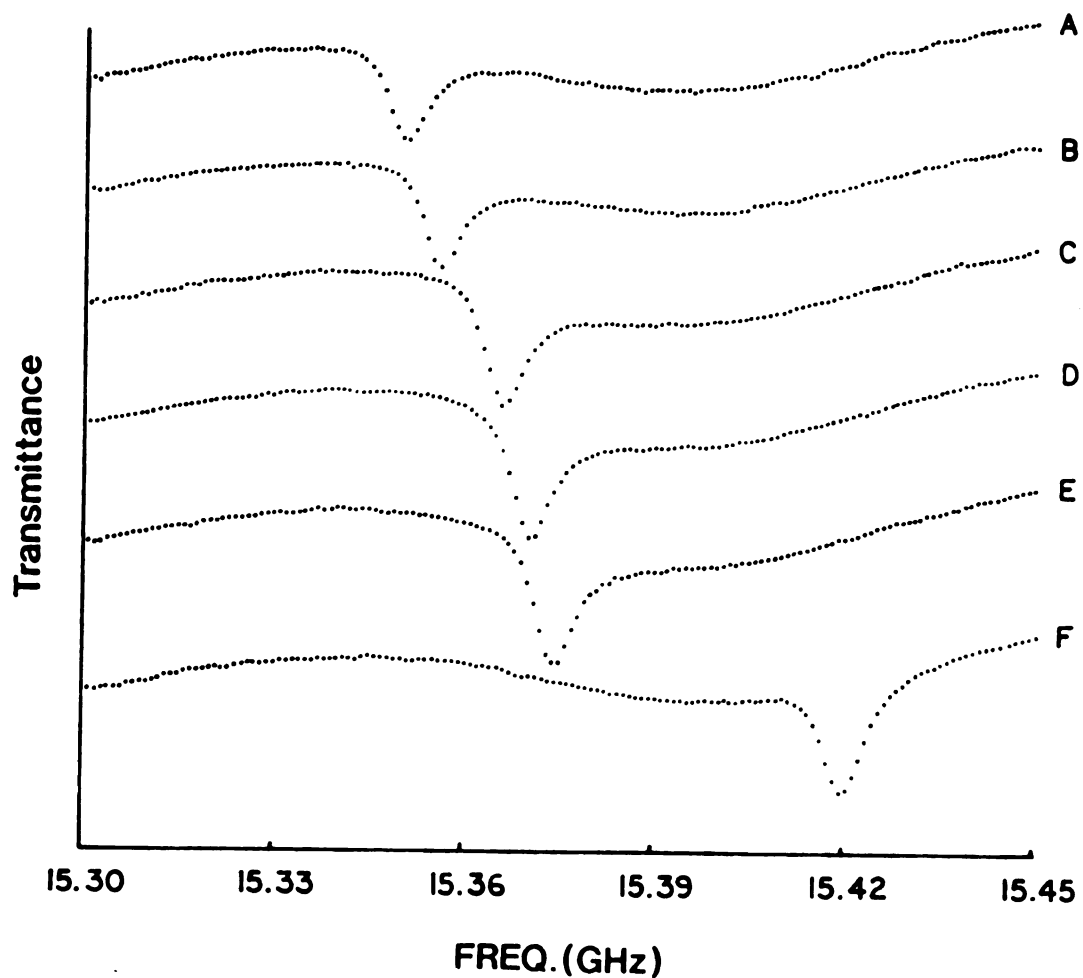


Figure 9. Variation of the position of the pumped molecular velocity group with pumping frequency. The transition is $Q_{R(5,3)}$ of the $2\nu_3 - \nu_3$ band of $^{13}\text{CH}_3\text{F}$. The $Q_{R(4,3)}$ transition of the ν_3 band was pumped at a different frequency for each the spectra A-F.

velocity group in the upper state was monitored by a weak probe field. The increased population for a small range of velocity is shown in the spectra. From this kind of variation, the tunability of the waveguide CO_2 laser could be determined to be greater than 110 MHz, which is a reasonable value considering the CO_2 pressure broadening.

One of the advantages of infrared pumping is to transfer only the molecular velocity group which is in resonance with the laser frequency. Since the waveguide CO_2 laser was frequency modulated for stabilization purposes, actually a range of velocity groups was pumped. By increasing the modulation amplitude the range of velocities pumped could be increased. Figure 10 shows the variation of the width of the molecular velocity group pumped with modulation amplitude. For this spectrum, the positive sideband generated from the $9\text{P}(46)\text{CO}_2$ laser line and P-band microwave radiation was used at ~ 108 mTorr of sample pressure. The $^Q\text{R}(4,3)$ transition in the ν_3 band was pumped and the $^Q\text{R}(5,3)$ transition in the $2\nu_3 + \nu_3$ band was probed. From these spectra, the need for a highly stable pumping laser was confirmed to study the velocity preserving collisional process.

Three-Level Double Resonance

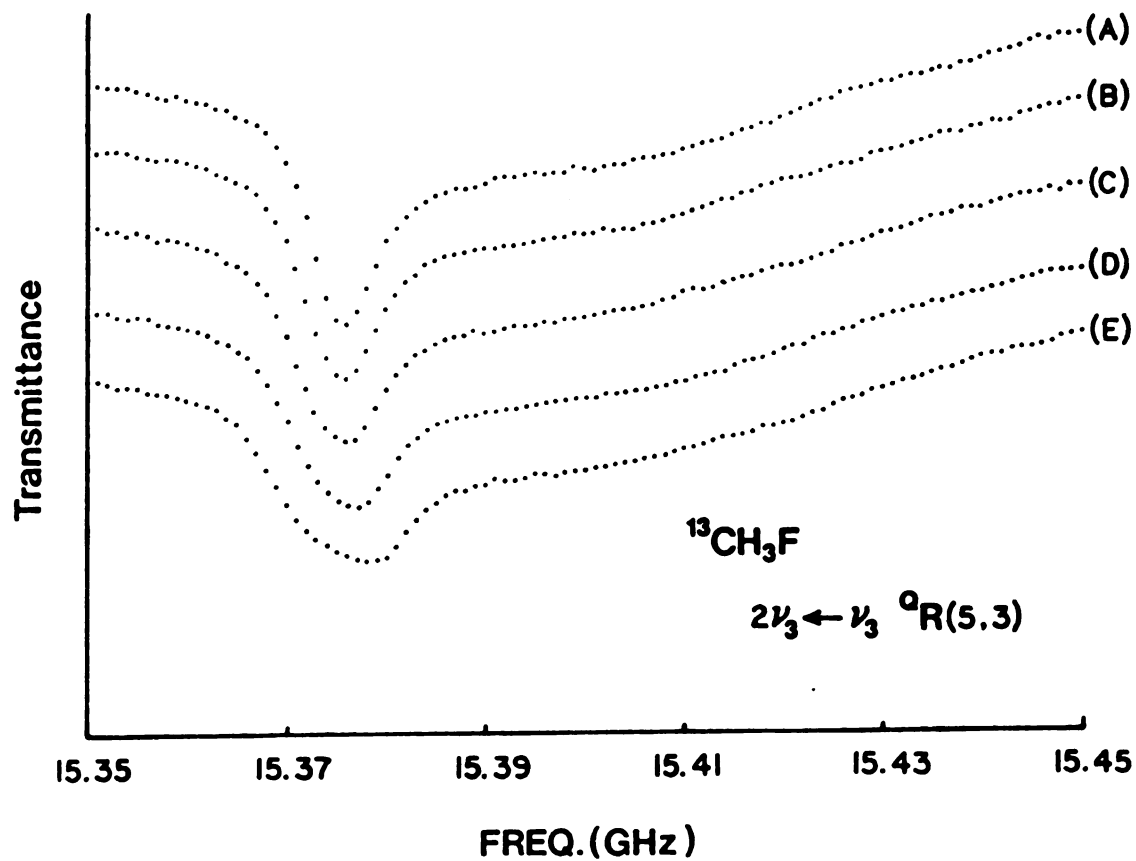


Figure 10. Variation of the range of the molecular velocity group pumped with the modulation amplitude of the pumping laser. The modulation amplitude was increased in steps from (A) to (E). The $^\text{Q} \text{R}(4,3)$ transition of the ν_3 band was pumped.

For the three-level double resonance (combination of B and C) which has the upper state of the transitions in common, the $Q_R(4,3)$ and $Q_P(6,3)$ transitions of the ν_3 band were pumped and monitored, respectively. Since one component of the molecular velocity groups was transferred into the upper state by pumping, the upper state was overpopulated at a particular velocity. Therefore, as shown in Fig. 11, the $Q_P(6,3)$ transition shows a saturation-dip at a frequency corresponding to the pumped velocity group. By tuning the laser frequency, the saturation-dip was shifted to another position, as shown in Fig. 12. In this experiment, the positive sideband generated from the $9P(50)CO_2$ laser line and P-band microwave radiation was used and the sample pressure was ~ 20 mTorr. The $9P(50)CO_2$ laser line is very weak in our system and many commercial CO_2 lasers cannot generate this radiation. However, by adjusting the laser gas mixture to the optimum condition for the $9P(50)CO_2$ laser line, approximately 100 mW of laser power could be obtained. Even with this low power for the sideband generator, excellent spectra were obtained (Figs. 11 and 12). This fact demonstrates the usefulness of the infrared-microwave sideband system for both linear and nonlinear spectroscopy. By using isotopic CO_2 lasers, we can get almost continuously tunable sideband radiation throughout the 9 - 11 μm region.

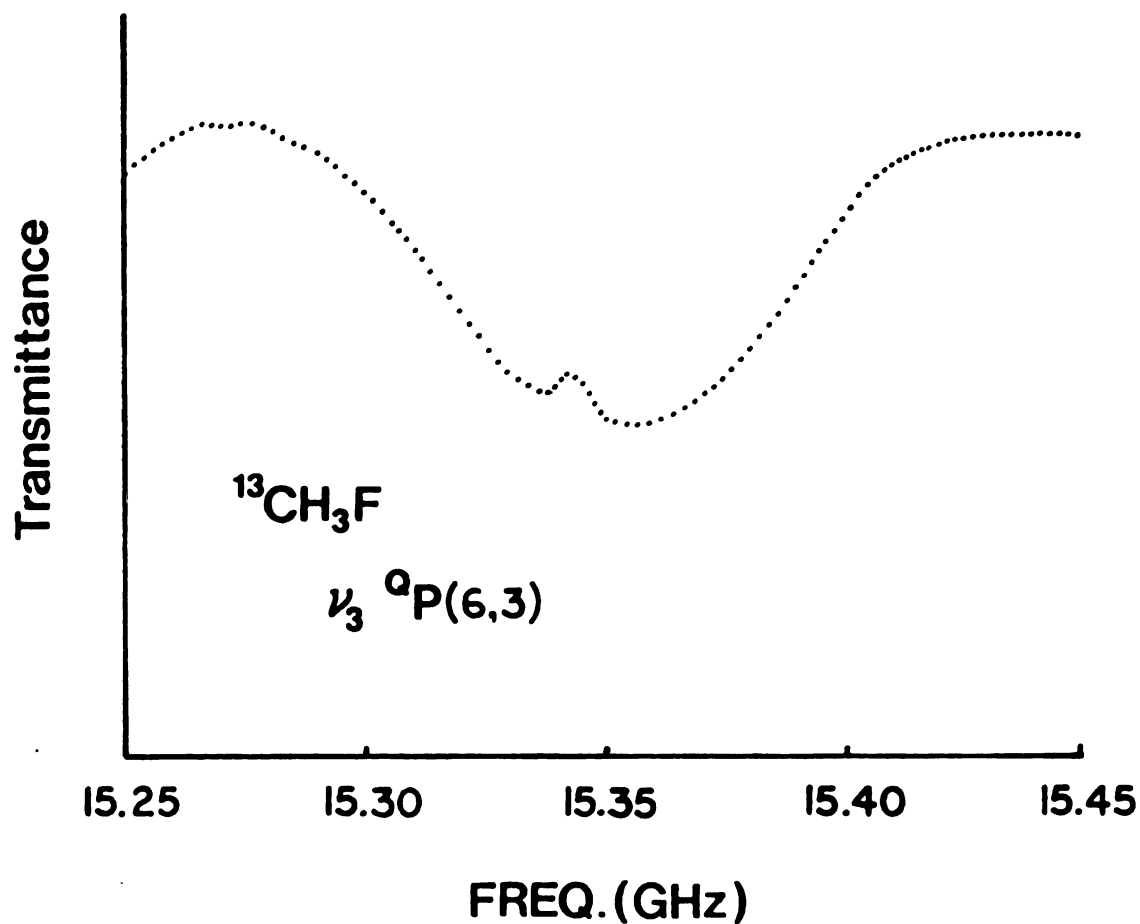


Figure 11. Observation of a saturation-dip in the $^Q\text{P}(6,3)$ transition in the ν_3 band from three-level double resonance with a common level in the upper state. The $^Q\text{R}(4,3)$ transition in the ν_3 band was pumped.

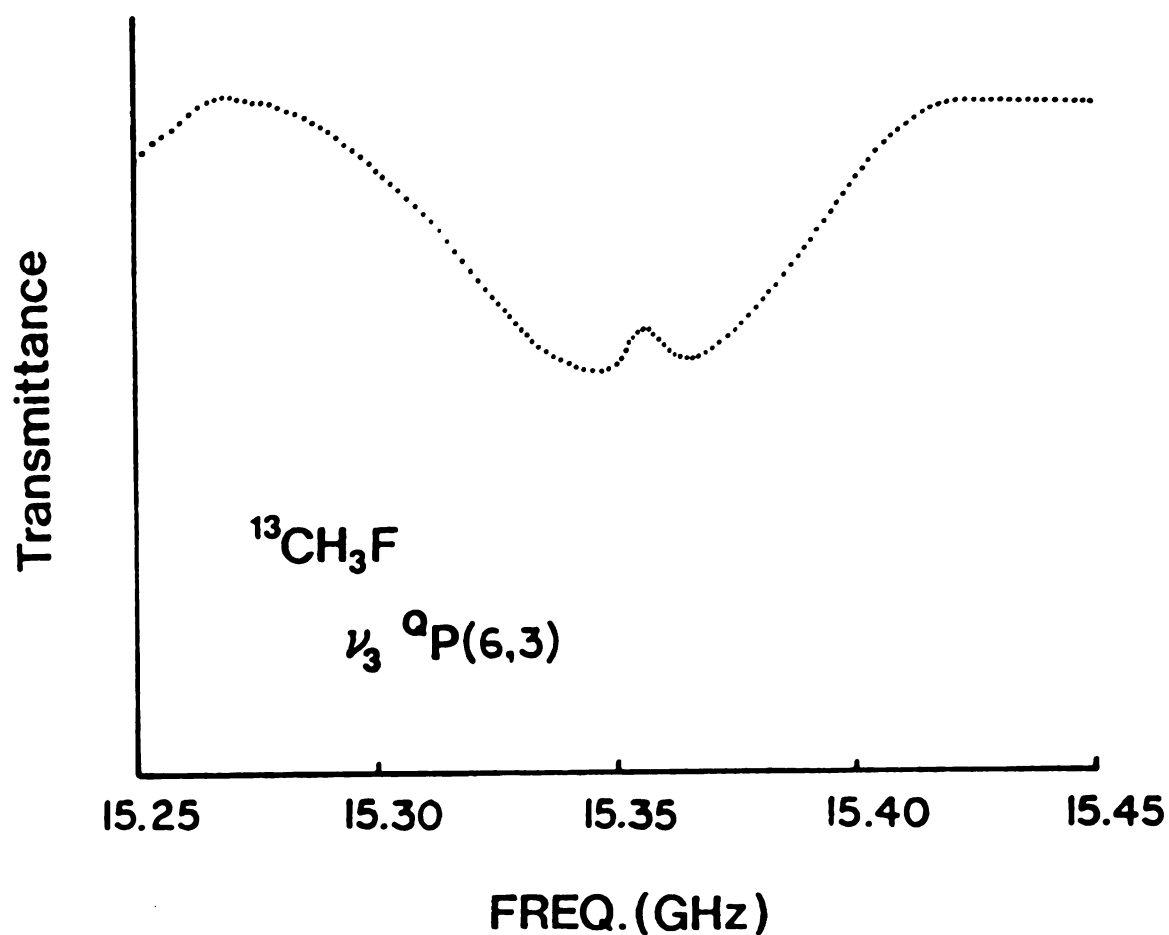


Figure 12. Observation of a saturation-dip in the $^{\text{Q}}\text{P}(6,3)$ transition in the ν_3 band from three-level double resonance with a common upper level. The pumping frequency in this figure has been shifted slightly from that in Figure 11.

As a result of the depletion in population of the $J = 4$, $K = 3$ level in the ground state of $^{13}\text{CH}_3\text{F}$ achieved by pumping the $^{\text{Q}}\text{R}(4,3)$ transition, the $^{\text{Q}}\text{P}(4,3)$ transition also shows a saturation-dip at a particular velocity group; this is shown in Fig. 13. The probing transition was monitored by scanning the negative sideband generated from the $9\text{P}(46)\text{CO}_2$ laser line and X-band microwave radiation at ~ 46 mTorr of sample pressure. This is a three-level double resonance (combination of B and D) with a common level at the lower state.

One of the advantages of infrared-infrared double resonance is to be able to observe the population difference between vibrational states compared to other types of double resonance. With the overpopulation at one velocity group achieved by pumping the $^{\text{Q}}\text{R}(4,3)$ transition of the ν_3 band, the $^{\text{Q}}\text{R}(5,3)$ transition of the $2\nu_3 + \nu_3$ band shows the pumping effect very clearly with a sharp saturation spike. Figure 14 shows this double resonance effect resulting from three-level double resonance with a common level between two transitions (combination of B and A). In this spectrum a sharp saturation-spike is seen, in which the position and the width of the spike depend on the pumping frequency and the modulation amplitude of a pumping laser, respectively. For the observation, the positive sideband generated from the $9\text{P}(46)\text{CO}_2$ laser line and P-band microwave radiation was

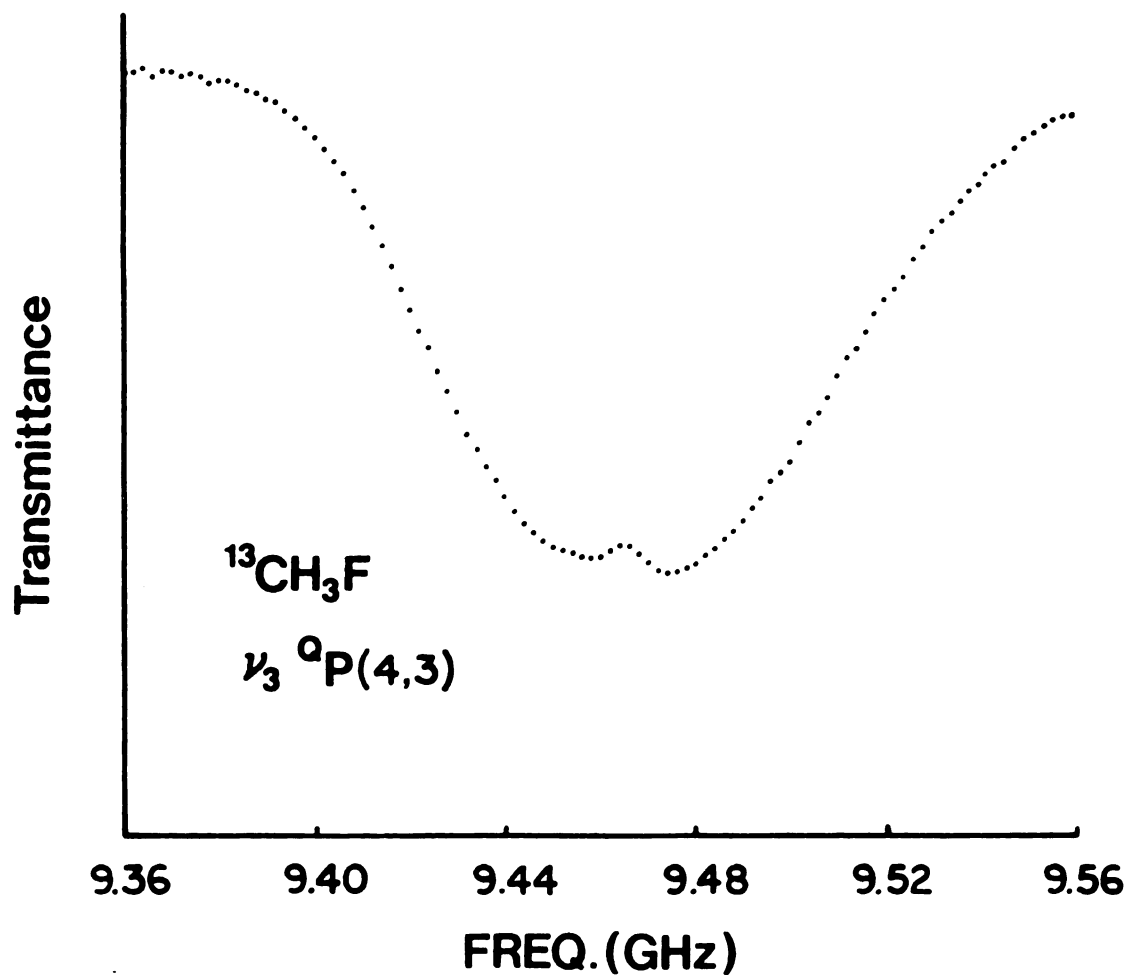


Figure 13. Observation of a saturation-dip in the $^{\text{Q}}\text{P}(4,3)$ transition in the ν_3 band from three-level double resonance with a common level in the lower state. The $^{\text{Q}}\text{R}(4,3)$ transition in the ν_3 band was pumped.

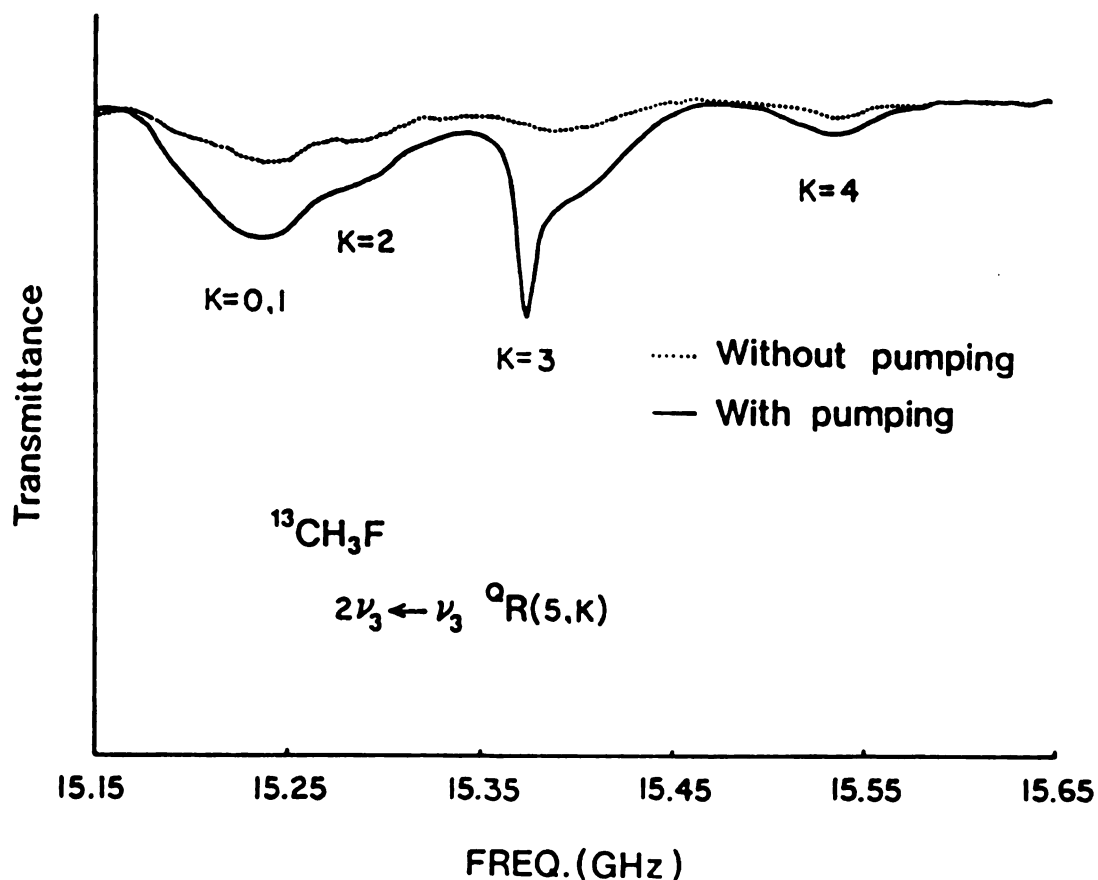


Figure 14. Observation of the increased intensity of the $^\text{Q} \text{R}(5,3)$ transition in the $2\nu_3 \leftarrow \nu_3$ band that results from three-level double resonance with a common level that is the upper state for the pumping transition and the lower state for the probing transition. Also shown is the increased intensity of the remaining $^\text{Q} \text{R}(5, \text{K})$ transitions that result from increased population of the $\nu_3 = 1$ state caused by pumping the $^\text{Q} \text{R}(4,3)$ transition in the fundamental band.

used and the sample pressure was ~96 mTorr.

Usually the rotational relaxation rate ($\sim 1 \mu\text{sec}$) is much faster than that of the vibrational relaxational rate ($\sim 1 \text{ msec}$). Both rates increase linearly with pressure. Under the conditions of our experiment, the rotational rate is so fast that a Boltzmann distribution is established among the populations of the rotational levels in both states and this saturation is not changed by variation in sample pressure up to ~1 Torr. However, the vibrational populations do not follow a Boltzmann distribution and are strongly affected by sample pressure.

Figure 15 shows the variation of the double resonance effect at the peak frequency of the direct pumping with sample pressure. This is a comparison of the peak height of the transferred spike in the $Q_R(5,3)$ transition in the $2\nu_3 - \nu_3$ band with pumping and without pumping. As the sample pressure increases, the double resonance effect (saturation effect) decreases because of the increase in the vibrational relaxation rate with the sample pressure.

Four-Level Double Resonance

According to the selection rule for collisional process ($\Delta J = 0, \pm 1, \Delta K = 0$), the possible candidates of four-level double resonance are the combinations of B and B

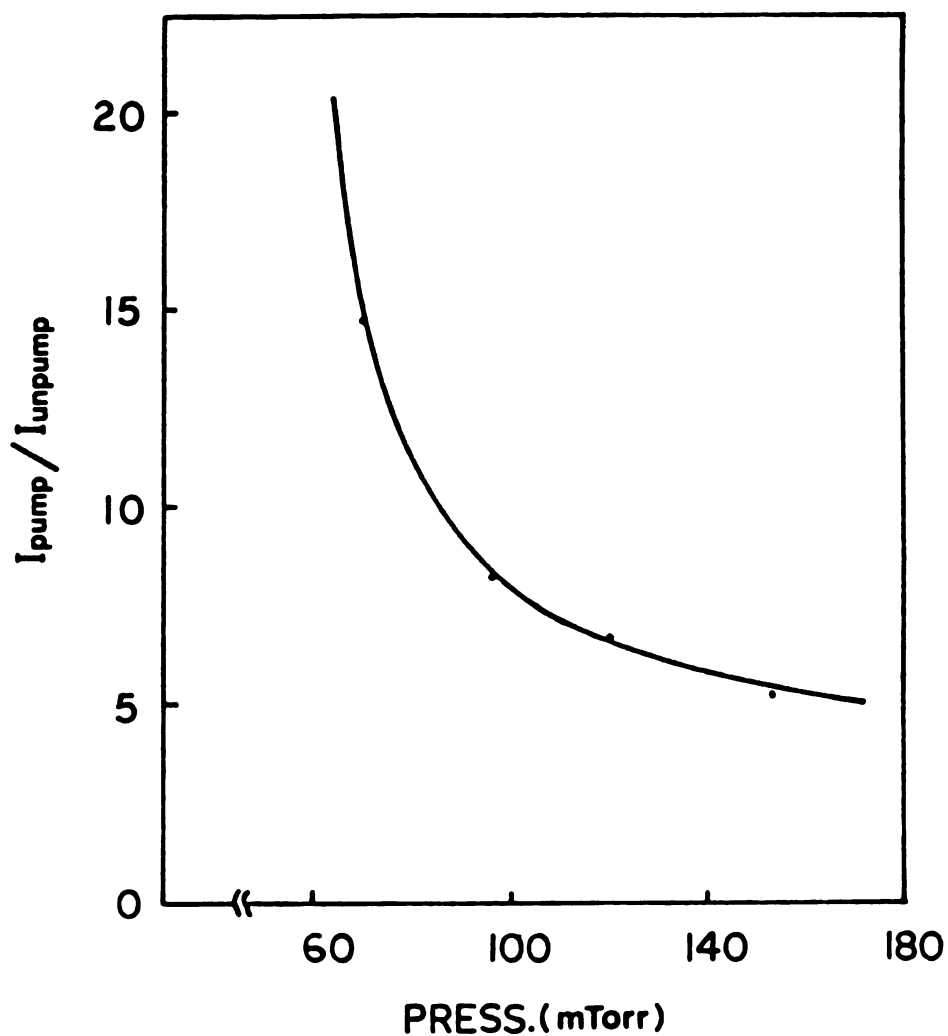


Figure 15. Variation of the double resonance effect on the intensity of the $Q_{R(5,3)}$ transition in the $2\nu_3 + \nu_3$ band with sample pressure. The lower level of this transition is directly pumped by pumping the $Q_{R(4,3)}$ transition in the ν_3 band. The solid line is a smooth curve drawn through the points.

and B and F in Fig. 8. No significant double resonance effects were observed for these combinations. We believe that this is because E and F are transitions in the fundamental band with high intensity and the collisional effect is small. For this experiment, the amplitude modulation of the probing radiation at 33.3 kHz was used. However, if we modulate the pumping radiation, it may be possible to observe the pumping effect from four-level double resonance on a fundamental band transition.

For the evidence for indirect pumping to all rotational levels in the excited state ($v_3 = 1$), the transitions $^Q P(22, K)$ of $2v_3 + v_3$ band were chosen because they are within the range of tunability of the sideband system and their energy levels and quantum numbers are much higher than that of the direct pumping level.

Comparison of peak heights with pumping and without pumping shows that the intensity of all the transitions was increased by a factor of 2 - 4. Figure 16 shows the spectrum obtained from this case of four-level double resonance, in which the negative sideband generated from the $10R(14)CO_2$ laser line and P-band microwave radiation was used with ~ 112 mTorr of sample pressure.

The $^Q P(17, 3)$ transition of the $2v_3 + v_3$ band was chosen for observation of the variation of the effect of indirect pumping with pressure, because its frequency is within the tunable range of a sideband system and its peak

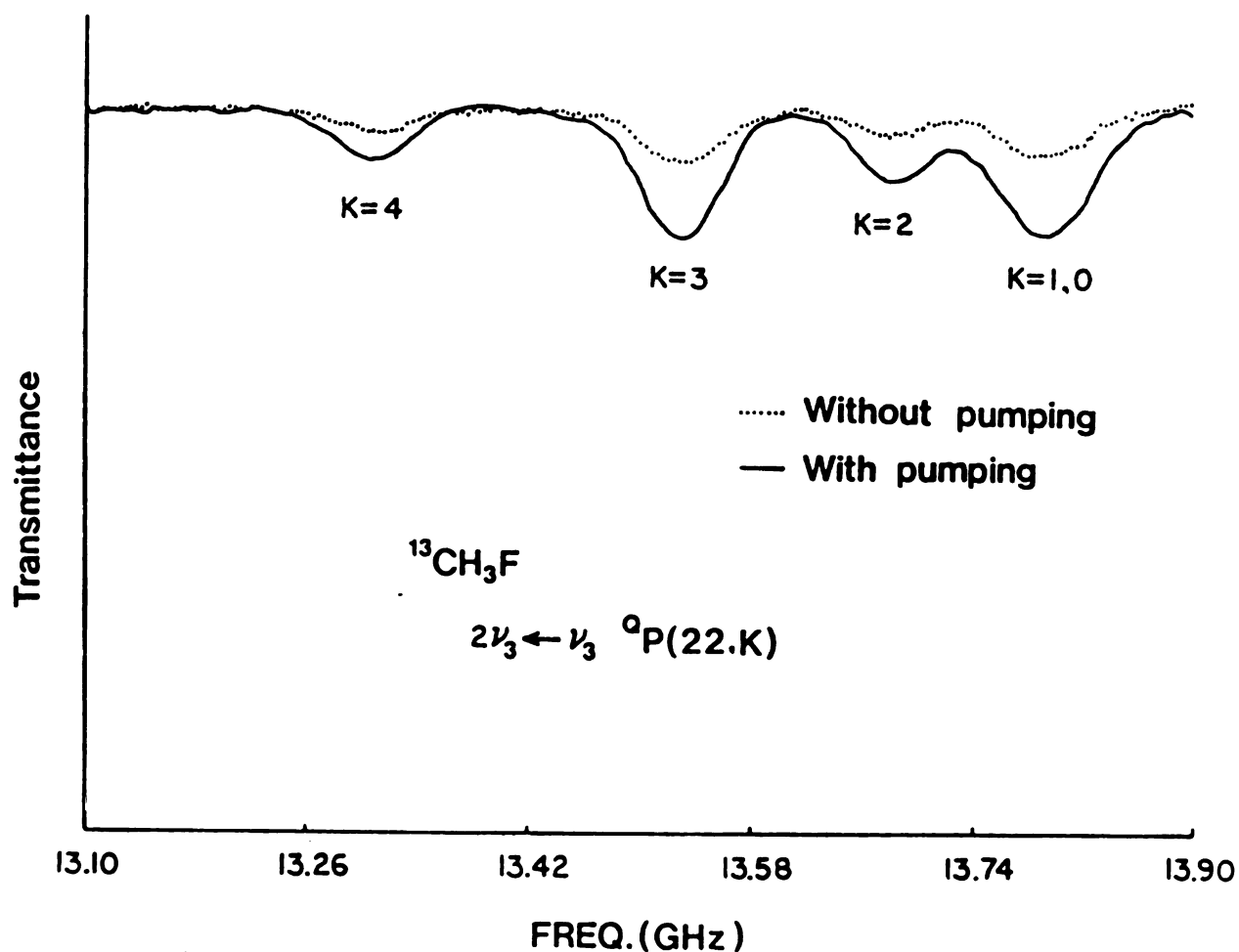


Figure 16. Observation of the indirect pumping effect to all rotational energy levels in the first excited vibrational state ($\nu_3 = 1$) by pumping the ${}^{\text{Q}}\text{R}(4,3)$ transition in the ν_3 band. The intensity of all transitions in the $2\nu_3 \leftarrow \nu_3$ band appears to increase with pumping.

is completely isolated from other transitions. From Fig. 17 it can be seen that the indirect pumping effect decreases with increasing sample pressure. As in the previous case of direct pumping, this phenomenon can be explained from the increasing vibrational relaxation rate with sample pressure. In Fig. 17, the ratio 1.0 means that there is no effect of indirect pumping on the intensity of the transition. The $10R(30)CO_2$ laser line and microwave radiation at a frequency of 15452 MHz were used to generate the negative sideband for this experiment.

The diagram in Fig. 18 may be used to explain indirect pumping phenomena. Without pumping, all vibration-rotation energy levels are subjected to the Boltzmann distribution. The population of the first excited state ($v_3 = 1$) is approximately 1% of that of the ground state and the population of the second excited state ($v_3 = 2$) is only 1% of that of the first excited state. We therefore write the relative populations as 99, 1, and 0.01. The effect of pumping causes a non-Boltzmann distribution in the ground state and first excited state. The population of (4,3) energy level in the ground state and of the (5,3) level in the first excited state are equalized by strong pumping of the $Q_R(4,3)$ transition. They therefore become 50 and 50. The overpopulation at the upper state decays to the ground vibrational state by vibrational relaxation and into other rotational levels in the first excited vibrational state by

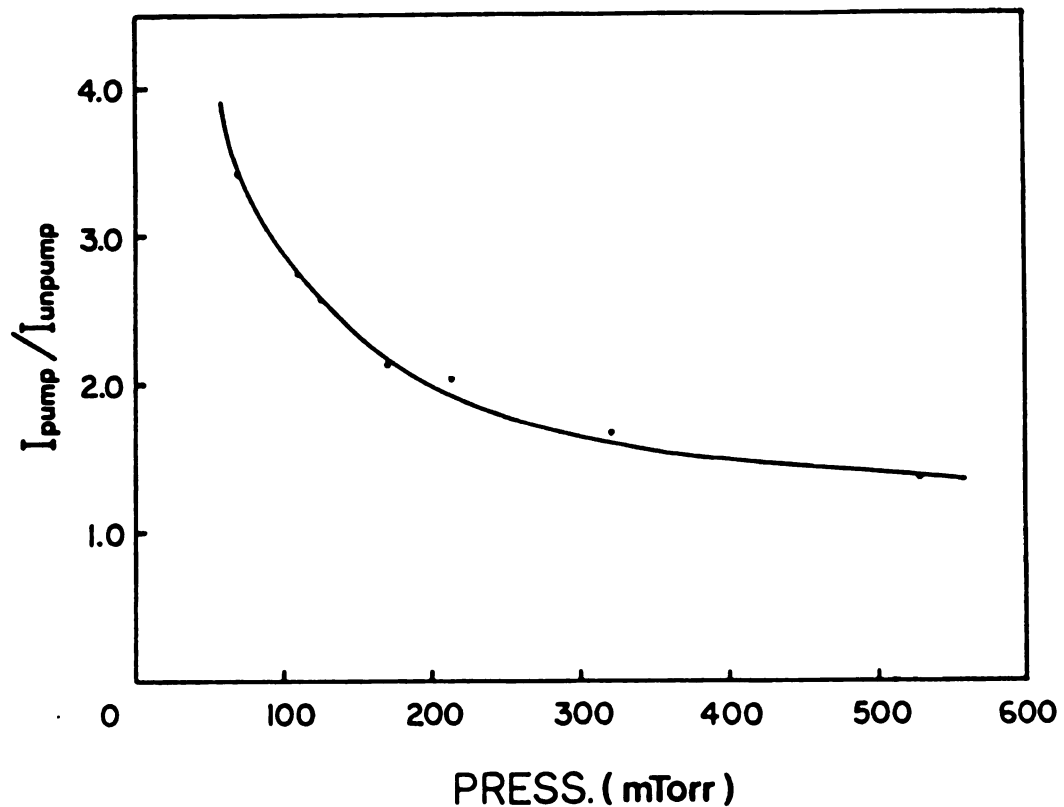


Figure 17. Variation of the effect of indirect pumping on the intensity of the ${}^Q\text{P}(17,3)$ transition of the $2\nu_3 + \nu_3$ band with sample pressure. The ${}^Q\text{R}(4,3)$ transition in the ν_3 band was pumped. The solid line is a smooth curve drawn through the points.

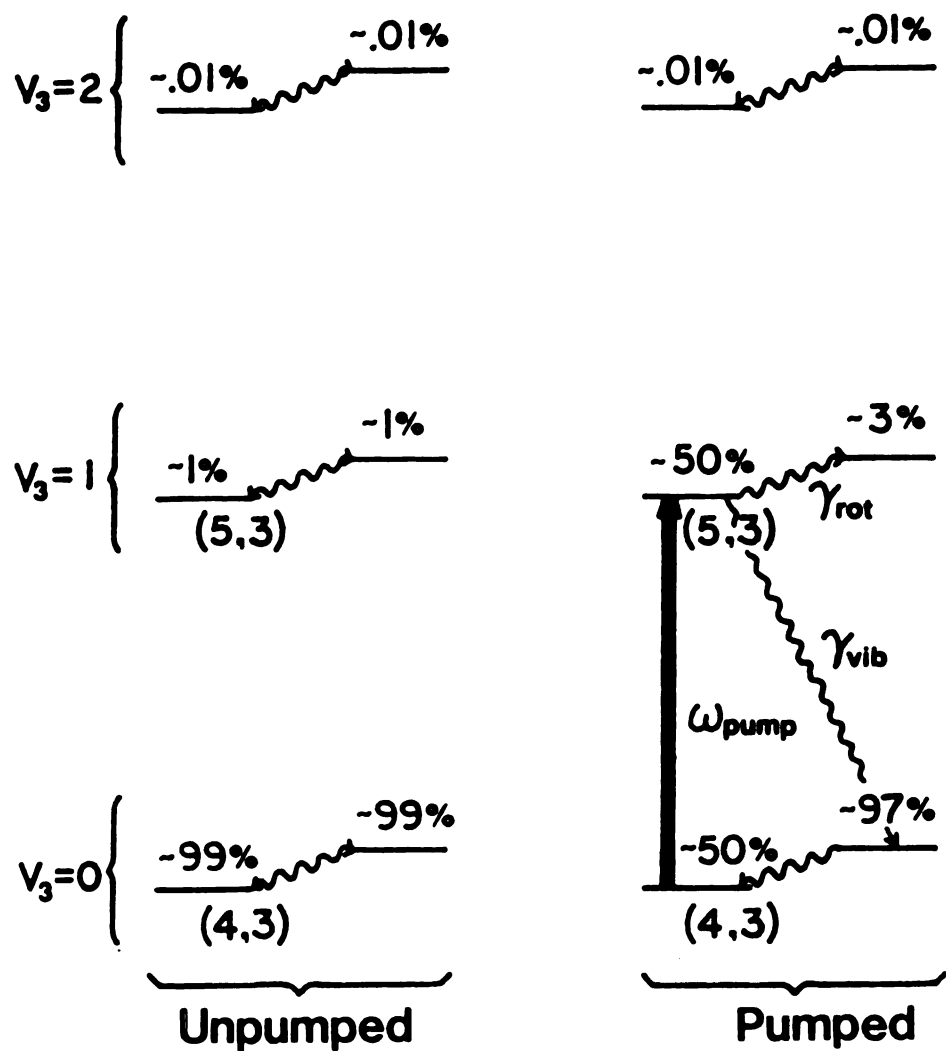


Figure 18. Schematic diagram of the molecular population changes caused by pumping the $^Q R(4,3)$ transition in the ν_3 band. The numbers above each level are relative populations.

either rotational relaxation,

$$(J, K, v_3=1) + (J', K', v_3=1) \rightarrow (J'', K'', v_3=1) + (J''', K''', v_3=1),$$

or by vibration-vibration energy transfer,

$$(J, K, v_3=1) + (J', K', v_3=0) \rightarrow (J'', K'', v_3=0) + (J''', K''', v_3=1).$$

In either case we imagine that collisions cause a small net loss in population of a connected level in the ground state and a corresponding gain in population of an excited state level.

At the steady state, the population difference between the ground vibrational state and the first excited vibrational state does not change very much by pumping ($99 - 1 = 98 \rightarrow 97 - 3 = 94$), while the population difference between the first excited state and the second excited state increases by a factor of 3 ($\sim 1 \rightarrow \sim 3$). This explanation seems to agree with the experimental results.

In order to confirm the above explanation explicitly, a frequency region was chosen in which a fundamental and a hot band transitions coexist. The region selected is the negative sideband tunable range generated from the $10R(20)CO_2$ laser line and X-band microwave radiation from 9.4 to 9.8 GHz. The evidence for indirect pumping to all rotational levels in the first excited vibrational state can

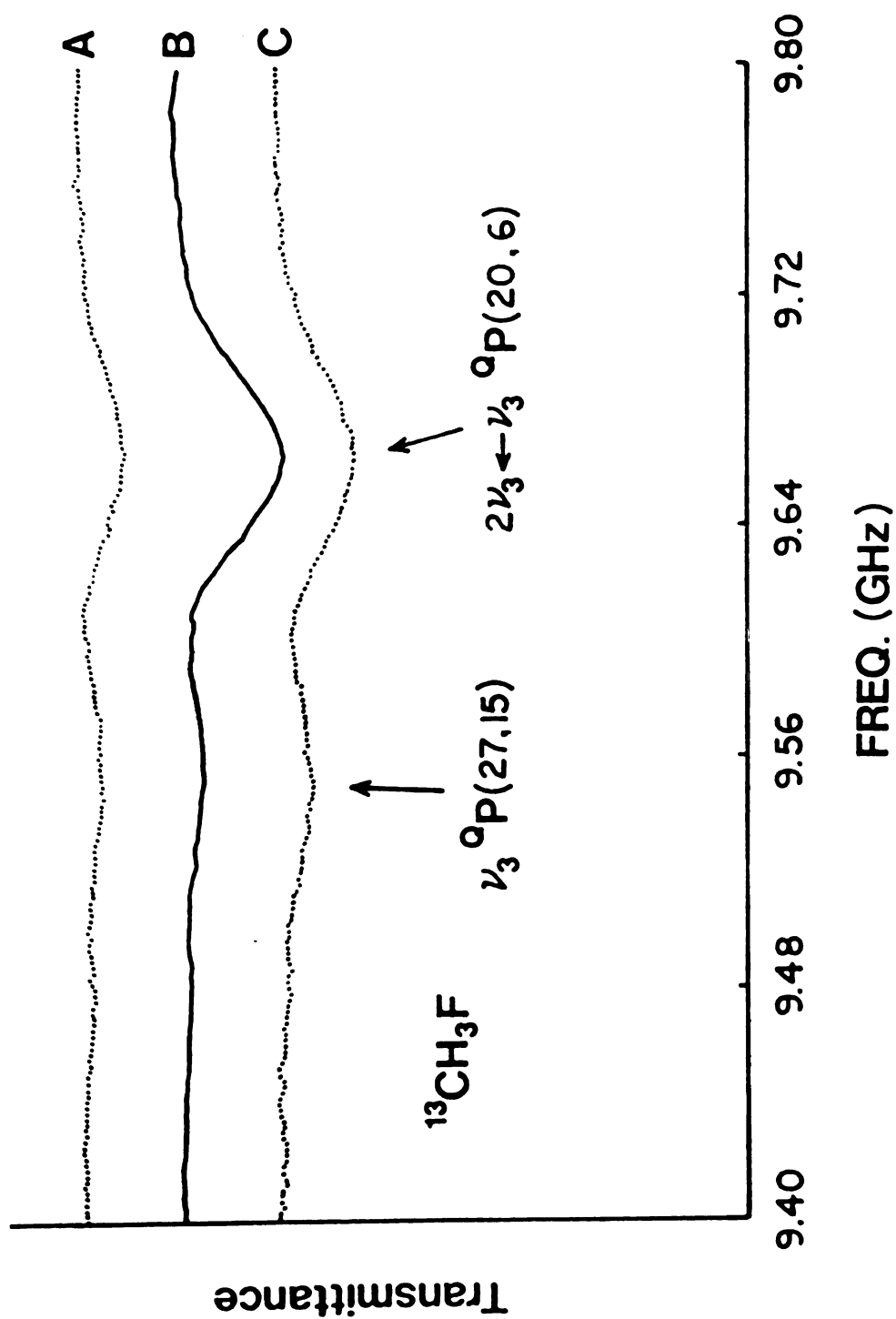


Figure 19. Comparison of the effects of indirect pumping and heating on transitions in the ν_3 fundamental and the $2\nu_3 \leftarrow \nu_3$ hot bands of $^{13}\text{CH}_3\text{F}$. The spectra was recorded (A) without pumping at room temperature, (B) with pumping of the $^{\text{Q}}\text{R}(4,3)$ transition in the ν_3 band at room temperature, and (C) without pumping at $\sim 100^\circ\text{C}$.

be seen in Fig. 19. The ν_3 fundamental and $2\nu_3 - \nu_3$ hot band transitions chosen are $^Q_P(27,15)$ and $^Q_P(20,6)$, respectively(61). For this example, the fundamental transition is seen to be weaker than the hot band transition. This is because the J and especially the K quantum number for the fundamental are enough larger than for the hot band transition that the lower level of the ν_3 transition is higher in energy than the lower level of the $2\nu_3 - \nu_3$ transition. Figure 19(A) indicates the spectrum obtained without pumping, Fig. 19(B) represents the spectrum obtained with pumping, and Fig. 19(C) exhibits the spectrum obtained by heating the sample cell to $\sim 100^\circ\text{C}$. In Fig. 19(B) only the hot band transition shows a significant change in intensity, whereas in Fig. 19(C) both the fundamental and the hot bands show increased intensity. This can be explained by the shift in the Boltzmann distribution to higher vibration-rotation quantum numbers as the temperature increases. Since the transitions chosen have high J and K values, the molecular population increases with the temperature. So the intensity of both transitions is increased by an amount proportional to the change in the Boltzmann factor. On the other hand, as a result of pumping the $^Q_R(4,3)$ transition at room temperature as shown in Fig. 19(B), the intensity of the transition in the fundamental band does not change, while the intensity of the transition in the hot band increases by a factor of 2 - 3 due to the

increased population of the $v_3 = 1$ state. This can be explained by the diagram shown in Fig. 18. These results also demonstrate that the four-level double resonance effects are not simply a result of heating the sample. The population of the $v_3 = 1$ vibrational level is increased, but the rotational temperature in the ground state is hardly changed. In most cases, the observation of a hot band transition is more difficult than that of a fundamental transition because of the small population in the first excited vibrational state (less than 1% of the ground state at room temperature if $\Delta E_v = 1000 \text{ cm}^{-1}$). In order to increase the intensity (spectrum signal) of hot band infrared transitions in gas samples, three methods have been used so far: increase the length of the sample cell in order to increase the beam path through the sample; increase the pressure of the sample in order to increase the number of molecules within the beam of radiation; and increase the sample temperature to increase the population of excited vibrational levels. But, when the sample pressure is increased, the collisional broadening effect ($\sim 20 \text{ MHz/Torr}$ for $^{13}\text{CH}_3\text{F}$) and the pressure shift of peak frequency ($\sim 3 \text{ MHz/Torr}$ for NH_3) should be considered. Also, the Doppler broadening increases with the temperature of sample. The application of the indirect pumping effect, however, to the observation of hot band transitions appears to be able to increase the intensity of $^{13}\text{CH}_3\text{F}$ transitions by a factor of

2 or more due to an increase of vibrational temperature without any additional considerations.

Until now, the only method used for distinguishing hot band transitions from fundamental band transitions is use of the shift of Boltzmann distribution with change in temperature. Unfortunately, as has been just seen, this method also increases the population of high J and K quantum states in the ground vibrational state. Therefore, the change in intensity upon heating or cooling the sample is not a reliable indicator of fundamental or hot band transitions. By contrast, the application of indirect pumping to the molecular system increases the intensity of hot band transitions and only weakly affects the intensity of fundamental band transitions.

In order to obtain evidence of vibration-vibration energy transfer, a sample that is an equimolar mixture of $^{12}\text{CH}_3\text{F}$ and $^{13}\text{CH}_3\text{F}$ was made. The $^{\text{Q}}\text{R}(4,3)$ transition in the ν_3 band of $^{13}\text{CH}_3\text{F}$ was again pumped. The pumping increased the intensity of the $^{\text{Q}}\text{Q}(12,9)$ transition in the $2\nu_3 + \nu_3$ band of $^{12}\text{CH}_3\text{F}$ as shown in Fig. 20, which confirmed the vibration-vibration energy transfer described by Preses and Flynn(60).

In summary, a waveguide CO_2 laser was used for pumping and an infrared-microwave sideband laser was used for probing infrared-infrared double resonance of $^{13}\text{CH}_3\text{F}$.

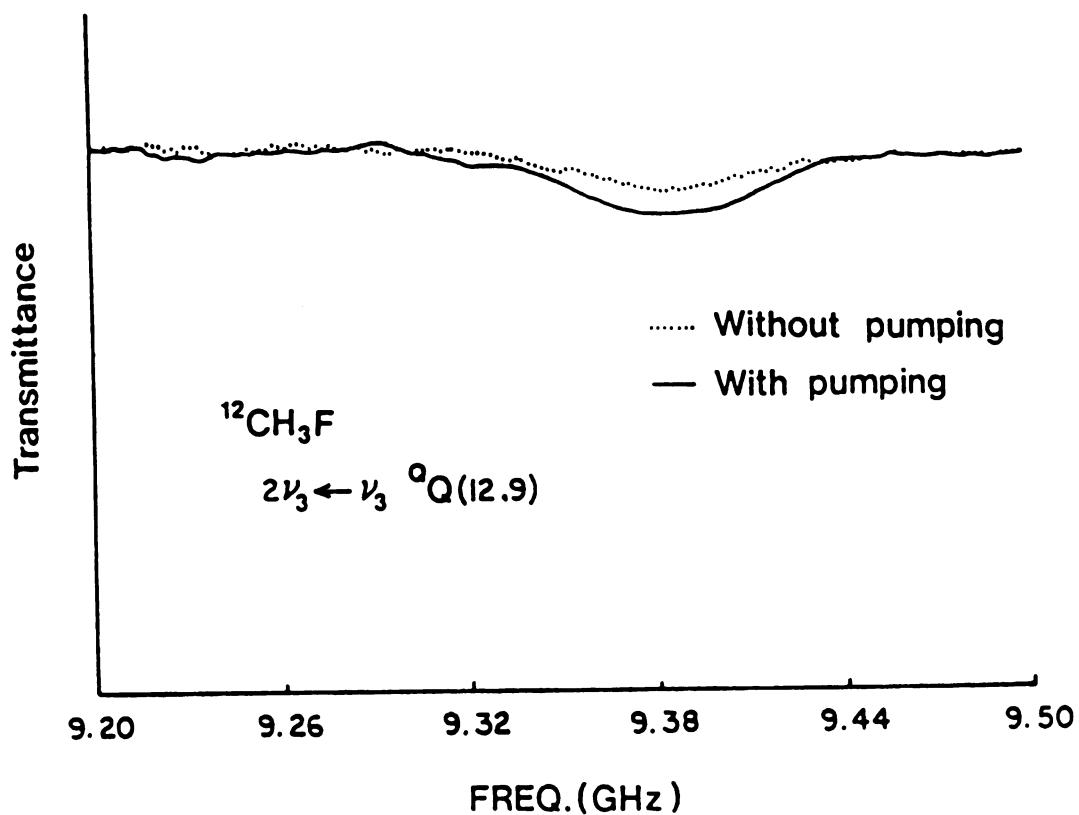


Figure 20. Observation of the effect of vibrational energy transfer between $^{13}\text{CH}_3\text{F}$ and $^{12}\text{CH}_3\text{F}$ on the intensity on the ${}^0\text{Q}(12,9)$ transition in the $2\nu_3 \leftarrow \nu_3$ band of $^{12}\text{CH}_3\text{F}$. The ${}^0\text{R}(4,3)$ in the ν_3 band of $^{13}\text{CH}_3\text{F}$ was pumped.

The observations included evidence for direct pumping of a particular velocity component by three-level double resonance, evidence for indirect pumping to all rotational levels in the first excited state ($v_3 = 1$) by four-level double resonance, and evidence for vibration-vibration energy transfer.

REFERENCES

1. T. Oka, Adv. in Atomic and Molecular Physics Vol. 9, 127-206(1973).
2. J. P. Toennies, Discuss. Faraday Soc. 33, 96-98 (1962).
3. T. Carrington, J. Chem. Phys. 31, 1418-1419 (1959).
4. R. G. Brewer, Science 178, 247-255 (1972).
5. G. Duxbury, Chem. Soc. Rev. 12, 453-504 (1983).
6. J. Brossel and F. Bitter, Phys. Rev. 86, 308-316 (1952).
7. A. P. Cox, G. W. Flynn, and E. B. Wilson, Jr., J. Chem. Phys. 42, 3094-3106 (1965).
8. A. M. Ronn and E. B. Wilson, Jr., J. Chem. Phys. 46, 3262-3263 (1967).
9. R. G. Gordon, P. E. Larson, C. H. Thomas, and E. B. Wilson, Jr., J. Mol. Phys. 50, 1388-1393 (1969).
10. J. B. Cohen and E. B. Wilson, Jr., J. Chem. Phys. 58, 456-467 (1973).
11. J. B. Cohen and E. B. Wilson, Jr., J. Chem. Phys. 58, 442-455 (1973).
12. T. Oka, J. Chem. Phys. 45, 754-755 (1966).
13. T. Oka, J. Chem. Phys. 45, 752-753 (1966).
14. T. Oka, J. Chem. Phys. 47, 4852-4853 (1967).
15. T. Oka, J. Chem. Phys. 47, 13-26 (1967).
16. T. Oka, J. Chem. Phys. 48, 4919-4928 (1968).
17. T. Oka, J. Chem. Phys. 49, 3135-3145 (1968).
18. T. Oka, J. Chem. Phys. 49, 4234-4235 (1968).
19. P. W. Daly and T. Oka, J. Chem. Phys. 53, 3272-3278 (1970).

20. A. T. Fabris and T. Oka, J. Chem. Phys. 56, 3168-3169 (1972).
21. A. M. Ronn and D. R. Lide, Jr., J. Chem. Phys. 47, 3669-3672 (1967).
22. H. Jetter, E. F. Pearson, C. L. Norris, J. C. McGurk, and W. H. Flygare, J. Chem. Phys. 59, 1796-1804 (1973).
23. L. Frenkel, H. Marantz, and T. Sullivan, Phys. Rev. A3, 1640-1651 (1971).
24. H. Jones and F. Kohler, J. Mol. Spectrosc. 58, 125-141 (1975).
25. T. Shimizu and T. Oka, J. Chem. Phys. 53, 2536-2537 (1970).
26. T. Shimizu and T. Oka, Phys. Rev. A2, 1177-1181 (1970).
27. W. A. Kreiner and H. Jones, J. Mol. Spectrosc. 49, 326-329 (1974).
28. M. Fourrier and M. Redon, Appl. Phys. Lett. 21, 463-464 (1972).
29. J. Lemaire, J. Thibault, F. Herlemont, and J. Houriez, Molec. Phys. 27, 611-624 (1972).
30. J. M. Levy, J. H. S. Wang, S. G. Kukolich, and J. I. Steinfeld, Phys. Rev. Lett. 29, 395-398 (1972).
31. J. M. Levy, J. H. S. Wang, S. G. Kukolich, and J. I. Steinfeld, Chem. Phys. Lett. 21, 598-602 (1973).
32. M. Fourrier and M. Redon, J. Appl. Phys. 45, 1910-1911 (1974).
33. S. Kano, T. Amano, and T. Shimizu, Chem. Phys. Lett. 25, 119-121 (1974).
34. S. M. Freund and T. Oka, Appl. Phys. Lett. 21, 60-62 (1972).
35. G. M. Dobbs, R. H. Micheels, J. I. Steinfeld, J. H. S. Wang, and J. M. Levy, J. Chem. Phys. 63, 1904-1913 (1975).
36. M. Redon, H. Gurel, and M. Fourrier, Chem. Phys. Lett. 30, 99-103 (1976).

37. S. Kano, T. Amano, and T. Shimizu, J. Chem. Phys. 64, 4711-4718 (1976).
38. C. K. Rhodes, M. J. Kelly, and A. Javan, J. Chem. Phys. 48, 5730-5731 (1968).
39. R. G. Brewer, Phys. Rev. Lett. 25, 1639-1641 (1970).
40. A. C. Luntz and R. G. Brewer, J. Chem. Phys. 54, 3641-3642 (1972).
41. A. C. Luntz, Chem. Phys. Lett. 11, 186-187 (1971).
42. A. C. Luntz, J. D. Swalen, and R. G. Brewer, Chem. Phys. Lett. 14, 512-513 (1972).
43. H. R. Schlossberg and A. Javan, Phys. Rev. Lett. 17, 1242-1244 (1966).
44. I. Burak, A. V. Nowak, J. I. Steinfeld, and D. G. Sutton, J. Chem. Phys. 51, 2275-2276 (1969).
45. J. I. Steinfeld, I. Burak, D. G. Sutton, and A. V. Nowak, J. Chem. Phys. 52, 5421-5434 (1970).
46. J. I. Steinfeld, I. Burak, D. G. Sutton, and A. V. Nowak, J. Chem. Phys. 53, 3390 (1970).
47. P. L. Houston, A. V. Nowak, and J. I. Steinfeld, J. Chem. Phys. 58, 3373-3380 (1973).
48. J. M. Preses and G. W. Flynn, Bull. Am. Phys. Soc. 17, 573-574 (1972).
49. S. M. Freund, J. W. Jones, A. R. W. McKellar, and T. Oka, J. Chem. Phys. 59, 3445-3453 (1973).
50. R. L. Shoemaker, S. Stenholm, and R. G. Brewer, Phys. Rev. A10, 2037-2050 (1974).
51. R. G. Brewer, R. L. Shoemaker, and S. Stenholm, Phys. Rev. Lett. 33, 63-66 (1974).
52. T. Oka and T. Shimizu, Phys. Rev. A2, 587-593 (1970).
53. B. J. Orr and T. Oka, J. Mol. Spectrosc. 66, 302-313 (1977).
54. J. Orr and T. Oka, Appl. Phys. 21, 293-306 (1980).
55. D. J. Bedwell and G. Duxbury, Chem. Phys. 37, 445-452

(1979).

56. G. Duxbury and H. Kato, Chem. Phys. 66, 161-167 (1982).
57. W. H. Weber and R. W. Terhune, J. Chem. Phys. 78, 6437-6446 (1983).
58. H. Kuze, H. Jones, M. Tsukakoshi, A. Minoh, and M. Takami, J. Chem. Phys. 80, 4222-4229 (1984).
59. W. A. Kreiner, A. Eyer, and H. Jones, J. Mol. Spectrosc. 52, 420-438 (1974).
60. J. M. Preses and G. W. Flynn, J. Chem. Phys. 66, 3112-3116 (1977).
61. S. K. Lee, R. H. Schwendeman, and G. Magerl, to be published.
62. L. Allen, J. H. Eberly, "Optical Resonance and Two-Level Atoms", John Wiley & Sons, Inc., New York, NY, 1975.
63. A. Javan, "Doppler free spectroscopy", in Advances in Laser Spectroscopy, ed. by F.T. Arecchi, F. Strumia, and H. Walther, Plenum Press, New York, NY, 1983.
64. K. Shimoda, "Infrared-microwave double resonance", in Laser Spectroscopy (R. G. Brewer and A. Mooradian, eds.), Plenum publishing Co., NY, 1974.
65. R. L. Abrams, Appl. Phys. Lett. 25, 609-611 (1974).
66. R. L. Abrams and W. B. Bridges, IEEE J. Quantum Electron. QE-9, 940-946 (1973).
67. H. Jones and F. Kohler, J. Mol. Spectrosc. 58, 125-141 (1975).